ICRR ANNUAL REPORT 2023



INSTITUTE

FOR

COSMIC RAY RESEARCH

THE UNIVERSITY OF TOKYO

ANNUAL REPORT
(APRIL 2023 – MARCH 2024)



Editorial Board

ASANO, Katsuaki

SAKAMOTO, Eri

TAKENAGA, Yumiko

NAKAMURA, Makio

ITO, Yoriko

©Institute for Cosmic Ray Research, The University of Tokyo

5-1-5, Kashiwanoha, Kashiwa, Chiba 277-8582, Japan

Telephone: (81) 4-7136-3102
Facsimile: (81) 4-7136-3115
WWW URL: http://www.icrr.u-tokyo.ac.jp/

TABLE OF CONTENTS

Preface

Research Divisions 1

Neutrino and Astroparticle Division 2
High Energy Cosmic Ray Division 32
Astrophysics and Gravity Division 66

Observatories and a Research Center 83

Norikura Observatory 84
Akeno Observatory 91
Kamioka Observatory 95
Kagra Observatory 96
Research Center for Cosmic Neutrinos 97
High Energy Astrophysics Facility in Canarias 98

Appendix A. ICRR Workshops and Ceremonies 100

Appendix B. ICRR Seminars 103

Appendix C. List of Publications 103

(a) Papers Published in Journals
(b) Conference Papers

Appendix D. Doctoral Theses 111

Appendix E. Public Relations 112

(a) ICRR News
(b) Public Lectures
(c) Visitors

Appendix F. Inter-University Research Activities 118

Appendix G. List of Committee Members 124

(a) Board of Councillors
(b) Advisory Committee
(c) Inter-University Research Advisory Committee

Appendix H. List of Personnel 125

PREFACE

This report summarizes the scientific activities of the Institute for Cosmic Ray Research (ICRR) of The University of Tokyo in the Japanese fiscal year (JFY) 2023.

ICRR is an inter-university research institute dedicated to the study of cosmic rays. The headquarters of ICRR is located in Kashiwa, Chiba prefecture, Japan. To promote various cosmic-ray-related studies efficiently, ICRR has three research divisions; the Neutrino and Astroparticle Division, the High Energy Cosmic Ray Division, and the Astrophysics and Gravity Division. ICRR operates four observatories in Japan; Kamioka Observatory and KAGRA Observatory (both located underground in Kamioka, Gifu prefecture), Norikura Observatory (2770 meters above sea level on Mt. Norikura, Gifu prefecture), and Akeno Observatory (Yamanashi prefecture). Additionally, it has one research center; the Research Center for Cosmic Neutrinos (Kashiwa, Chiba prefecture). Outside of Japan, there are three major experimental facilities located in Utah (USA), Yangbajing (Tibet, China), and on the island of La Palma island (Spain).

Many researchers from various Japanese institutions, as well as those from overseas, are involved in the research programs of ICRR. It should be noted that most of the scientific outputs from ICRR are the results of collaborative efforts by many researchers from various institutions. To produce outstanding results, it is very important to conduct experiments through international collaboration composed of top-level researchers from around the world. Consequently, all the experimental collaborations that ICRR is involved in are international. Due to these activities, ICRR was selected as one of the institutions in the "International Joint Usage/Research Center" program by Ministry of Education, Culture, Sports, Science and Technology -Japan (MEXT) in November 2018.

From JFY2020 to JFY2022, our inter-university research activities were deeply affected by the COVID-19 pandemic. Still, even during the pandemic, ICRR continued various research activities, such as continuous operation of the detectors, as described in previous reports. In JFY2023, our activities have returned normal; however, we have adopted effective methods that we have learned during the COVID-19 pandemic.

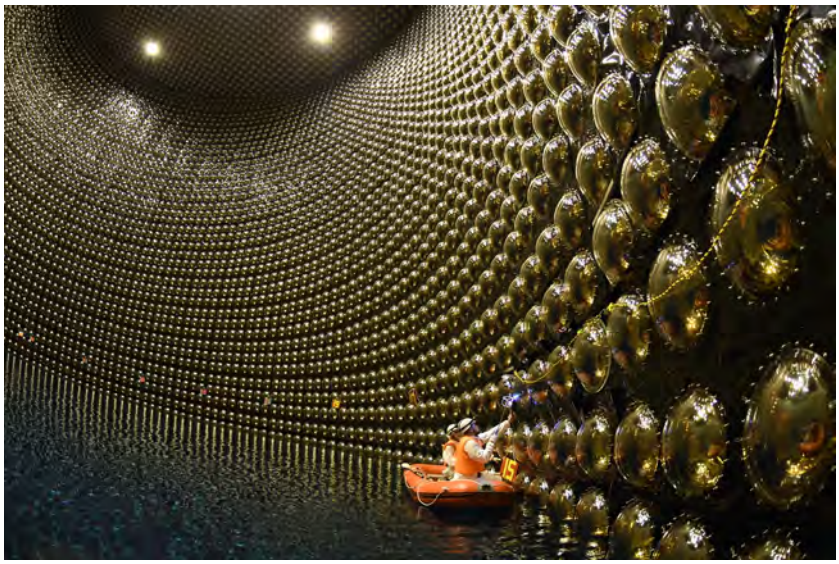
We hope that this report is useful for understanding the current research activities of ICRR. Finally, we appreciate the strong support of our colleagues in this research field, The University of Tokyo and MEXT. Their support is indispensable for the continued and exciting scientific outcomes of ICRR.



Masayuki Nakahata,
Director,
Institute for Cosmic Ray Research,
The University of Tokyo



The ICRR building at Kashiwa, Chiba, Japan.



The Super-Kamiokande detector (the photo was taken during refurbishment work in 2018).



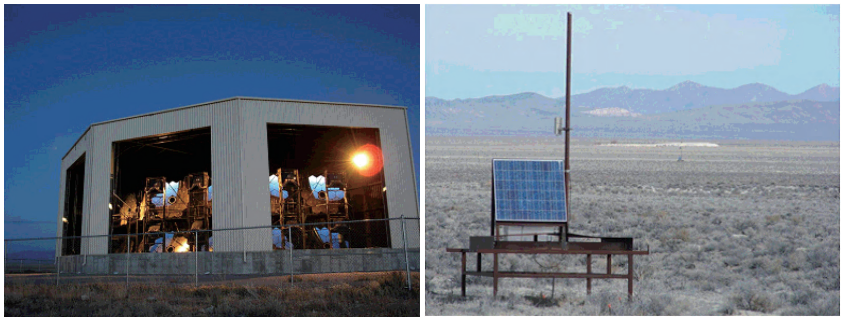
The ceiling part of the Hyper-Kamiokande main cavern under excavation. (March 2023)



The first Large Size Telescope of CTA installed at Observatory Roque de los Muchachos inaugurated on October 10 2018.



Tibet-III air shower array (37000 m^2) at Yangbajing, Tibet (4300 m in altitude).



Air fluorescence telescopes (left) and a scintillator surface detector (right) of the Telescope Array experiment in Utah, USA to explore the origin of extremely high energy cosmic rays.



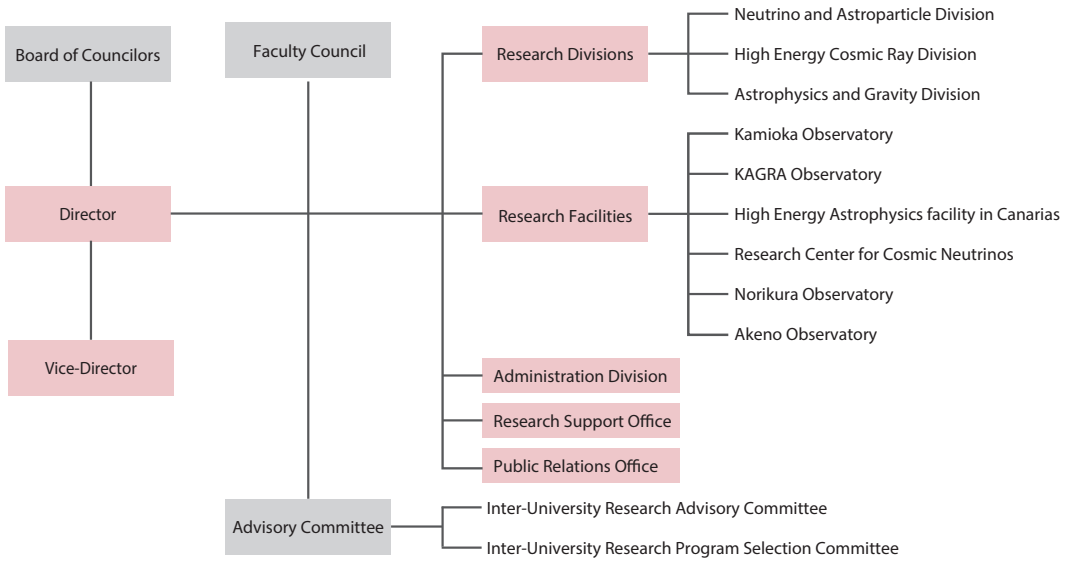


KAGRA's (left) 3km-long arm tunnel and (right) a sapphire mirror installed in a cryogenic suspension system.



Online public lecture co-organized with the Institute for the Physics and Mathematics of the Universe (Kavli IPMU).

Organization



Number of Staff Members (As of May 1, 2023)

	Scientific Staff	Technical Staff	Research Fellows	Administrators and Secretaries	Total
Neutrino and Astroparticle Div.	25	6	1	20	52
High Energy Cosmic Ray Div.	19	14	10	4	47
Astrophysics and Gravity Div.	19	14	4	10	47
Administration	0	0	0	20	20
Total	63	34	15	54	166

FY 2016-2023 Budget

	2016	2017	2018	2019	2020	2021	2022	2023
Personnel expenses	683 000	779 000	823 000	872 000	898 000	898 000	1 048 000	1 068 000
Non-personnel expenses	1 288 000	1 514 000	1 729 000	1 611 000	1 173 000	2 078 000	1 990 000	1 974 000
Total	1 971 000	2 293 000	2 552 000	2 483 000	2 071 000	2 976 000	3 038 000	3 042 000

(in 1 000 yen)

RESEARCH DIVISIONS

Neutrino and Astroparticle Division

- **Overview**
- **Super-Kamiokande**
- **T2K Experiment**
- **XMASS Experiment**
- **Hyper-Kamiokande**

High Energy Cosmic Ray Division

- **Overview**
- **Cherenkov Cosmic Gamma-Ray Group**
- **TA: Telescope Array Experiment**
- **Tibet ASγ Experiment**
- **ALPACA Project**
- **High Energy Astrophysics Group**
- **Other Activities**

Astrophysics and Gravity Division

- **Overview**
- **Gravitational Wave Group**
  - KAGRA Project
- **Observational Cosmology Group**
- **Theory Group**
  - Particle Phenomenology
  - Particle Cosmology

NEUTRINO AND ASTROPARTICLE DIVISION

Overview

This division aims to study particle physics with prime interests in physics of neutrinos and proton decay, and astroparticle physics with the use of underground experimental facilities.

The Super-Kamiokande (SK) detector is a 50 kton water Cherenkov detector using 11,129 50 cm-diameter photomultipliers (PMTs) for its inner detector and 1,885 20 cm-diameter PMTs for its outer detector. The data taking of SK started in April 1996 and 20th anniversary was celebrated in 2016. The neutrino oscillations in atmospheric neutrinos were discovered in 1998 and thereby it was demonstrated that neutrinos have a finite mass. In 2001, the accurate measurements of the ^{8}B solar neutrino flux by SK and SNO discovered that neutrino oscillations are the solution of the solar neutrino problem beyond doubt. These findings became the research achievement for which the Nobel Prize in Physics was awarded in 2015. After the epoch-making discoveries, precise measurements of atmospheric neutrinos and solar neutrinos have been performed and they unraveled various phenomena of neutrino oscillations. The evidence of tau neutrino appearance in atmospheric neutrinos was confirmed in 2013 and atmospheric neutrino anomaly has been finally concluded. The indication of day-night asymmetry of the solar neutrino flux, which is expected from the matter effect of neutrino oscillations, was reported in 2014. At present, the most interesting subjects in those observations are the determination of neutrino mass hierarchy using atmospheric neutrinos and the consistency check of solar(ν_e) and reactor($\bar{\nu}_e$) oscillations.

A high intensity neutrino beam experiment using the J-PARC accelerator (T2K) was started in 2009. The T2K experiment uses the SK detector as the far detector. Search for leptonic *CP* violation and the high precision measurement of oscillation parameters are main physics subjects in T2K. An indication of electron neutrino appearance was found in June 2011, and later the electron appearance has been established with greatly improved significance. Since 2014, anti-neutrino beam data also have been taken in order to search for *CP* violation. T2K later reported the exclusion of the conservation of *CP* symmetry in neutrino oscillations at more than 95% CL.

The search for nucleon decay is another important subject at SK because it gives a direct evidence for the Grand Unified Theories (GUTs). SK gives the current best limit which strongly constrains various GUT models.

If a supernova happens in our galaxy, thousands of neutrino interactions are expected at SK and they will reveal detailed mechanism of the supernova explosion. SK is the only detector in the world which can identify the direction of the supernova neutrinos. So, SK has been operated almost all the time with small dead time and if a supernova is observed at SK, we will send burst information to astronomers as soon as it is detected. In addition, SK aims to observe supernova relic neutrinos, which is an accumulated supernova burst neutrinos from the beginning of the universe. For this purpose, it is planned to add 0.1% of gadolinium into the Super-K tank (called SK-Gd project) in order to tag neutrons for $\bar{\nu}_e$ detection. A feasibility study for the SK-Gd project is being performed using a 200 ton tank which mimics the Super-K detector. Refurbishment of the Super-K tank and upgrade of the water circulation system were conducted in 2018, 0.01% gadolinium was dissolved in the detector water in the summer of 2020, and further additions in the summer of 2022 achieved 0.03% gadolinium concentration.

Another activity of the Neutrino and Astroparticle division is a multi-purpose experiment using liquid xenon aiming at the detection of cold dark matter, neutrino absolute mass using neutrinoless double beta decay, and low energy solar neutrinos. A 800 kg liquid xenon detector was constructed in an experimental hall near the SK site. Data taking continued for more than five years and completed in February 2019. Searches for dark matter interactions and rare phenomena in liquid xenon have been conducted and finally concluded in 2023. This activity is strengthened by participation in a major experiment at an overseas site.

The Hyper-Kamiokande (Hyper-K or HK) experiment is proposed as a joint project of the University of Tokyo and KEK by combining a next generation underground water Cherenkov detector and upgraded J-PARC neutrino beam. The Hyper-K detector is an order of magnitude larger in detector fiducial mass than Super-K and has discovery potential of leptonic *CP* violation and proton decays. The project has officially started by receiving its first Japanese funding in the beginning of 2020. Its construction schedule includes 5 years of the cavern excavation, 2 years of instrumentation, and data taking commencement in 2027. In parallel, the J-PARC beam delivered to the detector will be upgraded from 0.5 to 1.3 MW over the same time period.

SUPER-KAMIOKANDE

[Spokesperson : Masayuki Nakahata
(Kamioka Observatory, ICRR, The University of Tokyo)]

Atmospheric neutrinos

Atmospheric neutrinos are produced from the decays of secondary particles produced in the collision of primary cosmic rays with nuclei in the atmosphere. Atmospheric neutrinos have several remarkable features:

- The flavor ratio, $(\nu_\mu + \bar{\nu}_\mu)/(\nu_e + \bar{\nu}_e)$ is 2 (> 2 for above few GeV)
- Zenith angle distribution is up/down symmetry above a few GeV.

These features are realized without neutrino oscillations, and provide a useful constraint in the study of these neutrinos. Super-Kamiokande has been observing atmospheric neutrinos since 1996 and has accordingly made several important measurements with them, including the discovery of neutrino oscillations [1].

Starting in summer of 2020 SK was operated with a 0.01% concentration of Gd dissolved into the detector water. This period of the detector, SK6, lasted until 2022, when the concentration was increased to 0.03% marking the start of the SK7 period. Figure 1 shows the atmospheric neutrino data taken with Gd-loaded water in SK7 in comparison to data taken from SK6. There is no large change in the detector's ability to observe atmospheric neutrinos and the SK7 data are judged to be of similarly high quality as those in previous Gd-loaded and pure-water periods.

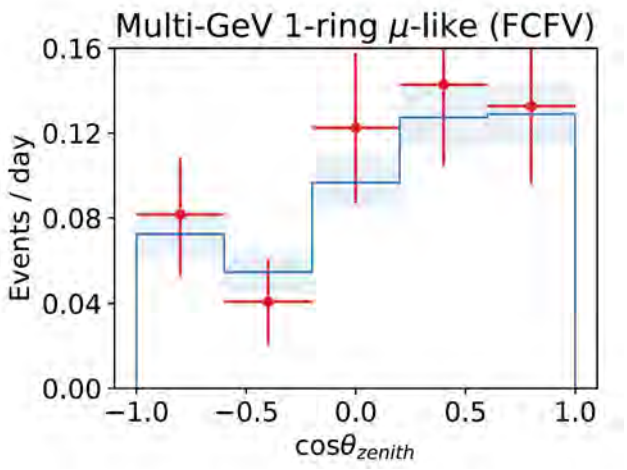


Fig. 1. Comparison of the atmospheric neutrino event rate in SK6 and SK7 for the multi-GeV μ-like sample.

Three flavor oscillations and the neutrino mass hierarchy

The SK atmospheric neutrino data are described at leading order by two-flavor $\nu_\mu \rightarrow \nu_\tau$ oscillations with maximal mixing (θ_{23}=π/4). However, sub-leading contributions via $\nu_\mu \rightarrow \nu_e$ oscillations induced by the mixing angle θ_{13} as well as the "solar" mixing parameters ($\Delta m^2_{12}, \theta_{12}$) provide the ability to probe currently unknown aspects of the standard neutrino oscillation paradigm, such as the existence of leptonic *CP* violation and the neutrino mass ordering (hierarchy). Understanding these open questions may bring important insight into larger questions, such as the origin and evolution of today's matter-dominated universe.

Several sub-leading oscillation effects are expected to appear in atmospheric neutrinos:

- Resonant enhancement of $\nu_\mu \rightarrow \nu_e$ oscillations due to matter along the neutrino path is expected to occur at energies between 2 and 10 GeV. This will manifest as an excess of upward-going electron-like events (e-like) in the atmospheric sample.
- This enhancement exists for either ν_e or $\bar{\nu}_e$ depending on the mass hierarchy. Therefore the mass hierarchy can be probed by understanding the relative amount of neutrino and antineutrino interactions in the detector.
- The combination of the solar oscillation parameters and the octant of $\sin^2\theta_{23}$ may enhance or suppress the event rate and, to some extent, alter the spectral shape of Sub-GeV electron-like data due to the $\nu_\mu \leftrightarrow \nu_e$ oscillations they induce.
- The standard oscillation paradigm includes a *CP*-violating factor, δ_{cp}, which is expected to induce several sub-dominant oscillation effects in many of the SK atmospheric neutrino samples, even if CP is conserved.

Super-Kamiokande has studied the effects of these oscillations on atmospheric neutrino data separated into fully-contained (FC) events, partially-contained (PC) events, and upward-going muon (UPMU) topologies. Fully-contained events are characterized by a primary interaction vertex that is located inside the fiducial volume of the detector and whose visible particles stop within the inner detector. On the other hand, though the primary vertex position of PC events is within the fiducial volume, they are characterized by having at least one charged particle escaping the inner detector and depositing light in the outer detector. In most cases the escaping particle is a muon. Upward-going muons originate from high energy muon-neutrino interactions in the rock surrounding the detector. Since all other particles are lost to interactions in the rock, only the muon is penetrating enough to reach the detector and be identified. The FC sample is separated into electron-like and muon-like (μ-like) subsamples by applying a particle identification algorithm to the most energetic Cherenkov ring of each event. Since PC and upward-going events are predominantly produced by muon neutrinos, no particle identification is applied. Though SK cannot distinguish on an event-by-event basis neutrino and antineutrino interactions, statistical separation of multi-GeV electron-like subsamples is performed to improve sensitivity to the mass hierarchy. A likelihood method designed to enhance the kinematic differences between neutrino and antineutrino interactions is applied to separate events into ν_e-like and $\bar{\nu}_e$-like subsamples.

Since the start of SK4 SK has had the ability to identify neutrons, albeit with a limited efficiency of 25%. In 2020 atmospheric neutrino events from this data set were separated into neutrino-like and antineutrino-like samples taking advantage of the fact that the former are expected to produce fewer neutrons on average than the latter. Further, a novel event selection based on a boosted decision tree was introduced to improve the classification of multi-ring events in all data periods. Using these new event selections all SK data until the end of the SK5 period (2020) were analyzed to update the analysis presented in [3]. In addition, the fiducial volume used in the current analysis has been expanded by 20%. With these improvements the analysis found a preference for the normal mass ordering (NO) of of between 78% and 96.7% over the range of oscillation parameter values allowed at the 90% confidence level. The preference at the best fit of the analysis is

92.3%. Further, the updated analysis shows no strong preference for the octant of $\sin^2\theta_{23}$ and has a weak preference for a non-zero CP-violating phase. These results have now been published in Ref. [4].

With the addition of gadolinium sulfate to the detector, Super-K's efficiency to observe neutrons has improved from 25% during the SK4 and SK5 phases to nearly 50% in SK7. Measurement of the number of neutrons produced in atmospheric neutrinos not only improves the separation between neutrino and antineutrino interactions for oscillation studies, but also improves the sensitivity to rare processes, such as proton decay, where atmospheric neutrinos are a dominant background. Figure 3 shows the time difference between neutron candidates observed in SK4, SK5, and SK6 relative to the timing of the parent neutrino interaction. The difference in the effective capture time, τ, reflects the change in Gd concentration across the SK periods and has been measured to be $\tau_{SK4} = 212 \pm 8\mu$s, $\tau_{SK5} = 115 \pm 3\mu$s, and $\tau_{SK6} = 64 \pm 1\mu$s.

Hadrons produced by neutrino interactions within nuclei may scatter on the surrounding nuclear medium and produce additional hadrons, including neutrons, via so-called final state interactions (FSI). Those hadrons may undergo additional scattering, or secondary interactions (SI) on oxygen molecules in the detector water, resulting in additional neutrons. The rate and strength of FSI and SI are not well known, resulting in considerable uncertainty in neutron production models which results in additional uncertainties on measurements that make use of neutron information, such as the oscillation analysis described above. Figure 4 shows the measured average neutron multiplicity following FC atmospheric neutrino interactions as a function of visible energy compared against a variety of FSI and SI models. In general, the data indicate fewer neutrons are observed relative to all model expectations for nearly all energies. These data are from the SK4 period, which has the largest available neutrino statistics among data where neutron tagging is possible.

Bibliography

[1] Y. Fukuda *et al.* [Super-Kamiokande Collaboration], Phys. Rev. Lett. **81**, 1562 (1998).

[2] R. Wendell *et al.* [Super-Kamiokande Collaboration], Phys. Rev. D **81**, 092004 (2010).

[3] K. Abe *et al.* [Super-Kamiokande Collaboration], Phys. Rev. D **97**, no. 7, 072001 (2018).

[4] T. Wester *et al.* [Super-Kamiokande], Phys. Rev. D **109**, 072014 (2024).

Solar Neutrinos

Introduction

Solar neutrinos constitute by far the largest component of neutrino flux on the Earth among those produced from natural sources. Most of solar neutrinos are produced by proton-proton fusion, $p + p \rightarrow d + e^+ + \nu_e$, and its subsequent fusion reactions (pp-chain)[1]. They are categorized into the *pp*, *pep*, ^{7}Be, ^{8}B and *hep* neutrinos. Among these, Super-Kamiokande is sensitive to ^{8}B and *hep* neutrinos, which have relatively higher energy that extends up to $\sim$20 MeV.

Past observations of solar neutrino flux by Super-Kamiokande (SK) [1] and the Sudbury Neutrino Observatory (SNO) [2] led to the discovery of solar neutrino flavor conversion. Our current interest for solar neutrino measurements with the SK detector [3] is to make a precision test of the neutrino flavor conversion through the Mikheyev-Smirnov-Wolfenstein (MSW) effect [4, 5]. The MSW effect leads to a resonant conversion of the solar neutrinos within the Sun and results in an about 30% level of the survival probability above $\sim$5 MeV. The survival probability of lower energy neutrinos are described by the vacuum oscillation probability of $\sim 50\%$, and the transition region between the two lies at a few MeV region. This transition from the matter dominant oscillation to the vacuum dominant oscillation is often called as the "up-turn" of the solar neutrino spectrum. Current experimental data is not enough to directly demonstrate this "up-turn" because of the experimental sensitivity as well as the statics.

SK aims to directly test the "Spectrum up-turn" by precisely measuring energy spectrum of ^{8}B solar neutrino in this transition region. This measurement is important not only to test the MSW effect but also to test several alternative theoretical models, such as sterile neutrinos [6, 7], mass-varying neutrinos [8], non-standard interactions [9, 10] and so on.

The matter effect can also be tested with the matter in the interior of the Earth. Electron flavor neutrinos are regenerated due to the matter effect of the Earth, making the neutrino flux in night is larger than that in day by about a few % level depending on the neutrino oscillation parameters.

In this article, we report results of solar neutrino measurements using the data taken through the end the fourth SK data taking phase (SK-IV) in May 2018. This results are published in 2024 [11] with an analysis method improved from our previous publication with 1670 days data [12]. The total livetime used for this analysis is 5,805 days, with 2970 days from the SK-IV phase. In addition to the standard neutrino oscillation analysis,we briefly report the status of solar neutrino observation in the SK detector after loading the Gadolinium [13].

Analysis

For precisely measuring the energy spectrum of recoil electrons, the energy scale should be reduced and the removal of background events is essential. For that purpose, the detector simulation was improved with more accurate modeling of the PMT timing response and the non-uniformity of the water quality. For example, the energy reconstruction method was improved with a correction for the PMT gain drift and with a new correction of the energy scale non-uniformity. The correction for the gain drift was first introduced in 2017 and then refined in this analysis with an improved correction for the dark noise contribution. Furthermore, the correction for the PMT angular response was improved with more realistic simulation of the PMT response and arrangement. By introducing those improvements, the standard variation of the energy scale variation was reduced down to $\pm 0.5\%$, which is three times smaller than that previously estimated. For further reduction of background events, we newly developed algorithms locat-

*[1] with a subdominant ($\sim$1%) contribution from the CNO cycle

Fit	Hierarchy	$\sin^2\theta_{23}$	$\lvert\Delta m^2_{32,31}\rvert$ [$\times 10^{-3}$ eV^2]	δ_{CP}	$\sin^2\theta_{13}$	$\delta\chi^2$ (IO-NO)
SK only	NH	0.45	2.40	-1.89	0.020	–
	IH	0.48	2.40	-1.89	0.010	5.23
SK, θ_{13} constrained	NH	0.45	2.40	1.75	–	–
	IH	0.45	2.40	-1.75	–	5.69

Table 1. Best fit oscillation parameters obtained by the three flavor oscillation analysis. Fits are conducted for both the normal (NH) and inverted (IH) hierarchy assumptions The fit was performed assuming $\sin^2\theta_{13}$=0.0218, which is taken from the PDG.

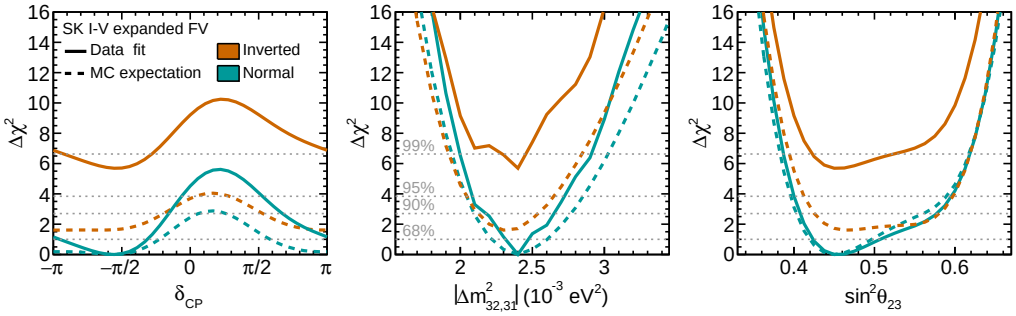


Fig. 2. Measured $\Delta\chi^2$ distributions for the $\Delta m^2_{23,31}$, $\sin^2\theta_{23}$, and δ_{cp} oscillation parameters for the Super-K only fit with $\sin^2\theta_{13}$ constrained to the value preferred by reactor measurements.

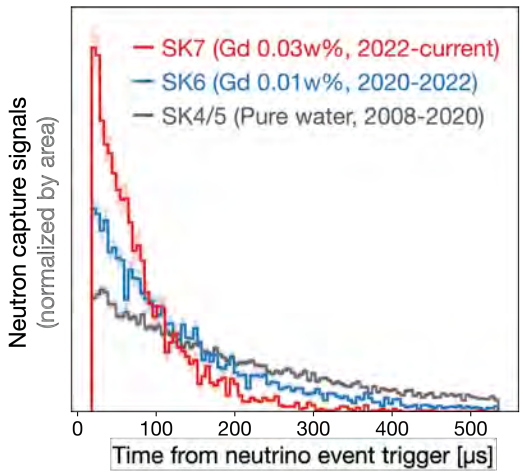


Fig. 3. Time difference between FCFV primary interaction and selected neutron candidates in SK4, SK5, and SK6.

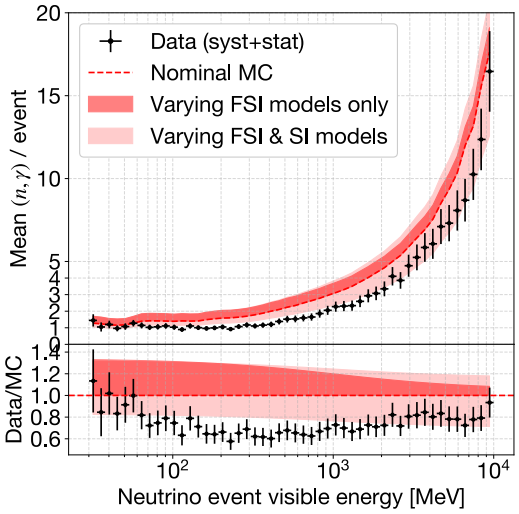


Fig. 4. Observed average neutron multiplicity following FCFV atmospheric neutrino interactions in SK4 as a function of the primary neutrino event's visible energy.

ing muon induced hadronic showers, both by improving the reconstruction of the energy deposited along the muon track, and by identifying neutrons using a recently-implemented low energy trigger [14]. New spallation cuts based on these algorithms allow to reduce the deadtime of the solar neutrino analysis by a factor of two, allowing a gain of the equivalent of one year of exposure at SK-IV. Moreover, the profiles of the neutron clouds produced in muon induced hadronic showers are well reproduced by the spallation simulation, motivating its use to develop spallation reduction algorithms for future analyses. By applying this cut to the data sample, the signal efficiency improved about 12% while keeping the removal efficiency of muon spallation events about 90% [14].

^{8}B solar neutrino flux measurement

The SK detector observes solar neutrinos via elastic scatterings with electrons in pure water. The direction of a recoiled electron is highly correlated with the direction of the incident neutrino. Figure 5 shows the distribution of $\cos\theta_{\rm Sun}$ for solar neutrino candidates observed during the SK-IV phase. With the 2970 days of data in SK-IV, more than 60,000 events are observed over the background.

Adding the solar neutrino events observed in other phases, the total number of the solar neutrino events is more than 100,000. Based on this data, the ^{8}B solar neutrino flux is de-

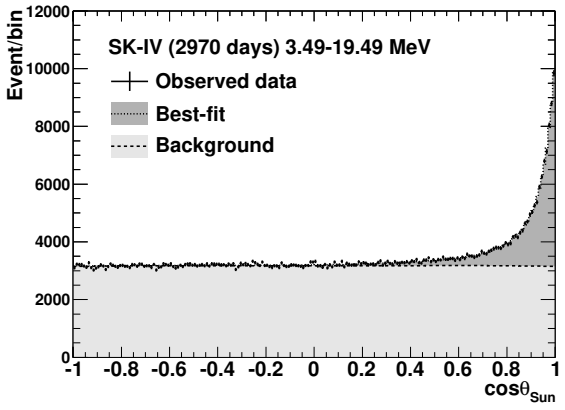


Fig. 5. The solar angle distribution in SK-IV. The horizontal axis shows the cosine of the solar angle $\cos\theta_{\rm Sun}$ and the vertical axis shows the number of the observed events. The black points shows the observed data, and the gray (light gray) histogram shows the best–fit (background) shape.

termined to be $(2.34\pm0.04)\times10^6$ /cm^2/sec assuming a pure electron neutrino flavor content. The ratio between the SK result and the SNO NC current flux (5.25×10^6 /cm^2/sec) [15] is found to be 0.447 ± 0.008. Figure 6 shows the ^{8}B solar neutrino flux measured by solar neutrino experiments, such as SK, SNO, Borexino, KamLAND, and SNO+. A comparison between different interaction channels is a clear demonstration of the existence of non-electron neutrino components in ^{8}B solar neutrinos.

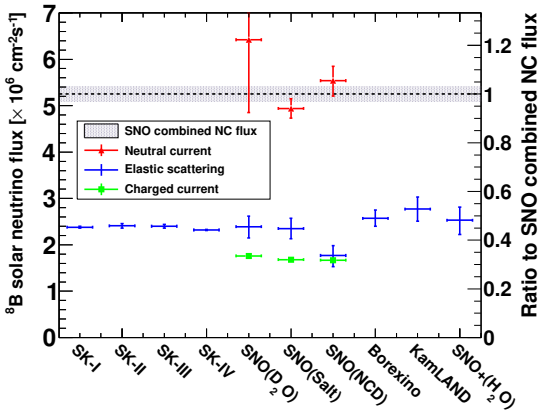


Fig. 6. Comparison of ^{8}B solar neutrino flux among solar neutrino experiments. The measured flux of other experiments are obtained from the three phases of SNO, Borexino, KamLAND, and SNO+ (pure water). The left (right) vertical axis shows the measured flux without neutrino oscillation (the ratio of the measured flux to the SNO's neutral current flux.

The solar activity cycle is the 11 years periodic change of sunspots releasing the magnetic flux at the surface of the Sun. The number of the sunspots strongly correlated with the solar activity cycle. The solar neutrino data set which is used for this analysis spans more than 21 years and covers about two solar activity cycles. Figure 7 shows the SK yearly flux measured throughout the different phases of SK together with the corresponding sunspot number (Source: WDC–SILSO, Royal Observatory of Belgium, Brussels [16]). The χ^2 between observed data and no time dependence hypothesis is calculated with the total experimental uncertainties as $\chi^2/N_{\rm d.o.f} = 19.94/22$, where $N_{\rm d.o.f}$ is the number of freedom of this analysis. This calculation result corresponds to a probability of 58.9%. The SK solar rate measurements are fully consistent with a constant solar neutrino flux emitted by the Sun.

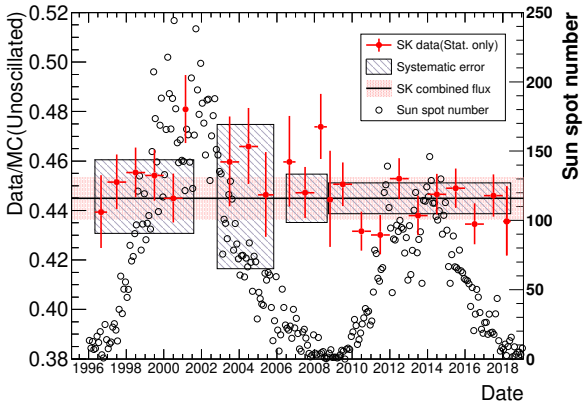


Fig. 7. The ratio of ^{8}B solar neutrino flux in SK over the SNO's NC current flux from 1996 to 2018. The red points show the yearly flux measured by SK (statistical uncertainty only), the gray bands show the systematic uncertainties for each SK phase, the black-horizontal line shows the combined measured flux with the uncertainty drawn as the red horizontal band. The back circles show the sunspot number provided from [16].

Using the 22-years data, we have also evaluated the annual modulation of solar neutrino flux due to the elliptic orbit of the Earth around the Sun. In this study, we determined the upper limit of the amplitude of the ^{8}B solar neutrino flux and the Kepler constants, such as eccentricity (ε) and perihelion shift ($\delta t_{\rm period}$). Table 2 summarizes the analysis results together with that from other experiments. The upper limit of the amplitude is the strongest constraint among the solar neutrino experiments.

Table 2. Comparison of time variation study results from SK [17], SNO [18], and Borexino [19] experiments.

	Amplitude [%]	Eccentricity ε [%]	Perihelion shift $\delta t_{\rm period}$ [day]
SK (^{8}B)	5.2	1.53 ± 0.35	-1.5 ± 13.5
SNO (^{8}B)	10.5	1.43 ± 0.86	–
Borexino (^{7}Be)	–	1.84 ± 0.32	7 ± 20

Energy spectrum analysis

Analysis of solar neutrino energy spectrum was performed using all the data from SK-I to SK-IV [1, 20, 21, 12, 11]. The data quality for SK-IV was significantly improved by installing the new front-end electronics for SK-IV [22], upgrading the water circulation system, and developing the upgraded calibration methods [23].

Owing to these upgrades, SK has achieved the lowest background (induced by radioisotopes in pure water, espe-

cially ^{214}Bi) among all the SK phases [11]. The energy threshold in SK-IV have been lowered to 3.49 MeV in recoil electron kinetic energy (SK-I: 4.49 MeV, SK-III: 3.99 MeV) and this enabled SK to measure the solar neutrino energy spectrum with higher sensitivity. In addition, in May 2015, the trigger threshold was changed from 34 observed PMT signals within 200 nsec to 31 hits [24, 25]. Because of this lower threshold, the detection efficiency between 3.49 MeV and 3.99 MeV was improved from ∼86% to ∼100%. This improvement led to further reduction of the statistical uncertainty below 4.99 MeV in SK-IV.

Figure 8 shows the energy spectra obtained from SK-I, -II, -III and -IV, overlaid with the predictions assuming the current oscillation parameters described in the next section. Because of long operation, low threshold of data acquisition, and the reduced systematic uncertainties for the spectrum measurement, the SK-IV energy spectrum data is statistically precise as demonstrated in Fig. 8.

Figure 9 shows the combined energy spectrum from SK-I to SK-IV with the predictions. Note that all SK the phases are combined without regard to energy resolution or systematic uncertainties, but those uncertainties are taken into account in the χ^2 calculation between the data and the prediction. Comparing χ^2 between the spectrum data and the predictions, the energy spectrum of SK is consistent within $\sim 1.2\sigma$ with the MSW up-turn prediction. By adding the energy spectrum from the SNO experiment, a distorted spectrum is favored by $\sim 2.1\sigma$.

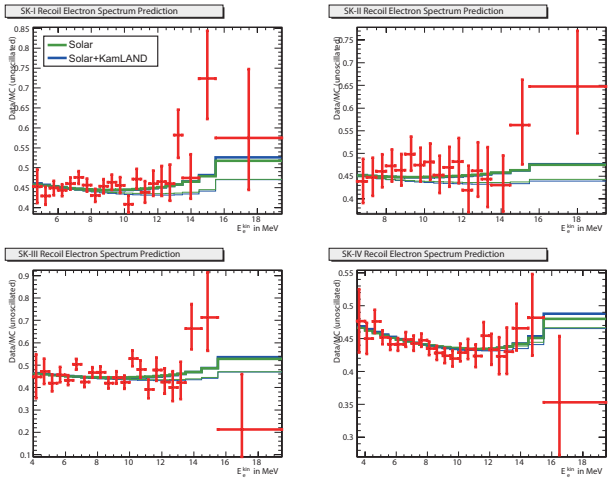


Fig. 8. SK-I, -II, -III and -IV recoil electron spectra divided by the un-oscillated expectation. The green (blue) thick line represents the best-fit to SK data using the oscillation parameters from the fit to SK and SNO (with KamLAND) data. The thick (thin) lines are distorted (not distorted) by adjusting the energy scale, resolution, and neutrino spectrum within uncertainties.

Day-night asymmetry

The day-night asymmetry of the solar neutrino flux for the full SK-IV data set was extracted with the same method described in Ref. [26]. Here, the day-night asymmetry is defined as,

$$A_{D/N} = \frac{\Phi_{\rm day} - \Phi_{\rm night}}{0.5(\Phi_{\rm day} + \Phi_{\rm night})},$$

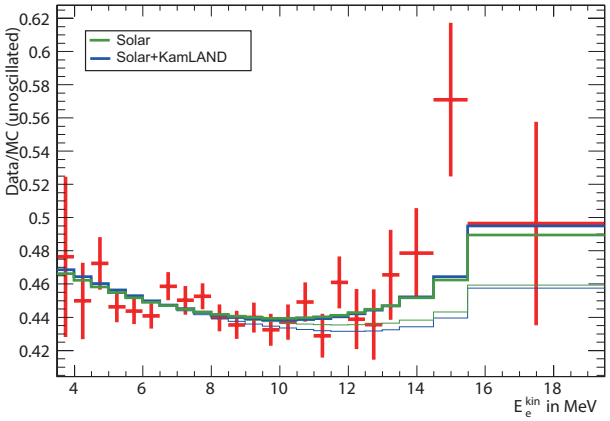


Fig. 9. The energy spectrum combining SK-I through SK-IV as a function of the recoil electron energy. The red points show the ratio of the data to the expected flux using a un-oscillated ^{8}B solar neutrino spectrum. The definition of curves are the same as that in Figure 8.

where $\Phi_{\rm day(night)}$ is the observed solar neutrino flux during day (night). In the analysis, we additionally fit the amplitude of the expected zenith angle variation to the observed data, which depends on the operation time of the SK detector. Figure 10 shows the comparison of the measured day-night flux asymmetry among four SK phases. The combined result is $A_{\rm D/N} = (2.86 \pm 0.85\,({\rm stat.}) \pm 0.32\,({\rm syst.}))\%$, where this value differs by 3.2σ level from zero. This result demonstrates that the existence of earth matter effects on solar neutrino oscillation.

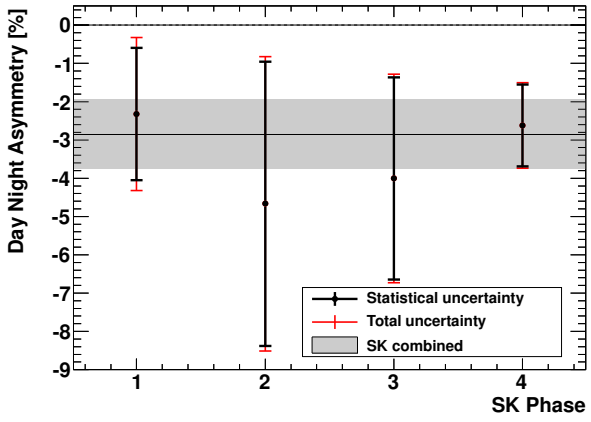


Fig. 10. Day/night asymmetries from amplitude fits by the four different SK phases. The black thick (red thin) bar shows the statistical (total) uncertainty and the gray band shows the combined value.

The asymmetry parameter depends on the expected zenith angle variation shapes and therefore on the oscillation parameters. The dependence on the mixing angle is negligible. Figure 11 shows the result of a day-night asymmetry amplitude fit as a function of Δm^2_{21} using the SK combined data from SK-I to SK-IV. In particular, at the solar+KamLAND best-fit value of $\Delta m^2_{21} = 7.5 \times 10^{-5}$ eV^2, the combined SK day/night amplitude fit corresponds to a slightly smaller asymmetry of $A_{\rm D/N} = (2.74 \pm 0.83\,({\rm stat.}) \pm 0.32\,({\rm syst.}))\%$, where an asymmetry of -1.7% is expected.

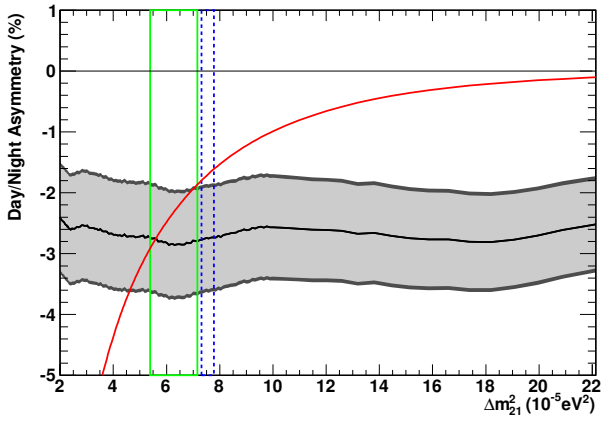


Fig. 11. SK-IV day/night amplitude fit dependence on Δm^2_{21}. The black line (gray band) shows the best-fit value of day/night asymmetry (its uncertainty). The red solid curve shows the expected day/night asymmetry. The green solid (blue dashed) box shows the 1σ range allowed by solar experiments (solar experiments and KamLAND).

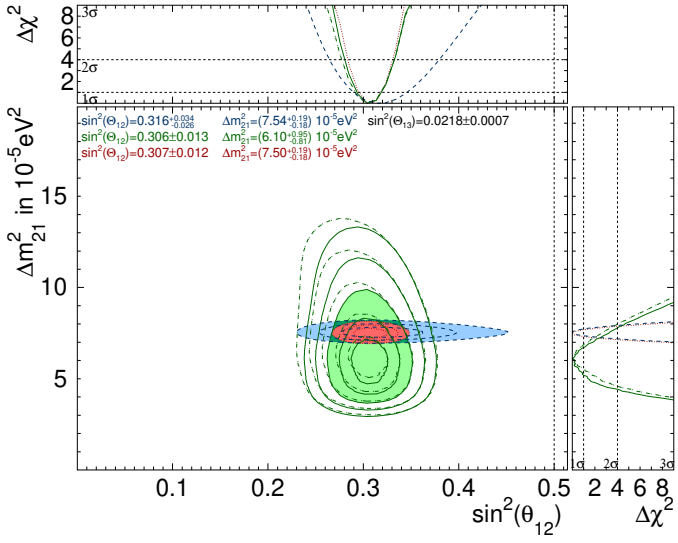


Fig. 12. The allowed contours for Δm^2_{21} vs. $\sin^2\theta_{12}$ from SK and SNO (green dashed line) and the all solar neutrino data (green solid line). The allowed contour from KamLAND is also shown in blue. The combined allowed region is shown in red.

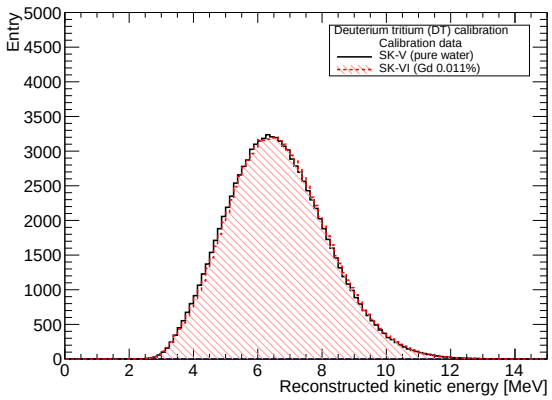


Fig. 13. The comparison of energy distribution between SK-V (pure water) and SK-VI (Gd concentration 0.011%). The calibration data was taken at the center position of the SK detector.

Oscillation parameter extraction

The oscillation parameters were extracted using the results from the solar neutrino measurements by radiochemical experiments (Homestake, SAGE, and GALLEX/GNO), and water Cherenkov experiments (SK and SNO) [15], and the liquid scintillator experiment (Borexino), as well as the reactor antineutrino measurement by KamLAND [27, 28]. Figure 12 shows the allowed parameter region from the SK+SNO data, all solar neutrino experiments, and the KamLAND data. SK significantly contributes to the measurement of the solar angle θ_{12}. From the SK+SNO data, the mixing angle is determined to be $\sin^2\theta_{12} = 0.305 \pm 0.014$ and the mass difference is determined to be $\Delta m^2_{21} = 6.10^{+1.26}_{-0.86} \times 10^{-5}$ eV^2 as shown in Fig. 12. The SK+SNO fit results favors a lower Δm^2_{21} value compared to the KamLAND best fit value of $\Delta m^2_{21} = 7.54^{+0.19}_{-0.18} \times 10^{-5}$ eV^2. Currently, the SK+SNO data disfavors the KamLAND best fit value at $\sim 1.5\sigma$, while it was $\sim 2\sigma$ in the previous analysis. Adding the KamLAND result, the oscillation parameters are determined to be $\sin^2\theta_{12} = 0.307 \pm 0.012$ and $\Delta m^2_{21} = 7.50^{+0.19}_{-0.18} \times 10^{-5}$ eV^2.

Solar neutrino observation after Gd-loading

Gadolinium was loaded into the Super-Kamiokande's pure water [13] to enhance detector's sensitivity to supernova relic neutrinos by tagging neutrons originated from the inverse beta decay of electron anti-neutrino interactions. The first Gd loading was conducted in 2020 July and the second was done in 2022 June.

In order to validate the detector performance, calibration data were taken after loading Gadolinium and compared with the results in pure water phase. For example, Figure 13 shows the reconstructed electron kinetic energy with the DT calibration device [29] before and after the Gd loading. The differences of the peak position and resolution between SK-V (pure water) and SK-VI (Gd concentration 0.011%) are less than $\pm 1\%$. Hence, the detector's energy scale is enough to continue to observe the solar neutrinos in the MeV region.

Figure 14 shows the typical distributions of $\cos\theta_{\rm Sun}$ before and after the Gd-loading. The peak of solar neutrinos around $\cos\theta_{\rm Sun} = 1$ is clearly observed even through we added the Gd into pure water. Figure 14 also demonstrates that no additional background exist in the energy range above 6.49 MeV even after the second Gd-loading. The background events below that level is under investigation since the detection efficiency for such events is different from that evaluated in pure water phase mentioned in the previous section. Based on the DT calibration and $\cos\theta_{\rm Sun}$ distribution, the SK detector can continue to conduct the solar neutrino observation using Gd-loaded water.

Summary and outlook

In summary, Super-Kamiokande has precisely measured the ^{8}B solar neutrino flux, its time variation and recoil electron spectrum. Using 5,805 days of data, more than 100,000 so-

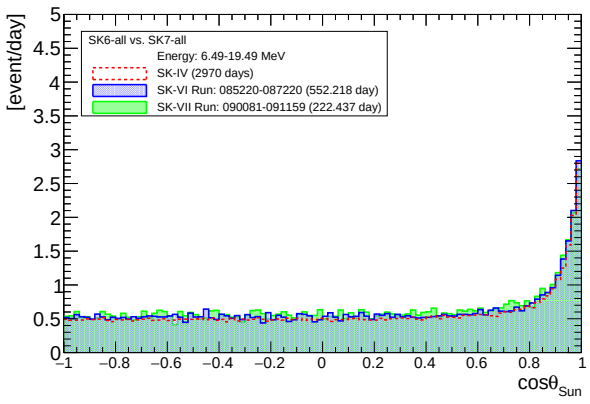


Fig. 14. The comparison of the cosine theta distribution between 6.49 and 19.49 MeV before and after the Gd-loading. The phases of SK-IV (red) was operated by filling pure water while SK-VI (blue) and SK-VII (light green) were operated by adding Gd into the detector's pure water. Even after dissolving additional Gd in the second Gd-loading, the background rate is unchanged because of developing ultra-low radio-purity Gd powder.

lar neutrino interactions were extracted over the background. No significant correlation between the observed solar neutrino flux and the sunspot number was found with more than 21 years of continuous observation of the solar neutrino flux. We have also set the strong constraint on the amplitude of annual modulation of the solar neutrino flux due to the elliptic orbit of the Earth around the Sun.

The measured energy spectrum of ^{8}B solar neutrino is consistent within $\sim 1\sigma$ with the MSW up-turn with both the solar best-fit parameters and the KamLAND best-fit parameters. The previously existed $\sim 2\sigma$ tension between the solar and KamLAND best fit Δm^2_{21} values was reduced to $\sim 1.5\sigma$ in this analysis. Combining the solar neutrino oscillation analyses by SK, SNO and KamLAND, the oscillation parameters are determined as $\Delta m^2_{21} = 7.50^{+0.19}_{-0.18} \times 10^{-5}$ eV^2 and $\sin^2\theta_{12} = 0.307 \pm 0.012$.

The Super-Kamiokande detector was recently upgraded by dissolving Gadolinium (Gd), and started a new phase of observation as SK-Gd. In order not to cause significant harm to the solar neutrino observation, ultra-pure $Gd_2(SO_4)_3$ powder with extremely low radio-impurity was newly developed and dissolved into the SK detector. Furthermore, the calibration data after the Gd-loading has been taken Enhanced neutron detection capability with Gd can be used to further reduce the cosmic-ray spallation backgrounds. We aim to further improve our solar neutrino measurements with additional data and analysis improvements in the SK-Gd era.

Bibliography

[1] J. Hosaka *et al.*, Phys. Rev. D **73**, 112001 (2006).

[2] Q.R. Ahmad *et al.*, Phys. Rev. Lett. **87**, 071301 (2001).

[3] Y. Fukuda *et al.*, Nucl. Instrum. Meth. A **501**, 418 (2003).

[4] S.P. Mikheyev and A. Y. Smirnov, Sov. Jour. Nucl. Phys. **42**, 913 (1985).

[5] L. Wolfenstein, Phys. Rev. D **17**, 2369 (1978).

[6] P.C. de Holanda and Y. Smirnov, Phys. Rev. D **69**, 113002 (2004).

[7] P.C. de Holanda and Y. Smirnov, Phys. Rev. D **83**, 113011 (2011).

[8] V. Barger *et al.*, Phys. Rev. Lett. **95**, 211802 (2005).

[9] A. Friedland *et al.*, Phys. Rev. B **594**, 347 (2004).

[10] O.G. Miranda *et al.*, J. High Energy Phys. **10** 008 (2006)

[11] K. Abe *et al.*, Phys. Rev. D **109**, 092001 (2024).

[12] K. Abe *et al.*, Phys. Rev. D **94**, 052010 (2016).

[13] K. Abe *et al.*, Nucl. Instrum. Meth. A **1027**, 166248 (2022).

[14] S. Locke *et al.*, Phys. Rev. D (accepted), arXiv:2112.00092 [hep-ex].

[15] B. Aharmin *et al.*, Phys. Rev. C **88**, 025501 (2013).

[16] WDC-SILSO, Royal Observatory of Belgium, Brussels. http://www.sidc.be/silso/datafiles

[17] K. Abe *et al.*, Phys. Rev. Lett. **132**, 241803 (2024).

[18] B. Aharmim *et al.*, Phys. Rev. D **72**, 052010 (2005).

[19] S. Appel *et al.*, Astropart. Phys. **145**, 102778 (2023).

[20] J.P. Cravens *et al.*, Phys. Rev. D **78**, 032002 (2008).

[21] K. Abe *et al.*, Phys. Rev. D **83**, 052010 (2011).

[22] H. Nishino *et al.*, Nucl. Instrum. Meth. A **610**, 710 (2009).

[23] K. Abe *et al.*, Nucl. Instrum. Meth. A **737**, 253 (2014).

[24] S. Yamada *et al.*, IEEE Trans. Nucl. Sci. **57**, 428 (2010).

[25] Y. Nakano, PhD thesis, The Univ. of Tokyo (2016).

[26] A. Renshaw *et al.*, Phys. Rev. Lett. **112**, 091805 (2014).

[27] S. Abe *et al.*, Phys. Rev. Lett. **100**, 221803 (2008).

[28] A. Gando *et al.*, Phys. Rev. D **88**, 033001 (2013).

[29] E. Blaufuss *et al.*, Nucl. Instrum. Meth. A **458**. 636 (2001).

Searches for nucleon decays

Among many physics models beyond the Standard Model (SM) of particle physics, Grand Unified Theories (GUTs) are promising models that can explain several features of the SM including the quantized hypercharge. One of the remarkable predictions of the GUTs is the decay of protons or bound neutrons, which are stable particles in the SM. Super-Kamiokande is the most sensitive experiment for these phenomena and has been looking for them since its beginning in 1996.

However, the minimal SU(5)-based grand unification was ruled out by a search for the proton decay, $p \to e^+\pi^0$, at Super-Kamiokande [1]. This SU(5) model was also rejected by the fact that there is no precise agreement at the GUT scale in the strength of the three gauge coupling constants extrapolated from precise measurements of these constants at LEP [2]. To avoid these experimental constraints, it is needed to lift the GUT scale and make the proton's lifetime longer than the experimental limit by introducing some extra fields as they are predicted by models beyond the SM (BSM) such as supersymmetry (SUSY). This addition of the extra degrees of freedom above the electroweak scale, which are not experimentally identified, will also modify the renormalization group equations of the three coupling constants and allow these constants to meet at the GUT scale.

Since any hints for the BSM have not been obtained in any experiments yet, it is particularly important to search for various nucleon decay modes to catch as wide types of modifications to the SM as possible. In this context, Super-Kamiokande officialized three analyses this year, $p \to \ell^+\pi^0\pi^0$, $n \to \bar{\nu}\pi^0$, and $p \to e^+X$, whose details will be provided in the rest of this section.

In all the three analyses, we try to select the target nucleon decay signals from the data while rejecting the background events, mostly the atmospheric neutrinos, as much as possible, by making use of features of events that the Super-Kamiokande detector provides for this discrimination. These features include the momenta of charged particles, which are roughly proportional to the amount of Cherenkov light. The total momentum and the total invariant mass are also powerful variables because the signals are decays of protons (938.3 MeV/c^2) or neutrons (939.5 MeV/c^2) almost at rest while the backgrounds are caused by neutrinos flying from the outside of the detector and giving momenta to the events. In addition, the detector can indicate the particle identification, the existence of electrons from decaying muons or pions, and the existence of neutrons kicked out of the nuclei.

Search for $p \to \ell^+\pi^0\pi^0$ decay

The most important proton decay modes, $p \to \ell^+\pi^0$ where ℓ^+ is either e^+ or μ^+, are caused in a wide range of GUT models. When these decays are possible, the SM's strong interaction also causes $p \to \ell^+\pi^0\pi^0$ at a comparable rate [3]. We searched for these decay modes at SK for the first time using all the pure data, which corresponds to 401.1 kton·years. After the event selections are applied, the simulated signal and backgrounds are obtained in the plane of the total momentum versus the total invariant mass and compared to the data as shown in Fig. 15. No significant excess over the background estimation was observed, and the lower limits on the partial lifetime were obtained as 7.2×10^{33} and 4.5×10^{33} years at 90% confidence level for $p \to e^+\pi^0\pi^0$ and $p \to \mu^+\pi^0\pi^0$, respectively. These results improve the limits in the previous research by the IMB-3 experiment [4].

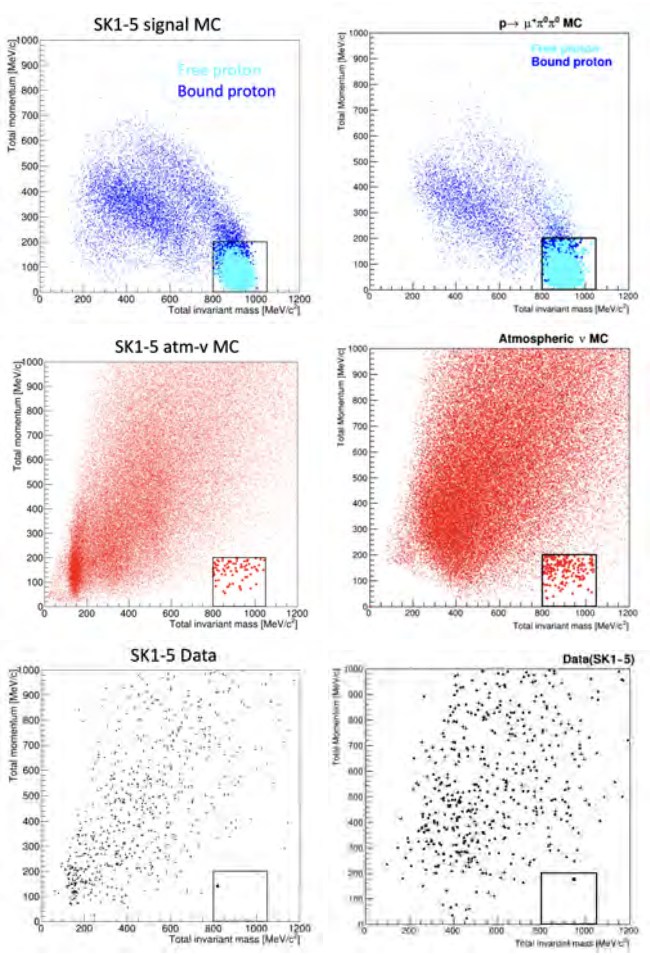


Fig. 15. Total momentum vs total invariant mass distribution in the $p \to e^+\pi^0\pi^0$ (left) and $p \to \mu^+\pi^0\pi^0$ (right) searches after all the selection cuts except the ones on the shown variables. The top, center, and bottom plots show the simulated signal from the proton decays, atmospheric neutrino backgrounds, and the data, respectively. For the signal distributions, the cyan dots show the contribution from proton decay evens in free protons (hydrogen), whereas the blue ones show decays of bound protons (Oxygen).

Search for $n \to \bar{\nu}\pi^0$ decay

Supersymmetric GUTs often predict the proton decay to $p \to \bar{\nu}K^+$. However, depending on the top-quark-related elements of the Cabbibo-Kabayashi-Maskawa matrix, this decay mode can be suppressed due to the destructive interference between the transitions involving the supersymmetric partners of the top and charm quarks [5, 6]. In such cases, neutron decay modes involving a pion can become dominant. In this year, the $n \to \bar{\nu}\pi^0$ decay has been searched for using all the pure water SK data, corresponding to 489.9 kton·years. In addition to increasing the amount of data, various improvements in the analysis method are employed as well as revising the simulation of the pions traveling in the nuclei after the neutron decay.

The distributions of the simulation and the data after applying the event selections are shown Fig. 16, and it suggests a good agreement between the data and the background prediction. The signal is tested by fitting the momentum spectrum in this figure, constraining the large contribution from the background events at the same time. The obtained lower limit on the lifetime is 1.1×10^{33} years at 90% confidence level, which is comparable with the previous search at SK [7]. The limit was not much improved because of the reduced survival probability of the decayed pions in the revised simulation.

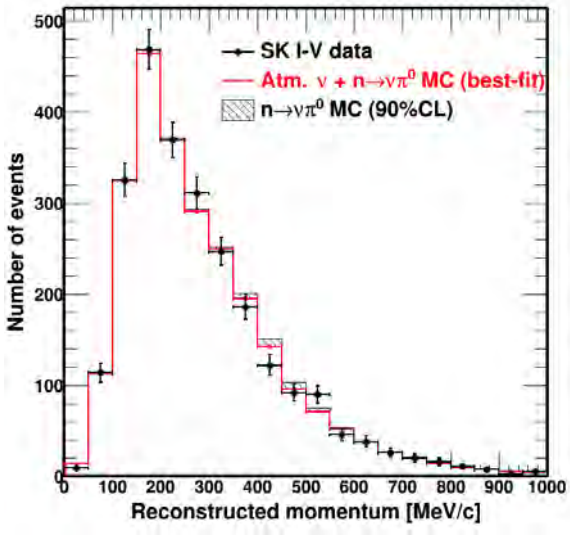


Fig. 16. Post-fit data MC distribution in the $n \to \bar{\nu}\pi^0$ analysis after all the selections are applied. The red histogram and the black points show the simulated atmospheric neutrino backgrounds and data distributions, respectively. The small hatched black histogram shows the neutron decay events at the obtained lower limit on the lifetime.

Search for $p \to e^+X$ decay

The single electron events are studied to search for the $p \to e^+X$ decay, where X is a massless, invisible particle. In this year, the analysis was extended to include the entire pure water SK periods, which corresponds to 401.1 kton·year. After applying all the event selection cuts, we searched for a bump in the single electron momentum spectrum as shown in Fig. 17. The data is fairly consistent with the background-only distribution. Similar to the $n \to \bar{\nu}\pi^0$ analysis, a spectral fitting was applied to test the signal. This results in a lower limit on the partial lifetime, which is 1.6×10^{33} years at 90% confidence level. The performance of the search is much improved from the previous research [8] mainly due to the increased amount of data.

Summary and prospects

The obtained limits on the lifetime for the four decay modes discussed above are summarized in Tab. 3 as well as their relevant numbers such as the signal efficiencies. In addition to these searches, other studies are ongoing targeting various nucleon decay modes. These studies include $p \to \ell^+\eta^0$, $n \to \bar{\nu}\eta^0$, $n \to e^-K^+$, and $p \to \mu^+X$, and they are all aiming for finalizing within a few years.

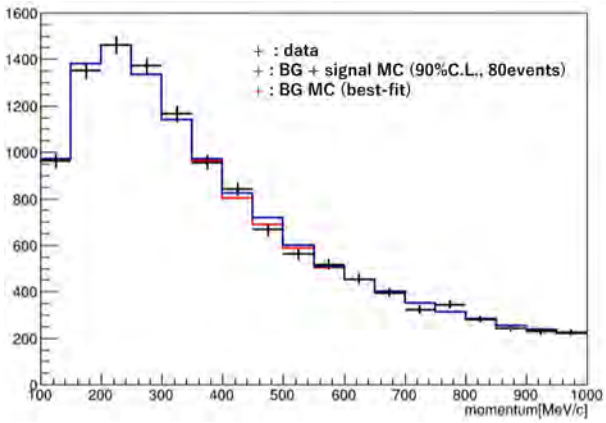


Fig. 17. Post-fit data MC distribution in the $p \to e^+X$ analysis after all the selections are applied. The red histogram and the black points show the simulated atmospheric neutrino background and the data, respectively. The blue histogram shows the signal contribution at its lower lifetime limit in addition to the background.

The current analysis efforts concentrate on the pure water, i.e. pre-gadolinium loading, phases. Enhanced analyses that make use of neutrons captured on the gadolinium are unseen yet and these are anticipated in the future.

Bibliography

[1] A. Takenaka *et al.*, Super-Kamiokande Collaboration, Phys. Rev. D **102**, 112011 (2020)

[2] U. Amaldi *et al.*, Phys. Lett. B **260** 447, (1991)

[3] M. Wise, *et al.*, Phys. Rev. D **23** 1591 (1981)

[4] C. McGrew, *et al.*, Phys. Rev. D **59** 052004 (1999)

[5] J. Hisano, *et al.*, Nucl. Phys. B 402 (1993) 46

[6] H. S. Goh, *et al.*, Phys. Lett. B 587 (2004) 105

[7] K. Abe, *et al.*, Super-Kamiokande Collaboration, Phys. Rev. Lett. **113** 121802 (2014)

[8] V. Takhistov, *et al.*, Super-Kamiokande Collaboration, Phys. Rev. Lett. **115** 121803 (2015)

EGADS: From R&D for the gadolinium project to standalone Supernova monitor

As mentioned above, although at SK a few SRN events a year are expected, SRNs have not been detected yet because of the large backgrounds that constrain our search. The observation of SRNs in general or neutrinos from distant supernovae in particular, would give us some information about the universe, for example the core collapse rate from SRNs, and about the neutrino itself too, for example its lifetime. The main signal from SRN is expected to be the inverse beta decay reaction ($\bar{\nu}_e + p \to e^+ + n$), in which a positron and a neutron are produced, the delayed coincidence between the positron interaction and the neutron capture should allow to reduce the background affecting this analysis.

Table 3. Summary of the nucleon decay searches at Super-Kamiokande in 2023-2024. The efficiency of the signals and the number of remaining backgrounds after the event selections are presented. The numbers of candidate events in the signal boxes are also shown. The $\times$ marks are shown for the $n \to \bar{\nu}\pi^0$ and $p \to e^+X$ searches because these analyses are dominated by the background events even after the selection and employ the spectral fitting. It does not make much sense to refer to the number of the remaining backgrounds and the observed events.

Decay mode	Efficiency(%)	Background (event)	Candidates (event)	Lifetime limit (90% C.L.)
$p \to e^+\pi^0\pi^0$	18.5	0.4	1	$> 7.2 \times 10^{33}$ yrs
$p \to \mu^+\pi^0\pi^0$	12.8	0.9	1	$> 4.5 \times 10^{33}$ yrs
$n \to \bar{\nu}\pi^0$	32.2	$\times$	$\times$	$> 1.1 \times 10^{33}$ yrs
$p \to e^+X$	95.4 (SK-IV,V)	$\times$	$\times$	$> 1.6 \times 10^{33}$ yrs



Fig. 18. In the LAB-E cavern, the 200-ton tank (a) with currently 240 photo-multipliers installed, the Gd pre-mixing and pre-treatment 15-ton tank (b), the selective filtration system (d), Gd removal resins (c) for test and a device to measure the water transparency (e) have been installed.

Before Gd loading in 2020, the SK detector had a poor neutron detection efficiency. It was then proposed to add 0.2% of gadolinium (Gd) sulfate by mass into SK in order to achieve a high neutron detection efficiency. Since Gd has a neutron capture cross section of 49.000 barns (about 5 orders of magnitude larger than that of protons) and emits a gamma cascade of 8 MeV, neutrons could be easily detected at SK (in space, vertices within tens of cm and in time, with the neutron capture delayed about 30 μsec).

EGADS (Evaluating Gadolinium's Action on Detector Systems) project was funded in 2009. The main motivation of EGADS was to show that by adding Gd, SK will be able to detect anti-neutrinos using the delayed coincidence technique, while keeping all its capabilities in the other analyses like solar and atmospheric neutrinos. Since then, a new hall near the SK detector has been excavated and a 200-ton tank with its ancillary equipment has been installed, see Fig.18, to mimic the conditions at SK. The selective water filtration system filters out water impurities while keeping the Gd in the water.

EGADS has been renamed as Employing Gadolinium to Autonomously Detect Supernovas after the installation of the new QBee electronics in 2017, following the Super-Kamiokande collaboration approbation of the SK Gd loading.

Water system operations

From January 2010 to July 2011 we circulated pure water through the 200-ton tank and proved that our water system is stable and achieves a high water quality. In 2013, from February 6th to April 20th, the 200-ton tank has been step wise loaded with Gd sulfate until the final 0.2% concentration was reached. Two values are monitored at three different depths: the Cerenkov light left after travelling 15 m (LL15) in water and the Gd concentration. Both values confirmed that we can achieve and maintain a good water quality and that Gd sulfate homogeneously and quickly dissolves in the 200-ton tank.

In summer 2013, we installed 240 photo-multipliers and the data taking started from September without Gd and with a DAQ based on old SK ATM modules. In April 2015, the target concentration of 0.2% $Gd_2(SO_4)_3$ was achieved. Figure 19 shows the time variation of LL15. The blue band in the figure shows typical values for SK-III and SK-IV. As shown in the figure, the transparency of 0.2% $Gd_2(SO_4)_3$ water is within the SK range. In addition to the good water transparency, no Gd loss has been detected since the EGADS detector reached the final concentration until it was emptied again after about 2 years and 5 months, in October 2017.

Detailed studies have evaluated the impact on current analyses at SK. These studies show that current analyses will be basically unharmed after adding Gd in SK and all other tests and studies conducted have shown no showstoppers. As a consequence, the SK collaboration decided in spring 2015 to approve the SuperK-Gd project. The results of these analysis were published in [1].

In order to test the Gd-loading in SK, the detector was refilled with pure-water in November 2017, and loaded with 0.02% $Gd_2(SO_4)_3$ in the end of March 2018. This loading was performed using only the pre-treatment and the fast re-circulation systems, with one pass, similar to what is expected for SK 0.02% loading.

Since then, different configurations of the water system have been tested in order to determine what is needed to ensure high water transparency in SK without band-pass system. Figure 20 shows the time variation of LL15 since this loading until May 2020. From March 2018 to June 2018 a slow but continuous decrease of the water transparency has been observed ith the fast re-circulation system only. From June 2018 to August 2018 the use of the band-pass system allowed to recover high water transparency. There-after the fast-re-circulation system only has been used.

In May 2019, the water system was stopped for about one week due to electrical damage following a power-cut. This

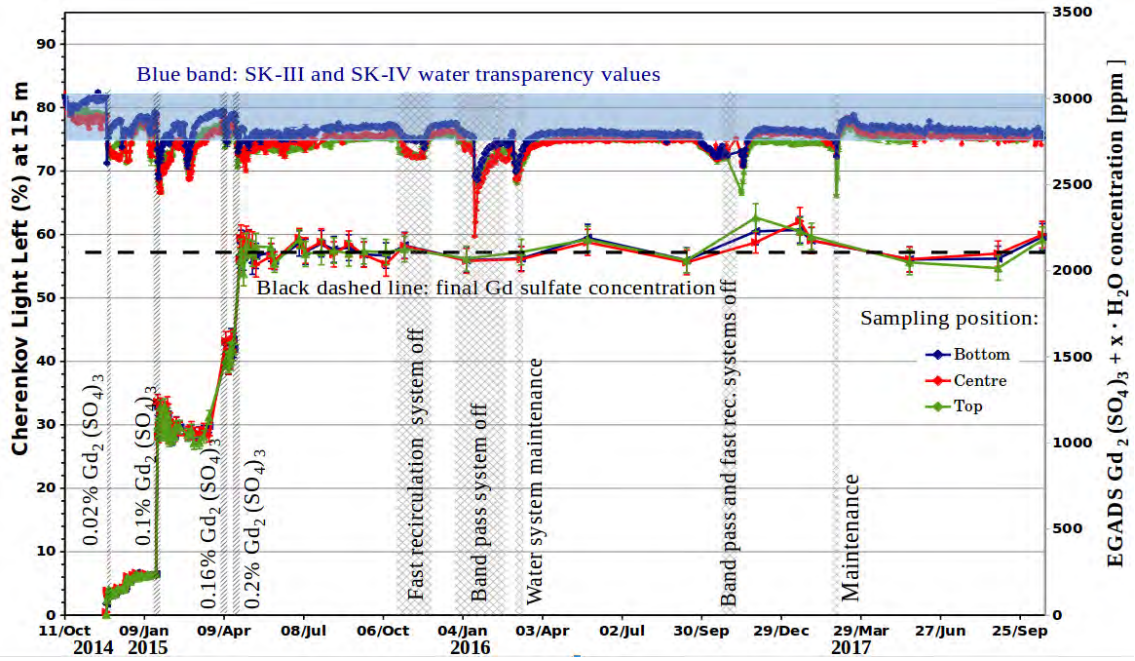


Fig. 19. Cerenkov light left at 15 m for Gd loaded water in EGADS until September 2017. The horizontal blue band are the typical values for SK-III and SK-IV. The vertical lines shows the injection dates where we also indicate the concentration (% in mass) in the 200-ton tank. The black dashed line shows the final expected concentration.

led to a reduction of the water transparency. After restarting, the water transparency was recovered. On September 2019 the water flow was modified so that only half of the flow pass through the special cation exchange resin. The water transparency remained stable and high. Finally, in November 2020, in order to simulate the future additional Gd loading in Super-Kamiokande, EGADS was loaded from 0.01% to 0.03% Gd concentration.

Ion exchange resin tests

Impurities in water Cerenkov detector's water can be removed using anion and cation resins as a standard method.

In case of Gd-loaded water, standard cation exchange resins are expected to also remove Gd. Hence, a special cation exchange resin has been developed and installed in EGADS, in addition to the usual anion exchange resin. The installation was done in January-February 2019 (in January, the new cation exchange resin was used alone, leading a water transparency drop). As showed in Figure 20, we observed an improvement of the water transparency compared than with only anion exchange resin. This increase was enhanced following the replacement of the TOC and UV lamps in March 2019, which stresses the importance of the ionization lamps for the water transparency.

Cation and anion exchange resins are commercial products which can be discontinued by their manufacturers. When this happens, in order to find and test new resins for Super-Kamiokande, we are using EGADS to demonstrate the performances of replacement candidates.

In 2021, the AmberJet 4400 anion exchange resin was discontinued by its manufacturer. In May 2021, we tested AmberJet 4002 which allowed to keep an high water transparency. The initial drops following the installation of this new resin were due to a too short resin flushing period.

In 2022, the AmberJet 1020 (Gd) special cation resin was discontinued by its manufacturer. A substitute candidate, Amberlite IR120B (Gd), was installed in the water system in December 2021. Data after one year and half showed acceptable results, though not as good as the AmberJet 1020 (Gd).

In 2023 Amberlite IR120B (Gd) will be discontinued by its manufacturer. In September 2023, we tested Amberlite HP1210 (Gd) in the EGADS water system, after two months of purge with purge water. Performances were equivalent to AmberJet 1020 (Gd).

DAQ operations

In June 2017, EGADS electronics have been upgraded from the ATM electronics to SK's QBee electronics, the DAQ system was also upgraded to use these new electronics. Thanks to this upgrade, the stability of the DAQ has been greatly improved, specially at high rate. Several SN tests were performed, and demonstrated that EGADS is able to detect and process a 10 second long burst of more than 100k Hz without trouble. This is much more than what is expected from a very close galactic SN burst: in case of Betelgeuse, about 25k events are expected according to Nakazato's model.

We developed an online fitter, HEIMDALL, based on SK WIT. It is able to reconstruct all the events online during a SN burst and then provides an alarm within few seconds. HEIMDALL is looking for IBD candidates, therefore taking advantage of the delayed coincidence to reduce the background. Thanks to this, EGADS is able to look for SN in the far end of our galaxy. This enable us to instantly and autonomously detect a galactic SN and report to local experts and neutrino

and astronomy community.

Bibliography

[1] Marti, Ll. et al., NIM-A 959, 163549 (2020)

SK-Gd

In SK-Gd project, the sensitivity of anti-electron neutrino observation has been improved significantly by detecting neutrons with gadolinium (Gd) (specifically, gadolinium sulfate octahydrate ($Gd_2(SO_4)_3 \cdot 8H_2O$)). Already in 2020, 0.01% Gd (about 13 tons in total weight of $Gd_2(SO_4)_3 \cdot 8H_2O$) has been introduced, achieving about 50% neutrino capture efficiency [1]. In June - July 2022 , we have increased Gd concentration to 0.03%to achieve 75% neutron capture efficiency[2].

Diffuse supernova neutrino background search

Diffuse Supernova Neutrino Background (DSNB) is a neutrino radiation background emitted from past supernova explosions that have occurred since the early universe after the Big Bang. If we can obtain information about DSNB, we can study the history of supernova explosions, such as when many supernova explosions have occurred in the universe. Many of the elements around us are believed to be created during nuclear fusion reactions in massive stars, during supernova explosions, or by mergers between neutron stars (high-density objects formed after supernova explosions). Therefore, understanding supernova explosions leads to understanding the synthesis of elements in the universe.

A search for DSNB has been performed using data obtained to date with Super-Kamiokande in the pure water phase, including all 2970 days of SK-IV data, and the results have been published in [3]. Before SK-Gd, signals of the neutron capture by hydrogen nuclei in pure water were used to reduce the background events by identifying neutrons with a detection efficiency of 20-30% and to limit the flux of DSNB with the world's highest sensitivity in the region below 31.3 MeV.

In 2023, we have published our first DSNB result from SK-Gd period[4]. First, a DSNB search using the conventional method was performed on the SK-VI data. As shown in Figure 21, neutron capture events were selected by applying various cuts, such as cut on the energy of the events. The achieved a final signal identification efficiency was about 36%. The energy spectrum of the final events is shown in Figure 22. 16 events are in the 7.5 MeV–29.5 MeV range, which is consistent with the expected background, and the number of accidental coincidence events is significantly reduced to 10-20% of SK-IV. The number of backgrounds is as expected. Figure 23 shows the limits on the flux of DSNB obtained from this SK-VI analysis. This result, with only 552 days of data, is comparable to that of SK-IV, which has five times the live time data [**?**].

Next, we developed a method to efficiently identify neutrons using a neural network, in order to reduce NCQE reaction events caused by atmospheric neutrinos, which are the largest background source of DSNB. The neural network was trained with 12 variables as input, including the number of PMT hits and the hit time. As a result, in addition to the capture by Gd, the capture by protons was efficiently identified, and the neutrino detection efficiency was 1.3 times higher than that of the conventional method. The resulting energy spectrum is shown in Figure 24.

Compared to Figure 22, the NCQE background is significantly reduced and the expected signal is increased. Even though the statistics is still small, it can be seen that we have already reached the range expected from the theoretical model above 13 MeV.

Bibliography

[1] K. Abe et al., Nucl. Instrum. Meth. A, 1027, 166248 (2022)

[2] K. Abe et al., Nucl. Instrum. Meth. A, 1065, 169480 (2024)

[3] K. Abe et al., Phys. Rev. D **104**, 122002 (2021)

[4] M. Harada et al., The Astrophysical Journal Letters, 951,L27 (2023)

T2K EXPERIMENT

[Spokesperson : Ken Sakashita]
KEK

The Tokai to Kamioka (T2K) experiment [1] is a long baseline neutrino oscillation experiment: a man-made beam of neutrinos is used to do precise studies of the oscillations of neutrinos. Accelerated protons are used to produce the neutrinos in the J-PARC center in the Ibaraki prefecture, which then travel 295 km to reach the Super-Kamiokande (Super-K) detector in the Gifu prefecture where they can be detected after oscillations. A complex of near detectors located 280 meters away from the proton target is used to monitor the neutrino beam, and constrain systematic uncertainties on the neutrino fluxes and interactions. T2K was the first long-baseline experiment to use the off-axis beam technique [2]: the beam is not aimed directly at Super-K, but in a direction making a 2.5° angle with the far detector direction. This gives increased sensitivity to neutrino oscillations while reducing the backgrounds by producing a narrow band neutrino beam centered on the energy corresponding to the first maximum of the $\nu_\mu \to \nu_e$ oscillation probability.

T2K realized the first observation of the appearance of a flavor of neutrinos through oscillation by detecting electron neutrinos in a beam of neutrinos produced in the muon flavor [3]. After achieving this milestone, the experiment has been using its ability to produce a beam of either neutrinos or anti-neutrinos to compare the oscillations of neutrinos and their antiparticles. This allows to study the main remaining open questions in neutrino oscillations (CP symmetry and ordering of the neutrino mass states) by looking at the differences between the oscillations $\nu_\mu \to \nu_e$ and $\bar{\nu}_\mu \to \bar{\nu}_e$. At the same time, T2K's physics goals include the precise measurement of the neutrino oscillation parameters θ_{23} and Δm^2_{32}

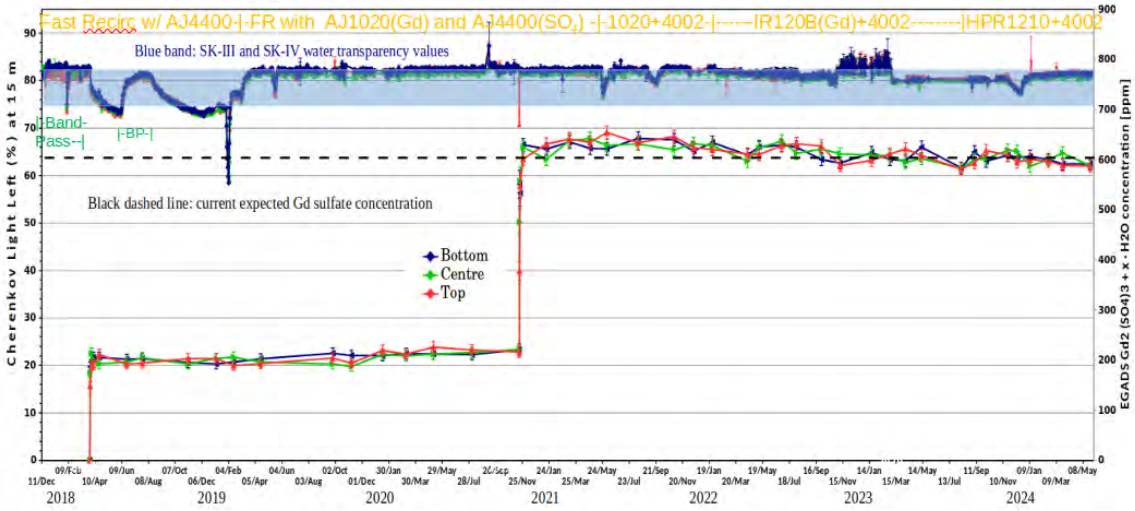


Fig. 20. Cerenkov light left at 15 m for Gd loaded water in EGADS since December 2018. The horizontal blue band are the typical values for SK-III and SK-IV. The vertical lines shows the injection dates where we also indicate the concentration (% in mass) in the 200-ton tank. The black dashed line shows the final expected concentration.

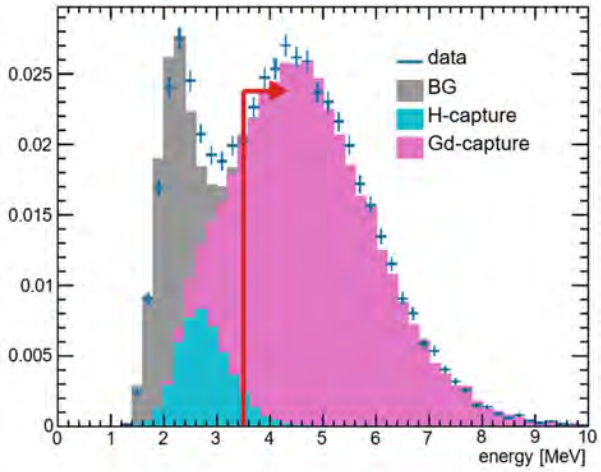


Fig. 21. Selection of neutron capture events by energy cut for the calibration data and its MC simulation with Am/Be neutron source

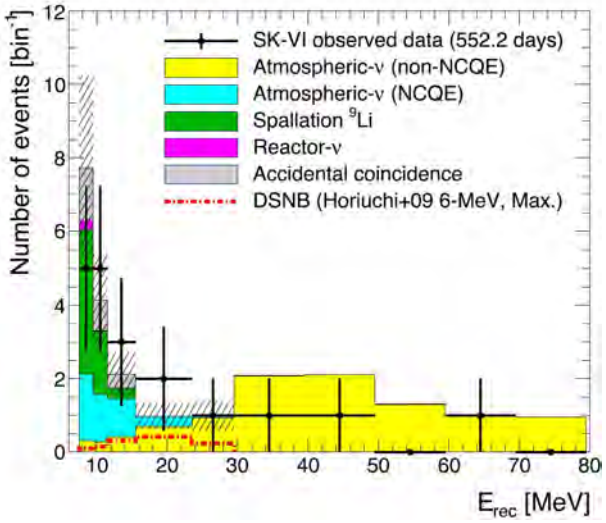


Fig. 22. Energy distribution of events remaining in the final sample in the SK-VI DSNB search using conventional cut-based analysis

through a precise study of the pattern of the disappearance of the muon neutrinos in conjunction with the data used to study the oscillation to the electron flavor. The experiment additionally performs searches for physics beyond the standard model, such as oscillations due to sterile neutrinos and CPT violation. Finally, the near detectors are used to perform a wide range of neutrino and anti-neutrino cross-section measurements.

In J-PARC, protons are accelerated to 30 GeV by a series of three accelerators, and hit a 1.9 interaction-length graphite target. The collisions produce hadrons, in particular charged pions and kaons, which are focused by three electromagnetic horns. The hadrons then go through a 96 m-long decay tunnel where they decay in flight into neutrinos. A beam dump at the end of the decay tunnel stops the remaining hadrons, while high energy muons (5 GeV/c or higher) can pass through this beam dump and are measured to provide a first, indirect monitoring of the neutrino beam. The horns can be used either with a positive current (ν-mode), in which case the beam is mainly made of ν_μ, or with a negative current ($\bar{\nu}$-mode) which gives a mainly $\bar{\nu}_\mu$ beam.

The near detectors are separated into two groups. On the axis of the beam, the INGRID detector, made of fourteen identical modules is used to monitor the beam direction and rate stabilities. Each module is made of a succession of iron plates to provide large target mass (7.1 tons per module) alternating with scintillator planes for detection. Using the number of events reconstructed in each module, the beam direction can be measured daily with better than 0.4 mrad accuracy. Located in the direction of Super-K, the off-axis detector ND280 is made of several detectors located inside a 0.2T magnet. The higher precision of those off-axis detectors allows to do more detailed measurements of the unoscillated neutrino beam. In neutrino oscillation analyses, the ND280 is used to provide information on the ν_μ and $\bar{\nu}_\mu$ unoscillated spectra directed at

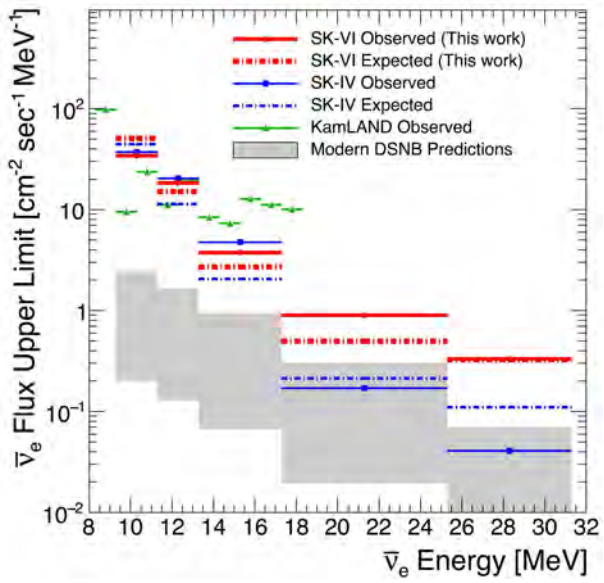


Fig. 23. Sensitivity of the DSNB flux of SK-VI (red dashed line) and the upper limit obtained (red solid line)

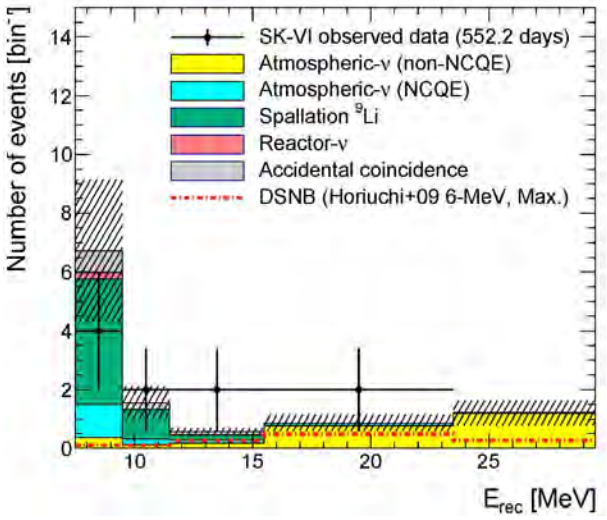


Fig. 24. Energy distribution of events remaining in the final sample in the SK-VI DSNB search using improved neural network analysis

SK, constrain the dominant backgrounds, and constrain the combination of flux and interaction cross sections.

The far detector, Super-K, is a 50 kton water Cherenkov detector, shielded from atmospheric muons by 1000 m of rock, or 2700 meters-water-equivalent (m.w.e.) mean overburden. To select events corresponding to the T2K beam, Super-K is synchronized via GPS to the J-PARC beamline. Hit information within $\pm 500 \mu s$ from the beam arrival timing is used for T2K data analysis. Events are reconstructed by detecting Cherenkov rings from charged particles produced by neutrino interactions. These events are separated into muon-like and electron-like events based on the light pattern of the most energetic ring, and additional selection cuts are applied to produce samples enriched in certain interaction modes. In 2020, Gadolinium was dissolved into the Super-Kamiokande detector at 0.01%, and the new phase of Super-K, SK-Gd, was started [4]. Additional gadolinium was loaded to Super-K in 2022, and the detector is currently operational with 0.03% gadolinium concentration. Additions of gadolinium significantly increased neutron detection capability, which will benefit T2K's neutrino interaction and oscillation measurements as well.

To study neutrino oscillations, the data observed at the far detector are compared to the predictions of the three-flavor oscillation model for different values of the oscillation parameters. To this end, a model of the experiment is constructed: the fluxes of the different flavors of neutrinos reaching the detectors are predicted by a series of simulations, and the interactions of ν and $\bar{\nu}$ in the detectors are simulated using the NEUT Monte Carlo event generator [5]. First, the flux and properties of the proton beam reaching the target are measured by the proton beam line monitors. Interactions of the protons in the graphite target and production of secondary hadrons are then simulated using the FLUKA package [6]. Measurements from hadron production experiments, in particular NA61/SHINE [7], are used to tune this part of the simulation and the out-of-target interactions. The propagation and decay-in-flight of the hadrons in the decay tunnel are then simulated using the GEANT3 and GCALOR [8] packages. The predictions from this model are compared to the data observed in the near detectors to tune the predictions for the far detector by constraining the model parameters. The result of this near detector fit provides the initial values and uncertainties of the flux and interaction model parameters used in the far detector analysis to measure parameters describing neutrino oscillations.

T2K started collecting physics data in January 2010. Data up to run 10 were taken during the pure-water phase of the Super-K detector. Run 11 corresponds to the first data taking period with gadolinium dissolved in Super-K water at 0.01% Gd concentration. In the run 11 data, evidence for the signal corresponding to the capture of neutrons on gadolinium was seen, in the form of an excess of low energy events after the trigger. A long shutdown to upgrade the accelerator used to produce the neutrino beam took place at the end of run 11. The experiment took a short period of beam data after this upgrade, run 12, which unfortunately lasted only a few days due to troubles at the accelerator. Nevertheless, neutrino interactions were successfully observed at the far detector during run 12. The first large amount of data taking after the accelerator upgrade happened in run 13, which started in Nov. 2023 and is expected to end in July 2024. In December 2023, stable operation with a record beam power of 760 kW was achieved, reaching for the first time the 750 kW design power of the facility.

The details of the data that have been collected at the far detector can be found in Table 4. Over the whole period, the event rates and the beam direction were found to be consistent with the expectations and stable by the measurements of the muon monitor and the on-axis near detector. In particular, the beam direction remained stable well within the $\pm$1mrad target.

An upgrade of the off-axis near detectors has also been performed. A set of new detectors have been installed to replace the π^0 detector in the upstream part of the ND280 detec-

Table 4. T2K data taking periods and integrated numbers of protons on target (POT) that can be used in the far detector analysis. Run 13 is still ongoing at the time of writing, final POT number for this run is expected to be larger.

Run Period	Dates	$\times 10^{20}$ POT ν	$\overline{\nu}$
Run 1	Jan.2010 - Jun.2010	0.32	–
Run 2	Nov.2010 - Mar.2011	1.11	–
Run 3	Mar.2012 - Jun.2012	1.60	–
Run 4	Oct.2012 - May.2013	3.60	–
Run 5	May.2014 - Jun.2014	0.24	0.51
Run 6	Oct.2014 - Jun.2015	0.19	3.55
Run 7	Feb.2016 - May.2016	0.48	3.50
Run 8	Oct.2016 - Apr.2017	7.17	–
Run 9	Oct.2017 - May.2018	0.20	8.79
Run 10	Oct.2019 - Feb.2020	4.73	–
Run 11	Mar.2021 - Apr.2021	1.76	–
Run 12	Apr.2023 - Apr.2023	0.09	–
Run 13	Nov.2023 - Feb.2024	3.12	–
Total	**Jan.2010 - Feb.2024**	**24.63**	**16.35**

tor complex. The new detectors will bring improved ability to study neutrino interactions, with a larger efficiency for high-angle events, lower threshold to detect protons, and the ability to reconstruct neutron energy. This will allow T2K to improve the model of neutrino interactions used to study neutrino oscillations, and reduce the associated systematic uncertainties. The new detectors have been installed in two steps, and from the start of run 13, neutrino data were collected in the partially improved ND280 detector (Fig. 25). The installation of the remaining parts of the detector were completed in May 2024, and data taking with the full upgraded near detector is expected for the last part of run 13.

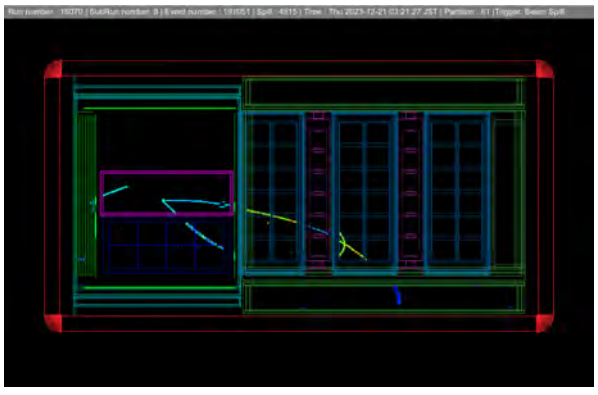


Fig. 25. An event display of the partially upgraded off-axis near detector, with a neutrino interaction candidate in the newly installed "SuperFGD" and a track entering the newly installed "bottom High Angle TPC" while another track is entering the original ND280 detectors. From [9].

Measurements of the ν_μ and $\overline{\nu}_\mu$-induced coherent charged pion production cross sections on ^{12}C by the T2K experiment

T2K reported a measurement of the coherent charged pion production cross section on ^{12}C nuclei [16]. The paper presents the first measurement of the antineutrino induced coherent pion-production cross section on ^{12}C at a mean neutrino energy of 0.85 GeV. In addition, the previous T2K measurement of neutrino-induced coherent pion production [17] is updated by doubling the size of the available data set and updating the systematic uncertainty estimates.

Charged current coherent pion production in (anti-)neutrino-nucleus scattering, $\nu_\mu(\overline{\nu}_\mu)+A \rightarrow \mu^{-(+)}+\pi^{+(-)}+A$, is a process in which a neutrino scatters coherently off a target nucleus. This process leaves the nucleus in its ground state, with the W-boson fluctuating to a charged meson (usually a pion) in the final state. The interaction results in an unchanged nucleus, a lepton and pion in the final state and no other particles. The most common theoretical description of this process is based on Adler's partially conserved axial vector current (PCAC) theorem[18], which connects the forward scattering amplitude (where the square of the 4-momentum transferred to the hadronic system, $-q^2 = Q^2$ is equal to zero) with the divergence of the axial current. The most common model currently used by Monte Carlo (MC) neutrino event generators has been the Rein-Sehgal (RS) model [19]. This uses pion-proton and pion-deuterium data along with a simple A-scaling and ad hoc description for nuclear effects like pion absorption. It was developed for neutrino energies above approximately 5 GeV where the mass of the final state lepton has minimal effect. The newer Berger-Sehgal (BS) model [20] updates this approach with the use of pion-carbon scattering data, which features a significant reduction in the resonance peak. The two models are identical for pion kinetic energies above 1.5 GeV, and employ a similar A-scaling technique. Different characterizations of the pion scattering data (pion-proton for RS, and pion-carbon for BS) in various generators can account for observed differences in their model predictions.

An additional systematic uncertainty was motivated by the report of a suppression of CC-1π resonant events at low Q^2 from the MINERvA experiment[21]. This effect has not been observed or excluded by T2K, which has different neutrino beam energies and nominal MC models, but the potential effect of such an observation in T2K on the cross section result was studied nonetheless. Analysis of a simulated data set with an artificially suppressed CC-RES cross section at low Q^2 resulted in a noticeable bias in the extracted cross section, which was not covered by the model uncertainties considered in this analysis. Since it is unclear whether this suppression should be expected in the T2K data, the bias seen in this study is covered with an additional systematic uncertainty on the extracted (anti)neutrino CC-COH cross section of 16% (24%).

The flux-averaged cross-sections are measured in a reduced final state particle kinematic phase space for which $p_{\mu,\pi} > 0.2$ GeV, $\cos(\theta_\mu) > 0.8$, and $\cos(\theta_\pi) > 0.6$. The $\overline{\nu}_\mu$ cross section results are shown in Fig. 26. The cross section reported here is energy-averaged over the incoming neutrino flux and restricted to a specific region of the parameter space

of produced muon and pion kinematics. As such, it cannot be directly compared to a theoretical model providing the cross section as a function of neutrino energy. A valid comparison requires the theoretical cross section to be integrated over the T2K flux and phase space restrictions applied. Horizontal lines in Fig. 26 show model predictions after this procedure has been applied.

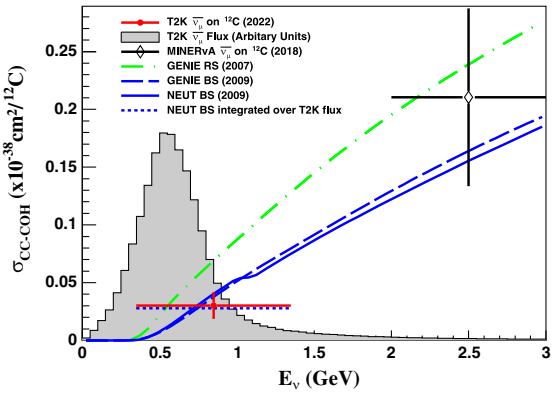


Fig. 26. The T2K $\bar{\nu}_\mu$ CC-COH cross section measurement on C assuming $F(A) = A^{1/3}$. The measurement uncertainty shown is the quadratic sum of the statistical and systematic components. The x-axis error bar covers one standard deviation of the T2K flux around the mean (anti)neutrino energy of $(0.85)0.85$ GeV. The 2016 ν_μ T2K result (same E_ν range, center point offset slightly for clarity of the figure) [17], and the MINERvA result [22] (for E_ν between 2–3 GeV) are also shown for comparison. Note the phase space between the different measurements are not exactly the same.

The T2K ν_μ CC-COH and $\bar{\nu}_\mu$ CC-COH cross-sections on ^{12}C are $(2.98 \pm 0.37(\text{stat.}) \pm 0.31(\text{syst.})^{+0.49}_{-0.00}(\text{Q}^2\,\text{model})) \times 10^{-40}$ cm^2 and $(3.05 \pm 0.71(\text{stat.}) \pm 0.39(\text{syst.})^{+0.74}_{-0.00}(\text{Q}^2\,\text{model})) \times 10^{-40}$ cm^2, assuming an A-scaling of $A^{1/3}$. The uncertainty labelled as "Q^2 model" corresponds to the potential bias caused by the low Q^2 CC-RES suppression study. This study presents the first measurement of the $\bar{\nu}_\mu$ CC-COH cross-section at a mean neutrino energy less than 1 GeV. In addition, the ν_μ CC-COH measurement is consistent with the previous 2016 T2K result but with the fractional total uncertainty reduced from 46% to 23%. It is notable that the measured neutrino and antineutrino coherent pion production cross-sections are themselves consistent, as expected from theory. Both the NEUT Berger-Sehgal and the GENIE Rein-Sehgal model predictions are compatible with the data within the measurement uncertainties.

First measurement of muon neutrino charged-current interactions on hydrocarbon without pions in the final state using multiple detectors with correlated energy spectra at T2K

T2K presented its first measurement of muon neutrino charged-current interactions without pions in the final state using multiple detectors with correlated energy spectra [23]. The near detectors (close to the neutrino source) used by T2K provide a unique opportunity to perform a combined measurement using the same neutrino beam with two detectors exposed to different but correlated spectra of incident neutrinos, and is the subject of the analysis presented in this paper. Neutrino detectors measure the rate of neutrino interactions, which is primarily a product of the neutrino flux and neutrino cross section. Changes in both the flux and cross-section models can cause the observed event rate to change, often in similar ways, and this degeneracy limits the ability to separate individual effects due to either the flux or cross section. The correlation between the different fluxes at the near detectors provides additional information that can be used to constrain the flux uncertainty and break some of the degeneracy between flux and cross section. The different neutrino energy spectra seen at each detector also presents an opportunity to study the energy dependence of neutrino interactions within the same analysis framework.

The T2K near detector complex houses the two detectors of primary interest for the analysis presented in this paper: a detector on the axis of the neutrino beam, called INGRID (Interactive Neutrino GRID), and a detector located 2.5 degrees off-axis, called ND280 (Near Detector at 280 meters). INGRID primarily serves as a neutrino beam and flux monitor, measuring the total rate of neutrino interactions and the beam direction. ND280 is dedicated to the study of the un-oscillated spectrum of neutrinos at 280 meters from the production point and neutrino interaction cross-section properties. The goal of this analysis was to perform a simultaneous fit to ND280 and INGRID data, extracting the muon neutrino flux-integrated differential cross section on hydrocarbon without pions in the final state as a function of the outgoing muon kinematics for both the off- and on-axis T2K flux. Signal events are defined by a neutrino interaction with an outgoing muon, zero pions, and any number of other hadrons in the final state and are referred to as CC-0π events (or topology).

The measured cross sections are compared to the predictions from a small selection of neutrino interaction models implementations in neutrino interaction generators (Fig. 27). The agreement between the measurement and models is quantified via the χ^2 (relative to the number of degrees of freedom). The model predictions were produced by generating a sufficiently large number of neutrino interactions on hydrocarbon using the T2K on- and off-axis flux for each model. Generated events that satisfy the CC-0π signal definition are selected to calculate the flux integrated cross section for each detector. Tab. 5 contains the χ^2 for the joint result and the χ^2 considering a single detector. The joint χ^2 for a given model comparison will be slightly different from the sum of the individual χ^2 values due to the correlations between the detectors. Overall the generator predictions do not describe the data well according to χ^2/N values ranging from approximately 1.5 to 3.0 for $N = 70$ degrees of freedom (measured bins) with 58 ND280 bins and 12 INGRID bins. The larger χ^2 values for ND280 compared to INGRID is primarily due to ND280 having a finer binning than INGRID. A unique aspect of this measurement is the ability to compare how a given model does for ND280 and INGRID individually and how the full result with correlations between ND280 and INGRID is better or worse than the naive sum. For example, the two GENIE models used in this paper show opposite behavior: one model describes ND280 better than the other but does worse

describing INGRID and vice versa. In conclusion, generator models continue to struggle to describe the data, and for the comparisons performed in this paper, the NEUT implementation of a LFG ground state plus the Nieves *et al.* multi-nucleon model has the smallest $\chi^2/N \sim 1.66$, which is still very poor agreement.

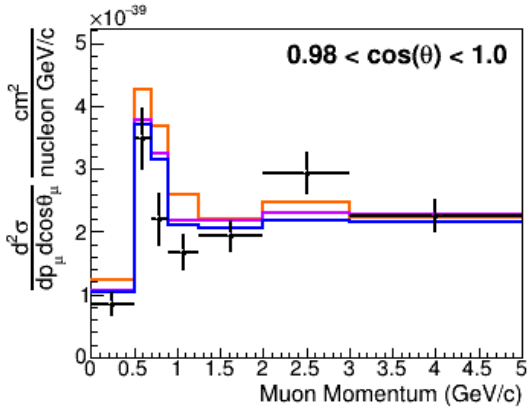


Fig. 27. Extracted ND280 cross section as a function of muon momentum for one of the ND280 angle bins compared to NEUT (purple), GENIE (blue), and NuWro (orange) predictions using a similar model (LFG + Nieves).

Model	ND280	INGRID	Joint
Nominal MC (NEUT)	136.34	18.21	158.71
NEUT LFG+Nieves	106.46	11.46	116.26
NEUT SF+Nieves $M_A = 1.03$	194.88	14.36	209.18
NEUT SF+Nieves $M_A = 1.21$	158.71	9.98	170.93
NuWro SF+Nieves	122.74	15.68	137.02
NuWro LFG+Nieves	125.88	12.75	141.04
NuWro LFG+SuSAv2	121.57	11.13	135.38
NuWro LFG+Martini	138.86	12.46	155.68
GENIE BRRFG+EmpMEC	141.40	12.80	156.05
GENIE LFG+Nieves	125.50	14.45	135.69

Table 5. Agreement between this result and the various model comparisons as measured by the χ^2 for both the joint result and when compared to each detector individually. ND280 has 58 cross-section bins and INGRID has 12 cross-section bins for a combined 70 total bins.

Measurements of neutrino oscillation parameters from the T2K experiment using 3.6×10^{21} protons on target

T2K presented new measurements of neutrino oscillation parameters using $19.7(16.3) \times 10^{20}$ protons on target (POT) in (anti-)neutrino mode at the far detector (FD) [14]. Compared to the previous measurement [15], the analysis features a number of improvements:

- **Data at the FD:** The data at INGRID and the FD increased by 4.73×10^{20} POT (+33%) in ν-mode, increasing the overall amount by 15%.
- **Data at the ND:** The data at the ND increased by 5.73×10^{20} POT (+99%) in ν-mode, and by 4.48×10^{20} POT (+116%) in $\overline{\nu}$-mode, increasing the overall amount by 106%.
- **Selections at the ND:** The increased data allowed for refining the $\overline{\nu}$-mode selections and re-binning all existing selections, improving the constraints on the systematic uncertainties from the ND in the oscillation analysis.
- **FD reprocessing:** An updated model for the dark rate and gain drift in the PMTs had a slight impact on the reconstruction and the number of observed data events. The processing introduced one more $\overline{\nu}$-mode electron-like event, and three fewer $\overline{\nu}$-mode muon-like events, and had no overall effect on the ν-mode samples.
- **Neutrino flux model:** The neutrino flux was constrained using charged pion production data on a replica of the T2K production target from NA61/SHINE [13]. Data on a thin target [24] was also used when appropriate. This reduced the flux uncertainties before the ND analysis from $\sim 9\%$ down to $\sim 5\%$ in the neutrino flux peak.
- **Neutrino interaction model:** Several changes to the neutrino interaction model were made. The largest changes were switching to a more sophisticated spectral-function based nuclear model for charged-current quasi-elastic (CCQE) interactions, introducing an additional uncertainty due to nuclear effects in the four-momentum transferred to the nucleus (Q^2), and adding an uncertainty for the nucleon removal energy. The nuclear-cascade model for pions was tuned to external data [25], and the FD parametrisation was constrained by the fit to ND data, whereas it was previously allowed to vary separately. The interaction model for pions re-scattering within the detector at the ND and FD were unified, and is identical to the pion final-state interaction model. However, constraints of re-scattering within the ND were not propagated to re-scattering at the FD, as the uncertainties were kept uncorrelated.

The results provide leading constraints on both the atmospheric oscillation parameters, $\sin^2(\theta_{23})$ and Δm^2_{32} and the CP-violating phase, δ_{CP}. Fig. 28 shows the 90% confidence regions in $\sin^2(\theta_{23}) - \Delta m^2_{32}$ for the normal ordering from the frequentist analysis, compared to NOνA, SK and IceCube. There is general agreement between the experiments, with T2K providing the strongest constraints on both parameters. Fig. 29 shows the $\Delta\chi^2$ distributions for δ_{CP} in both mass orderings with confidence intervals obtained using the Feldman-Cousins unified approach. A large region of $\sin\delta_{CP} > 0$ is excluded at $> 3\sigma$ confidence level (CL), whereas the CP-conserving values $\delta_{CP} = 0, \pi$ are excluded at 90% CL. In particular, $\delta_{CP} = \pi$ is just inside the 2σ interval.

Updated T2K measurements of muon neutrino and antineutrino disappearance using 3.6×10^{21} protons on target

T2K published an update of the analysis comparing the muon neutrino and antineutrino disappearance probabil-

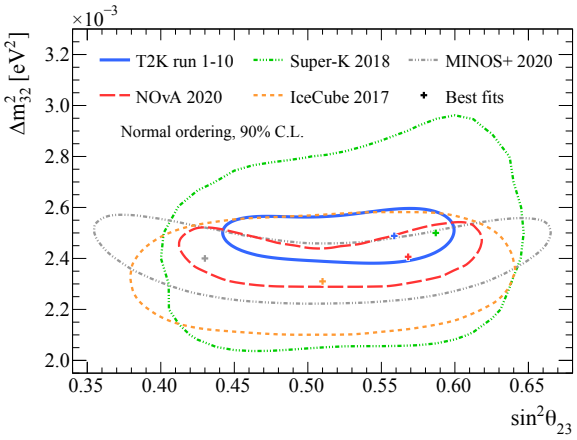


Fig. 28. Comparison of the 90% confidence regions in $\sin^2(\theta_{23}) - \Delta m^2_{32}$ for normal ordering with NOνA [26], Super-K [27], IceCube [28], and MINOS+ [29].

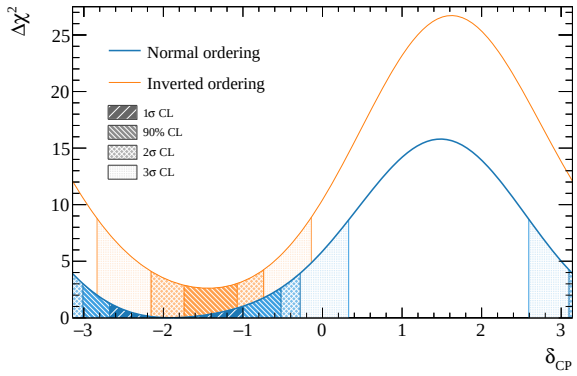


Fig. 29. The $\Delta\chi^2$ distribution in δ_{CP} from fitting to the data with the reactor constraint applied. The confidence intervals in the shaded regions are calculated using the Feldman-Cousins method.

ities [10]. In the standard three-flavor neutrino oscillation framework, the two disappearance probabilities are the same in the absence of matter effects (which are negligible at T2K energies and baseline, but are included in their calculation) so a mismatch could indicate a source of CPT violation or a source of nonstandard interactions [11].

The results presented in this paper represent an update to the previous T2K measurements [12]. Like the previous analyses, we allow the oscillation parameters for ν_μ (θ_{23} ,Δm^2_{32}) to vary separately from those of $\overline{\nu}_\mu$ ($\overline{\theta}_{23}$,$\overline{\Delta m^2_{32}}$) , while all other oscillation parameters are assumed to be the same for neutrinos and antineutrinos. Four significant updates have been made since the previous analysis. First, the number of protons on target (POT) collected in neutrino beam mode was increased from 1.49×10^{21} to 1.97×10^{21} by including T2K data up to February 2020. Second, the flux prediction was tuned to the $\pi^{\pm}$ yields from the surface of a T2K replica target measured by NA61/SHINE [13]. Third, the modeling of neutrino interactions on nuclear targets was improved. Finally, the selection of antineutrino events used to constrain uncertainties using T2K near detector was refined and the data set doubled.

The best-fit values obtained for oscillation parameters describing neutrino oscillations are $\sin^2(\theta_{23}) = 0.47^{+0.11}_{-0.02}$ and $\Delta m^2_{32} = 2.48^{+0.05}_{-0.06} \times 10^{-3}\text{eV}^2$ and those describing antineutrino oscillations are $\sin^2(\overline{\theta}_{23}) = 0.45^{+0.16}_{-0.04}$ and $\overline{\Delta m^2_{32}} = 2.53^{+0.10}_{-0.11} \times 10^{-3}\text{eV}^2$. The best-fit values for both neutrino and antineutrino oscillations agree within the uncertainties. In Fig. 30 we compare the constraints on $\sin^2(\theta_{23})$ and Δm^2_{32} coming from the three-flavor analysis to muonlike samples and the joint analysis to both electronlike and muonlike samples [14]. Since the parameters for ν_μ and $\overline{\nu}_\mu$ are compatible, we conclude that the measurements of the parameters describing the oscillations of muon neutrinos and antineutrinos are compatible with the three-flavor prediction and provide no indication of new physics.

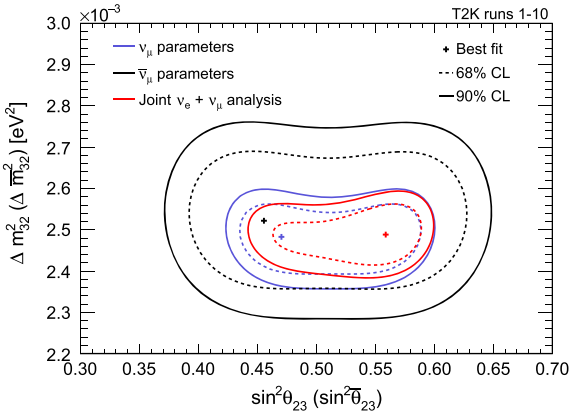


Fig. 30. Confidence regions of $(\sin^2(\theta_{23}), \Delta m^2_{32})$ for neutrinos and their barred parameters for antineutrinos. Corresponding regions from the standard PMNS formalism analysis [14] including ν_e samples are also shown for comparison.

Bibliography

[1] K. Abe *et al.* (T2K Collaboration), Nucl. Instrum. Meth. A **659**, 106 (2011).

[2] D. Beavis, A. Carroll, I. Chiang, *et al.*, Long Baseline Neutrino Oscillation Experiment at the AGS (Proposal E889), 1995. Physics Design Report, BNL 52459.

[3] K. Abe *et al.* (T2K Collaboration), Phys. Rev. Lett. **112**, 061802 (2014).

[4] K. Abe *et al.* (Super-Kamiokande Collaboration), Nucl. Instrum. Meth. A **1027**, 166248 (2022).

[5] Y. Hayato, L. Pickering, Eur. Phys. J. Spec. Top. (2021)

[6] T. Bhlen *et al.*, Nucl. Data Sheets **120**, 211 (2014).

[7] N. Abgrall et al. (NA61/SHINE Collaboration), Eur. Phys. J. C **76**, 84 (2016).

[8] C. Zeitnitz and T. A. Gabriel, Proceedings of International Conference on Calorimetry in High Energy Physics (World Scientific, Corpus Christi, Texas, 1992), ISBN 9789810213039, pp. 394-404.

[9] T2K press release, https://www.kek.jp/en/press/202401171405

[10] K. Abe *et al.* (T2K Collaboration), Phys. Rev. D **108**, 072011 (2023)

[11] C. A. Argüelles et al., Eur. Phys. J. C **83**, 15 (2023).

[12] K. Abe *et al.* (T2K Collaboration), Phys. Rev. D **103**, L011101 (2021)

[13] N. Abgrall et al. (The NA61/SHINE Collaboration), Eur. Phys. J. C **76**, 617 (2016).

[14] K. Abe et al. (The T2K Collaboration), Eur. Phys. J. C **83**, 782 (2023).

[15] K. Abe et al. (The T2K Collaboration), Phys. Rev. D **103**, 112008 (2021)

[16] K. Abe et al. (The T2K Collaboration), Phys. Rev. D **108**, 092009 (2023)

[17] K. Abe et al. (The T2K Collaboration), Phys. Rev. Lett. **117**, 192501 (2016).

[18] S. L. Adler, Phys. Rev. **135**, B963 (1964).

[19] D. Rein and L. Sehgal, Nucl. Phys. **B223**, 29 (1983).

[20] C. Berger and L. M. Sehgal, Phys. Rev. D **79**, 053003 (2009)

[21] P. Stowell et al. (MINERvA Collaboration), Phys. Rev. D **100**, 072005 (2019).

[22] A. Mislivec et al. (MINERvA Collaboration), Phys. Rev. D **97**, 032014 (2018)

[23] K. Abe et al. (The T2K Collaboration), Phys. Rev. D **108**, 112009 (2023)

[24] N. Abgrall et al. (The NA61/SHINE Collaboration), Phys. J. C **76**, 84 (2016).

[25] Guerra, E. S. Pinzon et al., Phys. Rev. D **99**, 052007 (2019)

[26] Acero, M. A. (NOvA collaboration), Phys. Rev. D **106**, 032004 (2022)

[27] K. Abe et al. (Super-Kamiokande Collaboration), Phys. Rev. D **97**, 072001 (2018)

[28] IceCube collaboration, data release, DOI: 10.21234/B4105H

[29] Adamson, P. et al. (MINOS+ Collaboration), Phys. Rev. Lett. **125**, 131802 (2020)

XMASS EXPERIMENT

[Spokesperson : Shigetaka Moriyama]
Kamioka Observatory, ICRR, the University of Tokyo

Introduction

The XMASS project was designed to detect dark matter, neutrinoless double beta decay, and ^{7}Be/pp solar neutrinos using highly-purified liquid xenon (LXe) scintillator in an ultra-low radioactivity environment [1]. The advantages of using LXe are a large amount of scintillation light yield, scalability of the size of the detector mass, easy purification to reduce internal radioactive backgrounds (BGs), and shielding ability against radiation from outside the detector due to a high atomic number ($Z = 54$) [2]. A breakthrough technology was developed to purify liquid xenon from the radioactive contaminant of ^{85}Kr found in commercial gas xenon [3]. This makes liquid xenon detectors suitable for rare event searches. The detector containing $\sim$830 kg of LXe, was constructed in September 2010. Commissioning data was taken from December 2010 to May 2012. Based on commissioning data results were published on DM searches [4, 5, 6], solar axions [7], and two-neutrino double electron capture on ^{124}Xe [8]. We also studied the possibility of detecting galactic supernova neutrinos via coherent elastic neutrino-nucleus scattering [9].

Analyzing the commissioning data we found that a majority of events at low energy originated from radioactive contamination in the aluminum seal of the photomultiplier tube (PMT) window. In order to minimize the impact of this BG, the detector was refurbished. The contaminated seals were covered with copper rings and plates to stop scintillation lights and radiation caused by this contamination to reach the inner detector volume. The PMT windows were cleaned with nitric acid, and copper parts were electropolished in order to remove possible surface contamination. After a year of detector refurbishment, data-taking resumed in November 2013 with background significantly reduced and continued for more than five years. We completed data taking in February 2019. Results were published from searches for annual modulation from dark matter [10, 11], solar Kaluza-Klein axions [12], two-neutrino double electron capture on ^{124}Xe [13], dark matter through elastic-scattering [14], hidden photons [15], inelastic-scattering off ^{129}Xe [16], sub-GeV dark matter [17], exotic neutrino-electron interactions [18], events coincident with the arrival of gravitational waves [19], and for neutrinoless quadruple beta decay of ^{136}Xe [20]. As the final result of XMASS-I, a paper describing direct dark matter searches with the full data set of XMASS-I was published [21]. It summarized the search for nuclear recoil signals in fiducial volume and the annual modulation signals from nuclear recoil and electron recoil with 1509.9 days live time. These searches covered the mass range from 0.32 to 10^4 GeV/c^2 with our cross-section limits in a single detector and provided the world's best results from a single-phase LXe detector.

In the following sections, we briefly introduce the XMASS-I detector and report the final physics results from XMASS-I experiment.

The XMASS-I detector

XMASS-I was a single-phase LXe scintillator detector located underground (2700 m water equivalent) at the Kamioka Observatory [22]. Figures 31 and 32 show a schematic drawing of the XMASS-I detector and a picture during the refurbishment work, respectively. It contained ∼830 kg of LXe in its active region. The active volume is viewed by 630 hexagonal and 12 cylindrical Hamamatsu R10789 PMTs arranged on an 80 cm diameter pentakis-dodecahedron support structure. These PMTs were developed to achieve low background requirements [23]. The largest contributions to the reduction of radioactivity came from the PMTs' stem and its dynode support. The glass stem was exchanged for a the Kovar alloy one, and the ceramic support was changed to a quartz one. The R10789 is the first model of Hamamatsu Photonics K. K. that adopted these materials for low background purposes and provided a groundbreaking step for further reductions of radioactivity in PMTs. A total photocathode coverage of more than 62% of the inner surface was achieved in XMASS. The almost spherical array of PMTs was supported in a double-walled vessel made of oxygen-free high conductivity copper [24]. The waveforms of each PMT were recorded with CAEN V1751 waveform digitizers with a 1 GHz sampling rate and 10 bit resolution. The detector was calibrated regularly with a ^{57}Co source inserted along its central vertical axis and an external ^{60}Co source. From the data taken with the ^{57}Co source at the center of the detector volume, the photoelectron (PE) yield was determined to be ∼14 PE/keV. Two different energy scales were used: keV$_{ee}$ represents an electron equivalent energy, and keV$_{nr}$ denotes the nuclear recoil energy. The scintillation decay time constant was investigated in liquid xenon with the XMASS detector. The results were summarized in [25] and [26].

In order to shield the LXe detector from external gammas, neutrons, and muon-induced BGs, the copper vessel was placed at the center of a ϕ10 m× 10.5 m cylindrical tank filled with pure water. This water tank was equipped with 72 Hamamatsu R3600 20-inch PMTs to provide both an active muon veto and a passive shield against external BGs. XMASS-I was the first direct detection dark matter experiment equipped with such an active water Cherenkov shield. The LXe and water Cherenkov detectors were called the Inner Detector (ID) and the Outer Detector (OD), respectively.

It is also worth noting that there were some important technical studies related to pulse-shape discrimination between nuclear recoils and electron recoils [27], radon removal using charcoal filters [28], scintillation performance of liquid xenon at room temperature [29], a ^{220}Rn calibration source [30], and 3-inch low background photomultiplier tubes [31] for future applications.

Direct dark matter searches with the full data set of XMASS-I [21]

One of the well-motivated dark-matter candidates is Weakly Interacting Massive Particle (WIMP) and is thought

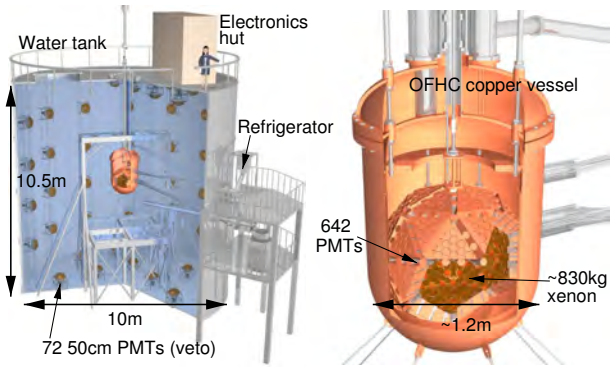


Fig. 31. Schematic drawing of the XMASS-I detector.

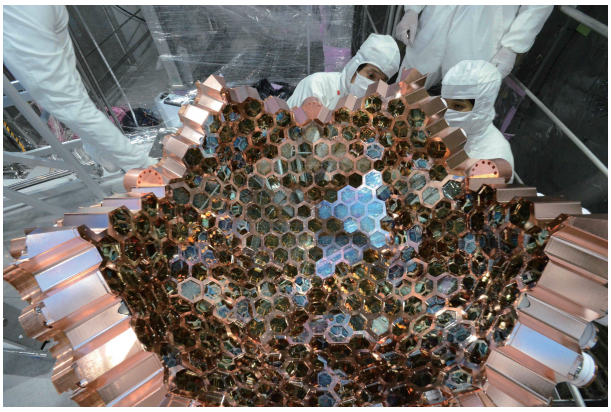


Fig. 32. The XMASS detector (the photo was taken during the refurbishment work in 2013).

to be observable through nuclear recoils or electron recoil produced in their elastic scattering interactions with target material. It is the main target of XMASS and we had reported many WIMP search results before [4, 5, 10, 11, 14, 16, 17].

As the final result of XMASS-I, a unique single-phase LXe detector, we conducted various WIMP dark matter searches with full-data set of XMASS-I. Over a long period of observation of XMASS-I, we accumulated 1590.9 live days of data with an analysis threshold of 1 keV$_{ee}$. A subset of later 768.8 days therein allows for an even lower analysis threshold of 0.5 keV$_{ee}$. We searched for a nuclear recoil signal in the detector's fiducial volume and also annual modulation signatures caused by a nuclear recoil (NR) and an electron recoil (ER) interactions.

Given that XMASS-I data were dominated by background originating from β events at the ID PMT entrance window seal at 30 keV$_{ee}$ or less, a fiducial volume (FV) analysis was developed to reduce this background. Following [14], we used two different position reconstruction methods. One was based on hit timings and the other was based on the PE distribution [22]. These methods were referred to as $R(T)$, and $R(PE)$, respectively. We used event radii $R(T) < 38$ cm and $R(PE) < 20$ cm for the FV selection. The fiducial target mass in this volume was 97 kg. To search for a potential WIMP signal the observed energy spectrum was fit as the sum of the corrected BG-MC and a simulated signal contribution of un-

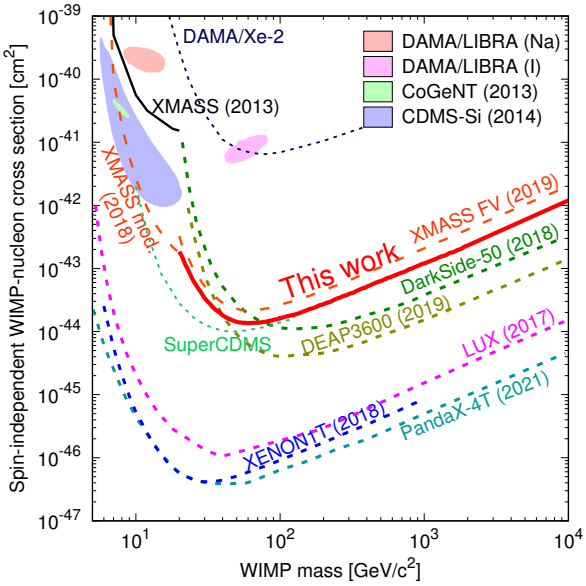


Fig. 33. The spin-independent WIMP-nucleon cross section limit as a function of the WIMP mass at the 90% CL for this work is shown as a solid thick line. Limits from other experiments as well as allowed regions by DAMA/LIBRA(NaI), CoGeNT and CDMS-Si are also shown.

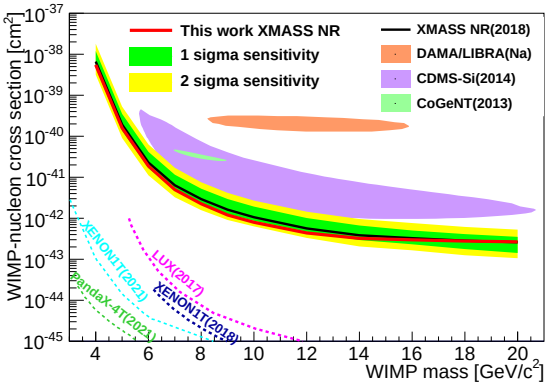


Fig. 34. Limits on the spin-independent elastic WIMP-nucleon cross section as a function of WIMP mass. The solid red line shows the XMASS 90% CL exclusion from the annual modulation analysis. The solid black line shows the 2018 XMASS result [11]. The $\pm1\sigma$ and $\pm2\sigma$ bands represent the expected 90% exclusion regions. Limits, as well as allowed regions from other searches based on event counting, are also shown.

known size for a specific WIMP mass in the energy range of 2–15 keV$_{ee}$. Applying the fiducial volume search with the target mass of 97 kg to the full 1590.9-days data set allowed us to improve our eariler world-best single-phase LXe limit on spin-independent WIMP interactions in XMASS (2019) [14] by a factor of 1.6 down to $1.4\times10^{-44}\,\mathrm{cm}^2$ for 60 GeV/c^2 WIMPs (90% C.L.) as plotted in Fig. 33. This is the most stringent limit among results from single-phase LXe detectors.

The velocity of the earth relative to the galactic DM halo changes as the Earth moves around the sun. This is because the Earth's velocity in its orbit around the Sun effectively adds to or subtracts from the Sun's velocity through a stationary halo. This causes a corresponding change in the expected DM signal rate of terrestrial detectors, with this relative velocity modulation affecting signal rates. Searches using this tell-tale signal rate modulation were already conducted with parts of the XMASS-I data for NRs from multi-GeV WIMPs [10, 11], as well as for the sub-GeV mass region where bremsstrahlung is expected to boost the signal [17]. Updated searches for an annual modulation signature, also extended to the full XMASS-I data set and using XMASS-I's full active target mass of 832 kg, improved on our own old limits [17] for NR by a factor of 1.3 to reach $2.3\times10^{-42}\,\mathrm{cm}^2$ for a $8\,\mathrm{GeV}/c^2$ WIMP. Fig. 34 shows the multi-GeV WIMP search result together with results from other experiments. We also updated our bremsstrahlung result, which for a $0.5\,\mathrm{GeV}/c^2$ WIMP reached a cross section limit of $1.1\times10^{-33}\,\mathrm{cm}^2$, an improvement of a factor 1.5. The newly added analysis exploiting the Migdal effect for low-mass WIMP searches closed the WIMP mass gap that previously existed in our analyses between the lower WIMP mass end of the NR modulation analysis and the upper WIMP mass end of our bremsstrahlung-based modulation analysis, reaching down to $1.4\times10^{-35}\,\mathrm{cm}^2$ for $0.5\,\mathrm{GeV}/c^2$ WIMPs. Two sub-GeV mass region search results are plotted in Fig. 35.

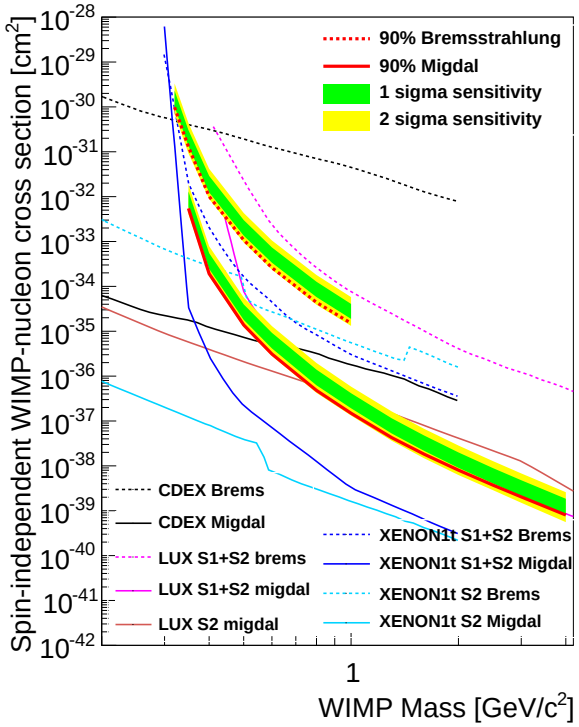


Fig. 35. Summary of the sub-GeV DM analysis results considering annual modulation with the Migdal effenct and the bremsstrahlung. The red solid line is the result of the Migdal analysis for 0.35-4 GeV/c^2 WIMP mass, the red dotted line is the result of the bremsstrahlung analysis for 0.32-1 GeV/c^2. Limits from other experiments obtained via Migdal and Bremsstrahlung effect are also shown for comparison.

Altogether, as summarized in Fig. 36, this WIMP searches cover the whole mass range from 0.32 to 10^4 GeV/c^2 with our cross section limits in a single detector, and are the world best results from a single phase LXe detector.

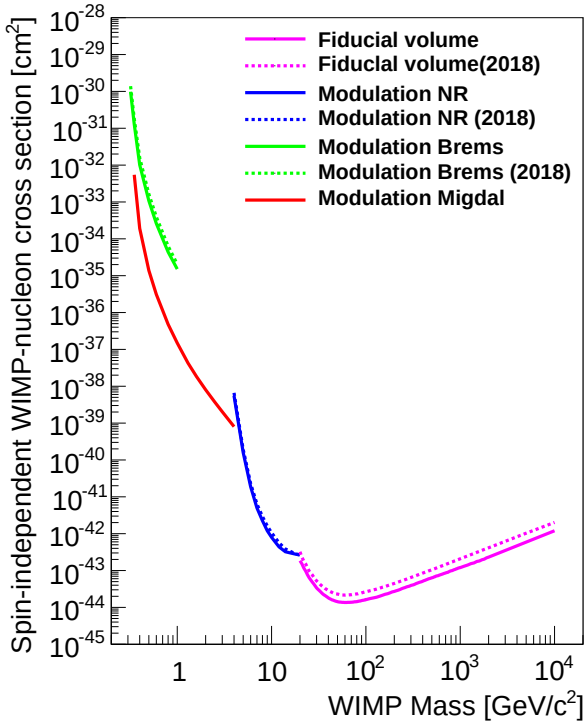


Fig. 36. Limits obtained from the various analyses presented in this paper. Solid lines are the new results, using the full XMASS-I data sets, presented in this paper, in particular the fiducial volume analysis, the muliti-GeV modulation analysis via NR and the sub-GeV modulation analysis via Migdal effect and bremsstrahlung. Dotted lines show our earlier results published [11, 14, 17].

Bibliography

[1] Y. Suzuki *et al.*, hep-ph/0008296.

[2] K. Abe *et al.* (XMASS Collaboration), Astropart. Phys. **35** (2012) 609.

[3] K. Abe *et al.* (XMASS Collaboration), Astropart. Phys. **31** (2009) 290.

[4] K. Abe *et al.* (XMASS Collaboration), Phys. Lett. B **719** (2013) 78.

[5] H. Uchida *et al.* (XMASS Collaboration), Prog. Theor. Exp. Phys. (2014) 063C01.

[6] K. Abe *et al.* (XMASS Collaboration), Phys. Rev. Lett. **113** (2014) 121301.

[7] K. Abe *et al.* (XMASS Collaboration), Phys. Lett. B **724** (2013) 46.

[8] K. Abe *et al.* (XMASS Collaboration), Phys. Lett. B **759** (2016) 64.

[9] K. Abe *et al.* (XMASS Collaboration), Astropart. Phys. **89** (2017) 51.

[10] K. Abe *et al.* (XMASS Collaboration), Phys. Lett. B **759** (2016) 272.

[11] K. Abe *et al.* (XMASS Collaboration), Phys. Rev. D **97** (2018) 102006.

[12] N. Oka *et al.* (XMASS Collaboration), Prog. Theor. Exp. Phys. **2017** (2017) 103C01.

[13] K. Abe *et al.* (XMASS Collaboration), Prog. Theor. Exp. Phys. **2018** (2018) 053D03.

[14] K. Abe *et al.* (XMASS Collaboration), Phys. Lett. B **789** (2019) 45.

[15] K. Abe *et al.* (XMASS Collaboration), Phys. Lett. B **787** (2018) 153.

[16] T. Suzuki *et al.* (XMASS Collaboration), Astropart. Phys. **110** (2019) 1.

[17] M. Kobayashi *et al.* (XMASS Collaboration), Phys. Lett. B **795** (2019) 308.

[18] K. Abe *et al.* (XMASS Collaboration), Phys. Lett. B **809** (2020) 135741.

[19] K. Abe *et al.* (XMASS Collaboration), Astropart. Phys. **129** (2021) 102568.

[20] K. Abe *et al.* (XMASS Collaboration), Phys. Lett. B **833** (2022) 137355.

[21] K. Abe *et al.* (XMASS Collaboration), Phys. Rev. D **108** (2023) 083022.

[22] K. Abe *et al.* (XMASS Collaboration), Nucl. Instrum. Meth. A **716** (2013) 78.

[23] K. Abe *et al.* (XMASS Collaboration), Nucl. Instrum. Meth. A **922** (2019) 171.

[24] K. Abe *et al.* (XMASS Collaboration), Nucl. Instrum. Meth. A **884** (2018) 157.

[25] H. Takiya *et al.* (XMASS Collaboration), Nucl. Instrum. Meth. A **834** (2016) 192.

[26] K. Abe *et al.* (XMASS Collaboration), JINST **13** (2018) P12032.

[27] K. Abe *et al.* (XMASS Collaboration), Nucl. Instrum. Meth. A **659** (2011) 161.

[28] K. Abe *et al.* (XMASS Collaboration), Nucl. Instrum. Meth. A **661** (2012) 50.

[29] K. Abe *et al.* (XMASS Collaboration), Nucl. Instrum. Meth. A **594** (2008) 148.

[30] M. Kobayashi, M. Yamashita, A. Takeda, K. Kishimoto, S. Moriyama, Journal of Physics: Conference Series 718 (2016) 042069 (TAUP2015).

[31] K. Abe *et al.* (XMASS Collaboration), JINST **15** (2020) P09027.

XENON EXPERIMENT

XENON ICRR group
[Principal investigator : Shigetaka Moriyama]
Kamioka Observatory, ICRR, the University of Tokyo

Introduction

The XENONnT experiment [1] is the most sensitive direct dark matter search experiment conducted at LNGS in Italy. The XENON collaboration includes about 180 collaborators from 27 institutions in 12 countries. From Japan, the University of Tokyo (ICRR and Kavli IPMU), Nagoya University, and Kobe University participate since 2017. The XENON group uses liquid xenon and employs a time projection chamber (TPC) shown in Fig. 37, characterized by its ability to discriminate between nuclear and electron recoil. The Japanese group is making a significant contribution toward the discovery of DM particles based on a purification technology for liquid xenon developed in XMASS and the neutron detection technology developed for Super-Kamiokande. The XENON collaboration completed XENONnT detector construction in 2020 and started data taking in 2021.

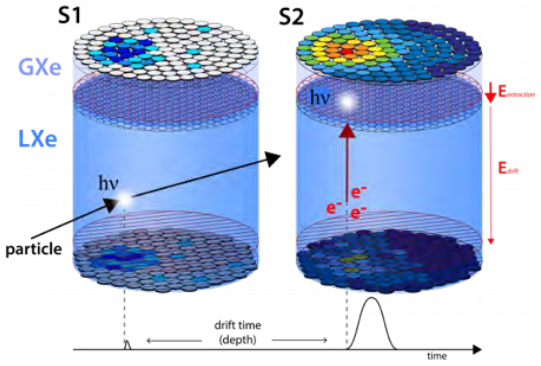


Fig. 37. Principle of operation of liquid xenon time projection chamber (TPC). The interaction of dark matter produces scintillation light S1, and electrons drifted by an electric field give a delayed signal S2; the observed pattern of S2 can identify the planar location of the interaction, and the time difference between S1 and S2 provides depth information. The ratio of S1 to S2 also holds information about the type of particle that caused the interaction. Figure from the XENON collaboration.

In this year, a blinded analysis of nuclear recoil (NR) data from the first science run of the XENONnT dark matter experiment (SR0) was reported [2]. With an exposure of 1.09 ton-years, we observe no excess above background and set new limits on spin-independent WIMP-nucleon cross section. A minimum upper limit of $2.58 \times 10^{-47}\,\mathrm{cm}^2$ for a WIMP mass of $28\,\mathrm{GeV/c^2}$ at 90% confidence level was obtained. The experiment has achieved an electronic recoil (ER) background level of $(15.8 \pm 1.3)\,\mathrm{events/ton\,yr\,keV}$, 5 times lower than XENON1T, keeping comparable detector resolutions and energy threshold. This results in a sensitivity improvement with respect to XENON1T by a factor of 1.7 at a WIMP mass of $100\,\mathrm{GeV/c^2}$. Details are shown in the section below.

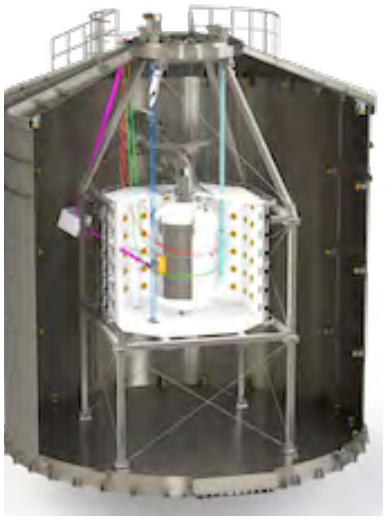


Fig. 38. Overview of the XENONnT detector. The white part is the neutron veto detector. The liquid xenon TPC is at the center, surrounded by the white reflective material, and 120 PMTs are used to detect the Cherenkov lights produced by gamma rays when neutrons are captured by gadolinium or other nuclei and used to identify the neutrons. The water tank is 10 m in diameter and 10 m in height, and 0.2% of gadolinium will be added to the entire system. Figure from the XENON collaboration.

There are some other publications describing low-energy calibration of XENON1T with an internal ^{37}Ar source [3], search for heavy dark matter near the Planck mass with XENON1T [4], detector signal characterization with a Bayesian network in XENONnT [5], the triggerless data acquisition system of the XENONnT experiment [6], search for events in XENON1T associated with gravitational waves [7], and design and perfoemance of the field cage for the XENONnT experiment [8].

Neutron background tagging utilizing SK-Gd technology

Background reduction is critical in rare event searches, and there are two primary background sources important in XENONnT: one is radon in liquid xenon, and the other is neutrons emitted from instrument components. The Japanese group is contributing to the realization and operation of a neutron veto (NV) detector that tags these neutrons and reduces the background by event basis, using the gadolinium-doped water Cherenkov detector technology developed at Kamioka for Super-Kamiokande [9]. Figure 38 shows a full view of the XENONnT detector, which is entirely housed in a water tank with a white reflective material optically isolating the NV immediately surrounding the liquid xenon TPC at its center. The NV is equipped with 120 PMTs. By adding 0.2% of Gd to the water in the whole tank, neutrons emitted from the detector components are expected to be captured by Gd with a high probability if they reach the NV after recoiling from xenon nuclei in the TPC. After capturing the neutron on Gd, we expect PMTs in the NV detector to observe Cherenkov light caused by gamma rays emitted from the Gd nucleus that captured the neutron. This enables us to tag neutrons that cause background for the WIMP search and thus maximize

the experiment's sensitivity. XENONnT aims to tag approximately 87% of such neutron events that are otherwise indistinguishable from dark matter events. During the construction period, the NV detector was completed. With the help of the Super-Kamiokande collaboration, about 3.0 tons of the purest grade of gadolinium sulfate was obtained in Japan and delivered to LNGS [10]. The Super-Kamiokande collaboration also helped us to design the water plant for our application. In 2021, the installation of a gadolinium-loaded water purification plant was completed, and in 2022, commissioning tests of the plant started using pure water and Gd-loaded water. They were successful, and the performance is being optimized. For the SR0 dataset, the NV operated with pure water, achieving 53% of the neutron tagging efficiency to reject neutron-originated background events. This meant that we could reduce neutron background by a factor of two. The gadolinium loading into the water tank started in 2023, aiming at 0.02% concentration of Gd, which is 10% of our target concentration. Even with this low concentration, we demonstrated the neutron tagging efficiency was around 77% (preliminary) using an AmBe neutron source, which is consistent with our Monte Carlo expectations.

First Dark Matter Search with Nuclear Recoils from the XENONnT Experiment [2]

Analysis of nuclear recoil events was conducted by using the SR0 dataset collected from July 6, 2021 to November 10, 2021 with a total exposure of (1.09 ± 0.03) ton-years. The total liquid xenon mass of the fiducial volume after considering the systematic uncertainty of the field distortion correction was (4.18 ± 0.13) ton. During SR0, the detector conditions were stable with an average LXe temperature of (176.8 ± 0.4) K and pressure of (1.890 ± 0.004) bar. The drift and extraction fields were set as $23\,\mathrm{V/cm}$ (corresponding to a maximum drift time of 2.2 ms) and $2.9\,\mathrm{kV/cm}$, respectively. Despite the lower-than-designed drift and extraction fields, the energy and position resolution, as well as the energy threshold, are comparable to those achieved with XENON1T. PMT gains for all PMTs were adjusted at the beginning of SR0 to achieve 2×10^6, and monitored by weekly calibrations with a pulsed low-intensity light source. The time dependence of the PMT gains was modeled and the signals were corrected, resulting in a gain variation $< 3\%$. Total 17 PMTs were excluded from analysis due to internal vacuum degradation, instability, light emission, or noise. The detected S1 and S2 were corrected to cS1 and cS2 considering position dependent detector response evaluated from ^{83m}Kr and ^{222}Rn decays. The photon and electron gains are found to be $g_1 = (0.151 \pm 0.001)$ PE/photon and $g_2 = (16.5 \pm 0.6)$ PE/electron, respectively, assuming the mean energy to produce a charge or light quantum to $13.7\,\mathrm{eV/quantum}$. The NR responses and the NV tagging efficiency were calibrated using an external ^{241}AmBe source which was placed in three positions close to the TPC cryostat. During SR0, the NV was operated as a pure water Cherenkov detector, tagging neutrons through their capture on hydrogen which releases a 2.22 MeV γ ray. The obtained NV tagging efficiency was $(53 \pm 3)\%$ with a live time reduction of 1.6% under the conditions of fivefold PMT coincidence and 5 PE threshold in 250 μs veto window. Figure 39 shows NR response, in addition, ER response obtained from ^{222}Rn and ^{37}Ar calibration source. The leakage fraction of the ER events below the NR median was $1.1^{+0.2}_{-0.3}\%$. The ROI was defined by cS1 between 0 and 100 PE and cS2 between 126 and 12 589 PE.

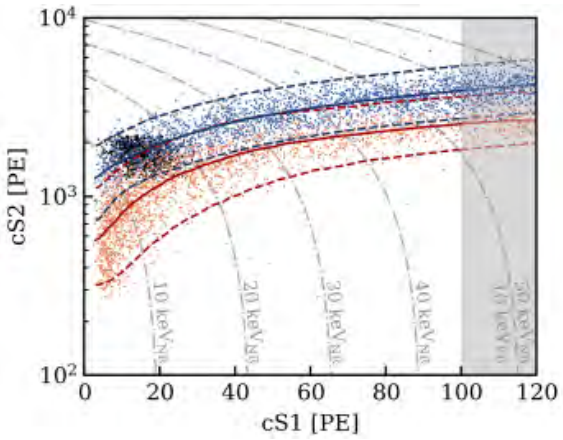


Fig. 39. NR and ER calibration data from ^{241}AmBe (orange), ^{222}Rn (blue), and ^{37}Ar (black). The median and the $\pm 2\sigma$ contours of the NR (ER) are shown in red (blue) thick and dotted lines, respectively. The gray dash-dotted contour lines show the reconstructed NR energy ($\mathrm{keV_{NR}}$).Figure from Ref. [2].

Data quality cuts were applied in order to include only well-reconstructed events and to suppress backgrounds. All cuts were optimized based on calibration data and simulations. Events tagged by the muon veto (MV) or NV are removed from the data selection as are multiple-scatter events since WIMPs are expected to be only single-scatter NR events. The MV uses a veto window of 1 ms with a fivefold PMT coincidence and a 10 PE MV event area threshold. A dedicated cut using a gradient boosted decision tree was developed to reduce the background due to randomly paired S1-S2 signals called accidental coincidences (ACs). This cut uses S2 area and shape, as well as interaction depth, and reduces the AC background by 65% at 95% signal acceptance.

Figure 40 shows the data in the cS1-cS2 space containing 152 events in ROI, 16 of which were in the blinded WIMP region. At high cS1 ($\gtrapprox 50$ PE), we observed more events which were consistent with ER events than our model or calibration data predict, in particular between cS1s of 50 and 75 PE. Of the 16 blinded events, 13 are found in the upper right of the horizontal event distribution. The ^{220}Rn, ^{83m}Kr, and ^{37}Ar calibration datasets do not exhibit any asymmetry, nor is any seen in the acceptances evaluated in the X, Y plane for any of the applied cuts.

The WIMP discovery p-value ($p \geq 0.20$, with the minimum for masses above $100\,\mathrm{GeV/c^2}$) indicates no significant excess with energies between 3.3 and $60.5\,\mathrm{keV_{NR}}$, and the resulting limits on spin-independent WIMP-nucleon cross section at 90% confidence level are shown in Fig. 41. A minimum upper limit was $2.58 \times 10^{-47}\,\mathrm{cm^2}$ for a WIMP mass of $28\,\mathrm{GeV/c^2}$. The experiment has achieved an ER background level of $(15.8 \pm 1.3)\,\mathrm{events/ton\,yr\,keV}$, 5 times lower than XENON1T, with comparable detector resolutions and energy threshold. This results in a sensitivity improvement

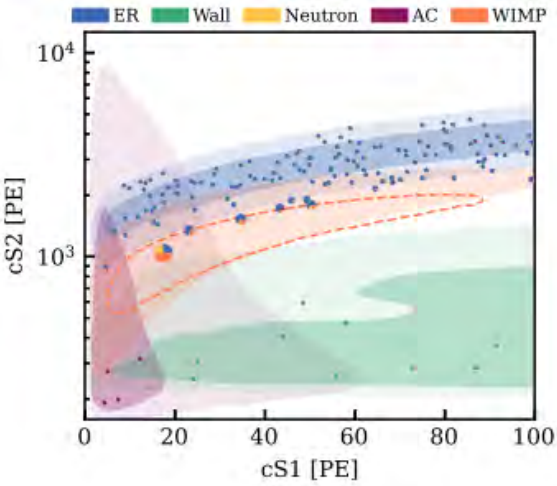


Fig. 40. SR0 DM search data in the cS1-cS2 space. Each event is represented with a pie chart showing the fraction of the best-fit model, including the expected number of $200\,\mathrm{GeV/c^2}$ WIMPs (orange) evaluated at the position of the event. The size of the pie chart is proportional to the signal model at that position. Distributions of background probability density are shown as 1σ (dark) and 2σ (light) for ER (blue), AC (purple), and wall (green). The orange dashed contour contains 50% of a $200\mathrm{GeV/c^2}$ WIMP signal. The neutron background has a similar distribution to the WIMPs. Figure from Ref. [2].

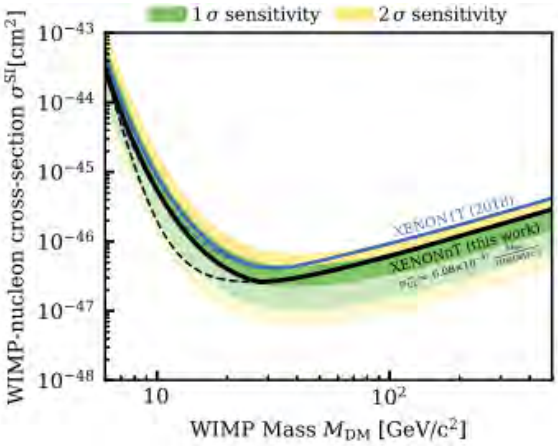


Fig. 41. Upper limit (black line) and sensitivity (color shaded region) on spin-independent WIMP-nucleon cross section at 90% confidence level as a function of the WIMP mass. A power constraint is applied to the limit to restrict it at or above the median unconstrained upper limit. The dashed lines show the upper limit without a power constraint applied. Figure from Ref. [2].

with respect to XENON1T by a factor of 1.7 at a WIMP mass of $100\,\mathrm{GeV/c^2}$.

Currently, XENONnT continues to take data, with a further reduction of ^{222}Rn ER background, using the radon distillation system with combined gaseous and liquid xenon flow. NV already started to operate with 0.02% of Gd concentration. In the future, data taking is planned with the NV operating as designed with Gd loaded into the pure water to increase the neutron tagging efficiency to 87% with a lower overall lifetime reduction.

Determination of Kr contamination in XENONnT [11]

Searching for rare events such as dark matter and solar pp neutrino signals requires background reduction and accurate background estimation. Xenon, the target material of the direct dark matter search experiment XENONnT, contains krypton and the radioactive isotope ^{85}Kr, which is a background source. ^{85}Kr emits β-rays (Q-value 687 keV), which cause background events, especially in the low energy region. Therefore, it is necessary to know the amount of ^{85}Kr with sufficient accuracy to obtain reliable significance when we observe signals. So far the abundance of ^{85}Kr in xenon is indirectly estimated using the total amount of Kr in xenon and the ^{85}Kr/Kr ratio in the air. However, the ^{85}Kr/Kr ratio in the air varies from period to period and has unknown uncertainty, as ^{85}Kr is mainly generated from nuclear fuel reprocessing plants. Therefore, a measurement independent of the ^{85}Kr/Kr ratio is desirable. Thus, the delayed coincidence measurement of β- and γ-rays emitted in the rare decay mode of ^{85}Kr was developed to directly measure the abundance of ^{85}Kr. We optimized the method to suppress the related background with sufficiently small while keeping the detection efficiency sufficiently large. Finally we applied the method to the SR0 data with an effective volume of (4.37 ± 0.14) t and an observation time of 97.1 days, and found no delayed coincidence events. The analysis concluded that ^{85}Kr concentration was consistent with zero and the 90% C.L. upper limit for the Kr concentration in xenon is 270 ppq (preliminary). The Kr concentration estimated from the ^{85}Kr/Kr ratio in the environmental air was consistent with this result.

In this analysis, the detection efficiency of rare decay events for ^{85}Kr is 32.1 ± 3.2stat ± 1.1sys %. The loss of detection efficiency is mainly because in some events, the β- and γ-ray derived signals cannot be separated due to the signal separation capability of the signal processing algorithm. Therefore, we plan to improve the separation algorithm to increase the detection efficiency of ^{85}Kr rare decay events.

Bibliography

[1] E. Aprile *et al.* (XENON collaboration), JCAP 11 (2020) 031.

[2] E. Aprile *et al.* (XENON collaboration), Phys. Rev. Lett. 131, 041003 (2023).

[3] E. Aprile *et al.* (XENON collaboration), Eur. Phys. J. C 83, 542 (2023).

[4] E. Aprile *et al.* (XENON collaboration), Phys. Rev. Lett. 130, 261002 (2023).

[5] E. Aprile *et al.* (XENON collaboration), Phys. Rev. D 108, 012016 (2023).

[6] E. Aprile *et al.* (XENON collaboration), JINST 18 P07054 (2023).

[7] E. Aprile *et al.* (XENON collaboration), Phys. Rev. D 108, 072015 (2023).

[8] E. Aprile *et al.* (XENON collaboration), Eur. Phys. J. C 84, 138 (2024).

[9] L. Marti, *et al.* (Super-Kamikande collaboration), Nucl. Instrum. Meth. A, 959, 163549 (2020); K. Abe *et al.* (Super-Kamiokande collaboration), Nucl. Instr. Meth. A, 1027 (2022) 166248.

[10] E. Aplile *et al.* (XENON collaboration), Eur. Phys. J. C (2022) 82:599.

[11] Y. Kaminaga, Master thesis, The University of Tokyo, March 2023.

HYPER-KAMIOKANDE

[Co-Spokespersons: Masato Shiozawa[1], Francesca Di Lodovico[2]]
1: Kamioka Observatory, ICRR, The University of Tokyo
2: Department of Physics King's College London

Introduction

The Hyper-Kamiokande (Hyper-K or HK) project [1] is the world-leading international scientific research project hosted by the university of Tokyo and High Energy Accelerator Research Organization (KEK) consisting of a next generation underground water Cherenkov detector and upgraded Japan Proton Accelerator Research Complex (J-PARC) neutrino beam. The Hyper-K project was approved by the Japanese Diet in 2020 and officially started.

Figure 42 shows a schematic drawing of the Hyper-K cylindrical detector. The detector is filled with 0.260 million metric tons of ultra pure water, which serves an order of magnitude larger fiducial mass of 0.188 million metric tons than Super-K, equipped with newly developed high-sensitivity photosensors, and a high-intensity neutrino beam produced by an upgraded J-PARC accelerator facility. It provides an enormous potential to discover leptonic charge-parity (CP) violation by observing neutrino and anti-neutrino beams from J-PARC, investigate the Grand Unified Theory by exploring proton decay, and determine the neutrino mass ordering by observing atmospheric neutrinos combining beam data. Hyper-K will also have far better capabilities to observe solar neutrinos and neutrinos from other astronomical sources than those of predecessor experiments.

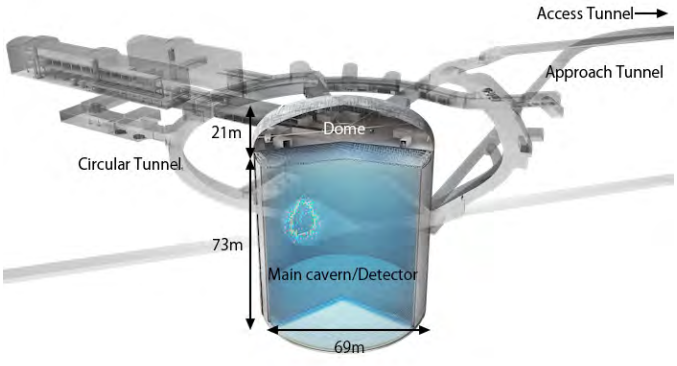


Fig. 42. Schematic view of the Hyper-K water tank and approach tunnel.

The Hyper-K international collaboration consists of about 583 researchers from 104 institutes in 22 countries. The detector technology has been developed based upon the successful Super-K experiment and feasibility studies have been completed by international group. The Hyper-K operation plans to start in 2027.

Physics

Hyper-K will have capability to measure the magnitude of the CP violation with high precision, which could explain the baryon asymmetry in the Universe. Figure 43 shows an expected significance of the CP violation discovery by ten years operation. With expected systematic error improvement, Hyper-K covers the 60% of the parameter space with 5σ or more as red dotted line shows in the figure. More than 8σ significance will be expected if $\delta_{CP} = -\pi/2$ as suggested by T2K [2] and NOνA [3] results.

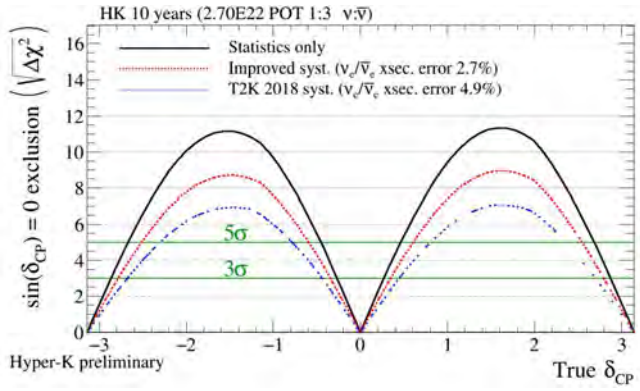


Fig. 43. Significance of the leptonic CP violation discovery with a 10-year observation in Hyper-K (HK) as a function of the unknown CP phase assuming the normal neutrino mass hierarchy. Red dotted line shows the result with expected systematic error improvement, blue dotted line shows the result with achieved systematic error by T2K 2018 and black line shows the result with only statistical error.

A proton decay $p \to e^+\pi^0$ is an important signal favored by many Grand Unified Theory models with a prediction close to the current limit of the proton decay life time. High sensitive Hyper-K PMTs result in strong background (atmospheric neutrinos) reduction and $p \to e^+\pi^0$ search in Hyper-K is expected to be "background-free" particularly in the free-proton enhanced signal region. Figure 44 shows the 3σ discovery potential for the $p \to e^+\pi^0$ mode as a function of year. Hyper-K is an only realistic proposal which can go beyond the proton lifetime of 1×10^{35} years.

As well as the supernova burst neutrino that was successfully observed in Kamiokande at once, undiscovered supernova relic neutrinos, accumulated by past all supernovae since the beginning of the universe, are interesting events to explore the history of heavy elements and the onset of stellar formation.

Construction status

The Hyper-K cavern is the largest artificial underground cavity in the world. The construction of the cavern and water tank is a crucial part of Hyper-K project. Figure 45 is schematic drawing of Hyper-K tunnels and the cavern. The excavation of 1873.5m access tunnel started in May 2021 and completed in February 2022. Then excavation of approach tunnel followed and finished in June 2022.

After the completion of approach tunnel, the excavation of Hyper-K cavern started. Figure 46 shows the dome section of main cavern that was completed in October 2023. The diameter of the cavern is 69 m, and the height of the ceiling is 21m.

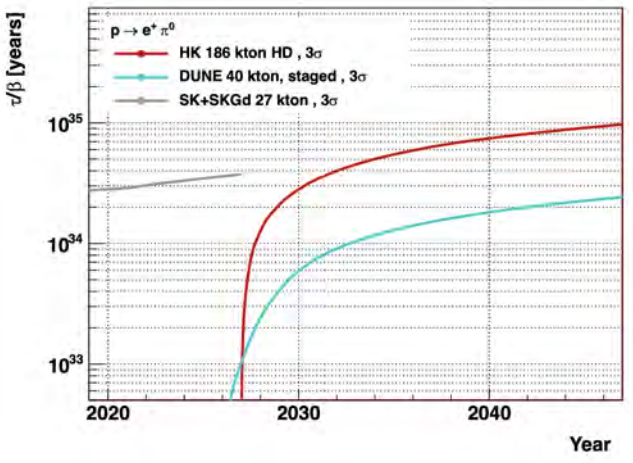


Fig. 44. The $p \to e^+\pi^0$ discovery reach in proton lifetime with 3σ significance as a function of year. It shows Hyper-K (HK) planing to start in 2027, superimposed with the ongoing Super-K (SK) and planned DUNE experiments. The DUNE project assumes 10 kton operation from 2026, toward full 40 kton by increasing 10 kton every year [4].

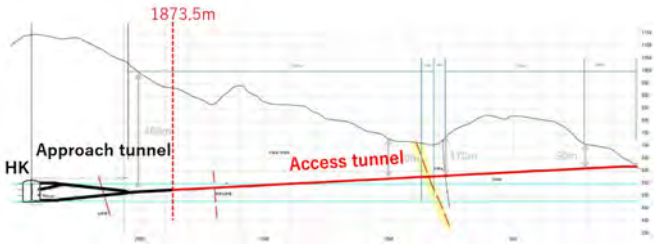


Fig. 45. Overview of the Hyper-Kamiokande excavation. The first part of tunnel is called as the access tunnel (red line). The black line after the access tunnel is the approach tunnel to reach the main cavern.

Then the last part, excavation of the cylindrical section below has begun. As shown in Figure 47 the work is ongoing up to 20m depth by the end of March 2024 and will be completed to 73m by end of 2024.



Fig. 46. The main cavern dome section (diameter: 69m, height: 21m) was completed in October 2023.



Fig. 47. The excavation of cylindrical section is ongoing (20m depth by the end of March 2024).

20-inch PMT, Delivery and inspection

Newly developed photomultiplier tubes R12860 by Hamamatsu Photonics K.K is shown in Fig. 48. The total detection

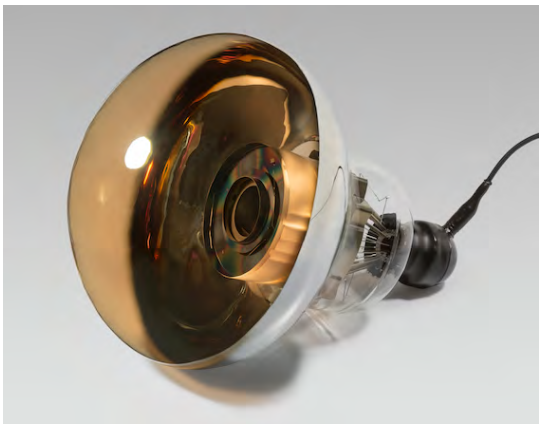


Fig. 48. New 50 cm photomultiplier tube with a box-and-line dynode (R12860, Hamamatsu Photonics K.K.).

efficiency of R12860 for single photon is twice higher than that of the Super-K PMT owing to 1.4 times higher quantum efficiency (about 32%) and improved photoelectron collection efficiency. The timing and charge resolutions at single photoelectron also becomes much better as 1.1 ns and 35% which can be compared with 2.1 ns and 53% of the Super-K PMT, respectively. Pressure tolerance of PMT was also improved up to the 125 m water depth, so that new PMT can be used under about 70 m depth of the detector water.

Since the start of mass production at October 2020, delivery of 400 PMTs for every month is ongoing. Total delivered number reached about 9000 by the end of FY2023 without any delay from the schedule. At the facility where delivered PMTs have been stored, inspections of the PMTs are also ongoing. The inspection consists of visual inspection for bulb and waterproof quality, signal check for signal property and noise rate, and long term stability check. The Figure 49 shows the dark room to check long term stability of 100 PMTs simultaneously. The delivery of PMTs continues until September 2026.

Electronics

The HK front-end electronics will be placed under water nearby PMTs to avoid long analog cable and degradation of



Fig. 49. Visual inspections of PMTs (top). Dark room for long term stability check of 100 PMTs (bottom).

PMT signal. This is another challenge of HK project. We have made a lot of efforts to develop water-tight equipments, high reliable front-end electronics, and communication under water.

The prototypes of frontend electronics have been developed and validated to work as a system before starting mass production in 2024. The Figure 50 shows the system test of frontend electronics on table before assembled into a water-tight vessel. The system consists of two digitizer boards, communication board and HV/LV modules.

The Figure 51 shows under-water test with 1 MPa tolerant water-tight vessel. The vessel contains full setup of frontend electronics and connected to 24 PMTs and DAQ system via optical fiber. The performance and functionalities have been comprehensively tested.

Bibliography

[1] "Hyper-Kamiokande Design Report," arXiv: 1805.04163.

[2] K. Abe *et al.* [T2K Collaboration], Nature 580, 339-344 (2020).

[3] P. Adamson *et al.* [NOνA Collaboration], Phys. Rev. Lett. 118, 231801.

[4] R. Acciarri *et al.* [The DUNE Collaboration], arXiv:1601.05471 [physics.ins-det].

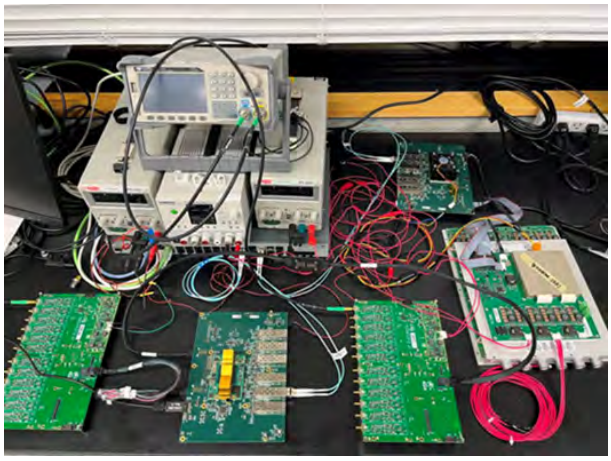


Fig. 50. System test of frontend electronics on table before assembled into a water-tight vessel. The system consists of two digitizer boards, communication board and HV/LV modules.

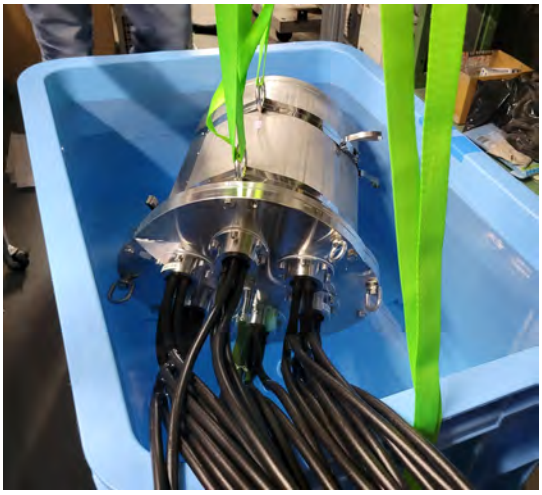


Fig. 51. Under-water test with 1MPa tolerant water-tight vessel. The vessel contains full setup of frontend electronics and connected to 24 PMTs and DAQ system.

HIGH ENERGY COSMIC RAY DIVISION

Overview

There are three major experimental research activities in the High Energy Cosmic Ray Division, the study of high energy gamma rays and the development of the next generation gamma-ray telescopes by the Cherenkov Cosmic Gamma Ray group, the study of extremely high energy cosmic rays by the Telescope Array (TA) group, and the study of very high energy cosmic rays and gamma rays by the Tibet ASγ group.

Other activities, such as experiments utilizing the Akeno observatory, the Norikura observatory, the Mt. Chacaltaya observatory (jointly operated with Bolivia) are closely related to inter-university joint research programs. Also an all-sky high resolution air-shower detector (Ashra) is in partial operation on the Hawaii island. The High Energy Astrophysics group created in the fiscal year 2009 aims to explore various high energy astrophysical phenomena, through theoretical and observational approaches.

The CANGAROO telescopes had been in operation in South Australia since 1992, with a 3.8 m small telescope and then with four 10 m telescopes. The major scientific objective was the study of Very High Energy (VHE) gamma-ray sources in our galaxy in the southern hemisphere. The mission of these telescopes was completed and the CANGAROO observation site was closed in 2011.

For further development of VHE gamma-ray astronomy, the Cherenkov Cosmic Gamma Ray group is working on the design study and development and construction of the next generation international ground-based gamma-ray observatory CTA which will offer an order of magnitude better sensitivity than currently running Cherenkov telescopes, three times better angular resolution, and wider energy coverage from 20 GeV to 100 TeV or higher. The construction of the first Large-Sized Telescope (LST) was completed on the CTA-North site in La Palma in 2018. High Energy Astrophysics Facility in Canarias was established as a base for the project in April, 2019.

At the Akeno observatory, a series of air shower arrays of increasing geometrical sizes were constructed and operated to observe extremely high energy cosmic rays (EHECRs). The Akeno Giant Air Shower Array (AGASA) was operated from 1991 to January 2004 and covered the ground area of 100 km^2 as the world largest air shower array. In 13 years of operation, AGASA observed a handful of cosmic rays exceeding the theoretical energy end of the extra-galactic cosmic rays (GZK cutoff) at around 10^{20} eV.

The Telescope Array (TA), a large plastic scintillator array with air fluorescence telescopes, has been constructed in Utah, USA, which succeeds AGASA and measures the EHECRs with an order of magnitude larger aperture than that of AGASA for the further study of EHECRs. The full-scale TA is accumulating data as the largest array viewing the northern sky and observed the energy spectrum with high statistics, which is in good agreement with the GZK suppression and found evidence for anisotropy of arrival directions of EHECRs. The TAx4, which is aimed at quadrupling TA, was partially constructed by March of 2019.

An air shower experiment aiming to search for celestial gamma-ray point sources started in 1990 with Chinese physicists at Yangbajing (Tibet, 4,300 m a.s.l.). This international collaboration is called the Tibet ASγ Collaboration. An extension of the air shower array was completed in 1995 and an emulsion chamber has been combined with this air shower array since 1996 to study the primary cosmic rays around the knee energy region. After successive extensions carried out in 1999, 2002 and 2003, the total area of the air shower array amounts to 37,000 m^2. The sun's shadow in cosmic rays affected by the solar magnetic field was observed for the first time in 1992, utilizing its good angular resolution at multi-TeV energy region. The group added underground water Cherenkov muon detector to detect cosmic gamma rays above 100 TeV. The group is planning to construct a new air shower array, called ALPACA, to cover the sky in the Southern hemisphere, and started the construction of its partial array in Bolivia in 2019.

The High Energy Astrophysics group is conducting theoretical researches on fundamental processes responsible for non-thermal particle acceleration in various astrophysical environments, including first-order diffusive shock acceleration, second-order stochastic acceleration in shock downstream regions, modification of shock structure by pick-up interstellar neutrals, as well as injection processes of suprathermal particles. In addition to these theoretical works, R/D studies for radio observations of pulsars and cosmic ray air showers are also being made.

Cherenkov Cosmic Gamma-Ray Group

CTA Project (Cherenkov Telescope Array)

CTA-Japan Consortium
[Spokesperson : H. Kubo, T. Saito]

Collaboration list:
Institute for Cosmic Ray Research, The University of Tokyo, Chiba, Japan; Department of Physics, Aoyama Gakuin University, Tokyo, Japan; Department of Physics, Hiroshima University, Hiroshima, Japan; Hiroshima Astrophysical Science Center, Hiroshima University, Hiroshima, Japan; Faculty of Science, Ibaraki University, Ibaraki, Japan; Institute of Particle and Nuclear Studies, High Energy Accelerator Research Organization (KEK), Ibaraki, Japan; Department of Physics, Konan University, Hyogo, Japan; Faculty of Medical Engineering and Technology, Kitasato University, Kanagawa, Japan; Graduate School of Science and Technol-

ogy, Kumamoto University, Kumamoto, Japan; Department of Physics, Kyoto University, Kyoto, Japan; Department of Applied Physics, University of Miyazaki, Miyazaki, Japan; Department of Physics, Nagoya University, Aichi, Japan; Solar-Terrestrial Environment Laboratory, Nagoya University, Aichi, Japan; Kobayashi-Maskawa Institute, Nagoya University, Aichi, Japan; Department of Earth and Space Science, Osaka University, Japan; Astrophysical Big Bang laboratory, RIKEN, Wako, Japan; Department of Physics, Rikkyo University, Tokyo, Japan; Department of Physics, Saitama University, Saitama, Japan; Department of Physics, Tokai University, Kanagawa, Japan; Faculty of Integrated Arts and Sciences, The University of Tokushima, Tokushima, Japan; Department of Astronomy, The University of Tokyo, Tokyo, Japan; Department of Physics, The University of Tokyo, Tokyo, Japan; Faculty of Science and Engineering, Waseda University, Tokyo, Japan; Department of Physics, Yamagata University, Yamagata, Japan; Faculty of Management Information, Yamanashi Gakuin University, Yamanashi, Japan.

CTA Project

During the past years, Very High Energy (VHE) gamma-ray astronomy has made spectacular progress and has established itself as a vital branch of astrophysics. To advance this field even further, we are constructing the Cherenkov Telescope Array Observatory (CTAO) [6], the next generation VHE gamma ray observatory, in the framework of a worldwide, international collaboration. CTAO is the ultimate VHE gamma-ray observatory, whose sensitivity and broad energy coverage will attain an order of magnitude improvement above those of current Imaging Atmospheric Cherenkov Telescopes (IACTs). By observing the highest energy photons known, CTAO will clarify many aspects of the extreme Universe, including the origin of the highest energy cosmic rays in our Galaxy and beyond, the physics of energetic particle generation in neutron stars and black holes, as well as the star formation history of the Universe. CTAO will also address critical issues in fundamental physics, such as the identity of dark matter particles and the nature of space and time.

VHE gamma rays from 100 GeV to 10 TeV can be observed with ground-based current IACTs. The history of VHE gamma ray astronomy began with the discovery of VHE gamma rays from the Crab Nebula by the Whipple Observatory in 1989. To date, the current generation IACTs featuring new technologies, such as H.E.S.S., MAGIC, and VERITAS, have discovered more than 200 Galactic and extragalactic sources of various types.

CTAO is designed to achieve superior sensitivity and performance, utilizing established technologies and experiences gained from the current IACTs. The project is presently in its pre-construction (prototyping) phase, with international efforts from Japan, US, and EU countries. It will consist of several 10s of IACTs of three different sizes (Large Size Telescopes, Middle Size Telescopes, and Small Size Telescopes)(Fig. 1). With a factor of 10 increase in sensitivity (1 mCrab $\sim 10^{-14}$erg s^{-1} cm^{-2}), together with a much broader energy coverage from 20 GeV up to 300 TeV. CTAO will bring forth further dramatic advances for VHE gamma-ray astronomy. The discovery of more than 1000 Galactic and extragalactic sources is anticipated with CTAO.

CTAO will allow us to explore numerous diverse topics in physics and astrophysics. The century-old question of the origin of cosmic rays is expected to be finally settled through detailed observations of supernova remnants and other Galactic objects along with the diffuse Galactic gamma-ray emission, which will also shed light on the physics of the interstellar medium. Observing pulsars and associated pulsar wind nebulae will clarify physical processes in the vicinity of neutron stars and extreme magnetic fields. The physics of accretion onto supermassive black holes, the long-standing puzzle of the origin of ultra-relativistic jets emanating from them, as well as their cosmological evolution, will be addressed by extensive studies of active galactic nuclei (AGN). Through dedicated observing strategies, CTAO will also elucidate many aspects of the mysterious nature of gamma ray bursts (GRBs), the most energetic explosions in the Universe. Detailed studies of both AGNs and GRBs can also reveal the origin of the highest energy cosmic rays in the Universe, probe the cosmic history of star formation including the very first stars, and provide high precision tests of theories of quantum gravity. Finally, CTAO will search for signatures from elementary particles constituting dark matter with the highest sensitivity yet. Realisation of the rich scientific potential of CTAO is very much feasible, thanks to the positive experiences gained from the current IACTs.

The CTA-Japan consortium [1] is contributing particularly to the construction of the Large Size Telescopes (LSTs, Fig. 2) and is involved in their development. The LST covers the low energy domain from 20 GeV to 3 TeV and is especially important for studies of high redshift AGNs and GRBs. The diameter and area of the mirror are 23 m and 400 m^2, respectively, in order to achieve the lowest possible energy threshold of 20 GeV. All optical elements and detectors require high specifications, such as high reflectivity, high collection efficiency, high quantum efficiency, ultra-fast digitization of signals, and so on. For this purpose, CTA-Japan has developed high quantum efficiency photomultipliers and ultrafast readout electronics (Fig. 3), and high precision segmented mirrors (Fig. 4). On the strength of their experiences gained from the construction of the MAGIC telescope, Max-Planck-Institute for Physics in Munich is responsible for the design of the 23-m diameter telescope structure, based on a carbon fiber tube space frame. The LSTs require very fast rotation (180 degrees in 20 seconds) to promptly observe GRBs. The first LST (LST-1) has been built in the CTA North, La Palma, Spain, in 2018, and now in the engineering run (Fig. 5). Three more LSTs will be built before 2025, then up to four more LSTs in the CTA South are expected to be built in the ESO site in Paranal, Chile.

The LST-1 has been regularly operated since January 2020, and has already shown an excellent performance even in a single telescope mode, certifing that LST-1 achieved the design performance expected by Monte Carlo simulations. Some of the recent results are shown below.

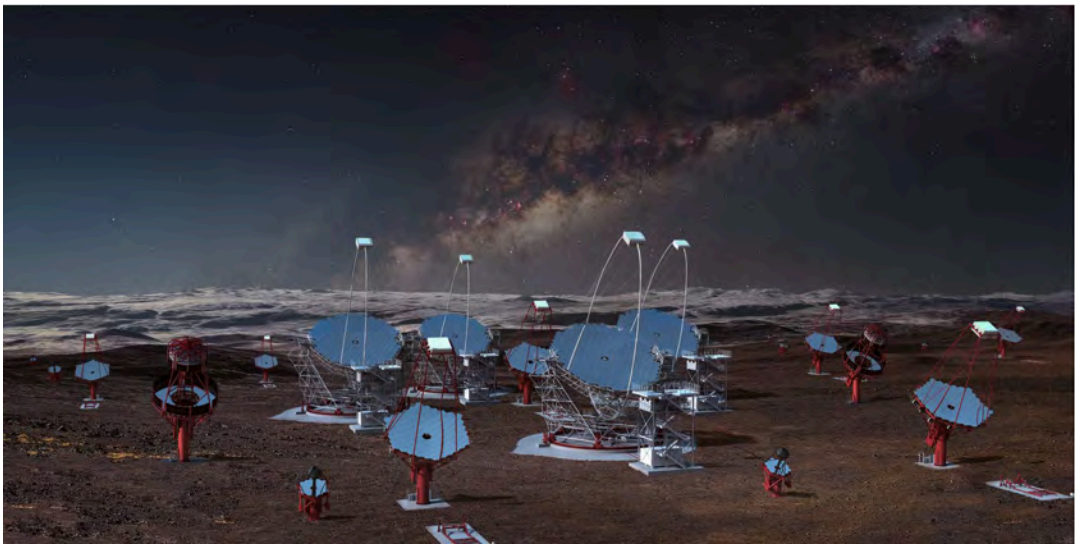


Fig. 1. Artist view of the CTA observatory (CTAO). CTAO consists of three types of telescopes, Large Size Telescopes (23 m diameter), Mid Size Telescopes (12 m) and Small Size Telescopes (4 m), and covers the broad energy band from 20 GeV to 300 TeV. [Credit: Gabriel Pérez Diaz (IAC)/Marc-André Besel (CTAO)/ESO/ N. Risinger (skysurvey.org)]



Fig. 2. Large Size Telescope (23 m diameter) designed by Max–Planck-Institute for Physics. CTA Japan is contributing to the design and and construction of the imaging camera at the focal plane, ultrafast readout electronics, and high precision segmented mirrors.



Fig. 3. Camera cluster for the Large Size Telescope (LST) developed by CTA-Japan. This cluster consists of seven high quantum efficiency photomultipliers (R11920-100), CW High Voltages, pre-amplifier, Slow Control Board, DRS4 Ultra fast waveform recording system and Trigger. The LST camera can be assembled with 265 of these clusters, cooling plates and camera housing.



Fig. 4. The high precision segmented mirrors for the Large Size Telescope (LST) developed by CTA-Japan in cooperation with Sanko Co.LTD. The mirror is made of a 60-mm thick aluminum honeycomb sandwiched by 3-mm thin glass on both sides. A surface protection coat consisting of the materials SiO_2 and HFO_2 is applied to enhance the reflectivity and to elongate the lifetime.

Galactic Center with LST-1

The Galactic Center region inhabits an array of particle accelerators: namely the supermassive black hole, supernova remnants, and pulsar wind nebulae. The region likely supplies the Galaxy with a significant amount of accelerated particles, even potentially reaching up to PeV energies. Hence very-high-energy gamma-ray observations of this region allow for a morphological study of cosmic-ray propagation around the supermassive black hole Sgr A*. The uniqueness of LST-1 is built upon two perspectives: the large-zenith-angle observa-



Fig. 5. The Large Size Telescope prototype (LST-1) constructed at Observatory de Roque de los Muchachos is now in the engineering run. The diameter of dish and mirror surface area are 23 m and 400 m^2.

tion and the wide field of view (FoV). The location requires LST-1 to observe the Galactic Center at the zenith distance (Zd) above about 58° in the horizontal coordinate system, which in general enhances the sensitivity at the high energy (typically above 1 TeV) at a cost of increased energy threshold. Additionally, in contrast with other northern Cherenkov telescopes in particular, the relatively wide FoV of LST-1 allows to maintain the sensitivity across the region where the reported longitudinal diffuse gamma rays are distributed. As such, even despite the mono-scopic observations, LST-1 can already provide a comparable, or rather better, view towards the Galactic Center region. LST-1 collected Galactic Center data of about 40 hours in 2021 and 2022. We analyzed data through our newly developed software. The sky map visualization in Fig. 6 highlights prominent signals of Sgr A* and SNR G0.9+0.1, and the diffuse emission along the Galactic plane. Our analysis reconfirmed the previous findings on the diffuse component with a higher detection significance; The spectral and morphological characteristics of the diffuse component can reasonably be associated with ultra-relativistic hadronic cosmic rays colliding with the dense gas. We have reported these results in some conferences (e.g. [12]).

Crab and Geminga Pulsars with LST1

Gamma-ray emission mechanism of pulsar are not fully understood and observation above 10 GeV is particularly important. That is one of main physics target of CTAO.

The phase diagram of the Crab Pulsar observation is shown in the top panel of Fig. 7, which certifies the low threshold energy of LST-1 and also the accuracy of the recorded event timings[14]. In addition to the two peaks which are often called P1 and P2, the bridge emission between them are also visible. The widths of the two peaks are clearly smaller than the ones in GeV range, suggesting the energy dependence of the pulse shape. Such a study is on-going by analyzing both Fermi-LAT and LST1 data, in order to understand further the gamma-ray emission mechanism of pulsars.

The LST-1 phase diagram of the Geminga pulsar (the bottom panel of Fig. 7) reveals statistically significant emission ($\sim 8\sigma$) for the P2[14]. This complements the previously published results of Fermi-LAT and MAGIC [17]. It should be noted that this phase diagram was obtained with 21 hours of observations, while MAGIC needed 80 hours to detect the pulsation with a similar statistical significance. This proves once again the high sensitivity of LST1 at the lowest energies ($10-30$ GeV). Still, P1, which is visible in Fermi-LAT data is not detected.

AGNs with LST1

Blazars are a sub-class of Active Galactic Nuclei (AGN) and constitute the most populous class of sources in the extragalactic VHE sky. They are characterized by rapid variability that spans from radio to VHE gamma rays (E ¿ 100 GeV), whose origin remains under debate. Detecting more VHE blazars at different energies and distances is crucial for a better understanding of their emission mechanisms. With its high sensitivity down to tens of GeV, LST-1 is the best suited instrument to observe gamma-ray sources such as AGN due to lack of absorption from photon-photon interactions with the extragalactic background light. From 2020 to 2022, LST-1 accumulated more than 150 hours of data of several well-known AGN with redshifts in the range 0.03 to 0.45: Mrk 421, Mrk 501, 1ES 1959+650, 1ES 0647+250, PG 1553+113. We analyzed the spectral variability from these observations [13]. Fig. 8 shows the spectrum energy distribution (SED) and intra-night light curve of Mrk 421 flaring event on 2022 May 18. The SED was measured down to tens of GeV, which prove that LST-1 is highly sensitive to gamma-ray sources with time variation above tens of GeV. These results foresee an exceptional performance of AGN detection with LST-1 in the future.

Construction of LST-2–4

Construction of the second to forth LSTs (LST-2–4) are progressing fast (see Fig. 9). The foundation, the drive rail and the camera access tower of all three telescopes are already built. The telescope structures and mirrors are expected to be completed within the year 2024. The cameras of LST-2–4 are currently in the Institute of Astrophysics in Canary islands (IAC) in Tenerife. The final integration test has been finished and the three cameras are waiting for transportation to La-Palma island (Fig. 10). They should be mounted in the first half of the yeaar 2025. Also, for the future upgrade of LST cameras, basic studies of Silicon photomultiplier (SiPM) and development of SiPM module is on-going in the laboratory of ICRR [15].

The Cherenkov Cosmic Gamma Ray group is also operating the MAGIC Telescopes [16] on La Palma, Canary Islands (See the next subsection). This facility is used not only for scientific observations but also for technological development toward the future observatory CTA.

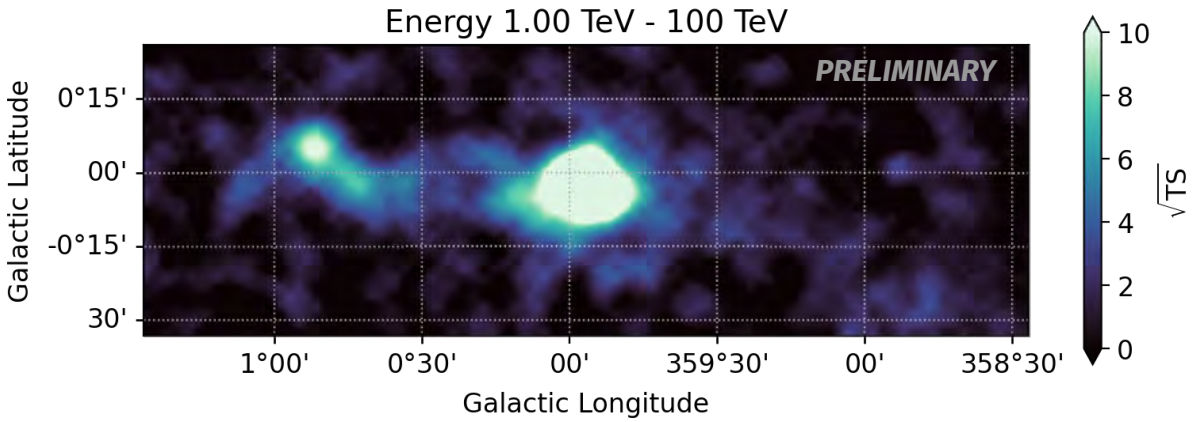


Fig. 6. Sky map of the Galactic Center region obtained with the LST-1 observations. The map is smeared with a Gaussian of a 0.08deg standard deviation."

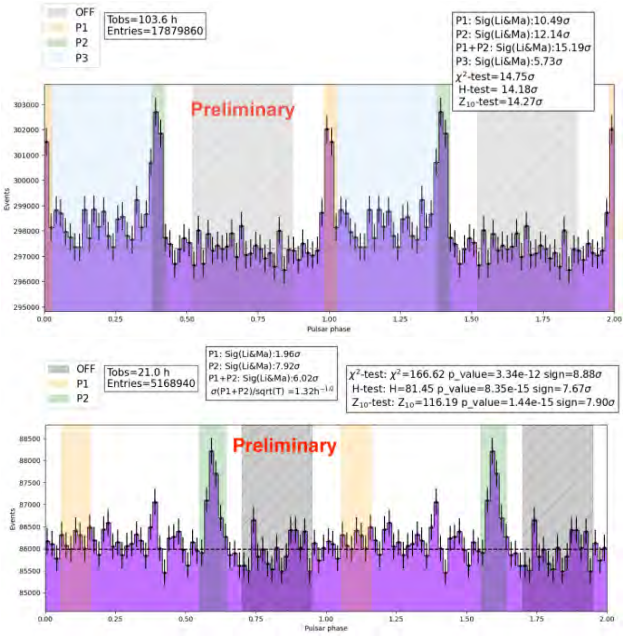


Fig. 7. Top: Phase diagram of Crab Pulsar as measured by LST-1. The pulsar is known to emit pulses of gamma rays during phases P1 and P2. The energy threshold in this observation is estimated about 40-50 GeV. Bottom: Phase diagram of the Geminga pulsar, where the emission of the second pulse peak (P2) is significantly detected.

Bibliography

[1] CTA Consortium website: http://www.cta-observatory.jp/ and http://www.cta-observatory.org/.

[2] Science with the Cherenkov Telescope Array, arXiv:1709.07997

[3] The Cherenkov Telescope Array potential for the study of young supernova remnants, Astropart. Phys. 62 (2015) 152-164.

[4] Introducing the CTA concept, The CTA Consortium, Astropart. Phys. 43 (2013) 3-18.

[5] Gamma-ray burst science in the era of the Cherenkov Telescope Array, S. Inoue et al., Astropart. Phys. 43 (2013) 252-275.

[6] Design Concepts for The Cherenkov Telescope Array, The CTA Consortium, Exper. Astron. 32 (2011) 193-316.

[7] Status of Very High Energy Gamma Ray Astronomy and Future Prospects, M. Teshima, The Astronomical Herald, 104 (2011) 333-342.

[8] Design Study of a CTA Large Size Telescope, Proc. of ICRC2012 at Beijing China, M. Teshima, arXiv:1111.2183.

[9] Introducing the CTA Concept, B. Acharya et al., Astroparticle Physics, 34 (2013) 3.

[10] Commissioning of the camera of the first Large Size Telescope of the Cherenkov Telescope Array, Proc. of ICRC2021 at Berlin Germany (Online), T. Saito et al., arXiv:2108.01920.

[11] Status of the LST project, J. Cortina, PoS (Gamma2022) 026.

[12] Galactic Center Studies with CTA-LST-1, S. Abe et al., Pos (ICRC2023) 574, 2023

[13] Observation of Active Galactic Nuclei with the Large-Sized Telescope prototype of the Cherenkov Telescope Array, R. Takeishi et al., Pos (ICRC2023) 635, 2023

[14] First results of pulsar observations with the LST-1, A. Mas-Aguilar et al., PoS (ICRC2023) 569, 2023

[15] Characterization of SiPM and development of test bench modules for the next-generation cameras for CTA-LST. T. Saito et al., Pos (ICRC2023) 635, 2023

[16] MAGIC Collaboration website: http://magic.mppmu.mpg.de/.

[17] Detection of the Geminga pulsar with MAGIC hints at a power-law tail emission beyond 15 GeV, MAGIC Collaboration, Acciari et al., A&A 643 L14 (2020)

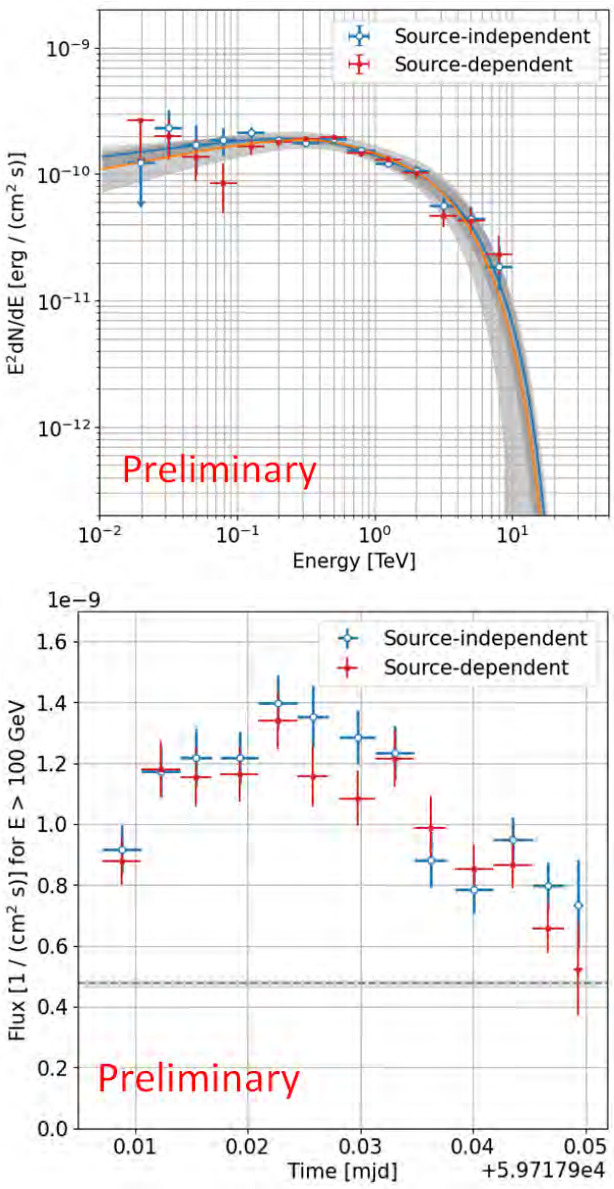


Fig. 8. Plots for Mrk 421 data on 2022 May 18. We performed source-independent and source-dependent analysis methods, which show good agreement between both results. (Top) Observed SED. (Bottom) Intra-night light curve with sub-hour timescale variability. Grey shows the Crab Nebula flux for reference.



Fig. 9. A web-cam image of LST4 construction as of March 12, 2024

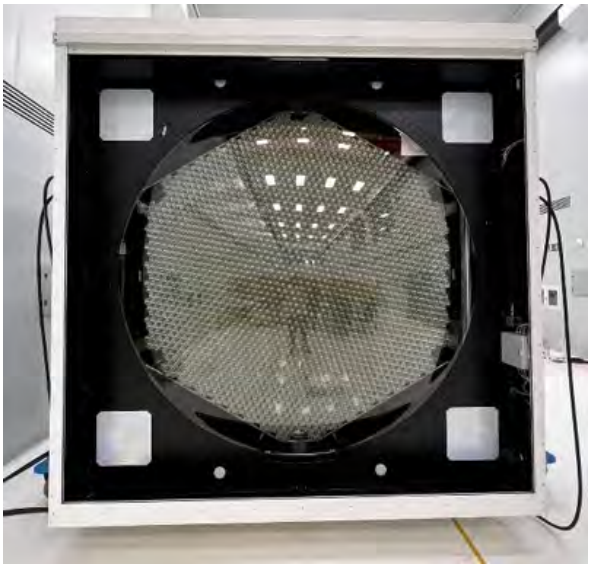


Fig. 10. The camera of the second LST (LST-2). The final integration test has been done in IAC in Tenerife.

MAGIC

The MAGIC Collaboration has built in 2004 a first large atmospheric imaging Cherenkov telescope, MAGIC-I, with a mirror surface of 236 m^2 and equipped with photomultiplier tubes of optimal efficiency. In 2009, a second telescope of essentially the same characteristics was added; MAGIC-II was installed at a distance of 85 m from MAGIC-I (Fig. 11). With the accent of these instruments on large mirror surface and best light collection, cosmic gamma-rays at an energy threshold lower than any existing or planned terrestrial gamma-ray telescope have become accessible. So far achieved has been a threshold of 25 GeV. The Japanese group has joined the MAGIC collaboration since 2010, and contributed to the operation, observations and data analyses. The MAGIC telescopes are upgraded with new cameras, electronics and partially new mirrors in 2012, and are now operated with an unprecedented sensitivity by an international collaboration of about 165 scientists from 24 institutes and consortia from 12 countries.

The recent highlights from MAGIC are, (1) The first detection of the Gamma Ray Burst GRB 190114C with the ground-based gamma-ray telescope MAGIC [1], [2], [3]), (2) Observation of sub-TeV gamma rays from the IceCube 170922A [4], [5], (3) the successful observation of pulsed gamma ray signal from the Crab pulsar up to TeV regime [6]), (4) the discoveries of the most distant blazers S3 0218+35 with the redshift of 0.944 and PKS 1441+25 with the redshift of 0.939 [7], (5) the observation of the very fast flare of 1-min time scale from the blazar inside Perseus cluster, IC310 [8]) the conclusions of a 15 years joint observation campaign of the gamma-ray binary HESS J0632+057 together with the Cherenkov telescope experiments H.E.S.S. and VERITAS. (6) Detection gamma-ray emission from SNRs, γ Cygni [9] and



Fig. 11. MAGIC Stereo System with two Cherenkov telescopes of 17 m diameters, so far achieved the threshold energy of 25 GeV with the sum trigger. It locates near the mountain top of the Roque de los Muchachos on the Canary Island of La Palma. Two telescopes are located with the distance of 85 m.

G106.3+2.7 [10], both suggesting the acceleration of hadronic cosmic rays. These results brought new questions on the pulsar emission mechanism, cosmic rays acceleration at SNRs, the EBL energy density, and gamma ray emission mechanism from the supermassive blackholes or vicinity of them.

Farthest VHE Gamma Ray Burst to date: GRB 201216C

So-called "long" gamma-ray burst GRB 201216C occurred on 16 December 2020 at a redshift $z = 1.1$ and was followed by the MAGIC telescopes as part of the transients monitoring program [11]. Whereas gamma-ray burst at such high redshifts are not uncommon, they usually lack VHE detections due to a substantial VHE gamma ray absorption at cosmological distances. Furthermore, the possible existence of VHE emission requires operation of additional radiation mechanisms, usually not identified in the lower-energy observations of the late time "afterglow" GRB emission. While the activity of such radiation components has been already demonstrated with MAGIC data [1], studies of the so far limited sample of known VHE-bright GRBs suggest the understanding of the highest energy afterglow emission is far from being complete.

MAGIC observations of GRB 201216C started 56 seconds following the burst detection with the SWIFT-BAT satellite and lasted for 20 minutes on December 16th (constrained by the burst visibility from MAGIC site) and another 4 hours on the subsequent night. A decaying VHE emission from the burst was detected with a total statistical significance of 6 sigma. This is the second firm detection of a GRB with the MAGIC telescopes after GRB 190114C; at its measured redshift of $z = 1.1$ this GRB is the most distant VHE source detected to date.

The VHE emission MAGIC detected is at odds with simple models of the "afterglow" emission and indicates the presence of an additional emission component dominating the emission above few tens of GeV. Performed analytic estimates and numerical modeling suggest a still different component is needed to describe the late-time radio emission, aligning with earlier studies on this burst. Both observations and models indicate a wind-like medium surrounding the burst, typical for long GRBs. The found best fit model parameters match those from previous GRB afterglow studies without VHE detection.

The rapid response and low-energy threshold of the

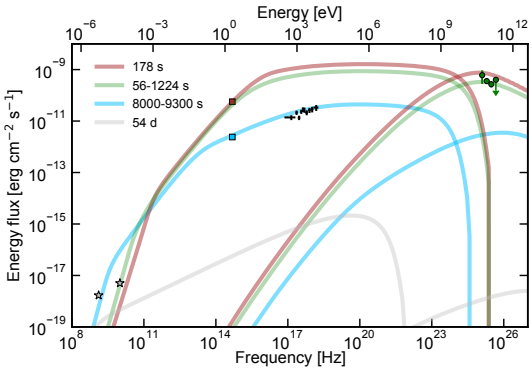


Fig. 12. Spectral energy distribution of the farthest to date VHE GRB 201216C at different times following the SWIFT-BAT detection on 2020 Dec 16 at 23:07:31 UT. Colored lines depict the two–component model predictions at the times marked in the legend. MAGIC measurements, denoted with green circles, highlight the presence of a second emission component, dominating GRB flux above few tens of GeV early within the "afterglow" phase. From [1].

MAGIC telescopes were key to detecting VHE emission this early in the afterglow phase. Combined with detections by other experiments, this detection presently suggests VHE emission is common in both high- and low-luminosity GRBs.

Multimessenger Characterization of Markarian 501 during Historically Low X-Ray and γ-Ray Activity

Blazars are among the most energetic sources in our universe and are prominent objects in the γ-ray sky. For many blazars, very-high-energy (VHE; E$>$ 0.1 TeV) γ-rays, combined with X-rays, provide a useful tool as they host most of the variable and rapidly evolving emission.

Therefore, MAGIC studied the broadband emission of the blazar Mrk 501 using multiwavelength observations from 2017 to 2020, performed with a multitude of instruments, including MAGIC, Fermi's Large Area Telescope (LAT), NuSTAR, Swift, GASP-WEBT, and the Owens Valley Radio Observatory (see Fig. 13 and [12]). Mrk 501 exhibited extremely low broadband activity, potentially helping to unravel its baseline emission. Despite this, significant flux variations were detected across all wave bands, with the most substantial changes occurring in X-rays and VHE γ-rays. A significant correlation ($>3\sigma$) between X-rays and VHE γ-rays was observed, supporting leptonic scenarios to explain the variable parts of the emission, even during low activity. This finding is further supported when extending the data from 2008 to 2020, identifying, for the first time, significant correlations between the Swift X-Ray Telescope and Fermi-LAT. Additionally, correlations between high-energy γ-rays and radio were found, with the radio lagging by more than 100 days, suggesting that the γ-ray emission zone is upstream of the radio-bright regions in the jet.

Furthermore, from mid-2017 to mid-2019, Mrk 501 showed historically low activity in X-rays and VHE γ-rays, with a stable VHE flux ($>$0.2 TeV) at 5% of the Crab Nebula's emission. The broadband spectral energy distribution (SED) of this 2-year long low state, potentially the baseline emission of Mrk 501, can be characterized with one-zone leptonic models and (lepto)-hadronic models that meet neutrino flux con-

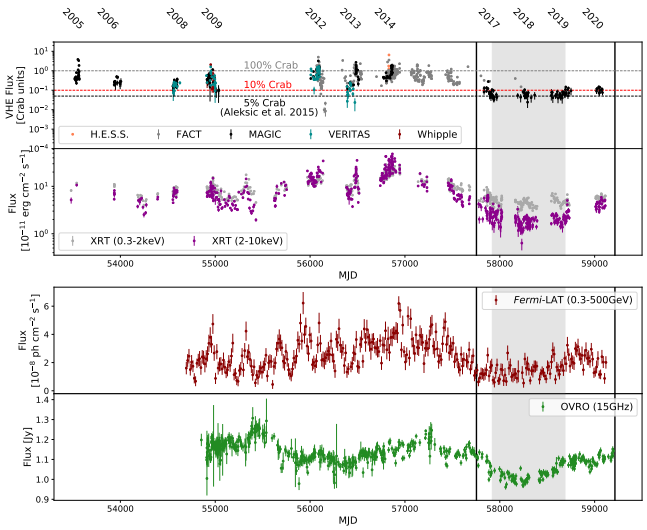


Fig. 13. Long-term Mrk 501 light curve spanning from February 2005 until end of 2020 displaying (from top to bottom) all published VHE data, Swift-XRT data, Fermi-LAT data, OVRO data. From [12].

straints from IceCube. MAGIC explored the time evolution of the SED toward the low state, suggesting that the stable baseline emission may be attributed to a standing shock, while the variable emission may result from an additional expanding or traveling shock.

Bibliography

[1] The first detection of a GRB at sub-TeV energies; MAGIC detects the GRB190114C., ATEL # 12390.

[2] Teraelectronvolt emission from the γ-ray burst GRB 190114C, MAGIC collaboration, Nature 575, 455 (2019).

[3] Observation of inverse Compton emission from a long γ-ray burst, MAGIC collaboration et al., Nature 575, 459 (2019).

[4] First-time detection of VHE gamma rays by MAGIC from a direction consistent with the recent EHE neutrino event IceCube-170922A, ATel #10817.

[5] Multimessenger observations of a flaring blazar coincident with high-energy neutrino IceCube-170922A, Science 12 July 2018, Science.eaat1378.

[6] Phase-resolved energy spectra of the Crab pulsar in the range of 50-400 GeV measured with the MAGIC telescopes, MAGIC Collaboration, Aleksić et al., A&A 540 (2012) A69.

[7] Discovery of Very High Energy Gamma-Ray Emission from the distant FSRQ PKS 1441+25 with the MAGIC telescopes, ATEL # 7416.

[8] Black hole lightning due to particle acceleration at subhorizon scales, MAGIC collaboration, Science 346 (2014) 1080-1084.

[9] Study of the GeV to TeV morphology of the γ Cygni SNR (G 78.2+2.1) with MAGIC and Fermi-LAT. Evidence for cosmic ray escape, MAGIC collaboration et al., A&A 670, A8 (2023)

[10] MAGIC observations provide compelling evidence of hadronic multi-TeV emission from the putative PeVatron SNR G106.3+2.7, MAGIC collaboration et al., A&A 671, A12 (2023)

[11] MAGIC detection of GRB 201216C at z = 1.1, Abe. H et al., MNRAS, 527, 3 (2024).

[12] Multimessenger Characterization of Markarian 501 during Historically Low X-Ray and γ-Ray Activity, MAGIC collaboration et al., ApJS, 266, 37 (2023).

LST1-MAGIC joint observations

The location of the LST array in the CTA North has an overlap with MAGIC telescopes, which allows us to perform the cross-calibration between LST and MAGIC telescopes. Also, by operating MAGIC telescopes and LSTs together, an improved sensitivity can be achieved. Below, ooint observations between LST-1 and MAGIC telescopes are reported.

LST1-MAGIC joint observation of BL Lac

One of the specific phenomena in blazars is intra-day variability, which is a flux variations within a day. It suggests existence of small emission regions and/or high Doppler-factor regions in the blazar, based on the restriction from the light crossing time. While detection of such variabilities would be of great help for understanding the particle acceleration mechanism of blazars, it requires very high telescope sensitivity because in many cases the amplitude of variability is small. A MAGIC - LST-1 joint observation, which has a higher sensitivity than MAGIC alone or LST-1 alone, will be the most effective method to study the intra-day variabilities in blazars in gamma-rays. Since 2020, one of the BL Lac type blazar BL Lacertae had been showing historical outbursts in several bands. Very High Energy (VHE) gamma ray flare was also detected. On August 8th, 2021, a long joint observation between LST1 and MAGIC were performed for this source. The flux level from the joint analysis was consistent with MAGIC only one, and it showed a possible minute scale flux variabilities. The physics interpretation of this interesting phenomenon is under discussion.

LST1-MAGIC joint observation of OP313

Observing and detecting VHE gamma rays from Flat Spectrum Radio Quasars (FSRQs), a subclass of Active Galactic Nuclei (AGN), presents significant challenges. These challenges stem from two primary absorption mechanisms: intrinsic gamma-ray absorption within the source itself, and enhanced absorption by the extragalactic background light, which is particularly pronounced for FSRQs due to their typically greater cosmological distances compared to other AGNs. However, thanks to the low-energy threshold of the LST-1 and the stereoscopic reconstruction capabilities of the MAGIC telescopes, we have succeeded in detecting VHE gamma rays

from a significant flare of the distant FSRQ OP 313 (z = 0.997) in December 2023 [4]. While the LST-1 mono observation data yielded higher significance due to a longer observation time, the simultaneous observation data from LST-1 and MAGIC, processed using `magicctapipe`, produced high-quality high level products with a tenfold improvement in the signal-to-background ratio. This highlights the superior sensitivity and the strong background-rejection capability of the combined LST-1 and MAGIC analysis. This achievement not only adds to the exclusive list of FSRQs detected at VHE but also establishes OP 313 as the most distant blazar ever detected in this energy range.

Hardware Stereo Trigger between MAGIC and LST-1

Leveraging the proximity of the MAGIC telescopes and LST-1, a project is underway to enable bidirectional exchange of trigger signals between the two inherently separate systems, facilitating joint observations at the hardware level. While a technique known as Software Coincidence has been established to combine observation data from MAGIC telescopes and LST-1 offline based on time stamps, this method can only extract relatively bright events that trigger all three telescopes, due to MAGIC's operational strategy of recording only stereo events.

To address this limitation, we have introduced optical fiber cables to enable the exchange of trigger signals between MAGIC and LST-1 and implemented a coincidence logic framework: Hardware Stereo Trigger system (HaST, for a conceptual diagram see Fig. 14)[5]. This fiscal year, we obtained test observation data using this system and confirmed that the introduction of events triggered between any two telescopes effectively improved the energy threshold by approximately 30 % (Fig. 15). Furthermore, the reception of stereo triggers on the LST-1 side has also been confirmed this year, which not only signifies the foundational completion of the system but also represents the first successful implementation of the stereo observation concept envisioned in the initial design of the LST's Trigger Interface Board. Despite the older IACT system being part of this process, this success paves the way for future stereo observations involving the forthcoming LST-2, LST-3, and LST-4 telescopes.

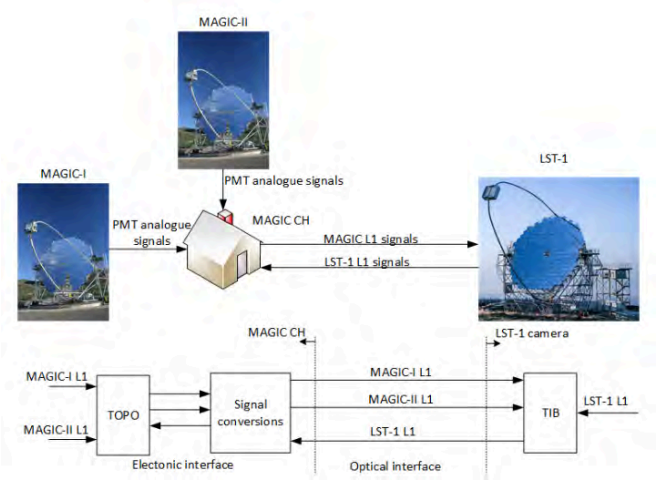


Fig. 14. Overview of the HaST system. The upper part of the image shows the signals between the three telescopes and the MAGIC CH. Below, the main hardware subsystems involved in the HaST are shown.

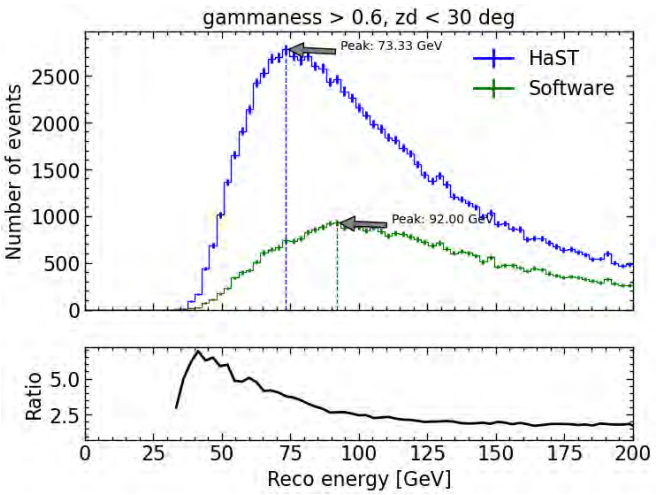


Fig. 15. Energy distribution of events from observations of the gamma-ray standard candle Crab Nebula with HaST activated. The figure compares the analysis of all the observation data with the analysis of events triggered by only three telescopes to mimic the conventional method, labeled as Software Coincidence. The introduction of HaST has led to an increased event rate and an improvement in the peak position, corresponding to the energy threshold, shifting towards lower energies.

Bibliography

[1] MAGIC observation of BL Lacertae flaring period in 2020, R. Imazawa, PoS (ICRC2023) 595, 2023

[2] LST-1 observations of an enormous flare of BL Lacertae in 2021, S. Nozaki, PoS (ICRC2023) 552, 2023

[3] Low energy performance boost through a hardware stereoscopic trigger between CTA LST1 and MAGIC, J. Baxter, PoS (ICRC2023) 700, 2023

[4] First detection of VHE gamma-ray emission from FSRQ OP 313 with LST-1, J. Cortina, Astronomers Telegram, 16381, 2023

[5] Low energy performance boost through a hardware stereoscopic trigger between CTA LST1 and MAGIC, J. Baxter, PoS (ICRC2023) 700, 2023

Other Activities

As a test bench for domestic R & D activities of future ground-based gamma-ray observatory projects, an old atmospheric Cherenkov telescope of 3 m diameter was repaired and then placed at the Akeno Observatory in November 2010. This telescope shown in Figure 16 (Akeno telescope, hereafter) is currently the only atmospheric Cherenkov telescope located in Japan [1]. We have developed an R & D imaging camera system with the Akeno telescope since 2009, the purpose of which is to make a battery-powered data acquisition system for a future mobile imaging atmospheric Cherenkov telescope array [2]. The system consists of 32 PMTs, of which detected Cherenkov light signals are read out by only four GHz-sampling analog memory ASICs.



Fig. 16. Akeno atmospheric Cherenkov telescope of 3 m diameter, located in the Akeno Observatory.

Utilizing some central PMTs of the above system, we also observed the optical Crab pulsar in Akeno. The purpose of this study is to investigate the efficient acceleration site of the Crab Nebula in a detailed manner, using simultaneous observations of radio and optical pulses passing through the nebula plasma. We performed the first observations of the optical Crab pulsar in January 2020 after developing a dedicated pulse counting system, followed by further observations in 2021 and 2022 with some improvements in the system. The data taken in January 2022 revealed a preliminary but 4.5σ signal at the main pulse phase of the Crab pulsar. The presence of the interpulse peak was also marginally observed in the lightcurve, suggesting that they could realistically be obtained from the optical Crab pulsar. This result indicates that the sensitivity of the Akeno telescope to the optical Crab pulsar is somewhat lower than originally anticipated. The data have been analyzed more carefully since 2023. We are also considering the future effective applications of this telescope.

Bibliography

[1] M. Ohishi et al., Proc. of 33rd Internat. Cosmic Ray Conf. (Rio de Janeiro), 587 (2013).

[2] T. Yoshikoshi et al., Proc. of 34th Internat. Cosmic Ray Conf. (The Hague), 887 (2015).

TA: Telescope Array Experiment

Spokespersons: S. Ogio[1] (Dec. 2017 - Dec. 2023), Y. Tsunesada[2] (Dec. 2023 - present), J.N. Matthews[3]

1 : ICRR, The Univ. of Tokyo

2 : Graduate School of Science, Osaka Metropolitan Univ.

3 : Dept. of Physics and Astronomy, Univ. of Utah

Collaborating Institutions:

Academia Sinica, Taipei, Taiwan; Chubu Univ., Kasugai, Japan; ERI, Univ. of Tokyo, Tokyo, Japan; Hiroshima City Univ., Hiroshima, Japan; Hanyang Univ., Seoul, Korea; ICRR, Univ. of Tokyo, Kashiwa, Japan; INR, Moscow, Russia; CEICO, Inst. of Phys, Czech Acad. of Sci., Prague, Czech Republic; Kanagawa Univ., Yokohama, Japan; KEK/IPNS, Tsukuba, Japan; Kochi Univ., Kochi, Japan; Loyola Univ. Chicago, Chicago, USA; Moscow M.V. Lomonosov State University, Moscow, Russia; National Centre for Nuclear Research, Warsaw, Poland; NICT, Tokyo, Japan; Osaka Electro-Comm. Univ., Neyagawa, Japan; Osaka Metropolitan Univ., Osaka, Japan; RIKEN, Wako, Japan; Shibaura Inst. Tech., Tokyo, Japan; Shinshu Univ., Nagano, Japan; SKKU, Suwon, Korea; Tokyo City Univ., Tokyo, Japan; ULB, Brussels, Belgium; UNIST, Ulsan, Korea; Univ. of Nova Gorica, Nova Gorica, Slovenia; Univ. of Utah, Salt Lake City, USA; Univ. of Yamanashi, Kofu, Japan; Yonsei Univ., Seoul, Korea

1. Introduction

The Telescope Array (TA) is the largest Ultra-High Energy Cosmic Ray (UHECR) observatory in the northern hemisphere. The main aim of TA is to explore the origin and nature of UHECRs by measuring the energy spectrum, arrival direction distribution and mass composition. The TA collaboration consists of approximately 150 researchers from USA, Russia, Korea, Belgium, Czech, Slovenia, Poland, Taiwan and Japan.

The TA detector consists of a surface array of 507 plastic scintillator detectors (SD) and three stations of fluorescence detectors (FD). It is located in the desert, approximately 200 km south of Salt Lake City in Utah in USA. The SDs were deployed on a square grid with 1.2-km spacing, and the SD array covers an area of approximately 700 km^2. Each SD has two layers of 1.2-cm-thick scintillator with an area of 3 m^2. The full operation of SDs started in March 2008. The duty cycle is approximately 95% on average. One northern FD station at the Middle Drum (MD) site uses 14 refurbished HiRes telescopes. Two southern FD stations at the Black Rock Mesa (BRM) and Long Ridge (LR) sites were built newly each with 12 telescopes. The MD FD views 3° - 31° and the BRM and LR FDs view 3° - 33° above horizon. All three FD stations started the observation in November 2007, and have duty cycles of approximately 10%.

TA found evidence for intermediate-scale anisotropy of arrival directions of cosmic rays with greater than 5.7×10^{19} eV of energy. With enhanced statistics, it is expected to observe the structure of the hotspot along with other possible excesses and point sources along with the correlations with extreme phenomena in the nearby universe. TA proposed TAx4 project to quadruple the effective area of the TA SD aperture including the existing TA SD array by installing additional 500 newly designed SDs on a square grid with wider, 2.08-km spacing between each. The layout of TAx4 is shown in Fig. 17.

The design of SD for the TAx4 experiment is identical to the design of SD for the TA Low energy Extension(TALE) experiment, which will be described in detail later. The basic design is common to TA , but the number and arrangement of wavelength shifter fibers (WLSF), the performance of the photomultiplier tubes (PMTs), and the wireless LAN module and used protocols are different. In the TAx4 and TALE, we use a PMT with significantly improved quantum efficiency and surface uniformity. This has allowed us to reduce the total length of WLFSs by 67% while maintaining the performance of the SD as a whole. A new wireless LAN module is used for the TAx4 and TALE SDs because the one used in TA was out of production.

Detector installation for TAx4 began in 2019, and 257 SDs were deployed in February and March 2019. By this installation, the total coverage area with SDs including the original TA SD array has been increased by a factor of 2.5. The new SD array started the data acquisition in April 2019. Since the new SD array is divided into two lobes, two FD stations are required to overlook each lobe in order to increase the number of hybrid events for the measurement of $X_{\rm max}$ and to confirm the energy scale. These FD stations consist of refurbished HiRes telescopes: four telescopes at the MD site and eight telescopes at the BR site. The TAx4 FD station at the northern site was constructed and started the stable observation in June 2018. The TAx4 FDs at the southern site were constructed and started the observation in 2019. The recent status of TAx4 was reported in [1].

The TA Low energy Extension (TALE) enables detailed studies of the energy spectrum and composition from $\sim 10^{16.5}$ eV. The main target of TALE is to clarify the expected transition from galactic to extra-galactic cosmic ray origins and the comparison of the data with Monte Carlo (MC) simulation that takes into account the results of the latest LHC experiments. The TALE detector is located north of the TA site (at around the MD FD station). The TALE FD station consists of 10 refurbished HiRes telescopes. The TALE FD views 31° - 59° in elevation angle. The TALE detectors are located at the northern corner of the TA detectors. The TALE FD operation was commenced in the spring of 2013. The TALE SD array consists of 80 SDs (40 SDs with 400-meter spacing and 40 SDs with 600-meter spacing). The TALE SD array was completed in February 2018 and is in stable operation. The mode energy of TALE hybrid events is $10^{16.8}$ eV. There is a plan to install additional 50 SDs with 100-meter spacing near the TALE FD station to observe even lower-energy cosmic rays, for which the mode energy is $10^{15.5}$ eV.

The TALE infill experiment is a further extension of TA-TALE detectors to observe low-energy cosmic rays down to the PeV region. TALE infill uses existing TALE-FD detectors and newly developed "infill" SDs with 100m spacing. 50 SDs used in the TALE infill array were manufactured at the Akeno observatory of ICRR in October 2021. In the summer of 2022, these detectors were transported to the TA site, and installed in the area between the TALE FD station and the TALE SD array in October 2022.

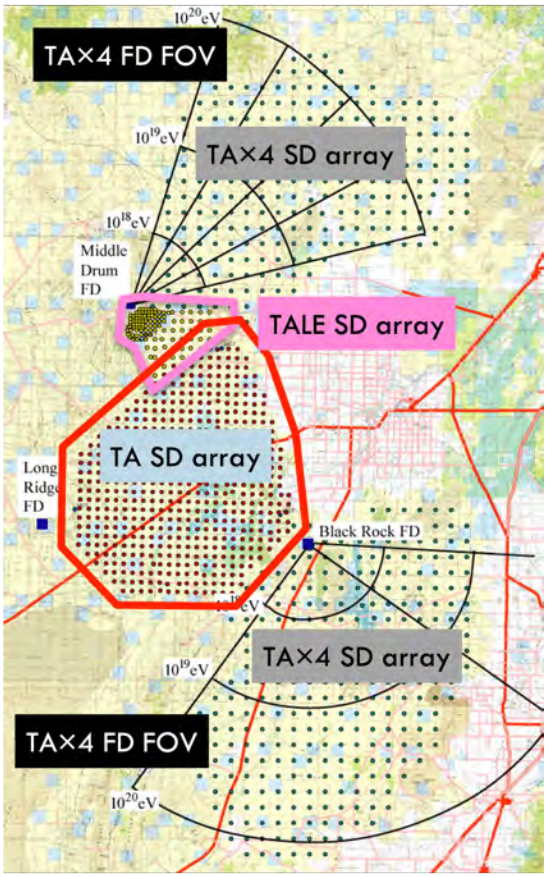


Fig. 17. The layout of the TA, TAx4, and TALE. The array of 507 SDs is the original TA SD array. There are three TA FD stations (Middle Drum to the north, Long Ridge to the west, and Black Rock Mesa to the east of the TA SD array) with black square symbols. The array of surface detectors to the north of the TA SD array is the TALE SD array. The additional TAx4 500 surface detectors will be located in separate lobes on the northeast and southeast sides of the TA SD array. The 257 SDs have already been deployed for TAx4. Additional two FD stations with refurbished HiRes telescopes for the TAx4 are located at the Middle Drum and Black Rock Mesa sites and view to the northeast and southeast as denoted each by the frame of the fan.

Notable developments during JFY2023

The TALE infill array started routine hybrid observations with TALE FDs in October 2023. An example of events detected by this hybrid system is shown in Fig. 18

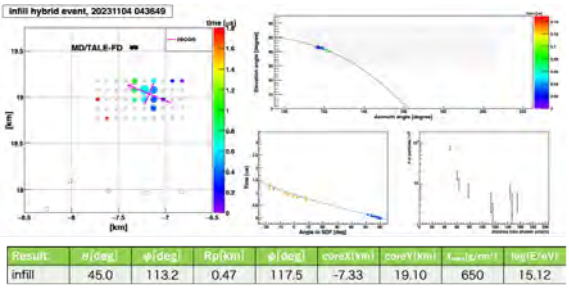


Fig. 18. An example of a hybrid event detected by the TALE infill experiment. The table below shows the parameters of the primary cosmic rays obtained from the event reconstruction. The energy is very small, about a quarter of the mode energy.

The accuracy of the TALE infill hybrid observation was evaluated by Monte Carlo simulations (Fig. 19): for cosmic rays at $10^{15.5}$ eV, the accuracy of determining Xmax is 29 g/cm^2 and the accuracy of determining energy E is 12.5 %. This is almost the same accuracy as the TALE hybrid (Xmax: 33 g/cm^2, E: 12.3 % for E$\geq 10^{16.5}$ eV), even though the energy is an order of magnitude lower.

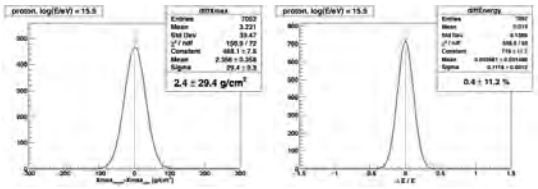


Fig. 19. The accuracy of the TALE infill hybrid observation was evaluated by Monte Carlo simulations.

The energy distribution of the hybrid events obtained from the observations from 23 November 2023 to 24 February 2024 is shown in Fig. 20. As expected, the mode energy is $10^{15.7}$ eV, indicating that the energy threshold has been lowered to $10^{15.0}$ eV.

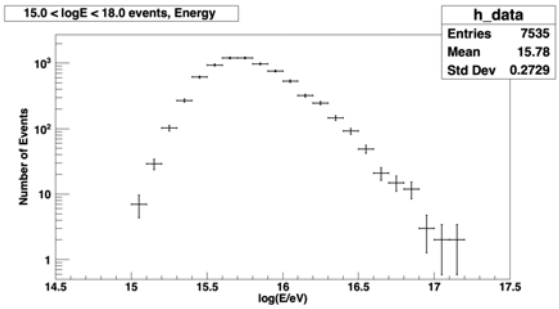


Fig. 20. The energy distribution of the hybrid events obtained from the observations from 23 November 2023 to 24 February 2024.

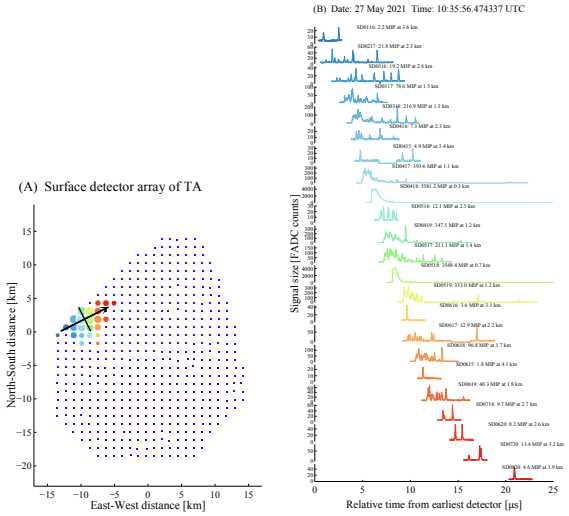


Fig. 21. The foot print of the event in the TA SD array and the corresponding detector waveforms od FADC conts for each SD.

Comparison to other observed events at energies above 100 EeV shows an isotropic distribution with no apparent clustering.

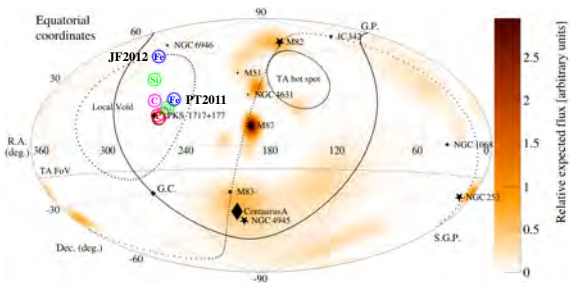


Fig. 22. Sky map in equatorial coordinates showing the arrival direction of the event.

2. Publications in refereed journals

The follwing papers were published by the TA collaboration published in refereed journals in JFY 2023.

An extremely high energy event named "Amaterasu"

We reported the detection of an extremely energetic particle recorded by the surface detector array of the Telescope Array experiment[2]. We detected a particle with an energy of 244 EeV on 27 May 2021. The event map and recorded signals by SDs are shown in Fig. 21.

Fig. 22 is a sky map in equatorial coordinates showing the arrival direction of the event(black circle). Also shown are calculated back-tracked directions assuming two models of the galactic magnetic field labelled JF2012 and PT2011. For each model, different symbols indicate the directions calculated for four possible primary species: proton (P, red), carbon (C, purple), silicon (Si, green), and iron (Fe, blue). For other details, see reference [2]. The arrival direction of this event does not align with any known astronomical objects thought to be a potential source of UHECRs, even after taking into account deflection by the GMF under various assumptions.

The energy spectrum measured by TA using 10 years of FD data

The data from the Black Rock Mesa (BRM) and Long Ridge (LR) fluorescence telescope sites were analyzed separately in monocular mode, with the calculated fluxes combined into a single spectrum (Fig. **??**). The 10-year monocular combined cosmic ray energy spectrum is observed to be in excellent agreement with previous measurements from the northern hemisphere[3]. We present fits of the combined spectrum to a series of broken power law models. The thrice-broken power law was observed to be the best fit considering the Poisson deviance per degrees of freedom. The three breaks suggest an additional feature of the spectrum between the previously observed Ankle feature at $10^{18.7}$ eV and the suppression at $10^{19.8}$ eV.

3. Other physics results

Update of TA Hotspot

The TA Hotspot refers to an excess of events with energies greater than 57 EeV, observed in the vicinity of the Ursa Ma-

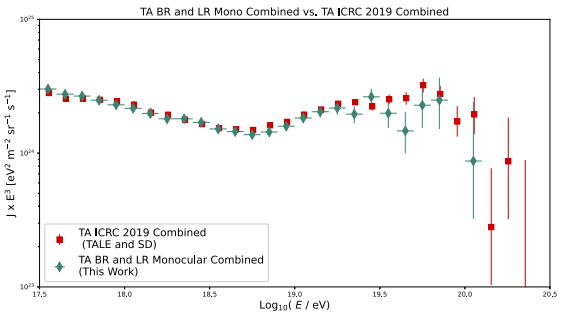


Fig. 23. Monocular combined spectrum vs. TA combined ICRC 2019 spectrum. The TA combined ICRC 2019 spectrum is offset slightly on the x-axis for ease of viewing.

jor constellation. We report the updates on the intermediate-scale anisotropy, the TA Hotspot, measured by the TA SD using the most up-to-date data, collected over 15 years[4]. The left panel of Fig. 25 shows the sky map of the Li-Ma significance using a 25°-radius circle angular window in equatorial coordinates. The color code indicates an excess (red) and a deficit (blue) of events compared to isotropy. The maximum Li-Ma significance is calculated to be 4.8σ at (144.0°, 40.5°), marked by black diamond symbols, in equatorial coordinates. To quantify how often such an excess appears anywhere in an isotropic UHECR sky within TA's field of view by chance, we conduct a Monte Carlo study. The chance probability of finding such an excess is estimated to be 2.7×10^{-3}, approximately equivalent to 2.8σ. We also examine the growth of the Hotspot over the years. The increase rate of the events inside the Hotspot circle is consistent with the linear increase within about 2σ, as illustrated in the right panel of Fig. 25.

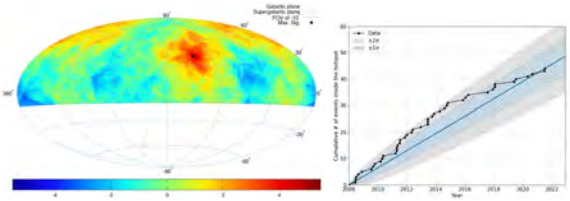


Fig. 24. Sky map of the TA Hotspot in equatorial coordinates using a Hammer projection and its growth over the years. (*left*): The color code represents the Li-Ma significance using a 25°-radius circle angular window in equatorial coordinates for 15 years of TA SD events with $E \geq 5.7 \times 10^{19}$ eV. (*right*): The black dots depict the cumulative number of events falling inside the Hotspot circle with a radius of 25°-radius circle at (144.0°, 40.5°). The blue solid line indicates the estimated event rate inside the Hotspot. The light blue and gray bands represent $\pm 1\sigma$ and $\pm 2\sigma$ deviations from a linear increase rate.

Update on the searches for anisotropies with Auger and TA

TA and Auger have established collaborative working groups since 2012. These groups have engaged in detailed discussions regarding the technical aspects of data analysis methods concerning energy spectrum, mass composition, and anisotropy. Here, we present the results of the anisotropy working group's analysis[5]. In the map of the flux and Li-Ma significance of UHECR on the sky, shown in Fig. **??** in both galactic and equatorial coordinates, we show the main "warm spots" in the southern hemisphere (in the direction of the Centaurus constellation) and in the northern hemisphere (two spots, one in the direction of the Perseus-Pisces region, and the other roughly in the direction of the Ursa Major region). We note that the high significance of the SBG sample is driven by the presence of two of the most prominent galaxies of the catalog (NGC4945 and M83) in the Centaurus region and a third, M82, in the Ursa Major constellation.

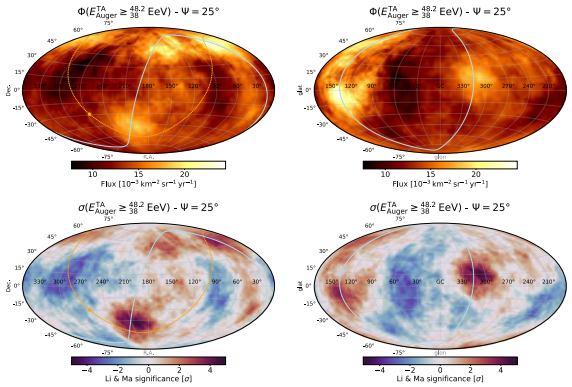


Fig. 25. Flux map (top row) and Li-Ma significance map (bottom row) at energies $E_{TA} \geq 48.2$ EeV, $E_{Auger} \geq 38$ EeV with a top-hat smoothing radius Ψ=25° in Equatorial (left) and Galactic (right) coordinates. The supergalactic plane is shown as a grey line. In the left plot, the orange line represents the Galactic plane and the star the Galactic center.

Mass composition by TA FD hybrid trigger mode

The analysis of UHECR observation data collected by the hybrid trigger mode of the TA experiment for 8.5 years of operation in the energy range from $10^{17.5}$ eV to $10^{19.5}$ eV was presented[6]. The mean logarithmic mass reported by the TA hybrid trigger analysis is compared to the mean logarithmic mass reported by the other results (see Fig. 26).

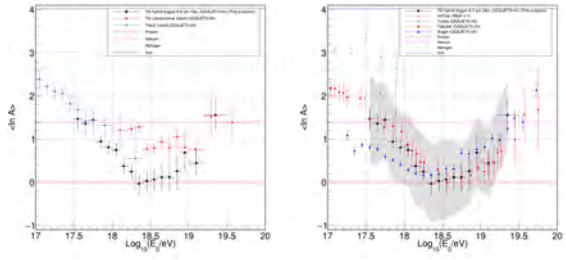


Fig. 26. (*left*) Comparison of <lnA> between this analysis and the other two observation modes in the TA experiment. The black circles represent the results of this analysis. (*right*) Comparison of <lnA> between this analysis and the other four experiments. The shaded area indicates the systematic uncertainties of the TA hybrid trigger analysis.

UHECR spectrum measured by the TAx4 SD array

The TAx4 SD array began operation in 2019 as an air shower array of 257 SDs and has been collecting data steadily since then. In 2023 we reported a UHECR energy spectrum based on TAx4 SD data obtained from October 2019 to October 2022[7]. (see Fig. 27).

We calibrate the energy measured by the TAx4 SD array with a newly developed method. In the method, energy is calibrated by comparing the number of events observed by the TAx4 SD array with that expected by the MC simulation, assuming the previously measured energy spectrum by the TA SD array. The energy scale, which is a factor to calibrate the energy to the FD energy, of the TAx4 SD array is determined to be 1.36 ± 0.05.

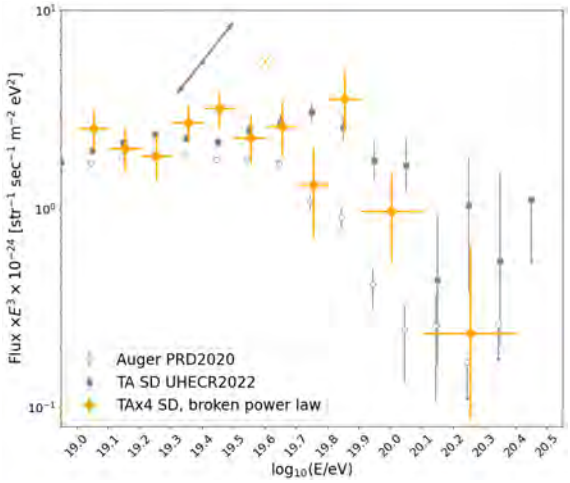


Fig. 27. The cosmic ray energy spectrum measured by the TA×4 SD array with three years of observation (orange diamonds). Those measured by the TA SD (gray squares) and the PAO (open circles) are also shown. Each point is slightly shifted horizontally for better visibility. The thick gray arrow represents the uncertainty of the energy scale of the TA experiment. The thin orange arrow represents the uncertainty of the energy scale of the TA×4 SD array for the TA energy scale.

Energy spectrum in the 2nd knee region with the TALE SD array

The TALE SD array has been in operation since February 2018 with 80 SDs. The TALE SD array DAQ is now running stably. The energy resolution is 25 % at $10^{16.7}$ eV and 10 % at $10^{19.0}$ eV, and the angular resolution is 3° $10^{16.7}$ eV and 1° $10^{19.0}$ eV eV. We evaluated the preliminary energy spectrum assuming a pure proton composition in the energy region from $10^{16.95}$ eV to $10^{18.85}$ eV[8] (see Fig. 28).

A study of the systematic effects on the energy scale

We evaluated the systematic deviation of energy scales for the energy spectrum of the highest energy cosmic rays observed by the TA SD array due to differences in atmospheric fluorescence yield and missing energy estimation. The energy dependence on the energy scales is also investigated and observationally confirmed by the constant intensity cut (CIC) method analysis[9].

We conduct systematic studies to assess the effects on the energy scale in energy spectra. We evaluate the systematic deviations in energy scales within the energy spectrum, originating from differences in atmospheric fluorescence yield and missing energy estimation. By adopting AirFly's fluorescence yield and Auger's missing energy estimation, we observe a shift in the scale factor between FD and SD in TA data from

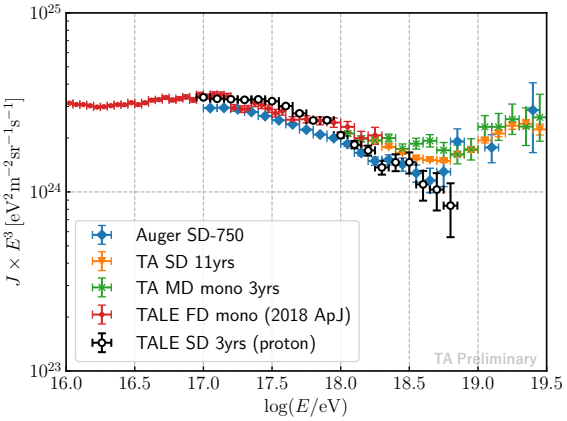


Fig. 28. The energy spectrum from the actual data obtained by the TALE SD array from October 2 2019 to September 28 2022, comparing with other TA and Auger results.

1.27 to 1.35. With this adjusted scale factor, we recalculate the energy spectrum using 14 years of TA SD data, employing both the standard and the CIC methods. Fig. 29 displays the energy spectra obtained by TA and Auger alongside the results of the systematic effect study. Significantly, the energy scale offset, which was approximately +9 % in the energies below $10^{19.5}$ eV, is reduced to about +1 % when we adopt the same energy assignments arising from the fluorescence yield and invisible energy models. Again, both the standard method, represented by blue triangles, and the CIC method, represented by red dots, yield consistent energy spectra.

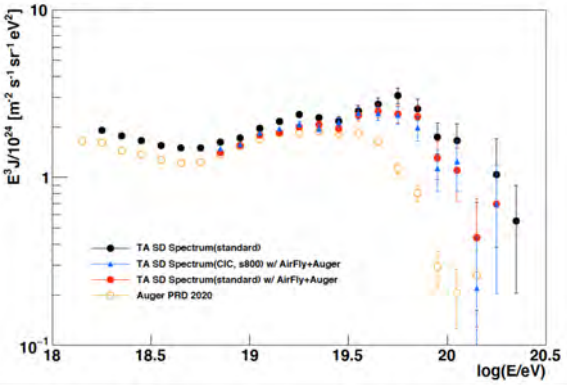


Fig. 29. Systematic effects on the energy scale in 14 year TA SD data. The black points indicate the spectrum obtained using 14 years of TA SD data analyzed using the standard TA fluorescence yield and missing energy corrections, while the orange open circles show the Auger results. The TA energy spectra obtained by adopting AirFly's fluorescence yield and Auger's missing energy estimation are shown with the red points (using the standard TA MC-based method) and the blue triangles (using the CIC method), respectively.

4. Other activities

Other research results and activities reported at ICRC2023, JPS meetings and/or other conferences are listed and introduced below.

- Measurement of energy spectrum with TALE in hybrid mode [10]

- Measurement of CR mass composition with TALE in hybrid mode [11]
- Measurement of energy spectrum with TAx4 FD monocular observation [12]
- Updates on TALE FD mono energy spectrum and composition [13]
- Search for UHE gamma rays [14]
- TA SD analysis for inclined air showers [15]
- Calibration of FDs using a UAV-mounted light source [16]
- Effects of atmospheric transparency on TA air shower analysis [17]
- Joint analysis of the energy spectrum measured at Pierre Auger observatory (PAO) and TA [18]
- Joint study of the arrival directions of UHECRs observed by PAO and TA [19]

5. Future Plans

Research and development of next-generation detectors

The TA experiment site is also a facility for the development of next-generation detectors, and prototype detectors for Auger@TA [20] EUSO [21][22], FAST [23][24] and CRAFFT [25] have been installed and are being used for joint observations with the TA experiment.

Discussions are also underway for the next-generation observatories, to measure the properties of the highest-energy cosmic rays with unprecedented accuracy in the future such as TA2 and GCOS (The Global Cosmic Ray Observatory) [26].

Bibliography

[1] E. Kido, *et al.*, "Updates of the surface detector array of the TAx4 experiment", PoS(ICRC2023), 239, 2023.

[2] Telescope Array Collaboration, "An extremely energetic cosmic ray observed by a surface detector array", Science 382, 903-907, 2023.

[3] R.U. Abbasi, *et al.*, "The energy spectrum of cosmic rays measured by the Telescope Array using 10 years of fluorescence detector data", Astropart. Phys. 151, 102864, 2023.

[4] J.H. Kim, *et al.*, "Anisotropies in the Arrival Direction Distribution of Ultra-High Energy Cosmic Rays Measured by the Telescope Array Surface Detector", PoS(ICRC2023), 244, 2023.

[5] L. Caccianiga, *et al.*, "Update on the searches for anisotropies in UHECR arrival directions with the Pierre Auger Observatory and the Telescope Array", PoS(ICRC2023), 521, 2023.

[6] H.S. Shin, " The Measurement of the Energy Spectrum and Depth of Maximum Shower Development of Ultra-High-Energy Cosmic Rays Collected by the Telescope Array with the Hybrid Trigger Mode", PhD thesis(U. Tokyo), 2023.

[7] K. Fujisue, "The measurement of the highest-energy cosmic ray energy spectrum with the extended surface detector array of the Telescope Array experiment", PhD thesis(U. Tokyo), 2023.

[8] I. Komae, *et al.*, "Measurement of the cosmic ray energy spectrum in the 2nd knee region with the TALE-SD array", PoS(ICRC2023), 405, 2023; "TA experiment 417: Analysis of the cosmic ray energy spectrum with the TALE-SD array 2", JPS meeting, Online, 2024.

[9] K. Fujita, *et al.*, "A study of the systematic effects on the energy scale for the measurement of UHECR spectrum by the TA SD array", PoS(ICRC2023), 400, 2023.

[10] H. Oshima, *et al.*, "Measurement of cosmic-ray energy spectrum with the TALE detector in hybrid mode", PoS(ICRC2023), 271, 2023.

[11] K. Fujita, *et al.*, "Cosmic ray mass composition measurement with the TALE hybrid detector", PoS(ICRC2023), 401, 2023.

[12] J.H. Kim, *et al.*, "Monocular and Hybrid Analysis for TAx4 Fluorescence Detectors", PoS(ICRC2023), 331, 2023.

[13] T. AbuZayyad, *et al.*, "Cosmic ray energy spectrum and mass composition with the TALE fluorescence detector", PoS(ICRC2023), 379, 2023.

[14] I. Kharuk, *et al.*, "Search for EeV photon-induced events at the Telescope Array", PoS(ICRC2023), 324, 2023.

[15] K. Takahashi, *et al.*, "TA SD analysis for inclined air showers", PoS(ICRC2023), 306, 2023.

[16] D. Sato, *et al.*, "Effect of optical properties of FDs on reconstruction analysis", PoS(ICRC2023), 227, 2023.

[17] K. Mizuno, *et al.*, "Effects of atmospheric transparency on TA air shower analysis", PoS(ICRC2023), 226, 2023.

[18] D.R. Bergman, *et al.*, "Measurement of UHECR energy spectrum with the Pierre Auger Observatory and the Telescope Array", PoS(ICRC2023), 406, 2023.

[19] M. Kuznetsov, *et al.*, "Possible interpretations of the joint observations of UHECR arrival directions using data recorded at the Telescope Array and the Pierre Auger Observatory", PoS(ICRC2023), 528, 2023.

[20] S. Mayotte, *et al.*, "Auger@TA: An Auger-like surface detector micro-array embedded within the Telescope Array Project", PoS(ICRC2023), 368, 2023.

[21] Z. Plebaniak *et al.*, "The EUSO-TA ground-based detector: results and perspectives", PoS(ICRC2023), 385, 2023.

[22] M. Bertaina "An overview of the JEM-EUSO program and results", PoS(ICRC2021), 406, 2021.

[23] S. Sakurai, "Detecting ultra-high-energy cosmic rays with prototypes of the Fluorescence detector Array of Single-pixel Telescopes (FAST) in both hemispheres", PoS(ICRC2023), 302, 2023.

[24] F.W. Bradfield, "Reconstruction procedure of the Fluorescence detector Array of Single-pixel Telescopes", PoS(ICRC2023), 303, 2023.

[25] Y. Tameda *et al.*, "Detector optimization and observation plan of the CRAFFT project for the next generation UHECR observation", PoS(ICRC2023), 329, 2023.

[26] R. Alves Batista *et al.*, "Science with the Global Cosmic-ray Observatory (GCOS)", PoS(ICRC2023), 281, 2023.

Tibet ASγ Experiment

[Spokesperson: M. Takita]

ICRR, The Univ. of Tokyo, Kashiwa, Chiba 277-8582

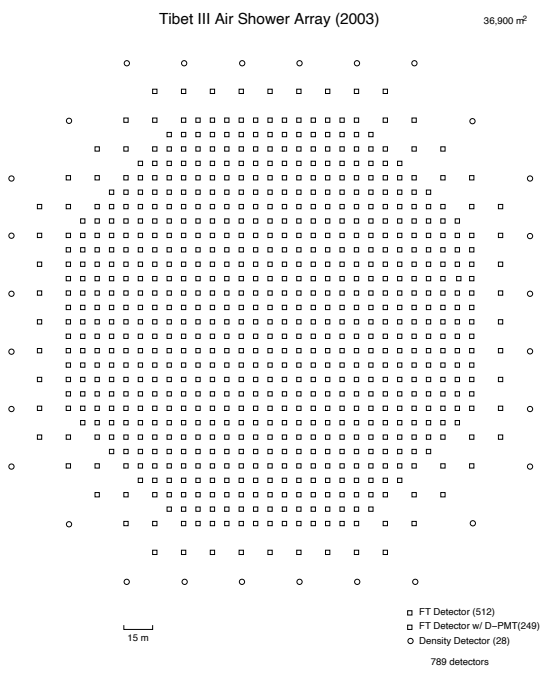


Fig. 1. Schematic view of Tibet III.

1. Experiment

The Tibet air shower experiment has been successfully operated at Yangbajing (90°31′ E, 30°06′ N; 4300 m above sea level) in Tibet, China since 1990. It has continuously made a wide field-of-view (approximately 2 steradian) observation of cosmic rays and gamma rays in the northern sky.

The Tibet I array was constructed in 1990 and it was gradually upgraded to the Tibet II by 1994 which consisted of 185 fast-timing (FT) scintillation counters placed on a 15 m square grid covering 36,900 m^2, and 36 density (D) counters around the FT-counter array. Each counter has a plastic scintillator plate of 0.5 m^2 in area and 3 cm in thickness. All the FT counters are equipped with a fast-timing 2-inch-in-diameter photomultiplier tube (FT-PMT), and 52 out of 185 FT counters are also equipped with a wide dynamic range 1.5-inch-in-diameter PMT (D-PMT) by which we measure up to 500 particles which saturates FT-PMT output, and all the D-counters have a D-PMT. A 0.5 cm thick lead plate is put on the top of each counter in order to increase the counter sensitivity by converting gamma rays into electron-positron pairs in an electromagnetic shower. The mode energy of the triggered events in Tibet II is 10 TeV.

In 1996, we added 77 FT counters with a 7.5 m lattice interval to a 5,200 m^2 area inside the northern part of the Tibet II array. We called this high-density array Tibet HD. The mode energy of the triggered events in Tibet HD is a few TeV.

In the late fall of 1999, the array was further upgraded by adding 235 FT-counters so as to enlarge the high-density area from 5,200 m^2 to 22,050 m^2, and we call this array and further upgraded one Tibet III. In 2002, all of the 36,900 m^2 area was covered by the high-density array by adding 200 FT-counters more. Finally we set up 56 FT-counters around the 36,900 m^2 high density array and equipped 8 D-counters with FT-PMT in 2003. At present, the Tibet air shower array consists of 761 FT-counters (249 of which have a D-PMT) and 28 D-counters as in Fig. 1.

The performance of the Tibet air shower array has been well examined by observing the Moon's shadow (approximately 0.5 degrees in diameter) in cosmic rays. The deficit map of cosmic rays around the Moon demonstrates the angular resolution to be around 0.9° at a few TeV for the Tibet III array. The pointing error is estimated to be better than $\sim$0.01°, as shown in Fig. 2, by displacement of the shadow center from the apparent center in the north-south direction, as the east-west component of the geomagnetic field is very small at the experimental site. On the other hand, the shadow center displacement in the east-west direction due to the geomagnetic field enables us to spectroscopically estimate the energy scale uncertainty at $\pm$12 % level, as shown in Fig. 3. Thus, the Tibet air shower experiment introduces a new method for energy scale calibration other than the conventional estimation by the difference between the measured cosmic-ray flux by an air shower experiment and the higher-energy extrapolation of cosmic-ray flux measured by direct measurements by balloon-borne or satellite experiments.

In 2007, a prototype 100-m^2 underground water Cherenkov muon detector was successfully constructed in Tibet to demonstrate the technical feasibility, cost estimate, validity of our Monte Carlo simulation. Data analyses demon-

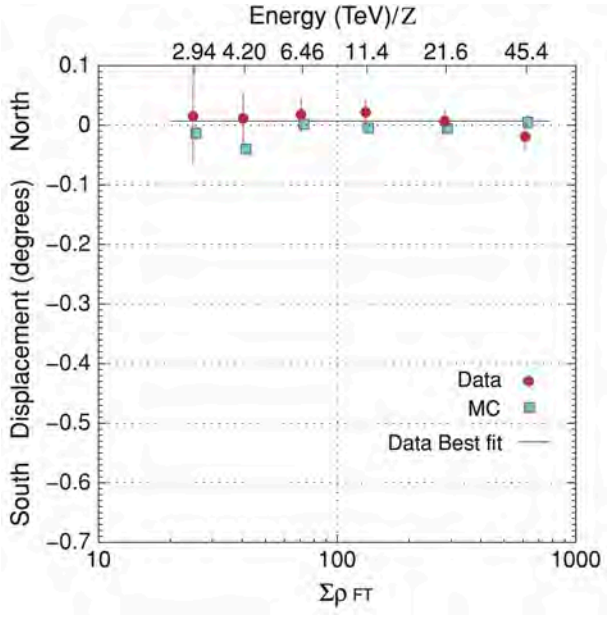


Fig. 2. From [1]. The Moon's shadow center displacement from the apparent position in the north-south direction as a function of energy, observed by Tibet III.

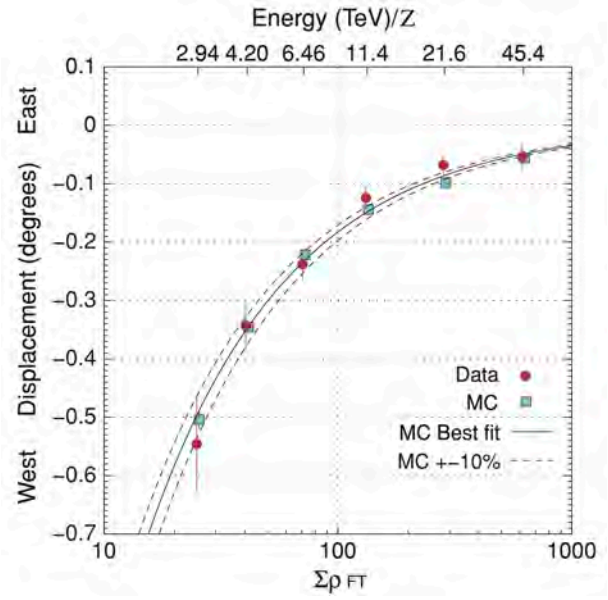


Fig. 3. From [1]. The Moon's shadow center displacement from the apparent position in the east-west direction as a function of energy, observed by Tibet III.

strate that our MC simulation reproduces real data quite reasonably.

After the success of the prototype underground muon detector, we added a large underground muon detector (MD) array and the experimental configuration was changed starting from February 2014. The current array consists of 597 plastic scintillation detectors with an area of 0.5 m^2 as shown by small dots in Fig. 4, covering an area of 65,700 m^2. The Tibet MD array (3,400 m^2 in total area) consists of 64 water-Cherenkov-type detectors located at 2.4 m underground of the AS array as shown by open squares in Fig. 4. Each detector is a waterproof concrete cell filled up with water of 1.5 m in depth, 7.35 m $\times$ 7.35 m in area, equipped with a 20-inch-diameter downward-facing photomultiplier tube (PMT) on the ceiling. The inner walls and floor have a white Tyvek sheet lining to efficiently gather catoptric water Cherenkov light. The electromagnetic component is shielded by the soil overburden which corresponds to $\sim$19 radiation lengths. The energy threshold for muons is approximately 1 GeV. A photon induced air shower has much less muons compared with a cosmic-ray induced one. The Tibet MD array enables us to significantly discriminate a cosmic-ray background event from a photon signal by means of counting the number of muons in an air shower.

2. Physics Results

Our current research theme is classified into 4 categories:

(1) Celestial gamma-ray point/diffuse sources,

(2) Chemical composition and energy spectrum of primary cosmic rays in the knee energy region,

(3) Cosmic-ray anisotropy in the multi-TeV region with high precision,

(4) Global 3-dimensional structure of the solar and interplanetary magnetic fields by observing the Sun's shadow in cosmic rays.

We will introduce a part of the results obtained in this fiscal year[2, 3] on celestial gamma-ray observation.

2.1. Standard gamma-ray point-source analysis

A photon induced air shower contains much less muons compared with a cosmic-ray induced air shower. Therefore, the MD array enables us to distinguish a photon signal event from a cosmic-ray induce background event. Using the AS and MD arrays, we analyzed the air shower data and muon data during 719 live days from February 2014 to May 2017.

Figure 4 (a) and (b) show the event display and the lateral distribution, respectively, of a typical photon-like event observed with $E = 251$ TeV from the Crab nebula[6]. The total uncertainty of the energy ΔE is defined as the quadratic sum of the absolute energy-scale error (12%) [1] and the energy resolution estimated by using MC events with the same θ and core distance from the array center (R). The ΔE of the 251 TeV photon-like event is estimated to be $^{+45}_{-43}$ TeV.

We reconstruct the arrival direction of an air shower by means of the relative timing information recorded at each scintillation detector. The color scale and circle size in Fig. 4 (a) stand for the relative timing (t) and the number of particle density (ρ) in an air shower. In the first place, we estimate the air shower core location weighted by ρ. The arrow head position and direction in the figure indicate the estimated core position and azimuthal direction. The t's in the air shower front are fitted by a conical shape, and its cone angle is optimized by the MC simulation depending on the air shower size. The

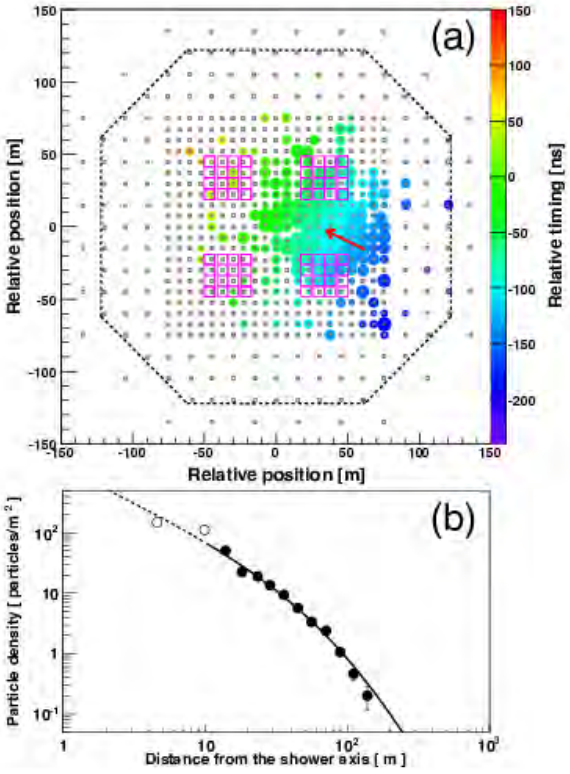


Fig. 4. From Ref.[6], references therein. (a) An event display of the observed photon-like AS of energy 251 TeV. The size and color of each circle represent the logarithmic particle density and the relative timing in each detector, respectively. The arrow head and direction indicate the AS core location and incident direction, respectively. Dots and open squares denote scintillation detectors and underground MDs, respectively. The enclosed area by the dashed line indicates the fiducial area of the AS array. (b) Lateral distribution of the photon-like shower event in panel (a). The solid circles and curve show the experimental data and fitting result by the Nishimura-Kamata-Greisen (NKG) function to the data recorded by detectors more than 10 m apart from the AS axis. The dashed curve and open circles are an extrapolation of the NKG function fitting and the unused data within 10 m from the AS axis.

angular resolutions (50% containment) are estimated to be approximately 0.5° and 0.2° for 10 TeV and 100 TeV photon, respectively.

The secondary particles in an air shower deposit energy, which is proportional to ρ, in a scintillator. The ρ at each detecto r is defined as the PMT output charge divided by the single particle peak which is monitored every 20 minutes to correct temperature dependence of each detector gain. The energy of each air shower is reconstructed using the lateral distribution of ρ, above 10 TeV. Figure 4 (b) shows an example of the lateral distribution of ρ. As an energy estimator, we use $S50$[7], which is defined as ρ at a distance of 50 m from the air shower axis in the best-fit Nishimura-Kamata-Greisen (NKG) function. The energy resolutions with $S50$, which depend on air shower core location and zenith angle, are roughly estimated to be 40% at 10 TeV and 20% at 100 TeV. On the other hand, the energy below 10 TeV was estimated directly from $\Sigma\rho$ corresponding to the sum of of the particle density measured by each scintillation detector, as the number of hit detectors is too low to fit $S50$. The absolute energy scale uncertainty is estimated to be 12 % by the westward displacement of the Moon shadow position.

The electromagnetic cascade in the air shower is strongly suppressed by the bremsstrahlung process in the overburden, while muons and a part of hadronic components penetrate into the underground MD array. The number of detected particles at an MD (N_μ) is defined as the output charge divided by the single muon peak which is monitored every 20 minutes. The sum of detected particles in all MDs (ΣN_μ) is used as a parameter to separate between photon and cosmic-ray induced air showers.

An event trigger is issued at any 4-fold coincidence with detectors recording more than 0.6 particles within the area enclosed by the dashed lines in Fig. 4. At air shower energies smaller than 10 TeV, we employ the same selection criteria and estimate the event energy as in the previous work[1], except for the MD selection criterion. At air shower energies greater than 10 TeV, we employ the following event selections: (1) zenith angle of arrival direction (θ) should be $\theta < 40°$; (2) number of available detectors for the air shower reconstruction should be ≥ 16; (3) among 6 detectors recorded with the largest ρ's, 5 should be contained in the fiducial area enclosed by the dashed lines in Fig. 4; (4) $\log(S50)$ should be > -1.2; (5) age parameter (s) in the best-fit NKG function should be $0.3 < s < 1.3$. (6) ΣN_μ should be $\Sigma N_\mu < 0.15(\Sigma\rho)^{2.8}$ or $\Sigma N_\mu < 3.6\times10^{-4}(\Sigma\rho)^{1.4}$, where $\Sigma\rho$ is the sum of particle density measured by the AS array. The MD cut is optimized for photon detection by our MC simulation.

To estimate the background contribution from cosmic rays, we adopt the Equi-Zenith Angle method which is the same as in our previous works [1]. The background counts are estimated from the number of events averaged over 20 off-source bins of the same size as the on-source bin located at the equi-zenith angle. The radius of the on/off-source bin is set to $R_{\rm sw}(\Sigma\rho) = 6.9/\sqrt{\Sigma\rho}$ (deg.). In order to efficiently extract signals in the higher energy region at low background level, the lower limit of $R_{\rm sw}$ is set to 0.5°, which corresponds to $\sim 90\%$ containment of photons above 100 TeV.

To generate air shower events in the atmosphere, Employed are the CORSIKA code v7.4000 with EPOS-LHC for the high-energy hadronic interaction model and FLUKA code v2011.2b for the low-energy hadronic interaction model. The very-high-energy photons at the top of atmosphere are inputted, assuming the power-law spectrum with a differential index -2.9 above 0.3 TeV. The generated secondary particles in an air shower are fed into the detector response simulation for the AS array developed based on the GEANT4 code v4.10.00. The MC simulation for the MD array considering the overburden has been developed based on the GEANT4 code. The electromagnetic and hadronic cascades by the secondary particles in the overburden, as well as the ray tracing of Cherenkov lights emitted in the water cells are simulated by the GEANT4 code. The number of photoelectrons detected in the 20-inch PMT is converted to N_μ referring to the single muon peakin each cell. The muon cut is determined to maximize the figure of merit $N_\gamma^{\rm MC}/\sqrt{N_\gamma^{\rm MC}+N_{\rm CR}^{\rm DATA}}$, where $N_\gamma^{\rm MC}$ and $N_{\rm CR}^{\rm DATA}$ denote the expected number of photons by the MC and the number of background events in the data af-

ter the muon cut. The photon-like events are defined as the remaining events after the muon cut.

2.2. HESS J1849-000

H.E.S.S. detected HESS J1849−000 as a TeV gamma-ray source. The emission in the TeV region is centered around an X-ray pulsar PSR J1849−0001, which is surrounded by a diffuse synchrotron X-ray PWN. The spin period, spin-down luminosity, and characteristic age of PSR J1849−0001 are $P = 38.5\,\mathrm{ms}$, $\dot{E} = 9.8\times10^{36}\,\mathrm{erg\,s^{-1}}$, and $\tau_c = 42.9\,\mathrm{kyr}$, respectively. Considering the positional correlation between the TeV gamma-ray emission and the pulsar, together with the energetic nature of the pulsar, HESS J1849−000 is thought to be the middle-aged PWN which is powered by the pulsar PSR J1849−0001 and is in transition state from a young, synchrotron-dominated phase to an evolved, inverse-Compton dominated phase, in view of the comparison of the energy fluxes of the diffuse keV X-ray and TeV gamma-ray emissions. The differential energy spectrum has a relatively hard index of $\simeq 2$, leading to the detection of nearby gamma-ray sources in the ultra-high energy range by HAWC (eHWC J1850+001 in $E > 56\,\mathrm{TeV}$) and LHAASO (LHAASO J1849−0001 at $E = 100\,\mathrm{TeV}$) [4, 5]. However, the energy spectrum has not been reported in the sub-Pev region.

We plot events, by opening a circular ON-source window with an angular radius of 0.6° centered at HESS J1849−000, $(\alpha, \delta) = (282.^\circ24, -0.^\circ04)$, while we estimate the background by counting number of events in 20 OFF windows, each of which has the same size as the ON-source window, with the equi-zenith angle method. The events in the ON-source and OFF windows are then binned into five logarithmically equal energy bins per decade. After the event selection described in the standard gamma-ray analysis in the previous subsection except for a wider zenith angle range 0-50° than 0-40° in the standard analysis, the detection significance of gamma rays from HESS J1849−000 becomes $4.0\,\sigma$ and $4.4\,\sigma$ levels above 25 TeV and 100 TeV, respectively.

The excess significance maps around the HESS J1849−000 region are shown in Figure 5 above 25 TeV and 100 TeV pixelized by $0.05^\circ \times 0.05^\circ$ pixels. We smooth the maps with the point-spread functions (PSF) of the experiment. In the map above 100 TeV, we found the pixel with the maximum significance, i.e., "the brightest pixel" at $(\alpha, \delta) = (282.^\circ33, 0.^\circ08)$, which is $0.^\circ15$ away from HESS J1849−000. the 68% statistical uncertainty in the brightest pixel's orientation is estimated to be $0.^\circ18$ by a Monte Carlo simulation. The pointing systematics of the experiment along the right ascension and the declination are also estimated to be $0.^\circ058$ and $0.^\circ055$, respectively. Thus, the total center position uncertainty of the observed gamma-ray emission is estimated to be $0.^\circ22$ at 68% C.L. Therefore, the center position of the sub-PeV gamma-ray emission observed by the Tibet ASγ experiment is consistent with that of HESS J1849−000. Meanwhile, the position of HESS J1852−000 deviates by $0.^\circ74$ in angular distance from the brightest pixel, corresponding to $3.0\,\sigma$ significance considering both the uncertainty in the center position of the observed sub-PeV gamma-ray emission ($0.^\circ22$) and the uncertainty in the position of HESS J1852−000. Therefore, the result disfavors

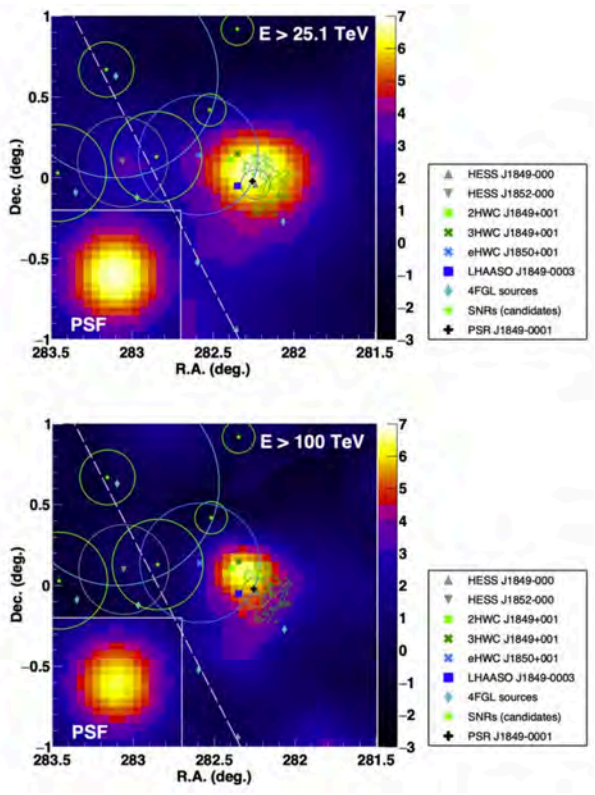


Fig. 5. Figures and captions from Ref.[2], references therein. *Top*: significance map of the HESS J1849−000 region above 25 TeV, pixelized by $0.05^\circ \times 0.05^\circ$ pixels and smoothed with the PSF. The white dashed line indicates the Galactic plane. Positions of nearby celestial objects in the sky region, including galactic SNRs (and the candidates), PSR J1849−0001, and gamma-ray sources, are plotted with symbols as presented in the right legend, and their extensions (if they have) are indicated with circles with the same colors as the symbols. Data on these nearby objects are cited from H.E.S.S., HAWC, LHAASO and Fermi-LAT) and SNRs and PSR J1849−0001. The green contours show the ^{12}CO ($J = 1-0$) line emission which is found near HESS J1849−000 in the analysis of the archive data published by the FUGIN survey. The emission is integrated with the velocity range of $93-100\,\mathrm{km\,s^{-1}}$ and the contour levels are 20, 30, 40, and 50 $\mathrm{K\,km\,s^{-1}}$. The lower-left inset shows the PSF. *Bottom*: significance map above 100 TeV smoothed with the PSF.

HESS J1852−000 as the origin of the observed sub-PeV gamma rays by the Tibet ASγ experiment.

The measured gamma-ray energy spectrum from HESS J1849−000 in an energy range between $40\,\mathrm{TeV} < E < 320\,\mathrm{TeV}$, is shown with the red points in Figure 6. This is the first measurement of gamma-ray energy spectrum from the source in the sub-PeV region. The differential energy flux is calculated only if the detection significance in an energy bin of gamma rays exceeds $2\,\sigma$. Otherwise, the 99% upper limit on the flux is calculated. We can fit the measured energy spectrum, assuming a simple power-law (PL) function with the best-fit parameters, to $\mathrm{d}N/\mathrm{d}E = (2.86\pm1.44)\times 10^{-16}(E/40\,\mathrm{TeV})^{-2.24\pm0.41}\,\mathrm{TeV^{-1}\,cm^{-2}\,s^{-1}}$ with $\chi^2/\mathrm{d.o.f.} = 0.47/3$.

The gamma-ray energy spectrum, together with the previous measurements, can be explained by the leptonic scenario where high-energy electrons accelerated by the PWN of PSR J1849−0001 radiate gamma rays through inverse Comp-

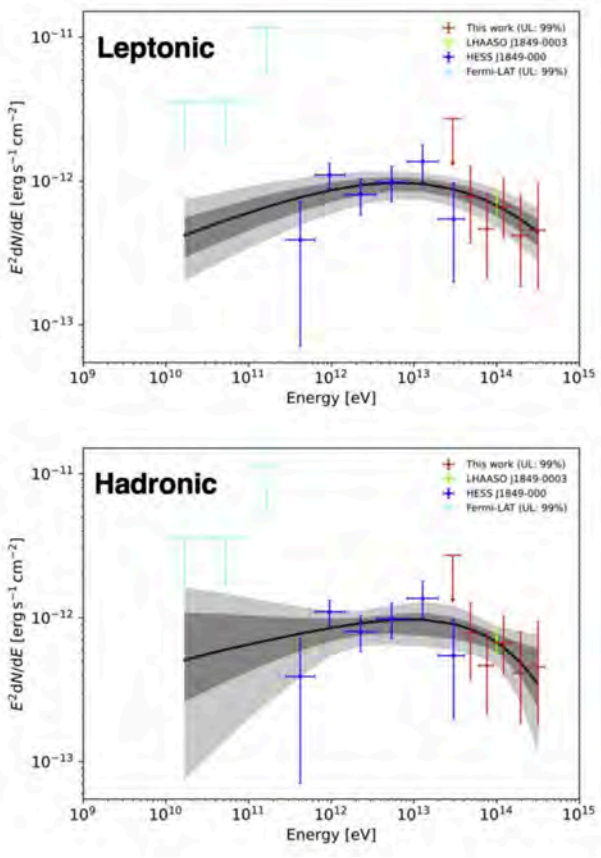


Fig. 6. Figures and captions from Ref.[2], references therein. *Top*: gamma-ray energy spectrum of HESS J1849−000 modeled with the leptonic scenario using Naima. The red data points are the result obtained in this work and the other points are cited from (Fermi-LAT, cyan); (H.E.S.S., blue); (LHAASO, green). The error bars of the data points show $1\,\sigma$ statistical uncertainty and the downward arrows present the 99% upper limits. The black curve shows the best-fit result to the whole spectrum, and the thick and thin gray bands show the $1\,\sigma$ and $2\,\sigma$ confidence intervals of the fit, respectively. *Bottom*: gamma-ray energy spectrum modeled with the hadronic scenario. For detailed descriptions, see Ref.[2].

ton scatterings. However, the scenario requires detailed theoretical modeling other than the one-zone model to explain the compact X-ray nebula around PSR J1849−0001 and the relatively small energy given to the electrons above 100 GeV ($\simeq 2\%$ of the spin-down power of PSR J1849−0001). Meanwhile, we can fit the energy spectrum assuming the hadronic scenario, as a molecular cloud is found in the gamma-ray emitting region. The cutoff energy assuming cosmic-ray protons is estimated to be $\log_{10}(E_{\rm p,cut}/{\rm TeV}) = 3.73^{+2.98}_{-0.66}$, suggesting that cosmic-ray protons are accelerated up to the PeV energy range in HESS J1849−000. As a possible way to explain the characteristics of the various measurements, HESS J1849−000 may be a PWN-SNR composite system. Future observations of gamma rays as well as neutrinos are important to determine the dominant contribution from hadrons or leptons to the observed gamma-ray radiations. We would like to point out that HESS J1849−000 is worth further investigation as one of PeVatron candidates from the theoretical and observational points of view.

For more details on the gamma rays in the 100 TeV region from HESS J1849-000, see [2].

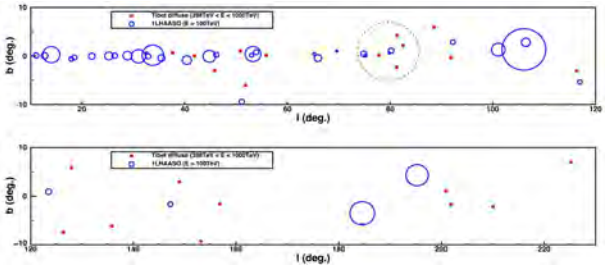


Fig. 7. Figures and captions from Ref.[3], references therein. Incoming directions of the Galactic diffuse gamma-ray events above 398 TeV observed by the Tibet ASγ experiment (red points) and the positions and extensions of the sub-PeV LHAASO sources: the gamma-ray sources detected by LHAASO above 100 TeV (blue circles; [8]) in the Galactic coordinates. The extensions of the sub-PeV LHAASO sources have 95% containment radii assuming a two-dimensional Gaussian morphology. For point-like sources, the 95% upper limits on the extensions are shown. The green dashed circle with a 6° radius encloses the Cygnus region centered at $(l, b) = (79.^\circ62, 0.^\circ96)$, the position of HAWCJ2030 + 409. Note that some of the sub-PeV LHAASO sources have $|b| > 10^\circ$ and thus are not shown in the plot.

2.3. Positional correlation between Tibet Galactic diffuse gamma rays above 398 TeV and 1LHAASO catalog gamma-ray sources above 100 TeV

The Tibet ASγ experiment succeeded in the first detection of sub-PeV Galactic diffuse gamma rays above 100 TeV along on the Galactic disk. The hadronic origin of the Tibet ASγ Galactic diffuse gamma-ray emission (GDE) events is supported by the observation of Galactic neutrinos by IceCube, as the energy spectrum of the Tibet ASγ diffuse gamma rays converted into the neutrino flux assuming the hadronic interaction model smoothly connects at $\simeq 60$ TeV with the all-sky Galactic-neutrino flux in the field of view of the Tibet ASγ experiment.

Surprisingly, there was no overlap between the Tibet ASγ GDE events above 398 TeV with the known TeV sources along the Galactic disk, supporting the diffuse nature of them. Recently, the LHAASO collaboration published their first catalog (1LHAASO catalog) of gamma-ray sources detected in $1\,{\rm TeV} < E < 25\,{\rm TeV}$ and/or $E > 25\,{\rm TeV}$, among which 43 sources are also detected above 100 TeV with more than $4\,\sigma$ detection significance[8]. The detection of the sub-PeV gamma-ray sources in the 1LHAASO catalog provide us with a good chance to investigate how much these sources contribute to the Tibet ASγ GDE events above 398 TeV.

Shown in Figure 7, are the incoming directions of the Tibet ASγ GDE events (red points) above 398 TeV and the positions and extensions of the sub-PeV LHAASO sources (blue circles; [8]). Assuming a two-dimensional Gaussian morphology, we calculate the extensions of 95% containment radii from the published extensions of the 39% containment radii[8]. We show the 95% upper limits on the extensions for point sources.

Astonishingly again, no Tibet ASγ GDE events above 398 TeV have their arrival directions within the extensions of the sub-PeV LHAASO sources. Therfore, none of the sub-PeV LHAASO sources is the origin of the Tibet ASγ GDE events

above 398 TeV. The number of accidental overlaps between the Tibet ASγ GDE events above 398 TeV and the sub-PeV LHAASO sources is estimated to be 0.86, while the expected number of gamma-ray events from the 22 newly-reported sub-PeV LHAASO sources is 1.2. Therefore, it is statistically consistent that there is no overlap between the Tibet ASγ GDE events above 398 TeV and the sub-PeV LHAASO sources. No overlap between the Tibet ASγ GDE events above 398 TeV and the sub-PeV LHAASO sources supports the diffuse nature of the Tibet ASγ GDE events above 398 TeV again.

For more details on this topic, see [3].

3. Other Activities

The emulsion-pouring facilities can meet the demands for making any kind of nuclear emulsion plates which are used for cosmic ray or accelerator experiments. The thermostatic emulsion-processing facilities are operated in order to develop nuclear emulsion plates or X-ray films. Using these facilities, it is also possible to make and develop emulsion pellicle in 600-micron thickness each. In this way, these facilities have been open to all the qualified scientists who want to carry out joint research programs successfully. Of recent, however, the shrinking demand for the facilities let us decide that we should suspend calls for joint research programs to utilize the emulsion-pouring facilities, starting from 2012.

4. Ongoing Research Plans with MD

(1) Chemical composition of primary cosmic rays making the knee in the all-particle energy spectrum

We have measured the energy spectra of primary cosmic-ray protons, helium, all particles around the knee energy region. The main component responsible for making the knee structure in the all particle energy spectrum is heavier nuclei than helium. The next step is to identify the chemical component making the knee in the all particle energy spectrum. We have a plan to install an Yangbajing Air shower Core detector array (YAC) near the center of Tibet III to distinguish the chemical component making the knee. We completed construction of YAC2 (124 detectors over $\sim$500m^2 in area), as is shown in Fig. 8, and started data-taking in 2014. YAC2 aims at mainly studying the energy spectra of proton and helium components in the knee energy region.

(2) Gamma-ray astronomy in the 100 TeV region

For the purpose of detecting high-energy cosmic gamma rays with an air shower array, a large underground muon detecter[9] is very effective to reduce cosmic-ray background. We added a large ($\sim$3,400 m^2) underground water Cherenkov muon detector (Tibet-MD) array under the present Tibet air shower array (Tibet AS $\sim$65,700 m^2). By Tibet AS + MD, we aim at background-free detection of celestial point-source gamma rays around 100 TeV with the world-best sensitivity



Fig. 8. YAC2 set up at Yangbajing.

and at locating the origins (PeVatrons) of cosmic rays accelerated up to the knee (PeV) energy region in the northern sky. The measurement of cut off energies in the energy spectra of such gamma rays in the 100 TeV region may contribute significantly to understanding of the cosmic- ray acceleration limit at the acceleration sites. Above 100 TeV, the angular resolution of Tibet AS with 2-steradian wide field of view is 0.2° and the hadron rejection power of Tibet MD is typically 1/1000 for a point-like source.

Development of Monte Carlo simulation is under way for comparison with real data. Various analysis tools are also extensively being developed.

As is described in the text, we succeeded in the first detection of photons with energies above 100 TeV from Crab in the world, opening a new energy (sub-PeV) window in astronomy. We have also succeeded in detection of gamma rays in the 100 TeV region from G106.3+2.7, Cygnus OB1 and OB2 regions, HESS J1843-033, HESS J1849-000 as well as sub-PeV diffuse gamma rays from the galactic disk. Analyses are under way in search of other sub-PeV gamma-ray sources.

Bibliography

References

[1] "Multi-TeV Gamma-Ray Observation from the Crab Nebula Using the Tibet-III Air Shower Array Finely Tuned by the Cosmic-Ray Moon's Shadow", M. Amenomori *et al.*, Astrophysical Journal, **692** , 61-72 (2009).

[2] "Observation of Gamma Rays up to 320 TeV from the Middle-aged TeV Pulsar Wind Nebula HESS J1849-000", M. Amenomori *et al.*, Astrophy. J. **954**, 200 (2023).

[3] "On the Source Contribution to the Galactic Diffuse Gamma Rays above 398 TeV Detected by the Tibet ASγ Experiment", S. Kato *et al.*, Astrophy. J. **961**, L13 (2024).

[4] A. U. Abeysekara *et al.*, Physical Review Letters, **124**:021102, (2020).

[5] Z. Cao *et al.*, Nature **594** 33 (2021).

[6] "First Detection of Photons with Energies beyond 100 TeV from an Astrophysical Source", M. Amenomori*et al.*, Physical Review Letters, **123** :051101-1-6 (2019).

[7] "Energy determination of gamma-ray induced air showers observed by an extensive air shower array", K. Kawata *et al.*, Experimental Astronomy, **44** 1-9 (2017).

[8] "The First LHAASO Catalog of Gamma-Ray Sources", Z. Cao *et al.*, Astrophy. J. Supplement **271**, 25 (2024).

[9] "Exploration of a 100 TeV gamma-ray northern sky using the Tibet air-shower array combined with an underground water-Cherenkov muon-detector array", T.K. Sako *et al.*, Astroparticle Physics, **32** , 177-184 (2009).

The Tibet ASγ Collaboration, as of 2023

M. Amenomori[1], Y. W. Bao[2], X. J. Bi[3], D. Chen[4], T. L. Chen[5], W. Y. Chen[3], Xu Chen[3,4], Y. Chen[2], Cirennima[5], S. W. Cui[6], Danzengluobu[5], L. K. Ding[3], J. H. Fang[3,7], K. Fang[3], C. F. Feng[8], Zhaoyang Feng[3], Z. Y. Feng[9], Qi Gao[5], Q. B. Gou[3], Y. Q. Guo[3], Y. Y. Guo[3], Y. Hayashi[10], H. H. He[3], Z. T. He[6], K. Hibino[11], N. Hotta[12], Haibing Hu[5], H. B. Hu[3], K. Y. Hu[3,7], J. Huang[3], H. Y. Jia[9], L. Jiang[3], P. Jiang[4], H. B. Jin[4], K. Kasahara[13], Y. Katayose[14], C. Kato[10], S. Kato[15], I. Kawahara[14], T. Kawashima[15], K. Kawata[15], M. Kozai[16], Labaciren[5], G. M. Le[17], A. F. Li[3,9,18], H. J. Li[5], W. J. Li[3,10], Y. Li[4], Y. H. Lin[3,7], B. Liu[19], C. Liu[3], J. S. Liu[3], L. Y. Liu[4], M. Y. Liu[5], W. Liu[3], H. Lu[3], T. Makishima[14], Y. Masuda[10], S. Matsuhashi[14], M. Matsumoto[10], X. R. Meng[5], Y. Meng[3,7], A. Mizuno[15], K. Munakata[10], Y. Nakamura[15], H. Nanjo[1], C. C. Ning[5], M. Nishizawa[20], R. Noguchi[14], M. Ohnishi[15], S. Okukawa[14], S. Ozawa[21], X. Qian[4], X. L. Qian[22], X. B. Qu[23], T. Saito[24], M. Sakata[25], T. Sako[15], T. K. Sako[15], T. Sasaki[11], J. Shao[3,9], T. Shibasaki[26], M. Shibata[14], A. Shiomi[26], H. Sugimoto[27], W. Takano[11], M. Takita[15], Y. H. Tan[3], N. Tateyama[11], S. Torii[28], H. Tsuchiya[29], S. Udo[11], R. Usui[14], H. Wang[3], S. F. Wang[5], Y. P. Wang[5], Wangdui[5], H. R. Wu[3], Q. Wu[5], J. L. Xu[4], L. Xue[8], Z. Yang[3], Y. Q. Yao[4], J. Yin[4], Y. Yokoe[15], Y. L. Yu[3,7], A. F. Yuan[5], L. M. Zhai[4], H. M. Zhang[3], J. L. Zhang[3], X. Zhang[2], X. Y. Zhang[8], Y. Zhang[3], Yi Zhang[30], Ying Zhang[3], S. P. Zhao[3], Zhaxisangzhu[5], X. X. Zhou[9] and Y. H. Zou[3,7]

[1]Department of Physics, Hirosaki University, Hirosaki 036-8561, Japan.
[2]School of Astronomy and Space Science, Nanjing University, Nanjing 210093, China.
[3]Key Laboratory of Particle Astrophysics, Institute of High Energy Physics, Chinese Academy of Sciences, Beijing 100049, China.
[4]National Astronomical Observatories, Chinese Academy of Sciences, Beijing 100012, China.
[5]Department of Mathematics and Physics, Tibet University, Lhasa 850000, China.
[6]Department of Physics, Hebei Normal University, Shijiazhuang 050016, China.
[7]University of Chinese Academy of Sciences, Beijing 100049, China.
[8]Institute of Frontier and Interdisciplinary Science and Key Laboratory of Particle Physics and Particle Irradiation (MOE), Shandong University, Qingdao 266237, China.
[9]Institute of Modern Physics, SouthWest Jiaotong University, Chengdu 610031, China.
[10]Department of Physics, Shinshu University, Matsumoto 390-8621, Japan.
[11]Faculty of Engineering, Kanagawa University, Yokohama 221-8686, Japan.
[12]Faculty of Education, Utsunomiya University, Utsunomiya 321-8505, Japan.
[13]Faculty of Systems Engineering, Shibaura Institute of Technology, Omiya 330-8570, Japan.
[14]Faculty of Engineering, Yokohama National University, Yokohama 240-8501, Japan.
[15]Institute for Cosmic Ray Research, University of Tokyo, Kashiwa 277-8582, Japan.
[16]Polar Environment Data Science Center, Joint Support-Center for Data Science Research, Research Organization of Information and Systems, Tachikawa 190-0014, Japan.
[17]National Center for Space Weather, China Meteorological Administration, Beijing 100081, China.
[18]School of Information Science and Engineering, Shandong Agriculture University, Taian 271018, China.
[19]Department of Astronomy, School of Physical Sciences, University of Science and Technology of China, Hefei 230026, China.
[20]National Institute of Informatics, Tokyo 101-8430, Japan.
[21]National Institute of Information and Communications Technology, Tokyo 184-8795, Japan.
[22]Department of Mechanical and Electrical Engineering, Shangdong Management University, Jinan 250357, China.
[23]College of Science, China University of Petroleum, Qingdao 266555, China.
[24]Tokyo Metropolitan College of Industrial Technology, Tokyo 116-8523, Japan.
[25]Department of Physics, Konan University, Kobe 658-8501, Japan.
[26]College of Industrial Technology, Nihon University, Narashino 275-8575, Japan.
[27]Shonan Institute of Technology, Fujisawa 251-8511, Japan.
[28]Research Institute for Science and Engineering, Waseda University, Tokyo 162-0044, Japan.
[29]Japan Atomic Energy Agency, Tokai-mura 319-1195, Japan.
[30]Key Laboratory of Dark Matter and Space Astronomy, Purple Mountain Observatory, Chinese Academy of Sciences, Nanjing 210034, China.

ALPACA Project

[Spokesperson: M. Takita]
ICRR, The Univ. of Tokyo, Kashiwa, Chiba 277-8582

Cosmic rays are supposed to be accelerated up to the knee energy (PeV) region at supernova remnants (SNRs), star formation regions and PWNe in the Galaxy. Therefore, we naturally expect gamma rays at 100 TeV energies, which originate in π^0 decays produced by the accelerated cosmic rays interacting with matter surrounding the acceleration sites. The gamma-ray emission of electron origin might be highly suppressed above 10 TeV due to rapid decrease of inverse-Compton cross section by the Klein-Nishina effect as well as synchrotron radiation energy loss in the strong magnetic field around the acceleration sites. The detection and spectral measurement of gamma rays in the 100 TeV region from their celestial sources, together with multi-wavelength (radio, X-ray, gamma-ray) observations, will be an important experiment enabling us to discriminate between the two processes (cosmic-ray/electron origins), to locate the acceleration site (PeVatron which accelerate cosmic rays up to PeV energies) of cosmic rays and to verify the standard acceleration model of cosmic rays. Furthermore, diffuse gamma rays from the Fermi bubbles recently reported by the Fermi-LAT group and sub-PeV neutrino events[1] detected by IceCube suggests that the Fermi bubbles be a PeVatron candidate. Similarly, the energy spectrum of diffuse gamma rays from the extended region around the Galactic center marginally measured by HESS up to approximately 10 TeV also strongly indicates existence of PeVatron[2], from which we expect to detect gamma rays at 100 TeV energies. In 2021, the Tibet ASγ experiment succeeded in the first detection of sub-PeV diffuse gamma rays from the Galactic disk. The natural interpretation is that the sub-PeV gamma rays are of cosmic ray origin. Therefore, this is the first experimental evidence that PeVatrons exist in the Galaxy. However, there has been no agreed-upon PeVatron in the northern sky so far. Thus, a wide field-of-view gamma-ray imaging at 100 TeV energies in the southern sky, where the HESS sources[3], the Fermi bubbles and the Galactic center are located within field of view, will be a key experiment.

5. Experiment

The ALPACA[4],[5] (Andes Large area PArticle detector for Cosmic ray physics and Astrophysics) is a cosmic-ray experiment with a large surface air shower array with a large underground muon detector array The experimental site (approximately 500 m$\times$500 m $\sim$250,000 m^2 in total area) is located on a flat high land called Chacaltaya Plateau (4,740 m above sea level, 16°23' S, 68°08' W), as shown in Fig. 1, around Mount Chacaltaya, near La Paz, Bolivia. In some part in this area, our detectors will be constructed.

We plan to set up a 3,600 m^2 underground (approximately one to a few meters) muon detector array (MD) and an 83,000 m^2 air shower array (AS). MD of water Cherenkov type is composed of four pools with each pool (approximately 1 m deep) containing sixteen 56 m^2 unit detectors. AS is made up of 401 1 m^2 plastic scintillation counters at 15 m spacing.

The AS field of view is roughly 2 steradian. The expected angular resolution of AS is approximately 1 degree at 5 TeV and 0.2 degrees around 100 TeV for gamma rays. For 100 TeV gamma rays, the AS energy resolution is estimated to be $\sim$20-25 %. The hadron rejection power of MD is more than 99.9 % at 100 TeV, while keeping most of gamma-ray events. Long-term detector stability, angular resolution, pointing accuracy and energy scale can be calibrated by the cosmic-ray shadow in the Moon as well as by some of the bright stable TeV gamma ray sources in the southern sky.



Fig. 1. From Ref.[4]. Experimental site for the ALPACA experiment, Chacaltaya Plateau (4,740 m above see level, 16°23' S, 68°08' W), near Mount Chacaltaya, in Bolivia.

6. Covered Physics

Our reserch target is divided into four in ALPACA:

1. Measurement of high-energy (5 TeV – 1 PeV) cosmic gamma rays.

2. Measurement of cosmic ray energy spectra around the Knee energy region (100 TeV – 100 PeV).

3. Measurement of cosmic ray anisotropy $>$ 5 TeV at sidereal time frame.

4. Measurement of the Sun shadow in cosmic rays $>$ 5 TeV.

We aim at low-background detection of celestial gamma rays in the 100 TeV region with the world-best sensitivity (an order of magnitude better than any previous/existing experiments) and at locating the origins of cosmic rays accelerated up to the knee energy region in the southern sky. Presuming a Crab-like gamma-ray source extending up with power-law index -2.6 located in the southern sky, the ALPACA experiment is sensitive to the source with $\sim$15 % Crab intensity during one calendar year, as is demonstrated in Fig. 2.

The AS + MD in the southern hemisphere will be a unique/complementary experiment to on-going experiments (FERMI, CALET, DAMPE, HESS, VERITAS, MAGIC, Tibet ASγ, HAWC, LHAASO) and future projects (CTA, SWGO) in this field, which are either located in the northern hemisphere or aiming at gamma-ray astronomy below 10 TeV region, or having narrow field-of-view, or not expected to start operation in the near future (within 5 to 10 years). Thus, the new energy window in the 100 TeV region observing gamma rays with wide field-of-view will be opened first in

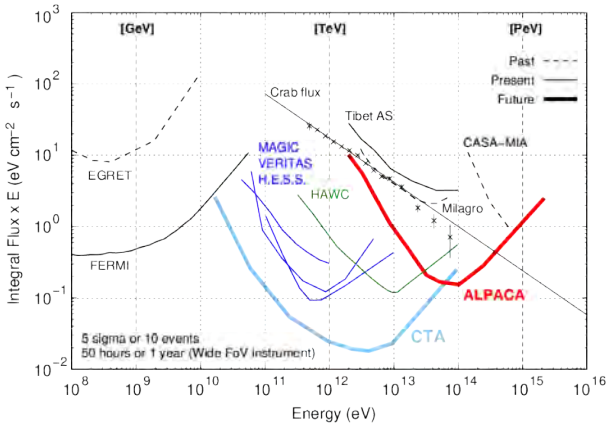


Fig. 2. Sensitivity of ALPACA to high-energy gamma-ray point source. Experimental data points are from HEGRA. The ALPACA sensitivity is evaluated from Ref.[6].

the southern sky by the ALPACA experiment. We expect to detect more than a score of known TeV sources, i.e., young SNRs (SN1006, RX J1713.7-3946, RX J0852.0-4622), Pulsar Wind Nebulae, the Galactic center, etc) in the 100 TeV region, some of which may be cosmic-ray PeVatron candidates. Furthermore, our wide field-of-view sensitivity to diffuse gamma rays allows us to study extremely diffuse gamma-ray sources which are difficult to detect by IACTs. The diffuse gamma rays from the Fermi bubbles recently reported by the Fermi-LAT group may be clearly detected, if they extend up to the 100 TeV region. Similarly, detection of diffuse gamma rays above 100 TeV from extended region from the Galactic center is promising, where the gamma-ray energy spectrum strongly suggests existence of PeVatron. The sub-PeV diffuse gamma rays along the Galactic disk in the southern sky are an interesting target to understand the PeV cosmic-ray propagation in the Galaxy. Detection and spectral measurement of gamma rays in the 100 TeV region from these celestial sources, together with multi-wavelength (radio, X-ray, gamma-ray) observations, are key points enabling us to discriminate between the two processes (cosmic-ray/electron origins), to locate the acceleration site of cosmic rays and to examine the standard acceleration and propagation model of cosmic rays. In astronomical point of view, we will open the ultra-high-energy (above 100 TeV) window in gamma-ray astronomy in the southern sky. Besides, gamma-ray emission from near-by extragalactic sources, e.g. M87, Cen A, gamma rays of dark matter origin, those from the Sun disk recently obseved by HAWC[8] may be interesting subjects.

We also aim at measuring energy spectra of proton, helium and iron components separately around the knee energy region with the new AS + MD. The standard cosmic-ray acceleration model at SNR predicts the knee energy of each nucleus component being proportional to Z (atomic number). We can discriminate proton and iron components by MD, as an iron nucleus produces approximately 2 times more muons than a proton with the same energy. Thus, the cosmic-ray acceleration scenario (SNR shock acceleration) will be verified by observing the linearly Z(atomic number)-dependent knee(=bent) positions of proton, helium, iron components around the knee energy region.

Precise cosmic-ray anisotropy measurement at sidereal time frame in the TeV energy region in the southern sky provides unique data for the community to understand the magnetic field structure in the heliosphere. The ALPACA experiment gives complementary data in the TeV region to those from IceCube above a few tens of TeV.

Furthermore, measurement of the Sun shadow in cosmic rays above the TeV energy region in the southern hemisphere also helps understand the modeling of the magnetic fields between the Sun and the Earth, complementary to the observations in the northern hemisphere.

7. ALPAQUITA

As a proto-type experiment, the ALPAQUITA[7] air shower array which is ∼25 % of the ALPACA air shower array in area has been constructed at the experimental site, Chacaltaya Plateau. The containers including materials and equipments necessary to construct the ALPAQUITA air shower array arrived at La Paz, Bolivia in early 2019. The main infrastructures including electricity, experimental hut, fence, cable guide drains were ready in 2021. Due to COVID19 problems, the construction of ALPAQUITA air shower array in the central part of ALPACA, as shown in a black octagon in Fig. 3 was delayed, but was completed in 2023, as is seen in Fig. 4. We will expand the ALPAQUITA air shower array, as shown in a red octagon in Fig. 3, under which we will add a ∼900-m^2 muon detector array in 2024.

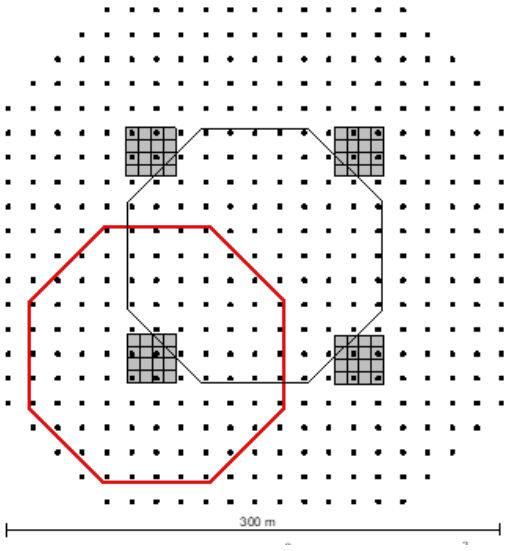


Fig. 3. ALPAQUITA air shower array configuration.



Fig. 4. ALPAQUITA air shower array completed in 2023.

The ALPAQUITA sensitivity to gamma rays from a point source is estimated by a Monte Carlo simulation[7], as is shown in Fig. 5. Even with the ALPAQUI TA air shower array with a 900 m^2 MD, we expect to detect several bright 100 TeV gamma-ray sources.

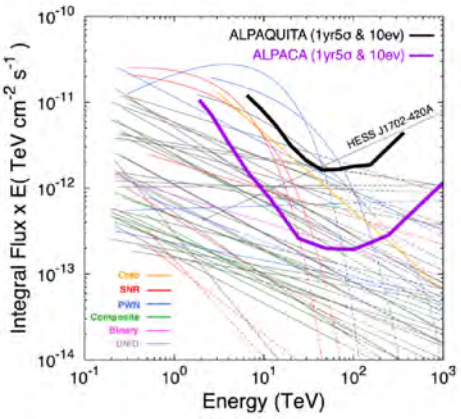


Fig. 5. From [7]. Sensitivity of the ALPAQUITA air shower array with a 900 m^2 MD (black curve) to point-like gamma-ray sources. The measured energy spectra of the H.E.S.S. sources are represented by solid curves, while the dashed curves represent the extrapolations of the measured spectra.

We succeeded in the detection of the Moon shadow in cosmic rays $> 8\ \sigma$ statistical significance with the ALPAQUITA array, as shown in Fig. 6.

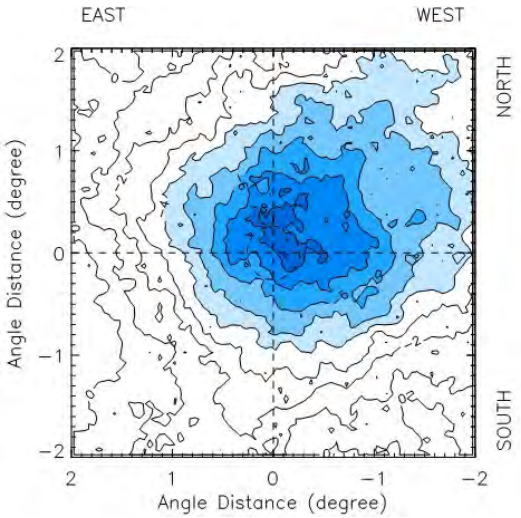


Fig. 6. Moon shadow observed by the ALPAQUITA air shower array. The detection significance is $> 8\ \sigma$, based on the data taken during 225 days from April 2023 to November 2023.

Figure7 shows the number of cumulative deficit events in the Moon shadow as a function of number of recorded cosmic-ray events. The angular resolution is consistent with approximately 1 $^\circ$ for cosmic rays around 5-10 TeV, as is expected by a Monte Carlo simulation.

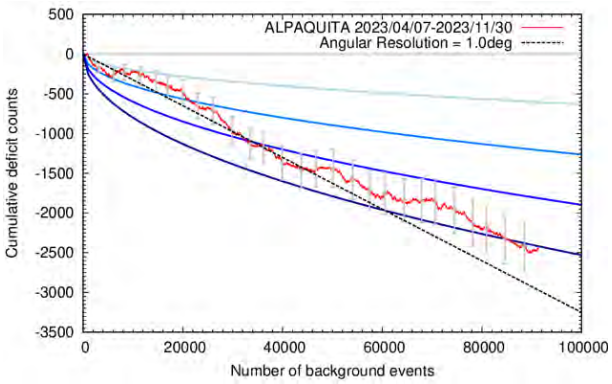


Fig. 7. Number of cumulative deficit events in the Moon shadow observed by the ALPAQUITA air shower array, as a function of number of recorded events, based on the data taken during 225 days from April 2023 to November 2023. The red curve shows the data, while the dashed curve is the expected one assuming the angular resolution of 1 $^\circ$.

8. ALPACA

The budget which affords to construct ALPACA was funded in 2022. We will set up ALPACA, a 3,600 m^2 underground muon detector array (MD) and an 83,000 m^2 air shower array (AS), shown in Fig. 8. MD of water Cherenkov type is composed of four pools with each pool containing sixteen 56 m^2 unit detectors. AS is made up of 401 1 m^2 plastic scintillation counters at 15 m spacing. We will finish construction of ALPACA in 2025.

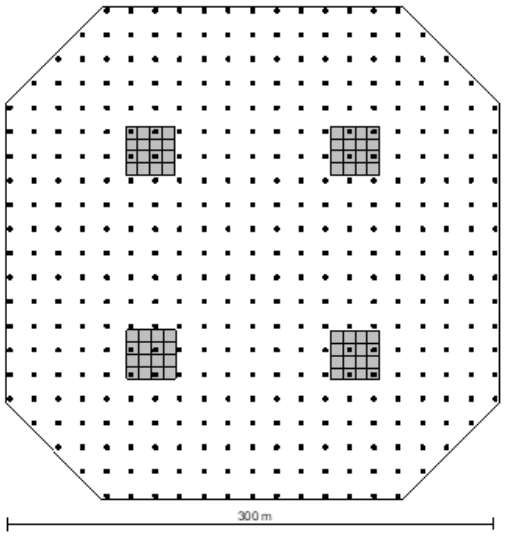


Fig. 8. Schematic view of the ALPACA experiment. The small black squares indicate 401 1 m^2 plastic scintillation detectors at 15 m spacing, forming an air shower array with 83,000 m^2 in area.The black large rectangles indicate four underground muon detector pools, each of which contains sixteen 56 m^2 muon detector units. The total area of the underground muon detector array is 3,600 m^2.

Bibliography

Papers and references

[1] C. Lunardini et al., PRD, **92**, 021301-1-5 (2015).

[2] A. Abramoswski et al., Nature, **531**, 476 (2016).

[3] H. Abdalla et al., A&A **612**, A1 (2018).

[4] M. Takita for the ALPACA Collaboration, THE EUROPEAN PHYSICAL JOURNAL, **145**, 01002-1-3, (2017).

[5] F. Aceves de la Cruz et al. (The ALPACA Collaboration), Proc. of ICRC2021, POS(ICRC2021)733, Online, July 12-23, (2021).

[6] T. K. Sako et al., Astroparticle Physics, **32**, 177 (2009).

[7] S. Kato et al (The ALPACA Collaboration), Experimental Astronomy, **52**, 85-107 (2021).

[8] A. Albert et al. (The HAWC Collaboration), Phys. Rev. Lett., **131**, 051201 (2023).

The ALPACA Collaboration, as of 2023

M. Anzorena[1], D. Blanco[2], E. de la Fuente[3,4], K. Goto[5], Y. Hayashi[6], K. Hibino[7], N. Hotta[8], A. Jimenez-Meza[9], Y. Katayose[10], C. Kato[6], S. Kato[1], I. Kawahara[10], T. Kawashima[1], K. Kawata[1], T. Koi[11], H. Kojima[12], T. Makishima[10], Y. Masuda[6], S. Matsuhashi[10], M. Matsumoto[6], R. Mayta[13,14], P. Miranda[2], A. Mizuno[1], K. Munakata[6], Y. Nakamura[1], C. Nina[2], M. Nishizawa[15], R. Noguchi[10], S. Ogio[1], M. Ohnishi[1], S. Okukawa[10], A. Oshima[5,11], M. Raljevich[2], T. Saito[16], T. Sako[1], T. K. Sako[1], J. Salinas[2], T. Sasaki[7], T. Shibasaki[17], S. Shibata[12], A. Shiomi[17], M. A. Subieta Vasquez[2], N. Tajima[18], W. Takano[7], M. Takita[1], Y. Tameda[19], K. Tanaka[20], R. Ticona[2], I. Toledano-Juarez[21,22], H. Tsuchiya[23], Y. Tsunesada[13,14], S. Udo[7], R. Usui[10], R. I. Winkelmann[2], K. Yamazaki[11] and Y. Yokoe[1]

[1]Institute for Cosmic Ray Research, University of Tokyo, Kashiwa 277-8582, Japan.
[2]Instituto de Investigaciones Físicas, Universidad Mayor de San Andrés, La Paz 8635, Bolivia.
[3]Departamento de Física, CUCEI, Universidad de Guadalajara, Guadalajara, México.
[4]Doctorado en Tecnologías de la Información, CUCEA, Universidad de Guadalajara, Zapopan, México.
[5]College of Engineering, Chubu University, Kasugai 487-8501, Japan.
[6]Department of Physics, Shinshu University, Matsumoto 390-8621, Japan.
[7]Faculty of Engineering, Kanagawa University, Yokohama 221-8686, Japan.
[8]Faculty of Education, Utsunomiya University, Utsunomiya 321-8505, Japan.
[9]Departamento de Tecnologías de la Información, CUCEA, Universidad de Guadalajara, Zapopan, México.
[10]Faculty of Engineering, Yokohama National University, Yokohama 240-8501, Japan.
[11]College of Science and Engineering, Chubu University, Kasugai 487-8501, Japan.
[12]Chubu Innovative Astronomical Observatory, Chubu University, Kasugai 487-8501, Japan.
[13]Graduate School of Science, Osaka Metropolitan University, Osaka 558-8585, Japan.
[14]Nambu Yoichiro Institute for Theoretical and Experimental Physics, Osaka Metropolitan University, Osaka 558-8585, Japan.
[15]National Institute of Informatics, Tokyo 101-8430, Japan.
[16]Tokyo Metropolitan College of Industrial Technology, Tokyo 116-8523, Japan.
[17]College of Industrial Technology, Nihon University, Narashino 275-8575, Japan.
[18]RIKEN, Wako 351-0198, Japan.
[19]Faculty of Engineering, Osaka Electro-Communication University, Neyagawa 572-8530, Japan.
[20]Graduate School of Information Sciences, Hiroshima City University, Hiroshima 731-3194, Japan.
[21]Doctorado en Ciencias Físicas, CUCEI, Universidad de Guadalajara, Guadalajara, México.
[22]Maestría en Ciencia de Datos, Departamento de Métodos Cuantitativos, CUCEA, Universidad de Guadalajara, Zapopan, México.
[23]Japan Atomic Energy Agency, Tokai-mura 319-1195, Japan.

High Energy Astrophysics Group

[Spokesperson: K. Asano]

ICRR, The Univ. of Tokyo, Kashiwa, Chiba 277-8582

Overview

The high energy astrophysics group has been making theoretical studies of violent astrophysical phenomena, in which nonthermal cosmic-ray particles are being accelerated. Targets of the group's study include high energy astrophysical objects such as supernova remnants/explosions, pulsars, pulsar wind nebulae, black hole/neutron star mergers, jets from active galactic nuclei (AGNs), and gamma-ray bursts (GRBs). We especially study the formation of relativistic outflows, particle acceleration in jets, emission mechanisms of electromagnetic waves or neutrinos, and electromagnetic counterparts for compact binary mergers. Our research carries the multi-messenger astronomy forward, which probes astronomical phenomena through collaborating observations of electromagnetic waves, cosmic rays, neutrinos, and gravitational waves.

Research Topic 1: Origin of Cosmic Ray Particles in Clusters of Galaxies with Neutrino and Radio Constraints

A fraction of merging galaxy clusters host diffuse radio emission in their central region, termed a giant radio halo

(GRH). The most promising mechanism of GRHs is the reacceleration of nonthermal electrons and positrons by merger-induced turbulence. However, the origin of these seed leptons has been under debate, and either protons or electrons can be primarily accelerated particles.

We demonstrate that neutrinos can be used as a probe of physical processes in galaxy clusters and discuss possible constraints on the number of relativistic protons in the intracluster medium with the existing upper limits by IceCube. We calculate radio and neutrino emission from massive ($M > 10^{14} M_{\odot}$) galaxy clusters using our cluster population model. This model is compatible with the observed statistics of GRHs, and we find that the contribution of GRHs to the isotropic radio background observed with the ARCADE-2 experiment should be subdominant.

Our fiducial model predicts the allsky neutrino flux that is consistent with IceCube's upper limit from the stacking analysis. We also show that the neutrino upper limit gives meaningful constraints on the parameter space of the reacceleration model, such as the electron-to-proton ratio of the primary cosmic rays and the magnetic field; in particular, the secondary scenario, where the seed electrons mostly originate from inelastic pp collisions, can be constrained even in the presence of reacceleration.

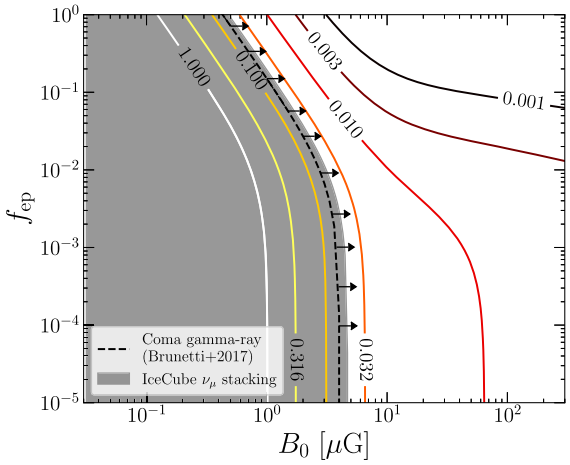


Fig. 1. Constraints on the electron-to-proton ratio of the primary cosmic rays $f_{\rm ep}$ in clusters of galaxies and the central magnetic field B_0. The shaded region is excluded from the neutrino upper limit by IceCube. The contour shows the fractional contribution to the all-sky neutrino intensity. The dashed line with arrows shows the minimum value of B_0 for the Coma cluster constrained by the Fermi-LAT upper limit in the reacceleration model.

Recent radio observations with the Low Frequency Array (LOFAR) discovered diffuse emission extending beyond the scale of classical radio halos. The presence of such megahalos indicates that the amplification of the magnetic field and acceleration of relativistic particles are working in the cluster outskirts, presumably due to the combination of shocks and turbulence that dissipate energy in these regions. Cosmological magnetohydrodynamical (MHD) simulations of galaxy clusters suggest that solenoidal turbulence has a significant energy budget in the outskirts of galaxy clusters.

We explore the possibility that this turbulence contributes to the emission observed in megahalos through second-order Fermi acceleration of relativistic particles and magnetic field amplification by the dynamo. We focus on the case of A2255 and find that this scenario can explain the basic properties of the diffuse emission component that is observed under assumptions that are used in previous literature.

More specifically, we conduct a numerical follow-up, solving the Fokker–Planck equation by using a snapshot of an MHD simulation and deducing the synchrotron brightness integrated along the lines of sight. We find that a volume-filling emission, ranging between 30% and almost 100% of the projected area, depending on our assumptions on the particle diffusion and transport, can be detected at LOFAR sensitivities. Assuming a magnetic field $B \sim 0.2$ μG, as derived from a dynamo model applied to the emitting region, we find that the observed brightness can be matched when $\sim 1\%$ of the solenoidal turbulent energy flux is channeled into particle acceleration.

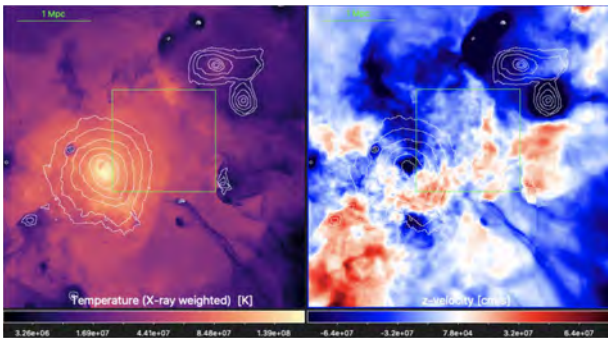


Fig. 2. Snapshot of the MHD simulation of galaxy clusters with megahalo: the X-ray-weighted gas temperature along the line of sight (left) and of the gas velocity along the line of sight (right).

Research Topic 2: Jets in Galaxy Clusters

Non-radiating protons in the radio lobes play an essential role in shaping the jet morphology, as demonstrated in recent radio and X-ray observations. However, since protons and electrons are not always in energy equilibrium due to weak Coulomb coupling, it is difficult to estimate the energy contribution of protons for the inflation of radio lobes.

We performe two-temperature three-dimensional MHD simulations of sub-relativistic jets in the galaxy cluster, while varying the jet magnetization parameters. Because the energy partition rate between electrons and protons in shock and turbulence is determined by plasma kinetic scale physics, our global simulations include electron instantaneous heating subgrid models for shock waves and turbulence.

We find that most of the bulk kinetic energy of the jet is converted into the thermal energy of protons through both shocks and turbulence. Thus, protons are energetically dominant. Meanwhile, thermal electrons stored in the lobe evolve toward energy equipartition with magnetic energy through turbulent dissipation. We further estimated the radio power and the mechanical jet power of radio lobes following the same method used for radio and X-ray observations, then we compared these powers with that of the observed radio jets. The

two-temperature model quantitatively explains the radiatively inefficient radio cavities, but it cannot reproduce the radiatively efficient cavity, even for strongly magnetized jets. This implies that a significant population of pair-plasma is needed to explain radiatively efficient radio cavities.

We construct mock X-ray maps of simulated jets from various viewing angles. Furthermore, we evaluate the shock Mach number from the density-temperature jump using the same method of X-ray observations.

Our results demonstrate that measurements from the density jump significantly underestimate the Mach numbers around the jet head at a low viewing angle. The observed post-shock temperature is strongly reduced by the projection effect, as our jet is in the cluster center where the gas density is high. On the other hand, the temperature jump is almost at unity, even if thermal electrons are in instant equilibration with protons. Upon comparison, we find that the shock property of our model is in good agreement with the results of Cygnus A observations.

Our simulations illustrate the importance of the projection effect in estimating the Mach number from the surface brightness profile. Furthermore, forward shock Mach numbers could serve as a useful probe for determining viewing angles for young, powerful radio jets.

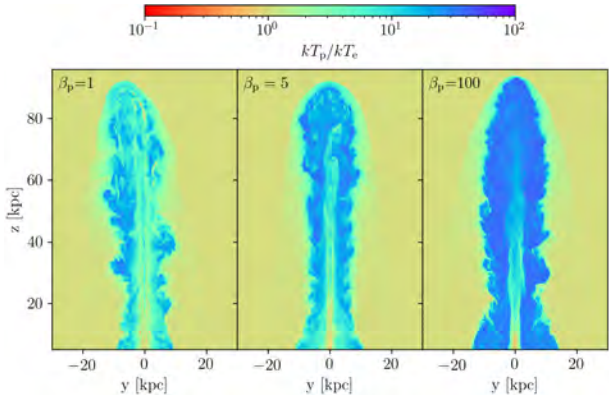


Fig. 3. Ratio of proton to electron temperature distributions of the jet with different values of proton plasma beta (β_p) propagating in a galaxy cluster.

We also simulate a jet–wind interaction in a galaxy cluster and the radio to gamma-ray and neutrino emissions from this "head–tail galaxy." Our simulation follows the evolution of CR particle spectra with energy losses and stochastic turbulence acceleration. We find that the reacceleration is essential to explaining the observed radio properties of head–tail galaxies, in which the radio flux and spectral index do not drastically change. Our models suggest that hard X-ray emissions can be detected around the head–tail galaxy in the Perseus cluster by hard X-ray satellites, such as FORCE, and they will potentially constrain the acceleration efficiency.

We also explore the origin of the collimated synchrotron threads, which have been found in some head–tail galaxies by recent high-quality radio observations. Thin and elongated flux tubes, connecting the two tails, are formed by strong backflows at an early phase. We find that these threads advect with the wind for over 300 Myr without disruption. The radio flux from the flux tubes is much lower than the typical observed flux. An efficient CR diffusion process along the flux tubes, however, may solve this discrepancy.

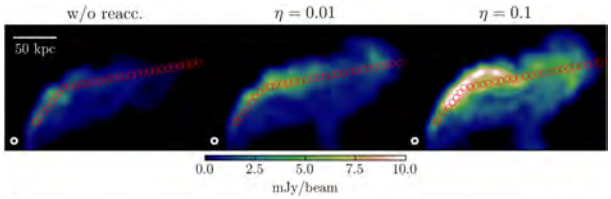


Fig. 4. 300 MHz radio maps of our simulated head-tail galaxies with different reacceleration efficiency η.

Research Topic 3: Dynamical Energy Dissipation of Relativistic Magnetic Bullets

To demonstrate the magnetic energy dissipation via relativistic shocks, we carry out spherically symmetrical one-dimensional special relativistic MHD simulations of highly magnetized outflows with an adaptive mesh refinement method. We first investigate the details of the dynamical energy dissipation via interaction between a single ejecta and an external medium. The energy dissipation timescales, which affect the early behavior of the afterglow emission in gamma-ray bursts, are estimated for a wide range of magnetization.

In addition, we demonstrate the internal shock dissipation in multiple interactions between magnetically dominated relativistic ejecta and kinetically dominated non-relativistic winds. Our numerical results show that ~ 10 percent of the magnetic energy in the ejecta can be converted into the thermal energy of the relativistic and low-magnetized outflows via shocks in the rarefaction waves or the winds. Such hot and less magnetized outflows are relevant for observed non-thermal emissions in blazars or gamma-ray bursts.

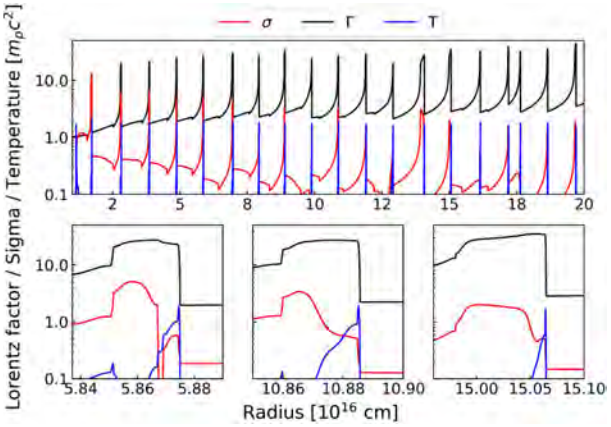


Fig. 5. A snapshot of our simulations for internal shock dissipation of magnetic bullets. The radial profile of the temperature T, Lorentz factor Γ, and magnetization σ are shown. The lower panels show zoom-ups for three characteristic regions.

Research Topic 4: Gamma-Ray Emission from Reverse Shock in GRB 180720B

GRBs are powered by collimated streams of plasma (jets) ejected by a newborn stellar-mass black hole or neutron star at relativistic velocities. Their short-lived (typically tens of seconds) prompt γ-ray emission from within the ejecta is followed by long-lived multi-wavelength afterglow emission from the ultra-relativistic forward shock. This shock is driven into the circumburst medium by the GRB ejecta. which are in turn decelerated by a mildly relativistic reverse shock. Forward-shock emission was recently detected as teraelectronvolt-energy γ-rays.

Such very high energy emission was also predicted from the reverse shock. We contribute to the interpretation of optical and gigaelectronvolt-energy γ-ray emission from GRB 180720B during the first few hundred seconds, which is explained by synchrotron and inverse-Compton emission from the reverse shock propagating into the ejecta, implying a low-magnetization ejecta.

The optical measurements show a clear transition from the reverse shock to the forward shock driven into the circumburst medium, accompanied by a 90-degree change in the mean polarization angle and fluctuations in the polarization degree and angle. This indicates turbulence with large-scale toroidal and radially stretched magnetic-field structures in the reverse and forward shocks, respectively, which tightly couple to the physics of relativistic shocks and GRB jets, namely launching, composition, dissipation and particle acceleration.

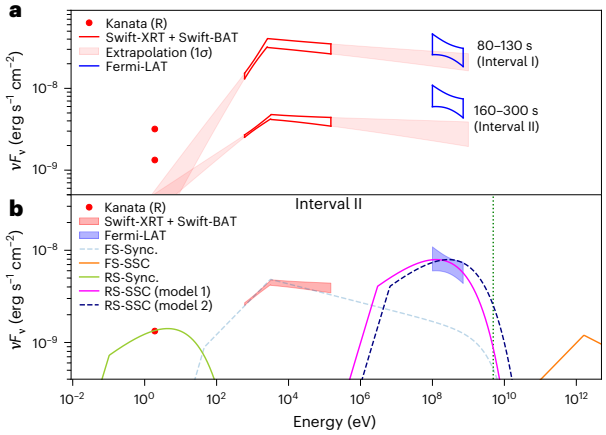


Fig. 6. Photon spectra (upper) and our modeling (lower) for the forward and reverse shock emissions in GRB 180720B.

Research Topic 5: General Relativistic Radiative Transfer Code

We develop a general relativistic radiative transfer code RAIKOU for multiwavelength studies of spectra and images including the black hole shadows around Kerr black holes. Important radiative processes in hot plasmas around black holes, i.e., (cyclo-)synchrotron, bremsstrahlung emission/absorption, and Compton/inverse-Compton scattering, are incorporated. The Maxwell–Jüttner and single/broken power-law electron distribution functions are implemented to calculate the radiative transfer via both thermal and nonthermal electrons.

Two calculation algorithms are implemented for studies of the images and broadband spectra. An observer-to-emitter ray-tracing algorithm, which inversely solves the radiative transfer equation from the observer screen to emitting plasmas, is suitable for efficient calculations of the images, e.g., the black hole shadows observed by the Event Horizon Telescope, and spectra without Compton effects. On the other hand, an emitter-to-observer Monte Carlo algorithm, by which photons are transported with a Monte Carlo method including the effects of Compton/inverse-Compton scatterings, enables us to compute multiwavelength spectra, with their energy bands broadly ranging from radio to very high energy gamma-ray.

The X-ray black hole shadows, which are formed via synchrotron emission and inverse-Compton scattering processes and will be observed in future X-ray interferometry missions, can be also computed with this algorithm. The code is generally applicable to accretion flows around Kerr black holes with relativistic jets and winds/coronae with various mass accretion rates (i.e., radiatively inefficient accretion flows, super-Eddington accretion flows, and others). We demonstrate an application of the code to a radiatively inefficient accretion flow onto a supermassive black hole.

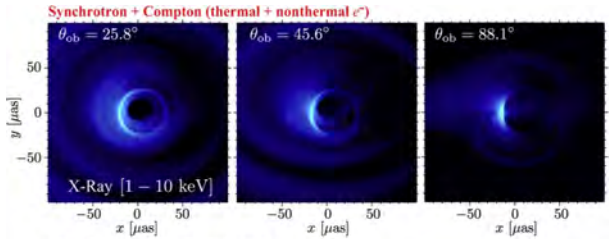


Fig. 7. Log-scale X-ray images of black hole shadow produced by our RAIKOU code.

Research Topic 6: VLBI Observations of Supermassive Black Holes and Jets

We also join VLBI observation campaigns to contribute to their theoretical interpretations.

We study the Galactic Center supermassive black hole (SMBH), Sagittarius A*, with the KVN and VERA Array (KaVA)/East Asian VLBI Network (EAVN) monitoring observations. Especially on 13 May 2019, Sgr A* experienced an unprecedented bright near infra-red (NIR) flare; so, we find a possible counterpart at 43 GHz. As a result, a large temporal variation of the flux density at the level $\sim 15.4\%$, with the highest flux density of 2.04 Jy, is found on 11 May 2019. Interestingly, the intrinsic sizes are also variable, and the area and major-axis size show a marginal correlation with flux density with $>\sim 2\sigma$.

Thus, we interpret that the emission region at 43 GHz follows the larger-when-brighter relation in 2019. The possible origins are discussed with the emergence of a weak jet/outflow component and the position angle change of the rotation axis of the accretion disk in time.

We also observe the nearby radio galaxy M87, which offers a unique opportunity to explore the connections between the central supermassive black hole and relativistic jets. Previous studies of the inner region of M87 revealed a wide opening angle for the jet originating near the black hole. The

Event Horizon Telescope resolved the central radio source and found an asymmetric ring structure consistent with expectations from general relativity. With a baseline of 17 years of observations, there was a shift in the jet's transverse position, possibly arising from an 8-to-10-year quasi-periodicity.

However, the origin of this sideways shift remains unclear. Our analysis of radio observations over 22 years suggests a period of about 11 years for the variation in the position angle of the jet. We infer that we are seeing a spinning black hole that induces the Lense–Thirring precession of a misaligned accretion disk. Similar jet precession may commonly occur in other active galactic nuclei but has been challenging to detect owing to the small magnitude and long period of the variation.

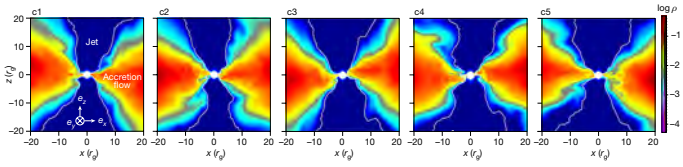


Fig. 8. Snapshots of mass density of our GRMHD simulation results for the M87 precession.

Research Topic 7: Role of Cosmic Rays in the History of the Milky Way

We study the long-term evolution of the Milky Way (MW) over cosmic time by modeling the star formation, cosmic rays, metallicity, stellar dynamics, outflows, and inflows of the galactic system to obtain various insights into the galactic evolution. The mass accretion is modeled by the results of cosmological N-body simulations for the cold dark matter. We find that the star formation rate is about half the mass accretion rate of the disk, given the consistency between observed Galactic diffuse X-ray emissions (GDXEs) and possible conditions driving the Galactic wind. Our model simultaneously reproduces the quantities of star formation rate, cosmic rays, metals, and the rotation curve of the current MW. The most important predictions of the model are that there is an unidentified accretion flow with a possible number density of $\sim 10^{-2}$ cm^{-3} and that part of the GDXEs originates from a hot, diffuse plasma which is formed by consuming about $\sim 10\%$ of supernova explosion energy. The latter is the science case for future X-ray missions: XRISM, Athena, and so on. We also discuss further implications of our results for the planet formation and observations of external galaxies in terms of multi-messenger astronomy.

Research Topic 8: CALET Project

We have joined CALET, CALorimetric Electron Telescope, which is a mission for the Japanese Experiment Module-Exposed Facility (JEM-EF) on the International Space Station. The CALET mission aims at revealing unsolved problems in high energy phenomena of the Universe by carrying out accurate measurements of high energy spectra of electrons, gamma-rays and nuclei.

Figure 10 shows the cosmic-ray Helium spectrum measured with CALET. The measured spectrum shows evidence of a deviation of the flux from a single power law by more

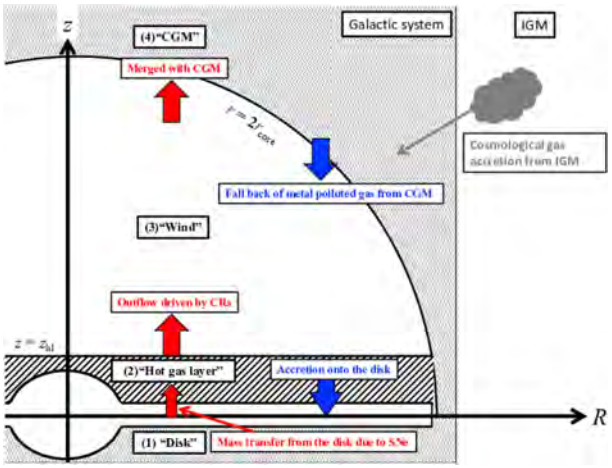


Fig. 9. Schematic illustration of our Milky Way evolution model.

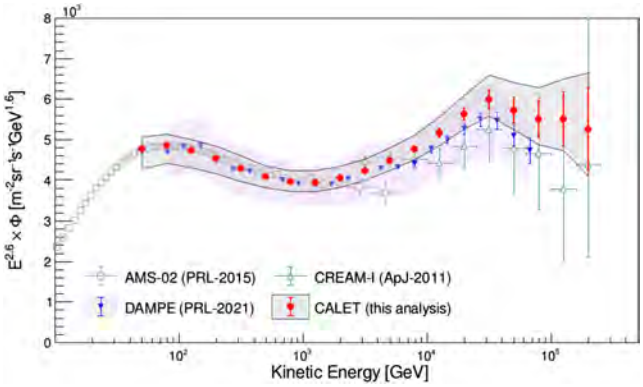


Fig. 10. Helium spectrum measured by CALET (red circles).

than 8σ with a progressive spectral hardening from a few hundred GeV to a few tens of TeV. This result is consistent with the data reported by space instruments including PAMELA, AMS-02, and DAMPE and balloon instruments including CREAM. At higher energy, we report the onset of a softening of the helium spectrum around 30 TeV (total kinetic energy). Though affected by large uncertainties in the highest energy bins, the observation of a flux reduction turns out to be consistent with the most recent results of DAMPE. A double broken power law is found to fit simultaneously both spectral features: the hardening (at lower energy) and the softening (at higher energy).

We also report the measurement of cosmic-ray electrons and positrons from 10.6 GeV to 7.5 TeV from over 7 years of observations. The observed energy spectrum becomes gradually harder in the lower energy region from around 30 GeV, consistently with AMS-02, but from 300 to 600 GeV it is considerably softer than the spectra measured by DAMPE and Fermi-LAT. At high energies, the spectrum presents a sharp break around 1 TeV, with a spectral index change from -3.15 to -3.91, and a broken power law fitting the data in the energy range from 30 GeV to 4.8 TeV better than a single power law with 6.9 sigma significance, which is compatible with the DAMPE results. The break is consistent with the expected

effects of radiation loss during the propagation from distant sources (except the highest energy bin). We have fitted the spectrum with a model consistent with the positron flux measured by AMS-02 below 1 TeV and interpreted the electron + positron spectrum with possible contributions from pulsars and nearby sources. Above 4.8 TeV, a possible contribution from known nearby supernova remnants, including Vela, is addressed by an event-by-event analysis providing a higher proton-rejection power than a purely statistical analysis.

Bibliography

Papers in refereed journals

1. Ataru Tanikawa, Kohei Hattori, Norita Kawanaka, Tomoya Kinugawa, Minori Shikauchi, Daichi Tsuna "Search for a Black Hole Binary in Gaia DR3 Astrometric Binary Stars with Spectroscopic Data", Astrophys. J., 946, 79(11pp) (2023).

2. X. Cheng, I. Cho, T. Kawashima, et al. "Monitoring the Size and Flux Density of Sgr A during the Active State in 2019 with East Asian VLBI Network", Galaxies, 11, 46(15pp) (2023).

3. R.-S. Lu, K. Asada, T. P. Krichbaum, et al. "A Ring-like Accretion Structure in M87 Connecting its Black Hole and Jet", Nature, 616, 686-690 (2023).

4. O. Adriani, Y. Akaike, K. Asano, et al. "Direct Measurement of the Cosmic-Ray Helium Spectrum from 40 GeV to 250 TeV with the Calorimetric Electron Telescope on the International Space Station", Phys. Rev. Lett., 130, 171002(8pp) (2023).

5. O. Adriani, Y. Akaike, K. Asano, et al. "Charge-Sign Dependent Cosmic-Ray Modulation Observed with the Calorimetric Electron Telescope on the International Space Station", Phys. Rev. Lett., 130, 211001(6pp) (2023). Erratum: Phys. Rev. Lett., 131, 109902(E)(2pp)

6. S. Abe, A. Aguasca-Cabot, I. Agudo, N. Alvarez Crespo, L. A. Antonelli, C. Aramo, A. Arbet-Engels, M. Artero, K. Asano, et al. "Multiwavelength Study of the Galactic PeVatron Candidate LHAASO J2108+5157", Astron. Astrophys., 673, A75(16pp) (2023).

7. H. Ro, M. Kino, B.-W. Sohn, et al. "Spectral Analysis of a Parsec-Scale Jet in M87: Observational Constraint on the Magnetic Field Strengths in the Jet", Astron. Astrophys., 673, A159(16pp) (2023).

8. Tomohisa Kawashima, Ken Ohsuga, Hiroyuki R. Takahashi "RAIKOU: A General Relativistic, Multiwavelength Radiative Transfer Code", Astrophys. J., 949, 101(30pp) (2023).

9. H. Abe, S. Abe, V. A. Acciari, et al. "Multimessenger Characterization of Markarian 501 during Historically Low X-Ray and γ-Ray Activity", Astrophys. J. Sup., 266, 37(43pp) (2023).

10. B. S. Prather, J. Dexter, M. Moscibrodzka, et al. "Comparison of Polarized Radiative Transfer Codes Used by the EHT Collaboration", Astrophys. J., 950, 35(23pp) (2023).

11. Takumi Ohmura, Katsuaki Asano, Kosuke Nishiwaki, Mami Machida, Haruka Sakemi "Nonthermal Emissions from a Head-Tail Radio Galaxy in 3D Magnetohydrodynamic Simulations", Astrophys. J, 951, 76(12pp) (2023).

12. F. Acero, A. Acharyya, R. Adam, et al. "Sensitivity of the Cherenkov Telescope Array to Spectral Signatures of Hadronic PeVatrons with Application to Galactic Supernova Remnants", Astropart. Phys., 150, 102850(28pp) (2023).

13. A. Acharyya, R. Adam, A. Aguasca-Cabot, et al. "Sensitivity of the Cherenkov Telescope Array to TeV Photon Emission from the Large Magellanic Cloud", Mon. Not. Roy. Astro. Soc., 523, 5353-5387 (2023).

14. Kosuke Nishiwaki, Katsuaki Asano, Kohta Murase "High-Energy Neutrino Constraints on Cosmic-Ray Reacceleration in Radio Halos of Massive Galaxy Clusters", Astrophys. J, 954, 188(9pp) (2023).

15. Y. Cui, K. Hada, T. Kawashima, et al. "Precessing Jet Nozzle Connecting to a Spinning Black Hole in M87", Nature, 621, 711-715 (2023).

16. Shogo B. Kobayashi, Hirofumi Noda, Teruaki Enoto, Tomohisa Kawashima, Akihiro Inoue, Ken Ohsuga "Decomposing the Spectrum of Ultraluminous X-Ray Pulsar NGC 300 ULX-1", Astrophys. J, 955, 124(21pp) (2023).

17. H. Abe, K. Abe, S. Abe, et al. "Observations of the Crab Nebula and Pulsar with the Large-Sized Telescope Prototype of the Cherenkov Telescope Array", Astrophys. J., 956, 80(25pp) (2023).

18. K. Akiyama, A. Alberdi, W. Alef, et al. "First M87 Event Horizon Telescope Results. IX. Detection of Near-horizon Circular Polarization", Astrophys. J. Lett., 957, L20(42pp) (2023).

19. O. Adriani, Y. Akaike, K. Asano, et al. "Direct Measurement of the Spectral Structure of Cosmic-Ray Electrons + Positrons in the TeV Region with CALET on the International Space Station", Phys. Rev. Lett., 131, 191001(7pp) (2023).

20. Yo Kusafuka, Katsuaki Asano, Takumi Ohmura, Tomohisa Kawashima "Dynamical Energy Dissipation of Relativistic Magnetic Bullets", Mon. Not. Roy. Astro. Soc., 526, 512-522 (2023).

21. K. Abe, S. Abe, A. Aguasca-Cabot, et al. "Star Tracking for Pointing Determination of Imaging Atmospheric Cherenkov Telescopes", Astron. Astrophys., 679, A90(12pp) (2023).

22. Takumi Ohmura, Mami Machida "Simulations of Two-Temperature Jets in Galaxy Clusters – I. Effect of Jet Magnetization on Dynamics and Electron Heating", Astron. Astrophys., 679, A160(19pp) (2023).

23. Takumi Ohmura, Mami Machida, Hiroki Akamatsu "Simulations of two-temperature jets in galaxy clusters – II. X-Ray Properties of the Forward Shock", Astron. Astrophys., 679, A161(15pp) (2023).

24. P. Torne, K. Liu, R. P. Eatough, et al. "A Search for Pulsars around Sgr A* in the First Event Horizon Telescope Data Set", Astrophys. J., 959, 14(27pp) (2023).

25. H. Abe, K. Abe, S. Abe, et al. "Performance of the Joint LST-1 and MAGIC Observations Evaluated with Crab Nebula Data", Astron. Astrophys., 680, A66(21pp) (2023).

26. Kosuke Nishiwaki, Gianfranco Brunetti, Franco Vazza, Claudio Gheller "Efficiency of Turbulent Reacceleration by Solenoidal Turbulence and its Application to the Origin of Radio Megahalos in Cluster Outskirts", Astrophys. J., 961, 15(12pp) (2024).

27. H. Abe, S. Abe, V. A. Acciari, et al. "MAGIC detection of GRB 201216C at $z = 1.1$", Mon. Not. Roy. Astro. Soc., 527, 5856-5867 (2024).

28. M. Arimoto, K. Asano, K. S. Kawabata, et al. "Gamma Rays from a Reverse Shock with Turbulent Magnetic Fields in GRB 180720B", Nature Astron., 8, 134-144 (2024).

29. K. Akiyama, A. Alberdi, W. Alef, et al. "The Persistent Shadow of the Supermassive Black Hole of M 87 . Observations, Calibration, Imaging, and Analysis", Astron. Astrophys., 681, A79(63pp) (2024).

30. Jiro Shimoda, Shu-ichiro Inutsuka, Masahiro Nagashima "The History of the Milky Way: The Evolution of Star Formation, Cosmic Rays, Metallicity, and Stellar Dynamics over Cosmic Time", Pub. Astron. Soc. J., 76, 81-97 (2024).

31. H. Abe, S. Abe, V. A. Acciari, et al. "Multi-Year Characterisation of the Broad-Band Emission from the Intermittent Extreme BL Lac 1ES 2344+514", Astron. Astrophys., 682, A114(26pp) (2024).

32. G. F. Paraschos, J.-Y. Kim, M. Wielgus, et al. "Ordered Magnetic Fields around the 3C 84 Central Black Hole", Astron. Astrophys., 682, L3(15pp) (2024).

Other Activities

Ashra NTA

[Spokesperson : M. Sasaki]

Collaboration list:
ICRR, The University of Tokyo, Chiba, Japan: **M. Sasaki, T. Aoki**; Physics Department, Toho University, Chiba, Japan: **S. Ogawa**; Academia Sinica, Taipei, Taiwan: **S. Haino**; Institute for Interdisciplinary Science, Okayama University, Okayama, Japan: **K. Yoshimura**; IPNS, KEK, Ibaraki, Japan: **M. Tanaka**; et al.

VHE Physics and Astronomy

Probing for VHE elementary particles will enable the discovery of VHE celestial objects and the elucidation of their phenomena. VHE neutrinos and photons can also probe super heavy dark matter and dark energy. Neutrino oscillations cause neutrino fluxes to homogenize between generations during propagation. VHE tau neutrinos skim the earth, are converted to tau, and after decaying in air become an upward air shower at a shallow elevation angle, emitting Cherenkov light and fluorescence. Thus, the tau neutrino observation can necessarily be a clear-cut tau appearance experiment. Also VHE muon neutrinos skim the earth emit photons producing air showers in the air. The NTA unit is a unique wide-angle, high-precision optical system with a light-branching trigger imaging system. It is particularly powerful for the simultaneous observation of Cherenkov light and fluorescence from VHE tau, muon, and photons.

NTA for VHE Tau, Muon, and Photon Probes

NTA will radially observe air-shower light in a vast amount of night-time air on the mountain within more than π sr field of view (FoV) covered with 1 minute square pixels (Fig.11) [1]. Tau (muon) neutrinos that skim the earth or hit mountains are converted to tau (muon) in rocks. The tau decays (muon-radiated photons) then generate a quasi-horizontal air shower. The tau (muon) shower signal appeared from the earth or the mountains is very clear and there are almost no background events. Downward coming photon showers are observed in both Cherenkov and fluorescence light. The Cherenkov light coming from a large zenith angle earns a large effective detection area. The lookout layout allows Cherenkov and fluorescence observations over a wide energy range. Fluorescence arriving from behind is advantageous for low-energy tau showers compared to Cherenkovs, which require more distance to achieve a large effective area due to their directional nature. The X_{max} of the fluorescent air shower is about 1 km from the detector, which is sufficient to detect 1-PeV class tau. Muons with long decay lengths have a high probability of appearing at low energies, and this layout allows them to be observed efficiently. These are the advantages of NTA's lookout layout.

The geo-propagation of tau by GEANT and ALLM simulations revealed emergent tau remembers the tau neutrino direction above 1 PeV with much better than 1 minute of accuracy. We also confirmed shower reconstruction with CORSIKA simulation, resulting in the point-back resolution of $0.1^\circ/\sqrt{E_{sh}/PeV}$ where E_{sh} is the shower energy. The emergent tau energy is deformed from the parent tau neutrino energy due to the inelastic nature of the charge current interaction and energy loss in the rock. It still allows for a relatively good energy reconstruction of ν_τ with the energy around 1 PeV. The energy resolution of tau neutrino was confirmed by

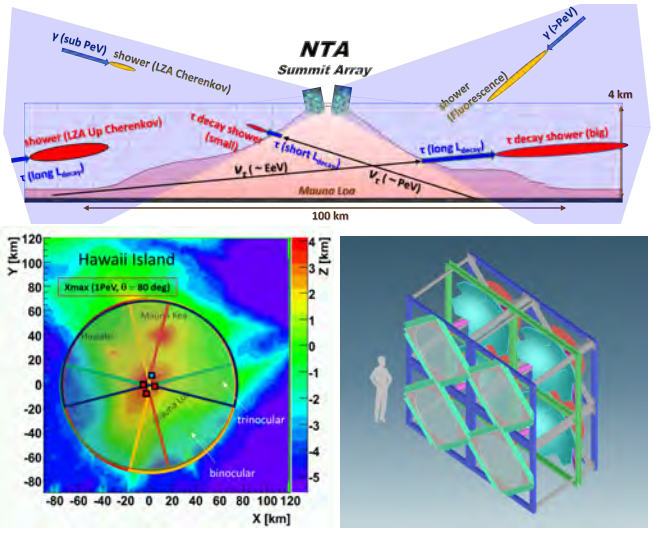


Fig. 11. Schematics of "lookout layout" for imaging tau, muon, and photon showers with NTA [1] (*top*). Contour map of the island of Hawaii (*left*) as input for the MC simulation. The radius of the wheel represents the distance to Xmax of the 1PeV shower coming toward NTA at 80° zenith. One of four stations on the mountainside is responsible for 210° azimuth range indicated by four fans. The basic design is a 1.5-fold scaled-up version of the Ashra-1 light collector, and four of these collectors are stacked together to form one NTA detector unit with the same FoV (*right*).

ANIS simulations to be 20∼40% around 1 PeV depending on the elevation.

The NTA's field of view can always cover the Galactic bulge in the southern night sky. The NTA detector unit's FoV center should be aligned with this arc, considering a high multi-eye observation ratio. NTA Galactic bulge monitor with viewing radius of 20° has a good advantage of including 12 % of total mass of the dark matter halo, assuming the Einasto profile. The effective detection area of the surface detector decreases rapidly depending on the cosine of the zenith angle. In the case of a surface detector at 16.4° south latitude and a 45° zenith angle cut, the observation time must be less than 2300 hours per year even if 100 % duty cycle. In the case of the NTA, the galactic center is in the moonless night sky for 980 hours per year, a ratio of only 2.3 to the surface detector above.

NTA proto-project, Ashra-1, was placed in 2008 at the north side (Fig.11 *left*). It allows for binocular and trinocular observation, resulting in a high multi-eye observation rate. The basic design is a 1.5-fold scaled-up version of the Ashra-1 light collector, and four of these collectors are stacked together to form one NTA detector unit with the same FoV (Fig.11 *right*). The effective pupil diameter is 3 m, providing good light gathering power. It can also facilitate background air-shower muon rejection, transport and construction.

Fig.12 compares the NTA annual exposure map to that by one light collector of Ashra-1, which searched for mountain-hitting tau and muon from Mauna Loa to Mauna Kea for 14 months (Obs03). The sensitivity of NTA to search for vast neutrino sources can be seen. Notably, NTA is able to search for tau and mu neutrinos in the central region of the Galaxy for several hundreds hours per year, as well as throughout the extra-galactic region.

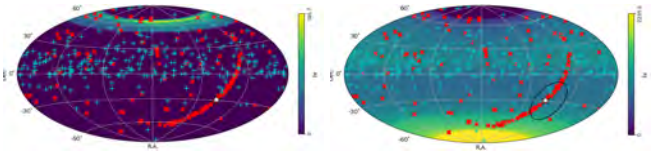


Fig. 12. Ashra-1 exposure time map for Cherenkov taus and muons in Obs03 with one light collector toward Mauna Kea (<186 hr) (*left*). NTA annual exposure time map for neutrinos (<2240 hr) (*right*). Red, light blue crosses, and white asterisk indicate the location of the Gamma Catalog objects [2], the IceCube Gold Bronze Tracks [3], and the Galactic center, respectively.

NTA Diffuse Neutrino Sensitivity

Fig.13 shows a comparison of diffuse neutrino sensitivity from various VHE neutrino detectors. NTA has the best sensitivity from a few PeV to 100 PeV. NTA is also capable of reliably confirming with high precision the PeV cosmic neutrino sources suggested by IceCube. Trinity observes Earth skimming neu-tau as well as NTA but only with Cherenkov light. The sensitivity of its higher energy part is determined by the large zenith angle shower, which is consistent with NTA. The NTA sensitivity at lower energy is superior to that of Trinity due to the tau and mu air-shower light observed near the mountain surface as mentioned.

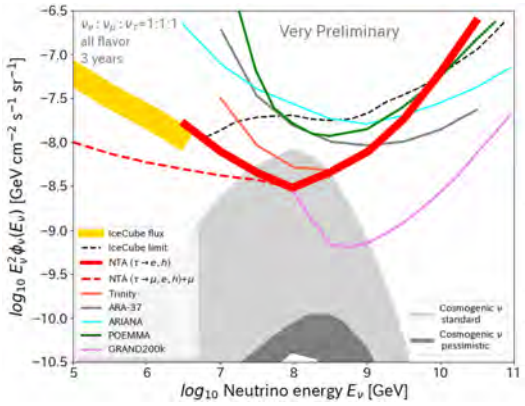


Fig. 13. A comparison of diffuse neutrino sensitivity from various VHE neutrino detectors. NTA tau and muon neutrino detection has the best sensitivity from a few PeV to 100 PeV [4]-[13].

NTA Dark Matter Sensitivity

As shown Fig.14, NTA's powerful wide-angle view of air-shower morphology from tau and photons with high precision shows that it has unparalleled sensitivity to neutrinos and photons from annihilation and decay of super heavy dark matter WIMP particles, especially near the unitarity bound.

Conclusions

Simultaneous wide-field, high-precision observations of Cherenkov and fluorescence showers from both tau, mu, and photon probes by NTA are strongly expected to be a key to VHE physics and VHE astronomy using multiple particles.

Bibliography

[1] NTA LOI (look-in layout array), M. Sasaki and G. W.-S. Hou,ArXiv:1408.6244 (2014). NTA look-out layout summit array, M. Sasaki, PoS (ICRC2017) 941. M. Sasaki, ICHEP2022.

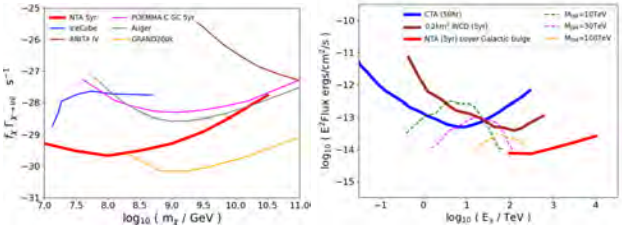


Fig. 14. 5-year sensitivities of NTA to DM decay width ($f_\chi \Gamma_\chi$) for $\nu\bar{\nu}$ channels and those of other experiments. NTA has the highest sensitivity in the 10 PeV to sub-EeV region (*left*). Figure adapted from [14]. Flux sensitivities of NTA for 5 yr, of a possible 2D observatory (0.2 km^2 WCD) for 5 yr and of CTA for 50 hr observation of the Galactic halo. The predicted DM annihilation rates into τ pairs are indicated. Figure is adopted from [15].

[2] https://github.com/gammapy/gamma-cat

[3] https://gcn.gsfc.nasa.gov/amon_icecube_gold_bronze_events.html

[4] J. Álvarez-Muñiz,et al.,Mechanics and Astronomy 63, 219501 (2019).

[5] J. F. Krizmanic,et al.,UHECR2018 (Paris).

[6] C. R. Persichilli,Thesis,Univ. California (2018).

[7] P. Allison,et al.,Phys. Rev. D93, 082003 (2016).

[8] R. A. Batista,et al.,J. Cosmol. Astropart. Phys.,01,002,(2019).

[9] M. Aartsen,et al.,Phys. Rev. D98,062003 (2018).

[10] A. Aab,et al.,arXiv:1708.06592.

[11] P. Gorham,et al.,arXiv:1902.04005.

[12] A. M. Otte,Phys. Rev. D99, 083012 (2019).

[13] M. Sasaki,PoS (ICRC2019) 1003.

[14] C. Guépin, et al., arXiv:2112.04801.

[15] A. Viana, et al., Astro2020 Science White Paper.

ASTROPHYSICS AND GRAVITY DIVISION

Overview

Astrophysics and Gravity Division consists of Gravitational Wave Group, The Observational Cosmology Group, Primary Cosmic Ray Group and Theory Group.

The Gravitational Wave Group conducts experimental research of gravitational waves with researchers of gravitational wave experiments and theory in Japan. The main items are the construction of the large-scale cryogenic interferometer (KAGRA) at Kamioka underground and the operation of CLIO. For this purpose, KAGRA observatory was established at the beginning of the fiscal year of 2016 to assist the construction of KAGRA gravitational wave telescope.

The Observational Cosmology Group studies cosmic history based on deep multi-wavelength observations in collaboration with worldwide researchers. This group has started a new optical deep survey project with the wide-field imager of Hyper Suprime-Cam mounted on the Subaru telescope.

Theory Group conducts both theoretical studies of the Universe and astroparticle physics.

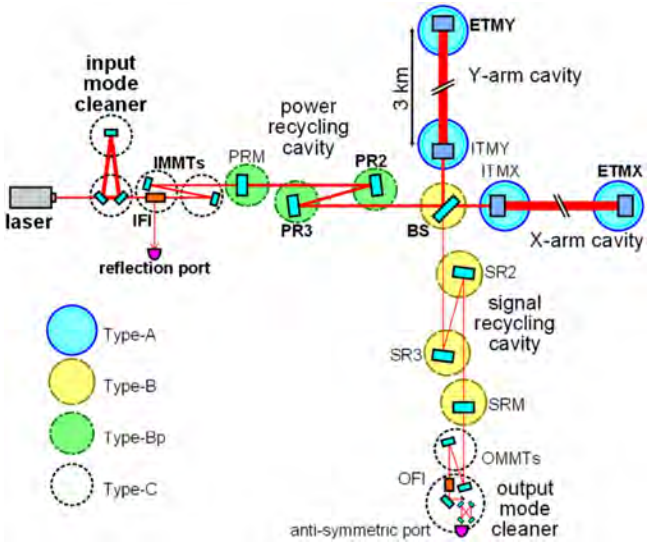


Fig. 1. Schematic view of the bKAGRA interferometer[3]. Type-A, Type-B, Type-Bp, and Type-C are the names of vibration isolation systems for each mirror.

Gravitational Wave Group

KAGRA Project Status

[Spokesperson : Takashi UCHIYAMA]
ICRR, The Univ. of Tokyo, Hida, Gifu 506-1205

Overview

KAGRA, Large-scale Cryogenic Gravitational wave Telescope, aims at detecting gravitational waves and developing gravitational wave astronomy, which was established by the first detection of gravitational waves by LIGO. KAGRA employs a 3 km L-shaped laser interferometer with a cryogenic mirror system placed underground at Kamioka[1]. The KAGRA development is divided into two stages: the initial KAGRA (iKAGRA) and baseline KAGRA (bKAGRA). The iKAGRA interferometer is a simple Michelson interferometer with a 2-Watt laser, room-temperature mirrors, and a simple vibration isolation system. We completed the iKAGRA interferometer with a test run in April 2016[2]. Then we proceeded to bKAGRA.

Figures 1 and 2 show a schematic view of the optical layout of the bKAGRA interferometer and the KAGRA vibration isolation systems. Table 1 shows the design parameter of the bKAGRA interferometer[3]. The bKAGRA interferometer will employ a Resonant Sideband Extraction (RSE) interferometer with a 180-Watt laser, cryogenic Sapphire mirrors, and several kinds of vibration isolation systems. The bKAGRA interferometer should attain a sensitivity high enough for the detection of gravitational waves with the help of the high-power laser and RSE interferometer to reduce the quantum noise, the cryogenic Sapphire mirrors to reduce the thermal noise, and the vibration isolation systems to reduce the seismic noise. Figure 3 shows designed sensitivities of bKAGRA in the cases of Broadband RSE (BRSE) and of Detuned RSE (DRSE), where the incoherent sum of the fundamental noise sources is assumed. The observation range for an inspiral and merger of neutron-star binary reaches 135 Mpc in BRSE and 153 Mpc in DRSE with the same definition of the observation range as LIGO and Virgo.

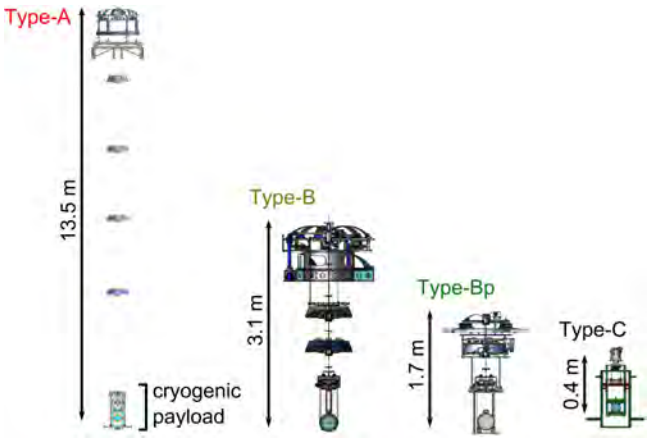


Fig. 2. KAGRA vibration isolation systems[3]. KAGRA equips four kinds of vibration isolation systems as Type-A, Type-B, Type-Bp, and Type-C.

The KAGRA observatory signed the three documents between LIGO and VIRGO in order to realize international joint

Table 1. The design parameters of the bKAGRA interferometer[3]

Arm cavity length	3000 m	Test mass size	ϕ22 cm × 15 cm
Laser wave length	1064 nm	Mass of test mass	22.8 kg
Input power at PRM	67W	Temperature of test mass	22 K
Arm intra-cavity power	340 kW	Beam radius at test mass	3.5 cm
ITM transmittance	0.4 %	PRC/SRC lengths	66.6 m
PRM transmittance	10 %	Detuning angle	3.5 deg
SRM transmittance	15 %	Homodyne angle	135.1 deg

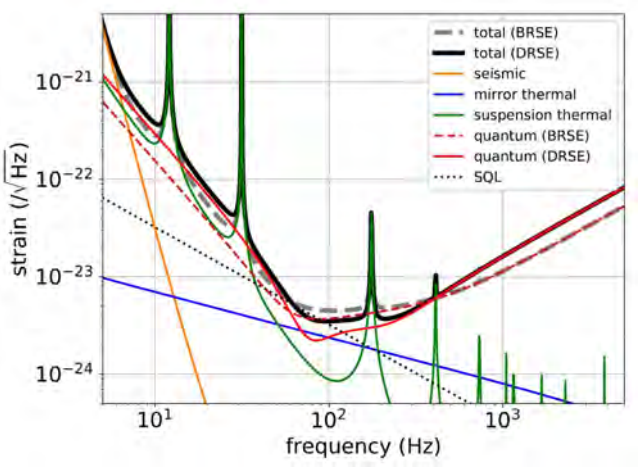


Fig. 3. The designed sensitivity of the bKAGRA interferometer[3]. "total", "seismic", "mirror thermal", "suspension thermal", "quantum", and "SQL" mean total sum of fundamental noise sources shown in this figure, seismic noise including gravity gradient noise, mirror thermal noise, suspension thermal noise, quantum noise, and standard quantum limit, respectively. The figure shows "total" and "quantum noise" in both Broadband RSE (BRSE) and Detuned RSE (DRSE) cases. The observation range for an in-spiral and merger of neutron-star binary reaches 135 Mpc in BRSE and 153 Mpc in DRSE with the same definition of the observation range as LIGO and Virgo.

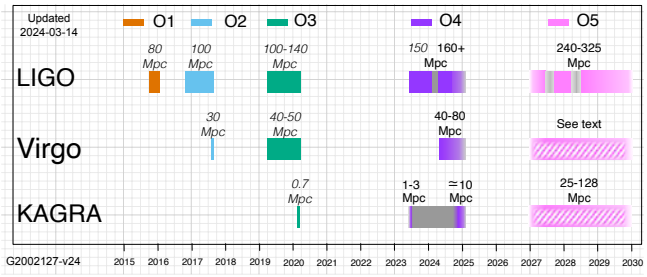


Fig. 4. International observation scenario[7]. The next international collaborative observation called O4 has already started on May 24, 2023. O4 will last 20 months including up to 2 months of commissioning breaks for maintenance. KAGRA performed the observation from May 24 to June 21, 2023, and resumed commissioning works. KAGRA will rejoin the observation the next year.

observation on October 4, 2019. The documents are the Memorandum of Agreement between VIRGO, KAGRA, and LIGO (main part)[4], Memorandum of Agreement between VIRGO, KAGRA, and LIGO (Attachment A)[5], and Letter of Intent for KAGRA to Join the O3 Run[6]. On the same day, the KAGRA observatory held a completion ceremony.

Figure 4 shows the international collaborative observation scenario[7] as of February 15, 2024. LIGO conducted Observation 1 (O1) from September 12, 2015, to January 19, 2016, and Observation 2 (O2) from November 30, 2016, to August 25, 2017. Virgo joined O2 on August 1, 2017. LIGO and Virgo started Observation 3 (O3) on April 1, 2019. Initially, O3 was planned to continue until the end of April 2020, but it was suspended on March 27, 2020, due to the influence of COVID-19[8]. After the finish of O3, KAGRA conducted the first international joint observation run with GEO600 from April 7 to 21, 2020. This observation called O3GK is regarded as an official joint observation with GEO600 by LIGO, VIRGO, and KAGRA. During O3GK, the observation range of almost 0.7 Mpc and the duty factor of 53 % were achieved.

The current international collaborative observation called O4 started on March 24, 2023, and it will last June 9, 2025[7]. KAGRA performed the observation from May 24 to June 21, 2023, and resumed commissioning works. During this observation run, the observation range of almost 1.3 Mpc and the duty factor of 80 % were achieved. KAGRA will rejoin the observation in 2025. The detail of the observation performed in O4 is explained in the section "Observation". The detail of commissioning works after the observation is explained in the section "Commissioning".

In FY2023, two large earthquakes occurred in Noto Penishura which is 100 km North of KAGRA. The first earthquake occurred on May 5, 2023. The magnitude of this earthquake was 6.5. KAGRA lost alignments of all the mirrors in vacuum chambers due to this earthquake. Fortunately, we could recover the alignments remotely without venting vacuum chambers and started the observing run on May 24.

The second large earthquake occurred on January 1, 2024. The magnitude of this earthquake was 7.6. The vibration levels on the surface around the KAGRA site and the underground KAGRA site were 5 minus and 3, respectively. The vibration levels were the largest in Hida city, Gifu prefecture in 100 Year. Fortunately, no blackouts, no fire accidents, no vacuum leakages occurred, and normal operations of the cryogenic systems and the vacuum pumping systems were kept. We noticed, however, that 10 mirror suspension systems showed malfunctions. Many magnets on mirrors were dropped. Undesired touching in suspension systems happened. Alignments of mirrors were lost. Finally, We decided to open all the vacuum chambers to repair the suspension sys-

tems and to recover the interferometer. The recovery works are still ongoing in June.

The rapidly progressing status of KAGRA was presented in many international conferences. Many papers about the progress of KAGRA were also published [11], [12], [13], [14]. We also presented activities on our web page.[15]

Bibliography

[1] "KAGRA: 2.5 generation interferometric gravitational wave detector", KAGRA collaboration, Nature Astronomy, Vol. 3, January 2019, 35-40

[2] "Construction of KAGRA: an underground gravitational-wave observatory", KAGRA collaboration, Prog. Theor. Exp. Phys. 2018, 013F01 (2018)

[3] "First cryogenic test operation of underground km-scale gravitational-wave observatory KAGRA", KAGRA collaboration, Class. Quantum Grav. 36 165008 (2019)

[4] https://gwdoc.icrr.u-tokyo.ac.jp/cgi-bin/DocDB/ShowDocument?docid=10663

[5] https://gwdoc.icrr.u-tokyo.ac.jp/cgi-bin/DocDB/ShowDocument?docid=10664

[6] https://gwdoc.icrr.u-tokyo.ac.jp/cgi-bin/DocDB/ShowDocument?docid=10813

[7] https://observing.docs.ligo.org/plan/

[8] https://www.ligo.caltech.edu/news/ligo20200326

[9] "First joint observation by the underground gravitational-wave detector KAGRA with GEO 600", The LIGO Scientific Collaboration, the Virgo Collaboration, and the KAGRA Collaboration, Prog. Theor. Exp. Phys. 2022 063F01(37 pages)

[10] "Performance of the KAGRA detector during the first joint observation with GEO 600 (O3GK)", The KAGRA Collaboration, Progress of Theoretical and Experimental Physics, 2022;, ptac093

[11] "Search for gravitational-lensing signatures in the full third observing run of the LIGO-Virgo network", The LIGO Scientific Collaboration, the Virgo Collaboration, the KAGRA Collaboration, Accepted by APJ

[12] "A Joint Fermi-GBM and Swift-BAT Analysis of Gravitational-Wave Events from the GWTC-3 Catalog", C. Fletcher et al, 2024 APJ 964 149 (2024)

[13] "Overview of KAGRA: Data Transfer and Management", T Akutsu et al, Progress of Theoretical and Experimental Physics, Volume 2023, Issue 10, October (2023)

[14] "Status of the underground gravitational wave detector KAGRA", the KAGRA Collaboration, PoS TAUP2023 (2024) 116

[15] http://gwcenter.icrr.u-tokyo.ac.jp/en/

Observation

[Spokesperson : Takahiro SAWADA]

ICRR, The Univ. of Tokyo, Hida, Gifu 506-1205

The LIGO-Virgo-KAGRA (LVK) collaboration's fourth observing run, known as O4, commenced on May 24, 2023 (Dates thereafter are in Coordinated Universal Time), and lasts around 24 months, including a nearly 3-month period of the break for upgrade and maintenance tasks. O4 is divided into two phases: O4a, which concluded in January 2024, and O4b, which will continue from April 2024 to June 2025. During O4a, the LIGO detectors in Hanford, Washington, and Livingston, Louisiana, operated with increased sensitivity, achieving around 30 % improvement compared to previous runs. This heightened sensitivity allows the detectors to observe a larger fraction of the universe and detect gravitational-wave signals more frequently, potentially identifying a merger every two or three days. KAGRA joined the observations from May 24 to June 20, 2023, achieving a duty factor of approximately 80 %, a significant improvement from the 53 % recorded during the O3GK run, and average binary neutron star (BNS) range of approximately 1.3 Mpc, nearly double the range from O3GK, due to advancements in noise reduction techniques.[1] In the second phase, O4b, the LIGO, and Virgo interferometers have been conducting observations. KAGRA hopes to rejoin the observations in early 2025 after completing necessary upgrades and recovery from a significant earthquake.[2]

Rapid Response Team During the observing run period, the Rapid Response Team (RRT) within the LVK collaboration plays a crucial role in the immediate validation of gravitational wave detection candidates and the timely issuance of alerts during observing runs. The team is divided into three regions across different time zones, each covering 8- or 4-hour shifts and ensures that it operates 24/7 for continuous monitoring and rapid response to detected gravitational-wave candidate events. A first preliminary alert is issued immediately after detection, followed by initial alerts after human vetting processes and update alerts as it becomes available. First preliminary alerts are typically issued within one minute from the gravitational- waves reaching Earth for binary black hole (BBH) mergers events, and with negative latency before the gravitational waves reach Earth for BNS mergers. This rapid response capability is essential for capturing transient astronomical phenomena through multi-messenger follow-up observations, deepening our understanding of the universe. During O3, the RRT consists of commissioning, computing, and calibration experts from each of the detector sites, pipeline experts, detector characterization experts, and follow-up advocates. During O4, the RRT operations are supported by the volunteer efforts of a much larger group of people in the LVK Collaboration. This success of RRT exemplifies the power of huge and international scientific collaboration. [3, 4]

Bibliography

[1] "Current status of cryogenic interferometric gravitational wave telescope KAGRA", K. Komori, JPS March

Meeting (2024).

[2] "LIGO, VIRGO AND KAGRA OBSERVING RUN PLANS", https://observing.docs.ligo.org/plan/

[3] "O4: Rapid Response to S230518h", LIGO Magazine issue 23, 9/2023

[4] "LIGO/Virgo/KAGRA Public Alerts User Guide", https://emfollow.docs.ligo.org/userguide/

Commissioning

[Spokesperson : Takafumi USHIBA]

ICRR, The Univ. of Tokyo, Hida, Gifu 506-1205

In FY2023, the commissioning phase can be divided into two phases: pre-O4a (before 15:00 UTC on 24 May) and post-O4a (after 23:00 UTC on 20 June). In the pre-O4a commissioning phase, the commissioning task was mainly focused on improving the stability of the interferometer and achieving the sensitivity better than 1 Mpc. In the post-O4a commissioning phase, the task was mainly focused on achieving the sensitivity better than 10 Mpc.

Pre-O4a commissioning One of the tasks in the pre-O4a commissioning is to tweak the mirror angles to find the good alignment for the main interferometer. The alignment of the Input Mode Matching Telescopes (IMMTs) and the Power Recycling (PR) mirrors are being optimized, and Beam Position Control (BPC) has been implemented on PR2 (the second PR mirror), improving the sensitivity by a factor of 2 and achieving the sensitivity of more than 1 Mpc.

The other task in the pre-O4a commissioning is to optimize the Alignment Sensing and Control (ASC) by using Wave Front Sensors (WFS). Before the O4a, ASCs to ETMX, ETMY, and BS were engaged by using REFL and AS WFSs, which greatly improves a stability of PRFPMI. Also, ASC to Output Mode Matching Telescope (OMMT) was implemented by using beacon signals to improve the alignment to Output Mode Cleaner (OMC), which also played an important role to make the interferometer stable.

Post-O4a commissioning The first important task in the post-O4a commissioning is to create a noise budget to understand the limiting noise sources of the current sensitivity. Thanks to the experience of noise budget generation after O3GK (the third international observing run with GEO600), a noise budget could be created in a short time and the limiting noise sources of the KAGRA sensitivity during the O4a run could be well understood: ITMX, ETMX, BS, and SR3 local control noise and Power Recycling Michelson Interferometer (PRMI) control noise at low frequencies, acoustic coupling at middle frequencies, and residual laser frequency noise, shot noise, and PD dark noise at high frequencies were limiting the sensitivity. This new noise budget is now prepared for publications.

To improve the low frequency sensitivity, the suspension local damping control update and further optimization of the ASC were performed. For the local damping control update, narrowband damping controls were implemented in ITMX and ETMX, which improved the control noise above 10 Hz by a factor of 10. BS and SR3 local damping controls were also optimized, reducing control noise by more than a factor of 10. In addition to the suspension local damping control update, ASCs with WFS have been updated from O4a. ITMX and ETMX WFS controls have been changed to differential HARD and SOFT modes. In addition, the remaining two DoFs have been controlled by QPD signals that monitor the beam axes of the arm transmission beams.

To improve the middle frequency sensitivity, several beam dumps were installed in the OMC vacuum tank, since scattered light from the ghost beam is considered to be the main cause of the large acoustic coupling noise. In addition, vibration analysis around the OMC vacuum tank was performed to understand the coupling from OMC vibration to sensitivity.

To improve the high frequency sensitivity, lock trial with higher power was tested. Since the limiting noises at high frequency were shot noise and PD dark noise, higher laser power would improve the sensitivity. PRFPMI could be locked by using RF signals with a laser power of 5 W, which was 1.2 W during O4a. This high power operation also helped to improve the low frequency sensitivity because PRMI control noise can be reduced. Unfortunately, the above commissioning effect for the sensitivity improvement haven't been confirmed with full configuration because of the damage of the suspensions due to the 2024 Noto Peninsula Earthquake, the effect of the commissioning to KAGRA sensitivity will be soon confirmed.

Input and Output Optics

[Spokesperson : Kenta Tanaka]

ICRR, The Univ. of Tokyo, Hida, Gifu 506-1205

The input and output optics (IOO) of KAGRA consist of the pre-stabilization laser (PSL), auxiliary locking system (ALS), input optics chain, and output optics chain. PSL includes the intensity stabilization system (ISS), the pre-mode cleaner (PMC), and the modulation system for the main interferometer. ALS includes the phase-locking system for the green beam each for X and Y arms, the fiber system, and the locking system for the arm cavities. The input optics chain includes the input mode cleaner (IMC), the input Faraday isolator (IFI), and two input mode matching telescopes (MMT). The output optics chain includes the output mode matching telescopes (OMT), the output Faraday isolator (OFI), and the output mode cleaner (OMC).

During O4a, the IMC duty cycle, which is the ratio between the time IMC operated and the whole observation time exceeded 98%. This value is slightly higher than the duty cycle in the O3GK observation even though the whole observation time in O4 was double longer than that of O3GK thanks to alignment control implementation for IMC after O3GK in FY2022.

After the O4a, we estimated the noise budget for the sensitivity during O4a. The dark current noise of the PD used for gravitational wave detection on the transmitted light side of the OMC was estimated to be sub-dominant at high frequencies above 100 Hz in the sensitivity spectrum. Our investiga-

tion conducted in July 2023 revealed that the cable from the vacuum chamber where the PD was located to the ADC circuit outside the clean booth was so long that it picked up noise. After we replaced this cable with a shorter one, the dark noise decreased to the noise level determined by the circuit, below the shot noise. In addition, we found a white spot on the surface of the PD that resembled a burn mark. So, we replaced this PD with a healthy one. With these improvements, the dark current noise of the PD reached the noise level which was sufficient to obtain the target sensitivity of 10 Mpc.

Around September 2023, we started to use the high-power laser which was introduced in 2022 to reduce the shot noise. The high-power laser, however, suddenly stopped during commissioning because the fiber connected to the laser output amplifier burnt in the laser housing. This high-power laser was sent to the manufacturer to find the reason for the fiber burning and repair. Immediately, we installed a spare high-power laser in the PSL room.

KAGRA suffered from the fluctuation in the laser output power due to temperature changes in the laser room. In January 2024, we finally found that this fluctuation originated from a mismatch between the polarization direction of the incident light on the electro-optic modulator (EOM) and the EOM orientation. So, we installed the half-wave plate (HWP) in front of the EOM and aligned the laser polarization direction with the nominal direction of the EOM. Consequently, the laser output power fluctuation became insensitive to temperature changes in the PSL room.

On January 1, 2024, an earthquake of intensity of 7 occurred at the Noto Peninsula as mentioned in the overview section. After the earthquakes subsided, the KAGRA interferometer conditions were inspected. Regarding the input optics in the PSL room, there was no significant damages. On the other hand, all IMC mirrors were suspected to have some troubles that could not be repaired without the IMC vacuum tank breaking. After we vented the IMC vacuum tanks, we performed more inspections, then we found that several magnets dropped off from two of three IMC mirrors. The repair of these IMC mirrors was completed in early March 2024. After recovering the IMC optical resonance and restoring the downstream alignment, the IMC vacuum tanks were pumped down. Finally, the IMC was completely recovered in April 2024.

Cryogenic system

[Spokesperson : Nobuhiro KIMURA]
ICRR, The Univ. of Tokyo, Hida, Gifu 506-1205

One of the unique features of KAGRA is the use of cryogenic sapphire mirrors in the 3 km arm cavities. In FY2023, we realized the stable operation of the KAGRA cryogenic system during O4a with 10 cryocoolers, and the commissioning of the cryogenic system for O4b with 16 cryocoolers.

Cryogenic system operation during O4a Figure5 shows the setup of KAGRA's cryogenic mirrors during O4a, along with the positional relationship of the vacuum vessel.

During O4a, four cryocoolers were operated at EXC. Two of four were used to cool the radiation duct shields and two of four were used to cool the inner/outer radiation shields in the EXC cryostat. Owing to the radiation-cooling effect, the sapphire mirror (ETMX) was cooled at around 85K. Although 85K is well below the temperature at which water frosting is expected at the vacuum level of $\sim 10^{-5}$ Pa, no serious reflectivity reduction of ETMX was observed, judged from the finesse of the X-arm Fabry-Perot cavity. On the other hand, two cryocoolers were used to cool radiation ducts at each cryostat of EYC, IYC, and IXC. Owing to the radiation-cooling effect, each sapphire mirror of ETMY, ITMY, and ITMX were cooled at around 250K.

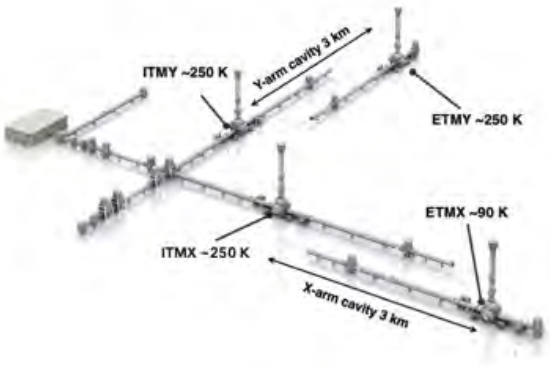


Fig. 5. Cryogenic mirrors for O4.

During O4a, temperatures in all cryostats were checked three times per day by the operation shift members to notice some troubles in the cryogenic system, especially in cryocoolers. Consequently, no serious troubles were reported during O4a.

Trial to cool ETMX at 20K After O4a, we tried to cool ETMX to around 20K by operating the last two cryocoolers of six cryocoolers per cryostat to cool the EX cryo-payload including ETMX. The ETMX was successfully cooled at around 20K. However, the reduction of the finesse of the X-arm FP cavity was observed when the temperature of ETMX went down around 28K, and the finesse kept decreasing for several days. We suspected this finesse reduction might be because of the frosting of nitrogen, judging from the vapor pressure curve at the cryogenic temperature. To check our guess, we heated up the cryo-payload with heaters that were attached to the intermediate mass. When the temperature of the ETMX was over around 28K, the finesse was recovered as we expected. So, we temporally concluded that the frosting of nitrogen happened around 28K. Each cryostat has 2-layer radiation shields whose inner radiation shield can catch nitrogen on its surface cooled around 10K. On the other hand, the radiation dust shields in front of and back of the test mass(TM) have only a one-layer radiation duct shield that is cooled at around 120K. So, it could not catch nitrogen on its surface and the nitrogen in the arm area where the temperature is at room temperature could easily reach TM.

Trial to cool all TMs below 100K In order to realize the 10Mpc BNS sensitivity of KAGRA, we need to cool all TMs below 100K. As demonstrated in ETMX, 4 of 6 cryocoolers

in each cryostat system should be operated to realize this temperature condition. In other words, the radiation duct shields should be cooled at around 120K, while two-layer radiation shields inside the cryostat should be cooled at around 10K for the inner radiation shield and 80K for the outer radiation shield. No cooling for the cryo-payload is necessary. Because we have already tried to cool ETMX at 20K and we learned that we should keep over 30K at ETMX to avoid frosting with maybe nitrogen, we kept over 30K temperature condition at ETMX by operating two cryocoolers for the cryo-payload and heaters at the intermediate mass at the same time. On the other hand, we have started two more cryocoolers to cool two-layer radiation shields at the EY, IY, and IX cryostat.

Temperatures at ETMY, ITMY, and ITMX could reach around 90K. However, we encountered several troubles in some cryocoolers. One of the troubles is the temperature enhancement at the first stage of the cryocoolers for the duct shield. When the temperature of the duct shield was over the temperature at which water absorbed on it could evaporate, the frosting of water on ETMX happened. To remove this frosted water, we needed to stop two cryocoolers for the two-layer radiation shield and to wait until the ETMX temperature reached around 180K at least or more (about 220K) at which the frosted water would be released. This recovery work took almost one month to realize the condition before troubles.

One of the reasons for this temperature enhancement was estimated to be the cooling power reduction due to disturbance of the pure He gas flow by frosted something (water?) inside the pure He gas path. To remedy this trouble, we recharged the pure He gas to attenuate the impure gas component. Another reason seemed to be the cooling power reduction due to the leak of the pure He gas at the flexible tube joint in the compressor. To remedy this trouble, we temporarily change the compressor itself with the other healthy one. Consequently, we successfully recovered the cooling power of these cryocoolers.

After the Noto-peninsula earthquake, we stopped all cryocoolers mainly for the seismic noise isolation system recovery works. So, we could deeply inspect the compressors for cryocoolers to find sources of the cooling performance reduction. The investigation is ongoing.

Digital system

[Spokesperson : Shoichi OSHINO]

ICRR, The Univ. of Tokyo, Hida, Gifu 506-1205

We plan to upgrade the digital system after the fourth phase of international joint observations. We have started to build a test bench system for this purpose. As a first step, we are building a system consisting of a boot server, data concentrator, frame writer, and real-time front-end. We will install the latest version of software developed at LIGO to build a system that will facilitate future collaborative observations.

We worked on updating the operating systems of the workstations used to control the interferometer and display various data. The software for gravitational wave observation and other software were verified, and the operating system was updated sequentially.

Almost all of the AC power supplies were replaced with DC power supplies in 2023 to reduce electrical noise sources affecting the gravitational wave interferometer.

IPC glitches affecting gravity wave data were reduced. Various studies have shown that it is related to the network speed of the servers that collect the sensors and control signal data. As a countermeasure, two 10Gbps network interfaces were installed on the server to increase the data inflow path. This dramatically reduced the amount of glitches.

Analog ELectronic circuits

[Spokesperson : Osamu MIYAKAWA]

ICRR, The Univ. of Tokyo, Hida, Gifu 506-1205

The Analog Electronics Group (AEL) has been continuously manufacturing the circuits that are necessary for KAGRA. We have produced several hundred different types of circuits, about a thousand as units, and several thousand as boards. In FY2023, KAGRA was in a situation to be ready for observation, so we did not need to make a completely new designed circuit. We have been replacing/repairing some circuits that had malfunctions, and manufacturing circuits that will be necessary in the future. The circuits we have manufactured in FY2023 are 100 of configuration boards for binary output card, 10 of BNC-D-sub converters, 10 of high power coil drivers, 10 of whitening filters, a laser shutter, several spares of common mode servo, and so on. The Timing slave and IRIG-B chassis are being designed and manufactured continuously into FY2024.

Over the past several years, the procurement of circuit components has been extremely difficult due to COVID-19. In FY2022, we actually had to suspend the production of some circuits, but in FY2023, the supply of components was almost recovered, and we were able to produce circuits as planned.

One of the most important roles of the AEL group recently is the establishment of a checking and investigation system for circuits. When a problem is found in accordance with KAGRA commissioning, etc., the relevant circuit is measured and, if necessary, the circuit will be brought back to the circuit room to fix the problem. Keeping spare circuits for replacement and the actual replacement work are also important roles. For example, noise on ADC/DAC cards has been measured for more than 100 cards with more than 5000 channels, over a period of years. We figured out why there was a delay in the switching of digital signals and worked with the Digital System subgroup to reduce the delay until no longer a problem in practical use.

It is important to provide circuits for KAGRA to be able to carry out observations and commissioning stably in the future. On the other hand, our members are getting older and 3 of 4 members will be retired or moved. I am very concerned about our AEL group after several years. We are responsible for the KAGRA circuits-related things that should hopefully be discussed with some new members.

Detector Charcterization

[Spokesperson : Hirotaka Yuzurihara]

ICRR, The Univ. of Tokyo, Hida, Gifu 506-1205

Data sharing with LIGO and Virgo In fiscal year 2023, the LIGO-Virgo-KAGRA (LVK) collaboration performed the international joint observing run. KAGRA joined the observing run during the first four weeks of O4a (2023 May 24 $\sim$ 2023 June 21). The data from GW observatories (LIGO, Virgo, and KAGRA) are collected to the cluster at California Institute of Technology (CIT). To search for the gravitational wave signals in the KAGRA data, it is necessary to know in advance which times of the data should be analyzed or which times should be excluded from the analysis. This information is called the data quality (DQ) flag.

The KAGRA Detector Characterization team's task is to provide LVK members with the DQ flags of the KAGRA data. In fiscal year 2023, we updated the DQ flags based on knowledge during the commissioning phase [1]. The updated DQ flags covered disturbances due to environmental noise as well as noise transients coming from instrument electrical glitches, operational errors caused by human activities, and so on. The DQ flags for O4a data were automatically generated at the KAGRA site, uploaded to the dedicated server, and shared with the data analysis members in the LIGO-Virgo-KAGRA collaboration.

Data quality evaluation for O4a data One of the most important roles of Detector Characterization is to prevent the false detection of gravitational waves. Gravitational waves (GWs) are very weak signals buried by various disturbances, such as the vibration of the mirrors that constitute an interferometer and the instability of the laser power and frequency. Such disturbances can also be detected as false GW events. Understanding the behavior and statistics of the detector noise is important for separating GWs from such false events.

It is known that the strain data contains many transient or non-stationary disturbances. Therefore, we provided various tools for understanding and mitigating noise sources [1]. By using the tools, we evaluated the KAGRA's O4a data.

In the study that focuses on non-Gaussian noise, S.Yamamura developed the tool to evaluate the non-Gaussianity of the strain data [3]. The developed tool processes and analyzes the strain data once an hour. The results are available on the internal web page. Monitoring the time variability of the Gaussianity effectively contributed to the noise hunting in the commissioning and the data evaluation during the observing run. One of the significant examples is to have found and visualized the scattered noise in the O4a data by monitoring the Gaussianity. S.Yamamura also extended the conventional method to evaluate non-Gaussian noise, called Rayleigh statistic, using a statistical hypothesis test to determine a threshold for non-Gaussian noise [2]. This extension can contribute to the initial detection of non-Gaussian noise and lead to further investigation of its origin.

Bibliography

[1] Hirotaka Yuzurihara, PoS ICRC2023 (2023), 1564

[2] Shunsei Yamamura, Hirotaka Yuzurihara, Takahiro Yamamoto, Takashi Uchiyama, arXiv:2403.12731 (submitted to CQG)

[3] Shunsei Yamamura, master thesis (ICRR, U-Tokyo)

Environment Monitors

[Spokesperson : Takaaki YOKOZAWA]

ICRR, The Univ. of Tokyo, Hida, Gifu 506-1205

Since the amplitude of the GW is extremely small, vibration from essential instruments, sound from outside of the experimental area, and so on, can produce noise source contamination that limits KAGRA sensitivity. To evaluate the noise sources, many sensors are installed at the KAGRA site, include seismometers, microphones, magnetometers, and accelerometers. The first is to characterize underground and cryogenic environments. KAGRA detector has two unique features, underground and cryogenic environment, and These features are essential for next-generation detectors. We installed various PEMs including accelerometers, microphones, magnetometers, thermometers, and weather stations.[2]

Towards the O4a observation, we performed the "tapping test" among almost all areas of the KAGRA experimental area. The main aim of this tapping test is to find the "critical point" to KAGRA sensitivity curve. If we can find the critical point, we can perform the characterization it with the various amplitude and frequencies using the shakers, speakers, and so on. As a result of the tapping test, we found several points at which vibration affects the KAGRA sensitivity and the largest critical point was the OMC(Output Mode Cleaner) chamber, which includes the PD to detect the gravitational waves. With the various shaker and speaker tests, we concluded that the acoustic noise around the OMC chamber limits the KAGRA sensitivity around 100 Hz. So we started the investigation about the OMC chamber.

Also, we evaluated the effect of the weather on the KAGRA detector using the O4a run data. The details of this study can be found in the master thesis of Shinya Miyamoto[1]. One of the interesting results is that when the wind near the KAGRA area became larger, the BNS detection range became worse (in other words, the sensitivity became worse). We studied more detail, then we found the amplitude of the wind speed is proportional to the ground motion, and non-linear and frequency-converted noise appeared around 60 - 100 Hz. Our guess is that increasing the ground motion enhanced the scattered noise at some point. So, the next step is to find the critical point for the scattered noise and to reduce the noise.

The study of offline noise subtraction is also ongoing, not only for independent component analysis but also for the DeepClean method. We are trying to establish the power line noise subtraction algorithm (60 Hz and its harmonics, already established in LIGO) with the online system.

Bibliography

[1] Shinya Miyamoto, master thesis (ICRR, U-tokyo)

[2] Takaaki Yokozawa, Pos ICRC2023(2023), 1557

Data Analysis, Computing environment

Hideyuki Tagoshi, Soichiro Morisaki, Tatsuya Narikawa, Nami Uchikata

ICRR, The Univ. of Tokyo, Kashiwa, Chiba, 277-8582

Data Analysis

The data analysis of KAGRA is now performed jointly with LIGO and Virgo under the LIGO-Virgo-KAGRA Memorandum of Agreement (MoA). The MoA defines the policy of joint data analysis and data sharing. In the LIGO-Virgo-KAGRA (LVK) Collaboration, there is a Data Analysis Council (DAC) which is a committee managing data analysis activities in LVK. Under DAC, there are four working groups regarding gravitational wave signal search, Compact Binary Coalescence working group (CBC), Burst working group (Burst), Continuous Wave Working group (CW), and Stochastic background working group (Stochastic). In LVK, there is also an Operations group that manages various data-related activities. From ICRR, Hideyuki Tagoshi is serving as a co-chair of DAC, and Soichiro Morisaki is serving as a co-chair of the Low Latency group in the Operations division.

The 4th observing run of LVK started in May 2023. We are participating in various activities of the O4 run.

As a part of the LVK Test of General Relativity paper being prepared by the LVK Collaboration, N. Uchikata and T. Narikawa are working on the modeled search for gravitational wave echoes after the merger of binary black holes. We have implemented waveform models used in our previous search to the LVK analysis pipeline and have been performing many test analyses using simulated signals. The analysis of the observed events is planned in FY2024.

S. Morisaki developed a rapid parameter estimation technique for O4, which enables optimal source localization of binary neutron star signal in around ten minutes after detection [S. Morisaki, PRD 108, 123040 (2023)]. He integrated this technique with the automated analysis pipeline [S. S. Chaudhary et al. including S. Morisaki, PNAS 121, no.18, e2316474121 (2024)], and it is being used for updating source localization and classification of signals detected in O4.

Various activities related to the data analysis of gravitational waves were also done during FY2023.

We have studied multipole tidal effects in the post-Newtonian gravitational-wave phase of binary neutron star coalescences. The new waveform model, MultipoleTidal, consists of the mass quadrupole, the current quadrupole, and the mass octupole moments. We apply the MultipoleTidal model to binary neutron star coalescence events GW170817 and GW190425. We find that the current quadrupole and the mass octupole moments give no significant impact on the inferred tidal deformability for the current observed events [T. Narikawa, PRD 108, 063029 (2023)].

If the remnant object of compact binary mergers does not possess the event horizon, we might observe additional pulse-like signals after the merger, which are called gravitational echoes. We have searched for such signals from 34 binary merger events observed in O3. We have performed a template-based search by using two different waveform models. We have not found any significant echo signals from our search. [N. Uchikata, T. Narikawa, H. Nakano, N. Sago, H. Tagoshi and T. Tanaka, PRD108, 104040 (2023)].

Recently Moroianu et al. (2022) have claimed that FRB20190425A, a fast radio burst detected by the Canadian Hydrogen Intensity Mapping Experiment (CHIME), is a potential electromagnetic counterpart of GW190425, a binary neutron star signal detected in O3. In addition, Bhardwaj et al. (2023) conclusively associated FRB 20190425A with UGC10667, potentially providing a direct host galaxy candidate for GW190425. Given these reports, we reanalyzed GW190425 with fixing its location to that of UGC10667. Fixing luminosity distance breaks its degeneracy with the viewing angle of the binary, and we found that the viewing angle is larger than 30 degrees at more than 99.99% credibility [M. Bhardwaj et al. including S. Morisaki, arXiv:2306.00948 (2023), I. M. Hernandez et al. including S. Morisaki, arXiv:2404.02496 (2024)]. For that large viewing angle, radio emission is expected to be blocked by ejecta along the line of sight, making the association unlikely.

Construction of next-generation gravitational-wave detectors, such as Einstein Telescope and Cosmic Explorer, is planned. Since their sensitive band is extended to lower frequencies and they can observe a binary neutron star signal from a few hours before the merger, Earth's rotation affects the observed waveform and helps improving the source localization precision. The long-wavelength approximation breaks down since the detectors' arms are longer and signal-to-noise ratios of signals are larger, and we can not ignore the dependency of detector responses on signal frequencies and gravitational-wave propagation directions, improving the source localization precision. We performed Bayesian parameter estimation of simulated binary neutron star signals observed with those detectors incorporating those effects. We found that it is possible to localize the source precisely ($\sim 10\,\mathrm{deg}^2$) even with a single Cosmic Explorer [P. Baral, S. Morisaki, I. M. Hernandez, and J. D. E. Creighton, PRD 108, 043010 (2023)].

In our previous research, we pointed out that KAGRA's auxiliary channels can be used to search for dark photons, vector particles behaving as dark matter. We developed a pipeline to analyze KAGRA's auxiliary channels to search for dark photons and conducted a search with KAGRA's O3 data. No significant candidates have been found, and we obtained upper bounds on dark photon's coupling constant [A. G. Abac et al. including S. Morisaki, arXiv: 2403.03004 (2024)].

Computing environment

As one of the main computing resources in KAGRA, the KAGRA main data server has been working at ICRR Kashiwa. The first main data server (System A) was decommissioned in November 2023, and the System B is operational now. It has a 4PB data storage and 512 computing cores.

All data taken by the KAGRA detector at the Kamioka site are packed into one file for every 32 seconds and are transferred continuously to the main data server at Kashiwa. Besides this, low-latency data transfer is also done by packing only the gravitational wave channel and a few other channels

into one file for every 1 second. For low-latency data transfer, the latency of about 3 seconds is achieved from Kamioka to Kashiwa (this time includes the time necessary for calibration). In order to share the low-latency data file among LIGO-Virgo-KAGRA, the low-latency data files are transferred to LIGO and Virgo. Low latency data files of LIGO and Virgo detectors are transferred to the KAGRA main data server.

We have another computing cluster that is mainly used for data analysis tasks. During FY2023, we introduced additional computing nodes, and the total computing cores of the system became 992 cores.

Observational Cosmology Group

[Spokesperson: Yuichi Harikane]

ICRR, The Univ. of Tokyo, Kashiwa, Chiba 277-8582

A JWST/NIRSpec First Census of Broad-Line AGNs at $\mathbf{z = 4-7}$: Detection of 10 Faint AGNs with $\mathbf{M_{BH} \sim 10^6 - 10^8\ M_\odot}$ and Their Host Galaxy Properties [1]

In collaboration with the members of National Astronomical Observatory of Japan.

We present a first statistical sample of faint type-1 AGNs at $z > 4$ identified by JWST/NIRSpec deep spectroscopy. Among the 185 galaxies at $z_{\rm spec} = 3.8 - 8.9$ confirmed with NIRSpec, our systematic search for broad-line emission reveals 10 type-1 AGNs at $z = 4.015 - 6.936$ whose broad component is only seen in the permitted Hα line and not in the forbidden [OIII]λ5007 line that is detected with greater significance than Hα. The broad Hα line widths of FWHM $\simeq 1000 - 6000$ km s^{-1} suggest that the AGNs have low-mass black holes with $M_{\rm BH} \sim 10^6 - 10^8\ M_\odot$, remarkably lower than those of low-luminosity quasars previously identified at $z > 4$ with ground-based telescopes. JWST and HST high-resolution images (Figure 6) reveal that the majority of them show extended morphologies indicating significant contribution to the total lights from their host galaxies, except for three compact objects two of which show red SEDs, probably in a transition phase from faint AGNs to low luminosity quasars. Careful AGN-host decomposition analyses show that their host's stellar masses are systematically lower than the local relation between the black hole mass and the stellar mass, implying a fast black hole growth consistent with predictions from theoretical simulations. A high fraction of the broad-line AGNs ($\sim 5\%$), higher than $z \sim 0$, indicates that a number density of such faint AGNs is higher than an extrapolation of the quasar luminosity function, implying a large population of AGNs in the early universe. Such faint AGNs contribute to cosmic reionization, while the total contribution is not large, up to $\sim 50\%$ at $z \sim 6$, because of their faint nature.

Bibliography

[1] Harikane, Y., Zhang, Y., Nakajima, K., Ouchi, M., Isobe, Y., Ono, Y., Hatano, S., Xu, Y., Umeda, H., 2023, The Astrophysical Journal, 959, 39

Pure Spectroscopic Constraints on UV Luminosity Functions and Cosmic Star Formation History From 25 Galaxies at $\mathbf{z_{spec} = 8.61 - 13.20}$ Confirmed with JWST/NIRSpec [2]

In collaboration with the members of National Astronomical Observatory of Japan.

We present pure spectroscopic constraints on the UV luminosity functions and cosmic star formation rate (SFR) densities from 25 galaxies at $z_{\rm spec} = 8.61 - 13.20$. By reducing the JWST/NIRSpec spectra taken in multiple programs of ERO, ERS, GO, and DDT with our analysis technique, we independently confirm 16 galaxies at $z_{\rm spec} = 8.61 - 11.40$, including new redshift determinations (Figure 7), and a bright interloper at $z_{\rm spec} = 4.91$ that was claimed as a photometric candidate at $z \sim 16$. In conjunction with nine galaxies at redshifts up to $z_{\rm spec} = 13.20$ in the literature, we make a sample of 25 spectroscopically-confirmed galaxies in total and carefully derive the best estimates and lower limits of the UV luminosity functions. These UV luminosity function constraints are consistent with the previous photometric estimates within the uncertainties and indicate mild redshift evolution towards $z \sim 12$ showing tensions with some theoretical models of rapid evolution. With these spectroscopic constraints, we obtain firm lower limits of the cosmic SFR densities and spectroscopically confirm a high SFR density at $z \sim 12$ beyond the constant star-formation efficiency models, which supports earlier claims from the photometric studies. While there are no spectroscopically-confirmed galaxies with very large stellar masses violating the ΛCDM model due to the removal of the bright interloper, we confirm star-forming galaxies at $z_{\rm spec} = 11 - 13$ with stellar masses much higher than model predictions. Our results indicate possibilities of high star-formation efficiency ($> 5\%$), hidden AGN, top-heavy initial mass function (possibly with Pop-III), and large scatter/variance. Having these successful and unsuccessful spectroscopy results, we suggest observational strategies for efficiently removing low-redshift interlopers for future JWST programs.

Bibliography

[2] Harikane, Y., Nakajima, K., Ouchi, M., Umeda, H., Isobe, Y., Ono, Y., Xu, Y., Zhang, Y., 2024, The Astrophysical



Fig. 6. Pseudo-color image of the discovered ten AGNs at z=4-7, created by combining three-color observational data obtained from either the James Webb Space Telescope or the Hubble Space Telescope.(Credit: NASA, ESA, CSA, Harikane et al.)

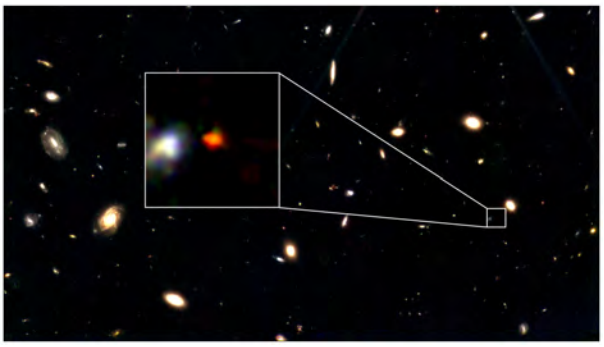


Fig. 7. The pseudo-color image of the galaxy CEERS2_588, a newly–confirmed galaxy at $z = 11$, presented at the center of the magnified view. This image is based on the data obtained by the James Webb Space Telescope. (Credit: NASA, ESA, CSA, Harikane et al.)

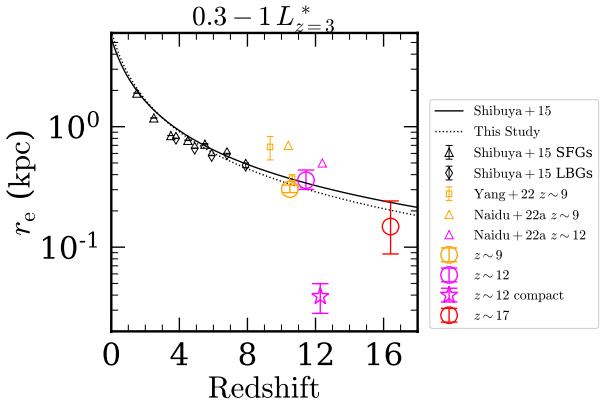


Fig. 8. Evolution of the half-light radius of star-forming galaxies with UV luminosities of (0.3–1) $L^*_{z=3}$. The orange, magenta, and red large open circles show bright objects in the $z \sim 9$, $z \sim 12$, and $z \sim 16$ galaxy candidate samples, respectively. The magenta open star denotes the very compact galaxy candidate, GL-z12-1.

Journal, 960, 56

Morphologies of Galaxies at $z \gtrsim 9$ Uncovered by JWST/NIRCam Imaging: Cosmic Size Evolution and an Identification of an Extremely Compact Bright Galaxy at $z \sim 12$ [3]

In collaboration with the members of National Astronomical Observatory of Japan, University of Tsukuba, Kitami Institute of Technology, and Georgia Institute of Technology.

We present morphologies of galaxies at $z \gtrsim 9$ resolved by JWST/NIRCam 2–5μm imaging. Our sample consists of 22 galaxy candidates identified by stringent dropout and photo-z criteria in GLASS, CEERS, SMACS J0723, and Stephan's Quintet flanking fields, one of which has been spectroscopically identified at $z = 11.44$. We perform surface brightness (SB) profile fitting with GALFIT for 6 bright galaxies with S/N = 10–40 on an individual basis and for stacked faint galaxies with secure point-spread functions (PSFs) of the NIRCam real data, carefully evaluating systematics by Monte-Carlo simulations. We compare our results with those of previous JWST studies, and confirm that effective radii r_e of our measurements are consistent with those of previous measurements at $z \sim 9$. We obtain $r_e \simeq 200$–300 pc with the exponential-like profiles, Sérsic indexes of $n \simeq 1$–1.5, for galaxies at $z \sim 12$–16, indicating that the relation of $r_e \propto (1+z)^s$ for $s = -1.22^{+0.17}_{-0.16}$ explains cosmic evolution over $z \sim 0$–16 for $\sim L^*_{z=3}$ galaxies (Figure 8). One bright ($M_{\rm UV} = -21$ mag) galaxy at $z \sim 12$, GL-z12-1, has an extremely compact profile with $r_e = 39 \pm 11$ pc that is surely extended over the PSF. Even in the case that the GL-z12-1 SB is fit by AGN+galaxy composite profiles, the best-fit galaxy component is again compact, $r_e = 48^{+38}_{-15}$ pc that is significantly ($> 5\sigma$) smaller than the typical r_e value at $z \sim 12$. Comparing with numerical simulations, we find that such a compact galaxy naturally forms at $z \gtrsim 10$, and that frequent mergers at the early epoch produce more extended galaxies following the $r_e \propto (1+z)^s$ relation.

Bibliography

[3] Ono, Y., Harikane, Y., Ouchi, M., Yajima, H., Abe, M., Isobe, Y., Shibuya, T., Wise, J. H., Zhang, Y., Nakajima, K., Umeda, H., 2023, The Astrophysical Journal, 951, 72

Redshift Evolution of the Electron Density in the ISM at $z\sim0-9$ Uncovered with JWST/NIRSpec Spectra and Line-Spread Function Determinations [4]

In collaboration with the members of National Astronomical Observatory of Japan.

We present electron densities $n_{\rm e}$ in the inter-stellar medium (ISM) of star-forming galaxies at $z=4-9$ observed by the JWST/NIRSpec GLASS, ERO, and CEERS programs. We carefully evaluate line-spread functions of the NIRSpec instrument as a function of wavelength with the calibration data of a planetary nebula taken onboard, and obtain secure [O II]$\lambda\lambda$3726,3729 doublet fluxes for 14 galaxies at $z=4.02-8.68$ falling on the star-formation main sequence with the NIRSpec high and medium resolution spectra. We thus derive the electron densities of singly-ionized oxygen nebulae with the standard $n_{\rm e}$ indicator of [O II] doublet, and find that the electron densities of the $z=4-9$ galaxies are $n_{\rm e}\gtrsim300$ cm^{-3} significantly higher than those of low-z galaxies at a given stellar mass, star-formation rate (SFR), and specific SFR. Interestingly, typical electron densities of singly ionized nebulae increase from $z=0$ to $z=1-3$ and $z=4-9$, which is approximated by the evolutionary relation of $n_{\rm e}\propto(1+z)^p$ with $p\sim1-2$ (Figure 9). Although it is not obvious that the ISM property of $n_{\rm e}$ is influenced by global galaxy properties, these results may suggest that nebula densities of high-z galaxies are generally high due to the compact morphologies of high-z galaxies evolving by $r_{\rm e}\propto(1+z)^{-1}$ ($r_{\rm vir}\propto(1+z)^{-1}$) for a given stellar (halo) mass whose inverse square corresponds to the $p\sim2$ evolutionary relation. The $p\sim1-2$ evolutionary relation can be explained by a combination of the compact morphology and the reduction of $n_{\rm e}$ due to the high electron temperature of the high-z metal poor nebulae.

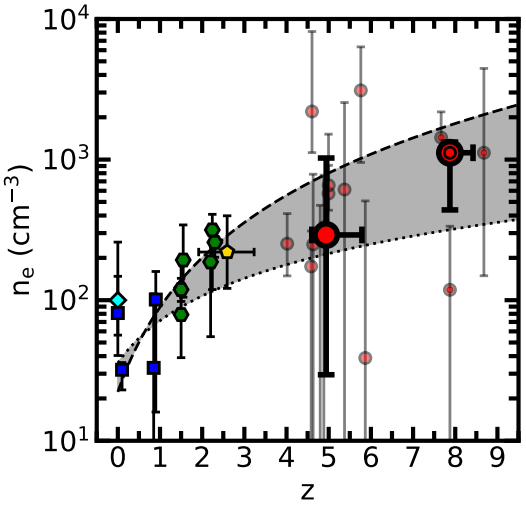


Fig. 9. Electron density $n_{\rm e}$ as a function of redshift. All of the measurements in this figure are based on the low-ionization lines (i.e., [O II] or [S II]). The large red circles and the large red double circles denote median and 16th-84th percentiles of the properties of the JWST galaxies at $z\sim4$–6 and $z\sim7$–9, respectively. The small red circles and the small red double circle represent the properties of each JWST galaxy at $z\sim4$–6 and $z\sim7$–9, respectively. The dotted and dashed curves represent $n_{\rm e}$ following $\propto(1+z)$ and $\propto(1+z)^2$ relations, respectively, which are determined by the galaxies at $z\sim0$–3. The JWST galaxies lie on the gap between the two functions (i.e., $n_{\rm e}\propto(1+z)$ and $\propto(1+z)^2$) filled with the gray shaded region.

Bibliography

[4] Isobe, Y., Ouchi, M., Nakajima, K., Harikane, Y., Ono, Y., Xu, Y., Zhang, Y., Umeda, H., 2023, The Astrophysical Journal, Volume 956, 139

JWST Identification of Extremely Low C/N Galaxies with [N/O]$\gtrsim0.5$ at $z\sim6-10$ Evidencing the Early CNO-Cycle Enrichment and a Connection with Globular Cluster Formation [5]

In collaboration with the members of National Astronomical Observatory of Japan, and University of Tsukuba.

We present chemical abundance ratios of 70 star-forming galaxies at $z\sim4$–10 observed by the JWST/NIRSpec ERO, GLASS, and CEERS programs. Among the 70 galaxies, we have pinpointed 2 galaxies, CEERS_01019 at $z=8.68$ and GLASS_150008 at $z=6.23$ (Figure 10), with extremely low C/N ([C/N]$\lesssim-1$), evidenced with C III]$\lambda\lambda$1907,1909, N III]λ1750, and N IV]$\lambda\lambda$1483,1486, which show high N/O ratios ([N/O]$\gtrsim0.5$) comparable with the one of GN-z11 regardless of whether stellar or AGN radiation is assumed. Such low C/N and high N/O ratios found in CEERS_01019 and GLASS_150008 (additionally identified in GN-z11) are largely biased towards the equilibrium of the CNO cycle, suggesting that these 3 galaxies are enriched by metals processed by the CNO cycle. On the C/N vs. O/H plane, these 3 galaxies do not coincide with Galactic HII regions, normal star-forming galaxies, and nitrogen-loud quasars with asymptotic giant branch stars, but globular-cluster (GC) stars, indicating a connection with GC formation. We compare C/O and N/O of these 3 galaxies with those of theoretical models, and find that these 3 galaxies are explained by scenarios with dominant CNO-cycle materials, i.e. Wolf-Rayet stars, supermassive ($10^3-10^5\,M_\odot$) stars, and tidal disruption events, interestingly with a requirement of frequent direct collapses. For all the 70 galaxies, we present measurements of Ne/O, S/O, and Ar/O, together with C/O and N/O. We identify 4 galaxies with very low Ne/O, $\log({\rm Ne/O})<-1.0$, indicating abundant massive ($\gtrsim30\,M_\odot$) stars.

Bibliography

[5] Isobe, Y., Ouchi, M., Tominaga, N., Watanabe, K., Nakajima, K., Umeda, H., Yajima, H., Harikane, Y., Fukushima, H., Xu, Y., Ono, Y., Zhang, Y., 2023, The Astrophysical Journal, Volume 959, 100

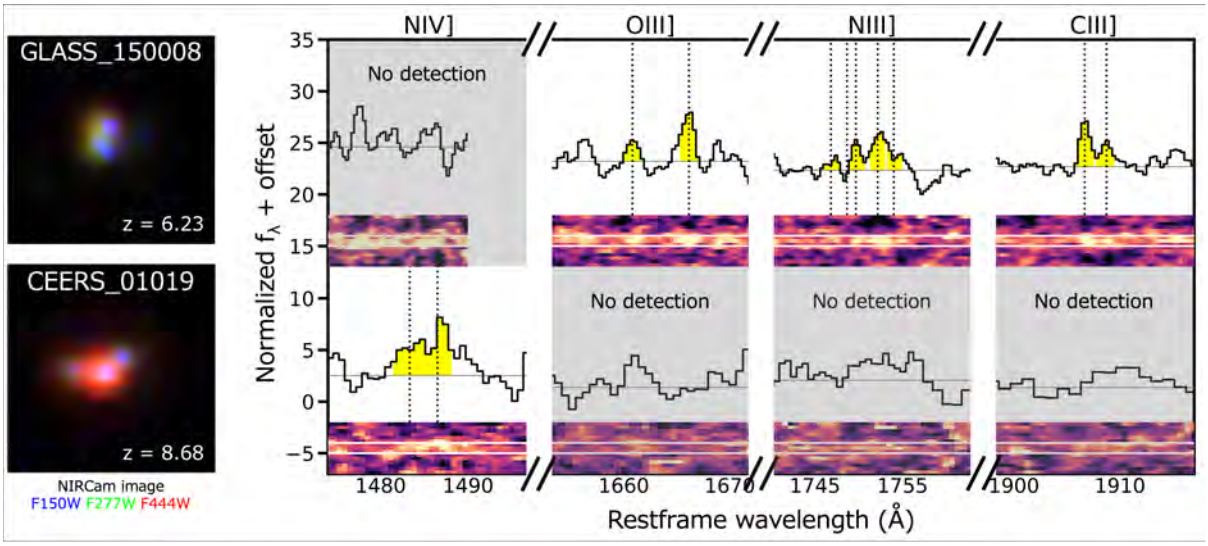


Fig. 10. Emission line detections of GLASS_150008 and CEERS_01019. (Left) $1'' \times 1''$ JWST/NIRCam image with blue/green/red corresponding to F150W/F277W/F444W. (Right) Smoothed 1D and 2D spectra around N IV], O III], N III], and C III] shown by the black solid lines and the color maps, respectively. The emission lines are highlighted in yellow, while the highlights for the undetected emission lines are omitted. Restframe wavelengths of the emission lines are shown by the vertical black dotted lines. The horizontal gray lines denote the continuum level. The horizontal white lines on the 2D spectra indicate the extraction aperture for the 1D spectra.

Theory Group

Overview

The theory group is active in elementary particle physics focusing on particle phenomenology, and in astroparticle physics focusing on particle cosmology. In particle physics, the main topics are theoretical studies of dark matter, inflation and extensions of the standard model. In astroparticle physics, the main topics are theoretical studies of inflation, thermal history of the early universe, dark matter, baryogenesis and big-bang nucleosynthesis.

After the discovery of the Higgs boson, the LHC has shown no strong hints on new physics. In this situation, we need to reconsider many ideas of new physics models as well as conventional strategies to search for them. Accordingly, our studies on beyond the Standard Model physics becomes more and more diverse.

Since the LIGO detectors detected the first confirmed gravitational waves (GWs) from colliding black holes on September 14, 2015, new era of GW astronomy began. So far, six GW events were detected by LIGO. Among them is the first detection of GW from binary neutron star. The discovery suggested strongly the existence of kilonova which can produce r-process elements. If they continue to find GW events from black holes and neutron stars, their origin becomes one of the most interesting topics.

The supersymmetric (SUSY) extension of the standard model (SM) in the particle physics is considered to be one of the most promising models beyond the standard model. It solves the naturalness problem for the Higgs boson mass term in the standard model, and it is also compatible with the grand unified theories (GUTs). Although no hints of the superparticles have been indicated from the LHC yet, the SUSY models are the most attractive candidates beyond the Standard Model. Our group has been studying phenomenological and cosmological aspects of the SUSY models.

Recent cosmological observations including the Planck data determine precisely the mean densities of matter and baryon in the Universe, and existence of non-baryonic dark matter is established. Weakly interacting massive particles (WIMPs) are considered to be good candidates of the dark matter. They act as the cold dark matter in the structure formation of the universe. Our group has been studying model building for dark matter and detectability in direct and indirect search experiments.

For understanding of the early universe, a role of the elementary particle physics is crucial. Recent progress in the particle physics such as grand unification theories and supersymmetry leads us to a more deeper insight into the fundamental aspects of the early universe. In the inflationary universe, the quantum fluctuations of the scalar field which drives the inflation become the density fluctuations and lead to formation of the structure observed in the present universe. On the other hand cosmology and astrophysics are used to test new theories in particle physics. Such particle cosmology is one of main subjects of our group.

Big Bang Nucleosynthesis (BBN) is one of the most important subjects in modern cosmology. Predicted abundances of the light elements are very sensitive to the cosmological scenario. On the other hand, physics beyond the standard model predicts the new particles which would have existed at the BBN epoch. Such particles may spoil the success of BBN, which leads to constraints on the new particles and the particle physics models.

The grand unified theories predict that our universe undergoes several vacuum phase transitions. In the course of phase transitions topological defects (monopoles, cosmic strings and domain walls) are generally produced depending on symmetries of the vacua. Our group has studied evolution of various topological defects.

Particle Phenomenology

[Spokesperson : M. Ibe]
ICRR, The Univ. of Tokyo, Kashiwa, Chiba 277-8582

Beyond Standard Model

• Probing for chiral Z' gauge boson through scattering measurement experiments [1]

In collaboration with the members of ICRR, Hokkaido Univ., Sichuan Univ.

Motivated by the observation of tiny neutrino mass can not be explained within the framework of Standard Model (SM), we consider extra gauge extended scenarios in which tiny neutrino masses are generated through seesaw mechanism. These scenarios are equipped with beyond the standard model (BSM) neutral gauge boson called Z' in the general $U(1)_X$ symmetry which is a linear combination of $U(1)_Y$ and $U(1)_{B-L}$. In this case, left and right handed fermions interact differently with the Z'. The Z' gives rise to different processes involving neutrino-nucleon, neutrino-electron, electron-nucleus and electron-muon scattering processes. By comparing with proton, electron beam-dump experiments data, recast data from searches for the long-lived and dark photon at BaBaR, LHCb and CMS experiments, the electron and muon $g-2$ data, and the data of the dilepton and dijet searches at the LEP experiment, we derive bounds on the gauge coupling and the corresponding gauge boson mass for different $U(1)_X$ charges and evaluate the prospective limits from the future beam-dump scenarios at DUNE, FASER(2) and ILC. We conclude that large parameter regions could be probed by scattering, beam-dump and collider experiments in future.

• New constraint on dark photon at T2K off-axis near detector [2]

In collaboration with the members of Ohu Univ., ICRR, KEK, Kyushu Univ., Univ. of Miyazaki

The T2K experiment is one of the most powerful long-baseline experiments to investigate neutrino oscillations. The off-axis near detector called ND280 is installed 280 m downstream from the neutrino production target to measure the neutrino energy spectrum. In this paper, we study the capability of the ND280 detector to search for the dark photon produced through the meson rare decay and proton bremsstrahlung processes at the proton beam dump. We find that the ten-year operation of T2K with the ND280 detector excludes the unexplored parameter region for the dark photon mass and kinetic mixing. We also show that a broader parameter region can be searched by the ND280 in the future T2K operation for dark photon as well as $U(1)_{B-L}$ gauge boson.

• Contribution of Majoron to Hubble tension in gauged $U(1)_{L_\mu - L_\tau}$ Model [3]

In collaboration with the members of ICRR, Saitama Univ., Yokohama National Univ.

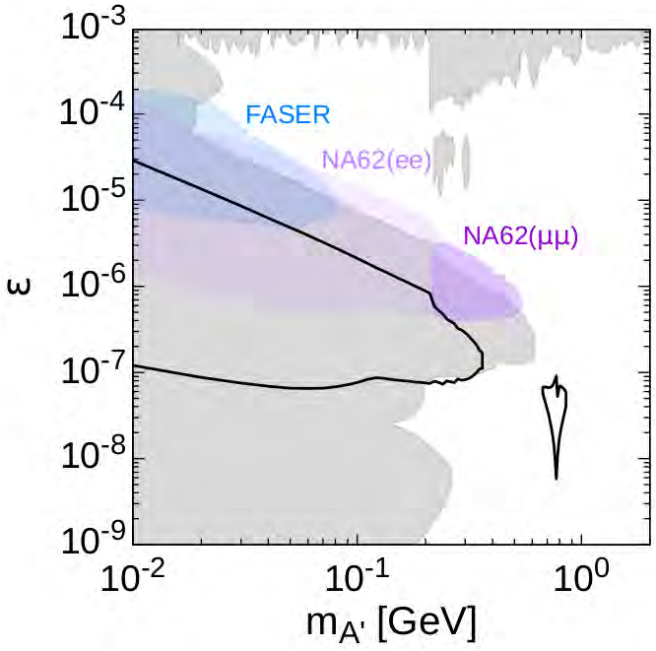


Fig. 11. Exclusion regions for the dark photon model. The regions surrounded by the black solid curves are the 95% C.L. exclusion regions with $N_{\rm pot} = 3.8 \times 10^{21}$, that are obtained in this work. The gray shaded areas are excluded by previous experiments and observations. Also, as a reference, the recent results of 90% C.L. exclusion regions by NA62 and FASER are shown as purple and blue shaded areas, respectively.

In this paper, we analyze parameter regions that can alleviate the Hubble tension in the $U(1)_{L_\mu - L_\tau}$ model with the broken lepton number $U(1)_L$ symmetry. As new particles, this model has a $U(1)_{L_\mu - L_\tau}$ gauge boson Z' and a Majoron ϕ, which can affect the early universe and the effective number of neutrino species $N_{\rm eff}$. If Z' and ϕ simultaneously exist in the early universe, Z'-ϕ interaction processes such as $Z'\nu_\alpha \leftrightarrow \phi\bar{\nu}_\beta$ occur. The comparison of $N_{\rm eff}$ between the cases with and without the Z'-ϕ interaction processes shows that these processes make a small contribution of $\mathcal{O}(10^{-4})$ to $N_{\rm eff}$, and it does not need to be considered for the alleviation of the Hubble tension. Based on these facts, we calculated $N_{\rm eff}$ for various Majoron parameters without the Z'-ϕ interaction processes to search parameters that could alleviate the Hubble tension. As a result, we found that the $U(1)_{L_\mu - L_\tau}$ gauge boson and Majoron can alleviate the Hubble tension in some parameter regions, and there is a non-trivial synergy contribution between Z' and ϕ. Moreover, the parameter region with a lighter mass $m_\phi \lesssim 2$ MeV and a larger coupling $\lambda \gtrsim 10^{-8}$ is excluded because it predicts too large $N_{\rm eff}$, i.e. $N_{\rm eff} \gtrsim 3.5$. The favored and restricted regions of the Majoron parameters depend on the Z' parameters because of the presence of the Z' contribution and synergy one.

• New Constraints on Gauged $U(1)_{L_\mu - L_\tau}$ Models via $Z - Z'$ Mixing [4]

In collaboration with the members of ICRR, Kyushu Univ., KEK, Univ. of Barcelona

It is known that the model based on $U(1)_{L_\mu - L_\tau}$ gauge symmetry can explain not only the discrepancy between the measured value of muon $g-2$ and the theoretical prediction, but also the structure of the neutrino mass and mixings. We revisit the analysis of the mass matrix structure in the minimal $U(1)_{L_\mu - L_\tau}$ models based on the latest experimental result, where the minimal stands for the symmetry breaking caused only by a single scalar field. We find that the model called type $\mathbf{2}_{+1}$, where an $SU(2)_L$ doublet scalar Φ_{+1} with the $U(1)_{L_\mu - L_\tau}$ charge $+1$ and the hypercharge $+1/2$, predicts the $\mathbf{B_3}$ texture and is marginally acceptable under the current neutrino oscillation data and cosmological observation. When the $U(1)_{L_\mu - L_\tau}$ gauge symmetry is broken by the vacuum expectation value of the standard model non-singlet representation such as Φ_{+1}, there are additional contributions to the flavor-changing meson decay process and atomic parity violation via the $Z-Z'$ mixing. We newly evaluate the model-dependent constraints on the model and conclude that the type $\mathbf{2}_{+1}$ model is robustly ruled out. The model is extended to have an additional vacuum expectation value of a standard model singlet scalar in order to avoid the stringent constraint from the flavor-changing meson decay. Finally, we find the allowed range of the ratio of these vacuum expectation values.

Bibliography

[1] K. Asai, A. Das, J. Li, T. Nomura and O. Seto, Phys. Rev. D **109** (2024) no.7, 075026 doi:10.1103/PhysRevD.109.075026 [arXiv:2307.09737 [hep-ph]].

[2] T. Araki, K. Asai, T. Iizawa, H. Otono, T. Shimomura and Y. Takubo, JHEP **11** (2023), 056 doi:10.1007/JHEP11(2023)056 [arXiv:2308.01565 [hep-ph]].

[3] K. Asai, T. Asano, J. Sato and M. J. S. Yang, [arXiv:2309.01162 [hep-ph]].

[4] K. Asai, C. Miyao, S. Okawa and K. Tsumura, [arXiv:2401.17613 [hep-ph]].

Extra dimension

• Model Building by Coset Space Dimensional Reduction Scheme Using Twelve-Dimensional Coset Spaces [1]

In collaboration with the members of ICRR, Yokohama National Univ., Saitama Univ.

We investigate the twelve-dimensional gauge-Higgs unification models with an eight- dimensional coset space as the extra space. For each model, we apply the coset space dimensional reduction procedure and examine the particle contents of the resulting four-dimensional theory. All combinations of inputs to the procedure are exhaustively analyzed under several assumptions. As a result, some twelve-dimensional SO(18) gauge theories lead to models of the $SO(10)\times U(1)$ grand unified theory in four dimensions, where fermions of the Standard Model appear in multiple generations along with scalars that may break the electroweak symmetry. The representations of the obtained scalars and fermions are summarized.

Bibliography

[1] K. Asai, J. Sato, R. Suda, Y. Takanishi and M. J. S. Yang, JHEP **11** (2023), 213 doi:10.1007/JHEP11(2023)213 [arXiv:2305.01421 [hep-ph]].

Supersymmetric Model

• Precise estimate of charged Higgsino/Wino decay rate [1]

In collaboration with the members of ICRR, Kavli IPMU

Higgsinos and Winos in the supersymmetric Standard Model are prime candidates for dark matter due to their weakly interacting nature. The mass differences between their charged components (charginos) and neutral components (neutralinos) become degenerate when other superparticles are heavy, resulting in long-lived charginos. In the case of the Winos, the mass difference is approximately 160 MeV across a wide range of the parameter space. Consequently, the chargino decays into the lightest neutralino, emitting a single charged pion. For Higgsinos, however, mass differences ranging from O(0.1) GeV to O(1) GeV are possible, leading to a variety of decay channels. In this paper, we extend our previous analysis of Wino decay to the chargino with a larger mass difference. We emphasize characterizing its decay signatures through leptonic and hadronic modes. By utilizing the latest experimental data, we perform a comprehensive study of the decay rate calculations incorporating these hadronic modes to determine the impact on the predicted chargino lifetime. Additionally, we conduct next-to-leading order (NLO) calculations for the leptonic decay modes. Our NLO results can be applied to the case of more general fermionic electroweak multiplets, e.g., quintuplet dark matter.

Bibliography

[1] M. Ibe, Y. Nakayama and S. Shirai, JHEP **03** (2024), 012 doi:10.1007/JHEP03(2024)012 [arXiv:2312.08087 [hep-ph]].

Topological Defect

• Revisiting metastable cosmic string breaking [1]

In collaboration with the members of ICRR, Kavli IPMU

Metastable cosmic strings appear in models of new physics with a two-step symmetry breaking $G \to H \to 1$, where $\pi_1(H) \neq 0$ and $\pi_1(G) = 0$. They decay via the monopole-antimonopole pair creation inside. Conventionally, the breaking rate has been estimated by an infinitely thin string approximation, which requires a large hierarchy between the symmetry breaking scales. In this paper, we reexamine it by taking into account the finite sizes of both the cosmic string and the monopole. We obtain a robust lower limit on the

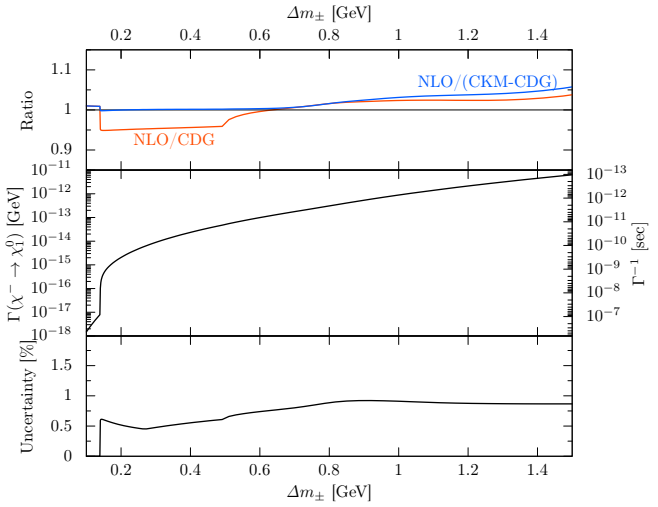


Fig. 12. The NLO chargino decay rate into one of the neutralinos for a 300 GeV Higgsino, including the associated uncertainty, is presented in the middle and bottom panel. The red line in the top panel depicts the ratio of our NLO result to the previous CDG estimate. In contrast, the blue line indicates the ratio to the CDG estimate corrected for the inclusion of the CKM matrix and the single Kaon mode. The data are available at `https://member.ipmu.jp/satoshi.shirai/Chargino_Decay/`

tunneling factor e^{-S_B} even for regimes the conventional estimate is unreliable. In particular, it is relevant to the cosmic string interpretation of the gravitational wave signals recently reported by pulsar timing array experiments.

Bibliography

[1] A. Chitose, M. Ibe, Y. Nakayama, S. Shirai and K. Watanabe, JHEP **04** (2024), 068 doi:10.1007/JHEP04(2024)068 [arXiv:2312.15662 [hep-ph]].

Particle Cosmology

[Spokesperson : M. Kawasaki]
ICRR, The Univ. of Tokyo, Kashiwa, Chiba 277-8582

Inflation

• Dai-Freed anomaly in the standard model and topological inflation [1]

In collaboration with the members of ICRR, Kavli IPMU, Tsung-Dao Lee Institute

When we impose the discrete symmetry in the standard model we have Dai-Freed global anomalies. However, interestingly if we introduce three right-handed neutrinos we can have an anomaly-free discrete Z_4 gauge symmetry. This Z_4 symmetry should be spontaneously broken down to the Z_2 symmetry to generate the heavy Majorana masses for the right-handed neutrinos. We show that this symmetry breaking naturally generates topological inflation, which is consistent with the CMB observations at present and predicts a significant tensor mode with scalar-tensor ratio $r > 0.03$. The right-handed neutrinos play an important role in reheating processes. The reheating temperature is as high as $\sim 10^8$GeV, and non-thermal leptogenesis successfully takes place.

• Hill-top inflation from Dai-Freed anomaly in the standard model — a solution to the iso-curvature problem of the axion dark matter [2]

In collaboration with the members of ICRR, Kavli IPMU, Tsung-Dao Lee Institute

The discrete symmetry Z_4 in the standard model (SM) with three right-handed neutrinos is free from the Dai-Freed anomaly. Motivated by this Z_4 symmetry, we constructed a topological inflation model consistent with all known constraints and observations. However, we assumed a specific inflaton potential in the previous work. In this paper we extend the inflaton potential in a more general form allowed by the discrete Z_4 gauge symmetry and show that consistent hilltop inflation is realized. We find that the Hubble parameter $H_{\rm inf}$ can be smaller than $\simeq 10^9$ GeV so that the isocurvature fluctuations of the axion dark matter are sufficiently suppressed. Furthermore, the running of the spectral index can be as large as $dn_s/\ln k \simeq 0.0018$ which will be tested in future CMB observations. Since this discrete Z_4 acts on the SM, the inflaton can couple to pairs of the right-handed neutrinos and hence the reheating temperature can be high as $\sim 10^{10}$ GeV, producing the cosmic baryon asymmetry naturally through the thermal leptogenesis.

Bibliography

[1] M. Kawasaki and T. T. Yanagida, JHEP **11** (2023), 106 doi:10.1007/JHEP11(2023)106 [arXiv:2304.10100 [hep-ph]].

[2] M. Kawasaki and T. T. Yanagida, JCAP **01** (2024), 014 doi:10.1088/1475-7516/2024/01/014 [arXiv:2306.14579 [hep-ph]].

Primordial Black Holes

• Clustering of primordial black holes from QCD axion bubbles [1]

In collaboration with the members of ICRR, Kavli IPMU, Tohoku Univ.

We study the clustering of primordial black holes (PBHs) and axion miniclusters produced in the model proposed to explain the LIGO/Virgo events or the seeds of the supermassive black holes (SMBHs) in arXiv:2006.13137. It is found that this model predicts large isocurvature perturbations due to the clustering of PBHs and axion miniclusters, from which we obtain stringent constraints on the model parameters. Specifically, for the axion decay constant $f_a = 10^{16}$ GeV, which potentially accounts for the seeds of the SMBHs, the PBH fraction in dark matter should be $f_{\rm PBH} \lesssim 7 \times 10^{-10}$. Assuming that the mass of PBHs increases by more than a factor

of $\mathcal{O}(10)$ due to accretion, this is consistent with the observed abundance of SMBHs. On the other hand, for $f_a = 10^{17}$ GeV required to produce PBHs of masses detected in the LIGO/Virgo, the PBH fraction should be $f_{\rm PBH} \lesssim 6 \times 10^{-8}$, which may be too small to explain the LIGO/Virgo events, although there is a significant uncertainty in calculating the merger rate in the presence of clustering.

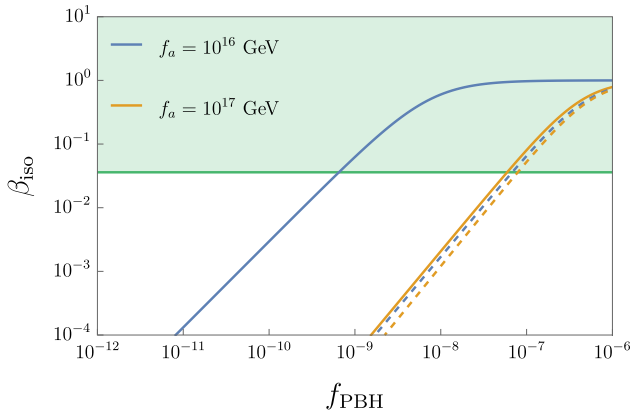


Fig. 13. Isocurvature perturbations from PBHs (dashed) and axion miniclusters (solid) for $f_a = 10^{16}$ GeV and 10^{17} GeV. The green-shaded region is constrained by the CMB observations, which set the upper bounds on $f_{\rm PBH}$.

• Primordial Origin of Supermassive Black Holes from Axion Bubbles [2]

In collaboration with the members of ICRR, Kavli IPMU, Tohoku Univ.

We study a modification of the primordial black hole (PBH) formation model from axion bubbles. We assume that the Peccei-Quinn scalar rolls down in the radial direction from a large field value to the potential minimum during inflation, which suppresses the axion fluctuations and weakens the clustering of PBHs on large scales. We find that the modified model can produce a sufficient number of PBHs that seed the supermassive black holes while avoiding the observational constraints from isocurvature perturbations and angular correlation of the high-redshift quasars.

Bibliography

[1] K. Kasai, M. Kawasaki, N. Kitajima, K. Murai, S. Neda and F. Takahashi, JCAP **10** (2023), 049 doi:10.1088/1475-7516/2023/10/049 [arXiv:2305.13023 [astro-ph.CO]].

[2] K. Kasai, M. Kawasaki, N. Kitajima, K. Murai, S. Neda and F. Takahashi, [arXiv:2310.13333 [astro-ph.CO]].

Gravitational Wave

• Enhancement of gravitational waves at Q-ball decay including non-linear density perturbations [1]

In collaboration with the members of ICRR, Kavli IPMU, Tohoku Univ.

The existence of a stochastic gravitational wave background is indicated by the recent pulsar timing array (PTA) experiments. We study the enhanced production of second-order gravitational waves from the scalar perturbations when the universe experiences a transition from the early matter-dominated era to the radiation-dominated era due to Q-ball decay. We extend the analysis in previous work by including the frequency range where density perturbations go non-linear and find that the resultant gravitational wave spectrum can be consistent with that favored by the recent PTA experiment results.

• Axion curvaton model for the gravitational waves observed by pulsar timing arrays [2]

In collaboration with the members of Johns Hopkins Univ., Univ. of Chicago, ICRR, Kavli IPMU, KEK, Sokendai, Tsung-Dao Lee Institute

The stochastic gravitational wave background (SGWB) recently detected by the PTA collaborations could be the gravitational waves (GWs) induced by curvature perturbations. However, primordial black holes (PBHs) might be overproduced if the SGWB is explained by the GWs induced by the curvature perturbations that follow the Gaussian distribution. This motivates models associated with the non-Gaussianity of the curvature perturbations that suppress the PBH production rate. In this work, we show that the axion curvaton model can produce the curvature perturbations that induce GWs for the detected SGWB while preventing the PBH overproduction with the non-Gaussianity.

Bibliography

[1] M. Kawasaki and K. Murai, JCAP **01** (2024), 050 doi:10.1088/1475-7516/2024/01/050 [arXiv:2308.13134 [astro-ph.CO]].

[2] K. Inomata, M. Kawasaki, K. Mukaida and T. T. Yanagida, Phys. Rev. D **109** (2024) no.4, 043508 doi:10.1103/PhysRevD.109.043508 [arXiv:2309.11398 [astro-ph.CO]].

Dark matter

• Affleck-Dine leptogenesis scenario for resonant production of sterile neutrino dark matter [1]

In collaboration with the members of ICRR, Kavli IPMU, Tohoku Univ.

Sterile neutrino is a fascinating candidate for dark matter. In this paper, we examine the Affleck-Dine (AD) leptogenesis scenario generating a large lepton asymmetry, which

can induce the resonant production of sterile neutrino dark matter via the Shi-Fuller (SF) mechanism. We also revisit the numerical calculation of the SF mechanism and the constraints from current X-ray and Lyman-α forest observations. We find that the AD leptogenesis scenario can explain the production of sterile neutrino dark matter by incorporating a non-topological soliton with a lepton charge called L-ball. Finally, we discuss an enhancement of second-order gravitational waves at the L-ball decay and investigate the testability of our scenario with future gravitational wave observations.

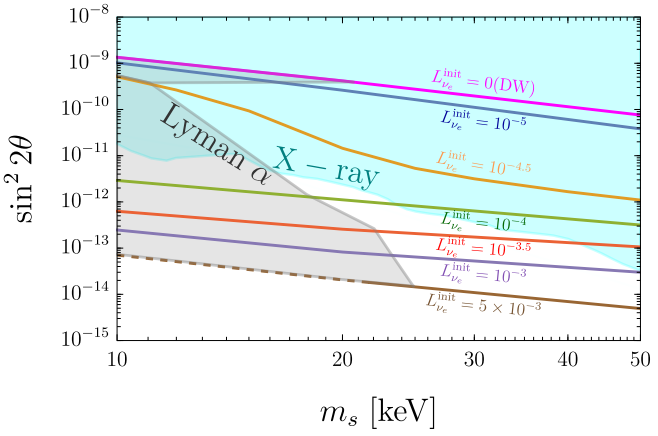


Fig. 14. m_s and $\sin^2 2\theta$ to explain all dark matter with the Lyman-α constraint (gray) and the X-ray constraint (light blue). We adopted the conservative X-ray constraint from A. Boyarsky, *et. al.* (2019), which is based on the NuStar observations.

Bibliography

[1] K. Kasai, M. Kawasaki and K. Murai, [arXiv:2402.11902 [hep-ph]].

Q-ball

• MeV gamma rays from Q-ball decay [1]

In collaboration with the members of Kanagawa Univ., ICRR, Kavli IPMU, RIKEN

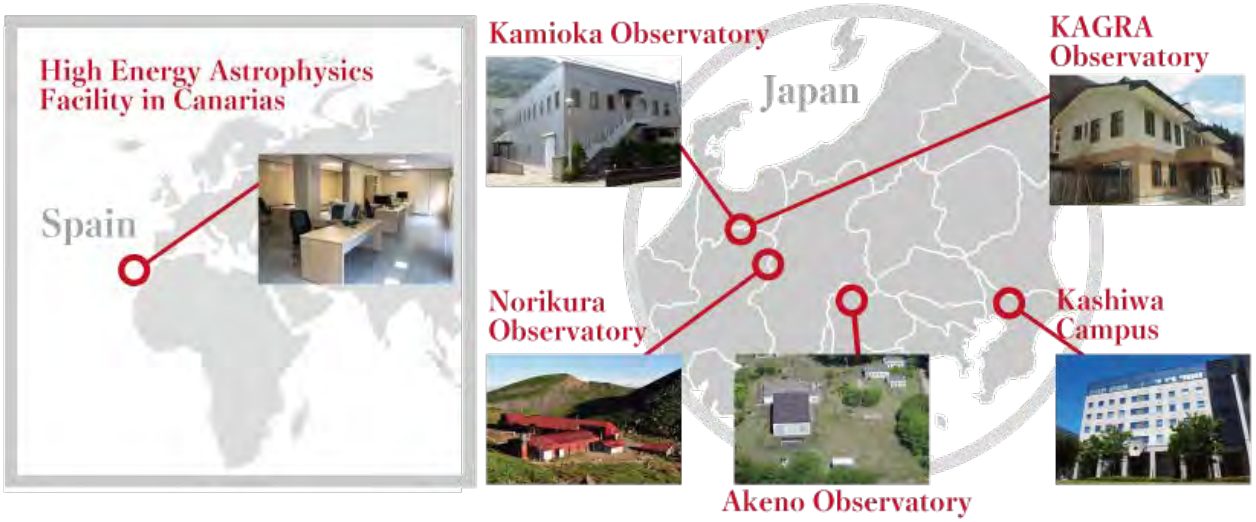
We study the supersymmetric Q balls which decay at present and find that they create a distinctive spectrum of gamma rays at around O(10) MeV. The charge of the Q ball is lepton numbers in order for the lifetime to be as long as the present age of the universe, and the main decay products are light leptons. However, as the charge of the Q ball decreases, the decay channel into pions becomes kinematically allowed towards the end of the decay, and the pions are produced at rest. Immediately, π^0 decays into two photons with the energy of 67.5 MeV, half the pion mass, which exhibits a unique emission line. In addition, $\pi^{\pm}$ decay into $\mu^{\pm}$, which further decay with emitting internal bremsstrahlung, whose spectrum has a sharp cutoff at $\sim$50 MeV. If the observations would find these peculiar features of the gamma-ray spectrum in the future, it could be a smoking gun of the supersymmetric Q-ball decay at present.

Bibliography

[1] S. Kasuya, M. Kawasaki and N. Tsuji, Phys. Rev. D **109** (2024) no.8, 083039 doi:10.1103/PhysRevD.109.083039 [arXiv:2403.01675 [hep-ph]].

OBSERVATORIES and A RESEARCH CENTER

Location of the Institute and the Observatories



Norikura Observatory

Location:	Norikuradake, Nyukawa-cho, Takayama-shi, Gifu Prefecture 506-2100
Telephone (Fax):	+81-50-3730-3809
Telephone (satellite):	+81-90-7721-5674
Telephone (car):	+81-90-7408-6224

Akeno Observatory

Location:	5259 Asao, Akeno-machi, Hokuto-shi, Yamanashi Prefecture 408-0201
Telephone / Fax:	+81-551-25-2301 / +81-551-25-2303

Kamioka Observatory

Location:	456 Higashi-mozumi, Kamioka-cho, Hida-shi, Gifu Prefecture 506-1205
Telephone / Fax:	+81-578-85-2116 / +81-578-85-2121

KAGRA Observatory

Location:	238 Higashi-mozumi, Kamioka-cho, Hida-shi, Gifu Prefecture 506-1205
Telephone / Fax:	+81-578-85-2343 / +81-578-85-2346

Research Center for Cosmic Neutrinos

Location:	5-1-5 Kashiwanoha, Kashiwa, Chiba Prefecture 277-8582
Telephone / Fax:	+81-4-7136-3138 / +81-4-7136-3115

High Energy Astrophysics Facility in Canarias

Location:	C/Via Lactea, s/n E-38205 La Lagua - Tenerife Espana

NORIKURA OBSERVATORY

Introduction

Norikura Observatory (36.10°N and 137.55°E) was founded in 1953 and attached to ICRR in 1976. It is located at 2770 m above sea level, and is the highest altitude manned laboratory in Japan (Fig. 1). Experimental facilities of the laboratory are made available to all the qualified scientists in the field of cosmic ray research and associated subjects. The AC electric power is generated by the dynamo and supplied throughout the observatory. The observatory can be accessed easily by car and public bus in summer (July-September). The 70th anniversary of Norikura Observatory was celebrated in 2023.



Fig. 1. Norikura Observatory

Norikura Observatory gave manned operation to the observations by the qualified scientists all the year until the year 2003. However, the feasibility of the automatic operation of Norikura Observatory during winter period has been tested since winter 2004 in order to study the possibilities to reduce maintenance and labor costs without causing serious inconveniences for the researches. A long-distance (∼40km) wireless LAN system (11M bps) was set up in 2003. Two new easy-to-handle and easy-to-maintain dynamos of 115 KVA each, as shown in Fig. 2 were installed in 2004 as well. The unmanned operation of Norikura Observatory has been mostly successful in winter, during which the battery backed-up solar panels and/or wind power generators kept supplying the electricity to the wireless LAN and on-going cosmic-ray experiments.

Present major scientific interests of the laboratory is focused on the modulation of high energy cosmic rays in the interplanetary space associated with the solar activity, the generation of energetic particles by the solar flares, and the particle acceleration mechanism in thunderclouds, all of which require long-term observation. These researches have been carried out by the group of user universities, where ICRR provides them with laboratory facility. A part of the facility has been open for the environmental study at high altitude such as aerosol-related mechanism in the atmosphere, observation of total ozone and UV solar radiation, for botanical study in the high-altitude environment, etc..



Fig. 2. A dynamo of 115KV.

Cosmic Ray Physics

Space weather observation using muon hodoscope

Mt. Norikura muon hodoscope has started its operation in May, 1998 aiming to observe a precursory signature of the interplanetary shock approaching the Earth. The detector succeeded for the first time to observe a loss-cone signature which is an intensity deficit within a narrow cone around the interplanetary magnetic field (IMF). The observation of the loss-cone precursor gives us unique information for the space weather forecast and for understanding the interplanetary disturbances in near Earth space. Following this successful observation, we started monitoring the intensity of ∼50 GeV cosmic rays over an entire sky around Earth with Global Muon Detector Network (GMDN). The GMDN consisted of 4 stations in Nagoya (Japan), Hobart (Australia), Sao Martinho (Brazil), and Kuwait City (Kuwait) and started operation in 2006. Muon detectors are complementary to neutron monitors monitoring a lower energy range below ∼10 GeV and the GMDN has a great advantage particularly in precise measurement of the cosmic ray anisotropy. Unfortunately, however, Mt. Norikura station became unattended station for most of the year since 2004. Because the generator is also stopped, we created a self-sustaining system that uses solar power to generate all the electricity needed. However, the weather environment at Mt. Norikura in winter is extremely harsh, and it is necessary to overcome various obstacles such as low temperatures, snowfall, and strong winds. In order to achieve stable continuous observation throughout the year, there are still many issues that need to be resolved. Meanwhile, in 2018, we installed another detector system at Syowa station in the Antarctic to expand the covering area to monitor and for integrated analysis of muon detectors and neutron monitors. The experiences at Mt. Norikura station was quite a help to start observation under severe environment in the Antarctic.

The unique feature of Syowa station is that it observes muon and neutron simultaneously, expecting a key roll for integrated analysis. Taking advantage of this feature, local environmental effects, such as temperature effect, on cosmic ray count rate were studied. A few space weather events were analyzed with this new GMDN. We found an interesting variations suggesting adiabatic acceleration in the flux rope. We also reported a result of the first integrated analysis.

Recent progresses are reported in [1][2][3][4][5][6].



Fig. 3. Solar panels at Mt. Norikura (top) and PCTs installing at Syowa station in the Antarctic (bottom).

Observation of solar neutrons in solar cycle 24 and 25

We have studied the acceleration mechanism of solar energetic particles by observing neutrons ($>$100 MeV) produced by the interaction between high energy ions and the solar atmosphere. These high energy ions are accelerated associated with very gigantic solar flares. As neutrons are neutral particles, they are thought to keep the information of the acceleration at the solar surface rather than accelerated ions which are reflected by the interplanetary magnetic field. Neutrons are attenuated by the earth's atmosphere, therefore a world-wide network of solar neutron observation has been operated since 2003. These stations are at high altitudes near the equator. The 64 m^2 solar neutron telescope at the Norikura observatory played the central role of the world-wide network. As the Norikura Observatory closes at the winter time, which is much longer than the summer time, the electricity of the solar neutron telescope had been maintained by batteries and solar cells.

Three achievements have been obtained by the observation of solar neutrons so far. The first is that the acceleration mechanism of solar energetic particles which produce solar neutrons is stochastic if it is assumed that neutrons are produced at the same time as the electromagnetic waves [7], [8]. The second is that there is at least one event neutrons are produced longer than hard X-rays [9]. The third is that the total energy which neutrons obtain during one solar flare does not exceed 0.1% of the energy of soft X-rays [10]. It is not clear the first achievement is obtained without assuming the production time of neutrons.

The observation of solar neutrons at Norikura has ceased in the summer of 2022. Several stations of the world-wide network of solar neutron observation have stopped observations recently. There are two stations which continue observing solar neutrons. One is at Sierra Negra (4,560 m) in Mexico. Another is at Chacaltaya (5,250 m) in Bolivia. The final puzzle of the acceleration mechanism of solar energetic particles is expected to be solved by the observation of these two stations. Recent progresses are reported in [11][12][13].

A new study for high precision measurement of muons

We are conducting a research to repurpose the proportional counter section of the solar neutron telescope previously operated by Nagoya University at the Norikura Observatory into a hodoscope-type high-precision muon telescope. During the unmanned operation period of the observatory, providing power to the instruments has become a challenge. It has been found that the solar panel and lead-acid battery system received from Nagoya University has serious issues with the power transmission cables from the solar panels and the lead-acid batteries. To address the issues with the power lines, we conducted repairs as much as possible, and currently, 67% of the solar panels can supply power to the power controller. As there were almost no issues with the solar panels themselves, it was revealed that the arrangement of the power lines, considering snowfall during winter, is crucial. Additionally, we have replaced the lead-acid batteries with new $LiFePO_4$ batteries, which have higher energy density and better cost performance per stored energy. Using this new system, we have been continuously operating a small-scale solar neutron telescope, a neutron monitor, and a Raspberry Pi-based environmental monitoring system since the summer of 2023. Unfortunately, the signal from the small-scale solar neutron telescope is lost just after the observatory became unmanned. However, the other instruments have been operating smoothly beyond the winter and into the 2024 spring.

Observational research on particle acceleration and cosmic-ray shower in thunderstorm electric fields via citizen science "Thundercloud Project"

Particle acceleration occurs in the strong electric field hidden by thunderclouds and lightning discharges, and various high-energy physics phenomena have been observed. This new interdisciplinary field covering cosmic ray physics, geophysics, and astronomy, is collectively called "high-energy atmospheric physics" (Dwyer et al., Space Science Reviews, 2012). For example, in the electric field in thunderclouds,

electrons are accelerated to 10 MeV or more and hit the atmosphere, producing bremsstrahlung, which is detected by ground and aircraft measurements (gamma-ray glow, Wada et al., Physical Review Research, 2018). Accelerated electrons in lightning discharges also produce bremsstrahlung. Such radiation events are detected outside the Earth's atmosphere by astronomical satellites and are called Terrestrial Gamma-ray Flash (TGF), and trigger photonuclear reactions (Enoto et al., Nature, 2017).

Our citizen science "Thundercloud Project" is a multi-site radiation monitoring of gamma rays from winter thunderclouds (gamma-ray glows) and high-energy radiation from lightning. For this project, we developed a portable radiation monitor called Compact Gamma-ray monitor (CoGaMo), which works only at the touch of a button, and installed it at about 70 locations around Kanazawa City with citizen supporters. The CoGaMo detectors have already succeeded in detecting several gamma-ray glows from thunderclouds. In particular, we reported a gamma-ray glow event coincided with a lightning discharge, suggesting a connection between the trigger of lightning and high-energy phenomena (e.g., electron acceleration) in the strong electric fields in thunderclouds [14] (Fig.4 (Top)). Mt. Norikura and other high mountains are other sites where we can detect gamma rays from thunderclouds. We are also planning to distribute CoGaMo detectors at Mt. Norikura. Furthermore, in this project, we newly developed a special board for radiation measurement called "PENGUIN," which can be used in combination with a Sony board-type computer "Spresense" (Fig.4 (Bottom)). With this board, a two-channel portable radiation monitor can be made and used for future observations.

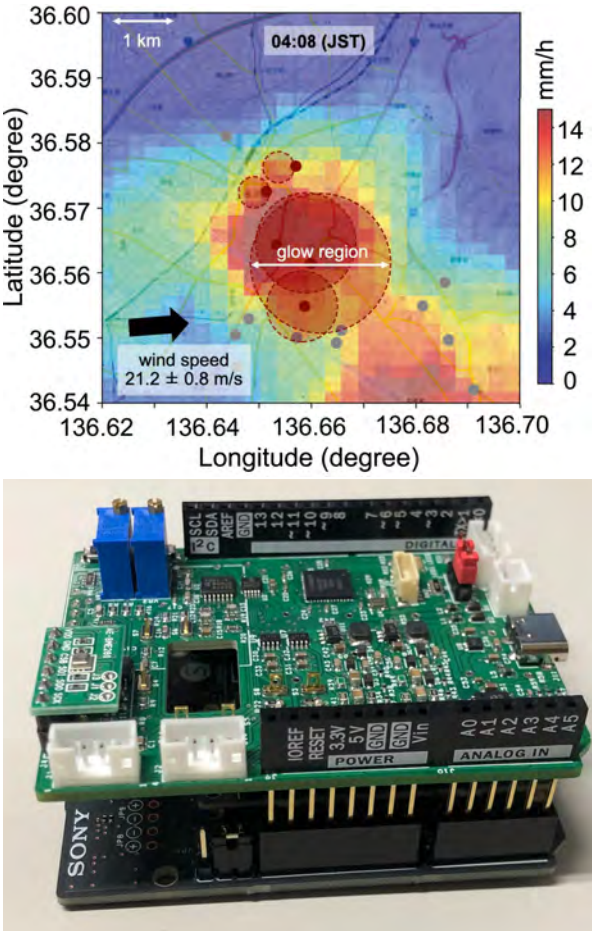


Fig. 4. (Top) Gamma-ray area irradiated from thunderclouds recorded by the Citizen Science "Thundercloud Project," overlaid on the map at Kanazawa and rainfall area estimated by radar (Tsurumi et al., GRL, 2023). (Bottom) PENGUIN (Physics and Engineering Utility Introduction) board developed for use with the Arduino-compatible board computer Sony Spresense.

Study of secondary cosmic rays from thundercloud

To study the relativistic electron acceleration mechanism by a thundercloud-derived electric field and the relation between thunder and cosmic-ray air showers, we started an experiment in 2015, mainly using gamma-ray detectors at Norikura Observatory. The experiment consists of gamma-ray detectors, a lightning sensor, an electric field meter, a weather monitor, and an air shower array consisting of five scintillation detectors. Gamma-ray detectors using three crystals, NaI, CsI, and BGO, cover a total energy range of more than three orders of magnitude from 70 keV to 120 MeV.

Observation period: 47 days from August 2nd to September 17, 2018

There were no reports of lightning near the observatory, but fluctuations in electric field meters indicating the passage of thunderclouds were observed multiple times. In particular, during the passage of Typhoon No. 21, large electric field fluctuations exceeding 100 kV/m were observed, but no significant gamma-ray flux increase in synchronization with the fluctuations was observed.

Observation period: 62 days from July 17 to September 12, 2019

There were more sunny days than usual. There were no reports of lightning strikes in the vicinity during the observation period, but several thunderclouds were passing through. The largest electric field fluctuation was around 60 kV/m caused by Typhoon No. 20 on August 16th.

Observation period: 33 days from August 4 to September 5, 2020

The experiment was conducted on a reduced scale due to activity restrictions due to the coronavirus pandemic. A lightning gamma-ray detector was installed at the Norikura Observatory, and the small air shower observation device was discontinued. The maximum electric field strength fluctuation during observation was moderate at 40 kV/m.

Observation period: 41 days from August 2nd to September 11, 2022

The experiment was conducted on the same scale as in 2019, except that a small air shower array was not installed. On August 18, when there were reports of lightning strikes and intercloud discharge within a 1 to 3 km radius, electric field fluctuations exceeding 100 kV/m, the highest during the period, were observed. However, perhaps because the discharge site was far away, no significant gamma-ray flux exceedances synchronized with fluctuations were observed.

Observation period: 24 days from August 14 to September 6, 2023

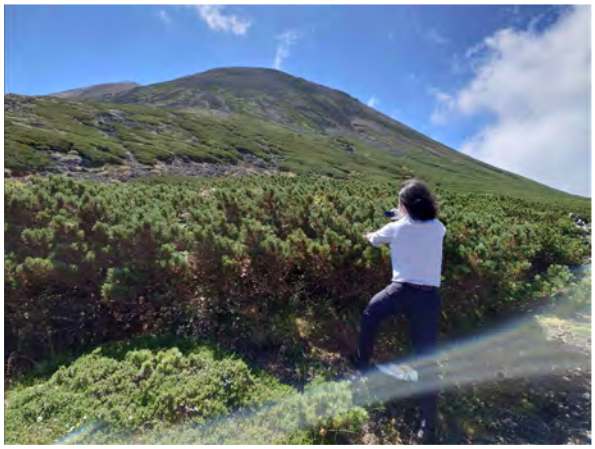
During the observation period, there were many sunny and cloudy skies, there were no lightning events in the vicinity, and the electric field fluctuation was only observed to be around 45 kV/m at the maximum. We hope to continue observing electric field fluctuation events of 100 kV/m or more, where we can expect an increase in gamma rays due to the electric field.

Research on annual variations of ^{14}C concentration in *Pinus pumila*

Radiocarbon (^{14}C) is a cosmogenic nuclide that is mainly produced in the atmosphere by high energy cosmic-rays. The radiocarbon is collected from the atmospheric CO_2 and fixed in tree rings by the photosynthesis. Solar activities and the extremely intense cosmic-ray events in the past have been investigated by measuring the ^{14}C concentration in the annual tree rings of old wood. However, since the amount of CO_2 in the atmosphere is affected by the global carbon cycle, the ^{14}C concentration in tree annual rings shows a delayed and attenuated response from the rate of the production. Thus, it is important to investigate the dependence of ^{14}C concentration in the plant using modern samples for which the number of sunspots and the amount of secondary cosmic rays are accurately observed.

Since 2018, we have been continuously collecting cones and leaves of *Pinus pumila* that live in the alpine zone of Mt. Norikura (Fig.5 (Top)) and Mt. Zao, and measuring ^{14}C concentrations using a high-sensitivity accelerator mass spectrometer at Yamagata University. In addition, to compare the effects of fossil fuels, *Pinus densiflora* samples were collected from urban areas in Tokyo and Tendo city, Yamagata Prefecture, and their ^{14}C concentrations were also investigated. Figure 5 (bottom) shows the ^{14}C concentration (Δ^{14}C) in cone seeds for each sample collection year. The ^{14}C concentration in *P. pumila* samples collected from Mt. Norikura and Mt. Zao decreased from 2018 to 2023. The Δ^{14}C values in *P. densiflora* samples from Tendo city were lower of Δ^{14}C in all years than those from Mt. Norikura and Mt. Zao, and no dependence on collection year was observed. *P. densiflora* samples from Tokyo showed the lowest Δ^{14}C values in all years among the samples collected, which also showed a decreasing trend from 2019 onwards. We plan to continue collecting data.

Recent progresses are reported in [15][16][17][18][19].



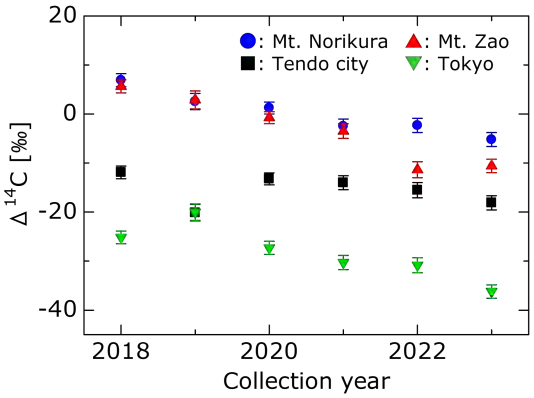


Fig. 5. (Top) Condition when collecting *Pinus pumila* at Mt. Norikura. (Bottom) Δ^{14}C values in cone seeds for each sample collection year.

Technical Development

Test experiment of the Fuel cell

The Norikura Observatory is currently unmanned from the end of October until July of the following year. During this period, even the diesel generator is offline, posing a substantial problem to continuous cosmic ray observation. Presently, a combination of solar panels and lead-acid batteries supplies power to detectors for this duration, but the output is naturally subject to weather conditions. Consequently, the motivation for research lies in utilizing environmentally friendly fuel cells to provide electricity more reliably for the period. Upon consultation with fuel cell system vendors and investigation of the operational performance of a small-scale fuel cell experimentally introduced by the observatory which experienced failures within a few years, several issues related to the observatory's location have emerged, namely its altitude of 2770 meters in a high mountainous area within a national park. Taking these factors into account, it has been concluded that, for the time being, efforts should be directed towards enhancing the stability of the conventional solar panel and battery system, with fuel cells serving a supplementary role.

Environmental Study

Monitoring the cloud water quality for evaluation of the SO_2 in-cloud oxidation process

In East Asia (China), the rapid economic growth has increased the fuel consumption, and the associated emissions from fossil fuels have risen since the 1980s [20]. The main substances are the primary aerosols, sulfur dioxide (SO_2), nitrogen oxides (NO_x), volatile organic compounds (VOC), ammonia (NH_3). Of these, the atmospheric SO_2 emitted from thermal power plants and factories progressively increased since 1980 and turned to decline from 2006. This is because since 11th Five-Year Plan (2006-2010), the Chinese government has set a restrictive target on SO_2 reduction and implemented flue-gas desulfurization (FGD) system. Since 2011, the FGD penetration in thermal power plants rapidly in-

creased, leading to the decreasing trend until the present-day.

It is well known that gaseous SO_2 is highly dissolved into cloud droplets and the subsequent oxidation brings formation of H_2SO_4, thereby generating acidic cloud and rain [21]. Such acidic substances are also thought to lead severe problem on terrestrial ecosystem and environment such as forests decline, acidity of lake and river, fish dead, etc. In the 1960-1990s, clouds of strong acid (pH = 3 to 4) were observed near the summit of Mt. Norikura [22][23][24]. Therefore, we have monitored the cloud water quality in this site (Fig.6 (Top)) to assess in-cloud oxidation (acidification) of gaseous SO_2 during summertime in 1999-2000 and 2022-2023. As a result, the cloud pH increased from 4.0 to 4.7 during the past 20 years (Fig.6 (Bottom)), while the NO_3^- and SO_4^{2-} concentrations of cloud water reduced to less than one-fifth, suggesting that cloud water is neutralized and purified. However, the cloud water H_2O_2 and O_3, the most important oxidant for gaseous SO_2 oxidation, were approximately the same level as 20 years ago.

Recent progresses are reported in [25][26][27][28].

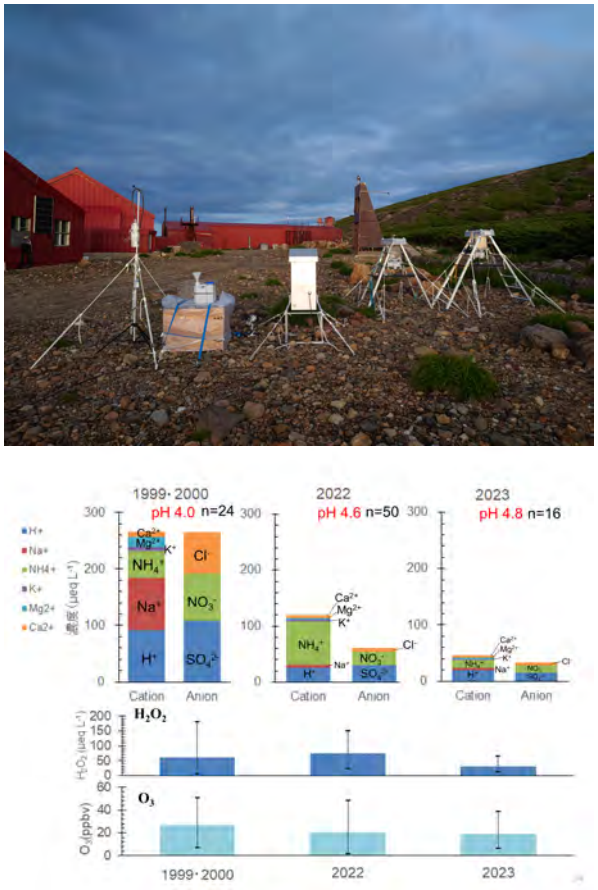


Fig. 6. (Top) Photograph showing gases, rainwater, cloud water, and aerosol sampling. (Bottom) Comparisons of cloud water and gas during 1999-2000, 2022, and 2023 at Mt. Norikura: (a) chemical compositions of cloud water; (b) H_2O_2 concentration of cloud water, and (c) O_3 gas concentration.

Seasonal and diurnal variations in soil respiration rates at a treeline ecotone

This study examined the seasonal and diurnal variations in soil respiration rates (R_S) during a growing season at the treeline ecotone (2800 m) on a volcanic mountain in Japan, using an automated measurement equipment. The aboveground biomass, the total R_S during the growing season, and the R_S per day during the growing season were low at 2800 m. Seasonal R_S variations positively correlated with those of soil and air temperatures. The mean volumetric soil water content (W_S) during the growing season was much low because of the scoria substrate. The monthly mean diel cycle of R_S was positively correlated with the soil temperature every month. The R_S decreased during the daytime especially in August, despite no changes in the W_S. Seasonal and diurnal R_S variations could be reproduced from soil and air temperatures, and W_S. Estimating soil respiration rate from these variables will help understand the future carbon budget of forests due to global warming.

Recent progresses are reported in [29][30][31][32][33][34][35].

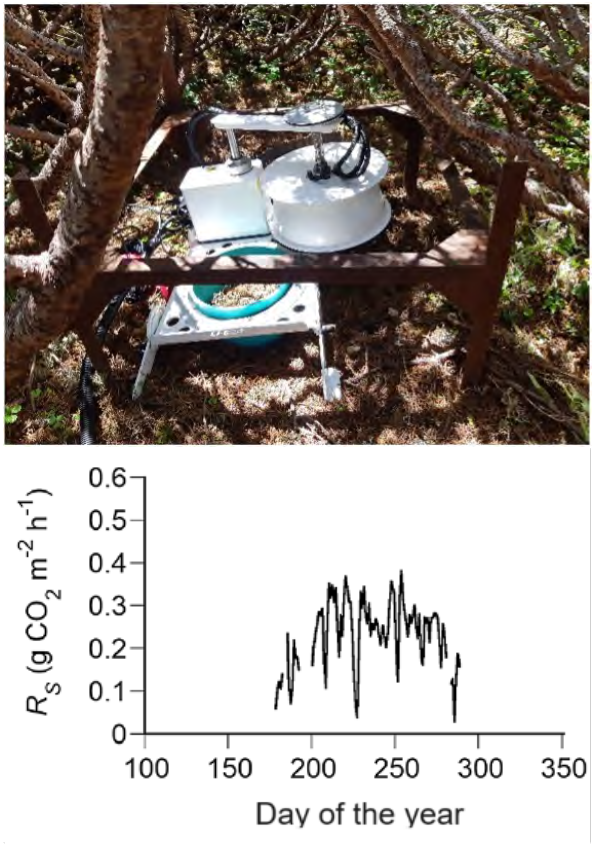


Fig. 7. (Top) Automated soil respiration measurement system in the *Pinus pumila* scrub. (Bottom) The seasonal change in daily mean soil respiration rates (R_S).

Bibliography

[1] R. Kataoka, T. Sato, C. Kato, A. Kadokura, M. Kozai, S. Miyake, K. Murase, L. Yoshida, Y. Tomikawa, and K. Munakata. Local environmental effects on cosmic ray observations at Syowa Station in the Antarctic:

PARMA-based snow cover correction for neutrons and machine learning approach for neutrons and muons. Journal of Space Weather and Space Climate, 12:37, October 2022.

[2] K. Munakata, M. Kozai, C. Kato, Y. Hayashi, R. Kataoka, A. Kadokura, M. Tokumaru, R. R. S. Mendonça, E. Echer, A. Dal Lago, M. Rockenbach, N. J. Schuch, J. V. Bageston, C. R. Braga, H. K. Al Jassar, M. M. Sharma, M. L. Duldig, J. E. Humble, I. Sabbah, P. Evenson, P. S. Mangeard, T. Kuwabara, D. Ruffolo, A. Sáiz, W. Mitthumsiri, W. Nuntiyakul, and J. Kóta. Large-amplitude Bidirectional Anisotropy of Cosmic-Ray Intensity Observed with Worldwide Networks of Ground-based Neutron Monitors and Muon Detectors in 2021 November. ApJ, 938(1):30, October 2022.

[3] W. Kihara, K. Munakata, C. Kato, R. Kataoka, A. Kadokura, S. Miyake, M. Kozai, T. Kuwabara, M. Tokumaru, R. R. S. Mendonça, E. Echer, A. Dal Lago, M. Rockenbach, N. J. Schuch, J. V. Bageston, C. R. Braga, H. K. Al Jassar, M. M. Sharma, M. L. Duldig, J. E. Humble, P. Evenson, I. Sabbah, and J. Kóta. A Peculiar ICME Event in August 2018 Observed With the Global Muon Detector Network. Space Weather, 19(3):e02531, March 2021.

[4] C. Kato, W. Kihara, Y. Ko, A. Kadokura, R. Kataoka, P. Evenson, S. Uchida, S. Kaimi, Y. Nakamura, H. A. Uchida, K. Murase, and K. Munakata. New cosmic ray observations at Syowa Station in the Antarctic for space weather study. Journal of Space Weather and Space Climate, 11:31, January 2021.

[5] R. R. S. Mendonça, C. Wang, C. R. Braga, E. Echer, A. Dal Lago, J. E. R. Costa, K. Munakata, H. Li, Z. Liu, J. P. Raulin, T. Kuwabara, M. Kozai, C. Kato, M. Rockenbach, N. J. Schuch, H. K. Al Jassar, M. M. Sharma, M. Tokumaru, M. L. Duldig, J. E. Humble, P. Evenson, and I. Sabbah. Analysis of Cosmic Rays' Atmospheric Effects and Their Relationships to Cutoff Rigidity and Zenith Angle Using Global Muon Detector Network Data. Journal of Geophysical Research (Space Physics), 124(12):9791–9813, December 2019.

[6] K. Munakata, T. Kuwabara, S. Yasue, C. Kato, S. Akahane, M. Koyama, Y. Ohashi, A. Okada, T. Aoki, H. Kojima and J. W. Bieber, "A "loss-cone" precursor of an approaching shock observed by a cosmic-ray muon hodoscope on October 28, 2003", Geophys. Res. Lett., 32, L03S04-1 4, doi:10.1029/2004GL021469, 2005 (January 11).

[7] Watanabe, K., et al., Astrophys. J., 592, 590-596, 2003

[8] Watanabe, K., et al., Astrophys. J., 636, 1135-1141, 2006.

[9] Sako, T., et al., Astrophys. J. Lett., 651, L69-L72, 2006.

[10] Lopez, D., et al., Astropart. Phys., 76, 19-28, 2016.

[11] Matsubara, Y., Gound level observation of solar neutrons (Japanese), RADIOISOTOPES, 68, 907-915, 2019.

[12] Muraki, Y., et al., Possible detection of solar gamma-rays by ground-level detectors in solar flares on 2011 March 7, Publ. Astron. Soc. Jpn, 72, 1-17, 2020.

[13] Newton-Bosch, J., et al., Atmospheric electric field effects on cosmic rays detected by the solar neutron telescope at Sierra Negra, J. Atmos. and S.-T. Phys., 253, 106156, 2023.

[14] Tsurumi, Enoto, Ikkatai, et al., "Citizen Science Observation of a Gamma-Ray Glow Associated With the Initiation of a Lightning Flash", Geophysical Research Letters, Volume 50, Issue 13, e2023GL103612 (2023).

[15] M. Takeyama, T. Moriya, H. Sakurai, H. Miyahara, F. Tokanai, Research of annual variations of ^{14}C concentrations in pinus pumila V, Extended Abstracts of the 84th JSAP Autumn Meeting, 20a-A310-3 (2023).

[16] M. Takeyama, T. Moriya, H. Sakurai, H. Miyahara, F. Tokanai, Research of annual variations of ^{14}C concentrations in pinus pumila IV, Extended Abstracts of the 83rd JSAP Autumn Meeting, 22a-C205-3 (2022).

[17] M. Takeyama, T. Moriya, H. Sakurai, H. Miyahara, F. Tokanai, Research of annual variations of ^{14}C concentrations in pinus pumila III, Extended Abstracts of the 82nd JSAP Autumn Meeting, 11a-N402-7 (2021).

[18] M. Takeyama, T. Moriya, H. Sakurai, H. Miyahara, F. Tokanai, Research of annual variations of ^{14}C concentrations in pinus pumila II, Extended Abstracts of the 81st JSAP Autumn Meeting, 8a-Z25-10 (2020).

[19] M. Takeyama, T. Moriya, H. Sakurai, H. Miyahara, F. Tokanai, Research of annual variations of ^{14}C concentrations in pinus pumila, Extended Abstracts of the 67th JSAP Spring Meeting, 14p-D209-4 (2020).

[20] Ohara,T. and Kurokawa, J. (2018) Long-term variation of emissions of air pollutants related to atmospheric aerosol in Asia, China and Japan. Earozoru Kenkyu 33: 95-101 (in Japanese).

[21] Seinfeld, J. H. and Pandis, S. N. (1998) Atmospheric chemistry and physics, John Wiley & Sons, New York, p. 1326, 1152.

[22] Okita, T.(1968). Concentration of sulfate and other inorganic metals in fog and cloud water and in aerosol. Journal of Meteorological Society Japan 46: 120-127.

[23] Minami Y. and Ishizaka Y. (1996). Evaluation of chemical composition in fog water near the summit of a high mountain in Japan. Atmospheric Environment 30: 3363-3376.

[24] Watanabe, K., Ishizaka, Y. and Takenaka, C. (1999). Chemical composition of Fog water near the summit of Mt. Norikura in Japan. Journal of Meteorological Society Japan 77: 997-1006.

[25] Kagawa, M., Katsuta, N. and Ishizaka, Y. (2021) Chemical characteristics of cloud water and the sulfate production under excess hydrogen peroxide in a high mountains region of central Japan. Water, Air, and Soil Pollution 237:177.

[26] Kagawa, M., Katsuta, N. and Ishizaka, Y. (2022) Selenite and selenate in clouds at a high-altitude mountain location in Central Japan. Atmospheric Research 276:106253.

[27] Kagawa, M., Katsuta, N., Naito, S., Masuki, Y., Yoshimizu, C., Chiba, H. and Tayasu, I. (2023) Sample pretreatment effects on isotopic compositions of oxygen and sulfur in $BaSO_4$ derived from atmospheric sulfate. Rapid Communications in Mass Spectrometry 37: e9659.

[28] Masako Kagawa (2023) Study of the dynamics of selenium in relation to the transport and oxidation of sulfur compounds in the atmosphere. The united graduate school of agricultural science, Gifu University. Doctor of Agriculture No.165.

[29] Takahashi, K., Otsubo, S. & Kobayashi, H. (2018) Comparison of photosynthetic traits of codominating subalpine conifers Abies veitchii and A. mariesii in central Japan. Landscape and Ecological Engineering 14: 91–97.

[30] Tateno, R., Tatsumi, C., Nakayama, M., Takahashi, K., Kerfahi, D. & Adams, J. (2019) Temperature effects on the first three years of soil ecosystem development on volcanic ash. Catena 172: 1–10.

[31] Takeda, S. & Takahashi, K. (2020) Elevational variation in abundance of coarse woody debris in subalpine forests, central Japan. Forest Ecology and Management 473: 118295.

[32] Takahashi, K. (2021) Productivity does not decrease at the climate extremes of tree ranges in the Japanese archipelago. Oecologia 197:259–269.

[33] Shimada, R. & Takahashi, K. (2022) Diurnal and seasonal variations in photosynthetic rates of dwarf pine Pinus pumila at the treeline in central Japan. Arctic, Antarctic, and Alpine Research 54:1–12.

[34] Takeda, S., Majima, R., Makita, N. & Takahashi, K. (2023) Five-year measurement data along a 1200 m elevational gradient reveals that global warming increases soil respiration. Frontiers in Forest and Global Change 6: 1145474.

[35] Takeda, S., Makita, N. & Takahashi, K. (2024) Seasonal and diurnal variations in soil respiration rates at a treeline ecotone and a lower distribution limit of subalpine forests. Journal of Plant Research.

AKENO OBSERVATORY

Introduction

The Akeno Observatory is situated in Akeno of Hokuto-city, 20 km northwest of Kofu and 130 km west of metropolitan Tokyo. The location is at the longitude of 138.5°E and the latitude of 35.8°N. The altitude is ∼900 m above sea level. It was established in 1977 as a research center for air shower studies in the very high energy region, and it has been administered by the ICRR as a facility of joint-university-use.

The 40th anniversary of the Akeno Observatory was held in 2017.

Akeno Air Shower Experiments

The Akeno Air Shower Experiment started in 1979 with an array covering 1 km^2 area (the 1 km^2 array, see Fig.1). The array was enlarged to 20 km^2 in 1984 and was gradually expanded to the Akeno Giant Air Shower Array (AGASA) of approximately 100 km^2 area by 1990. The AGASA was built

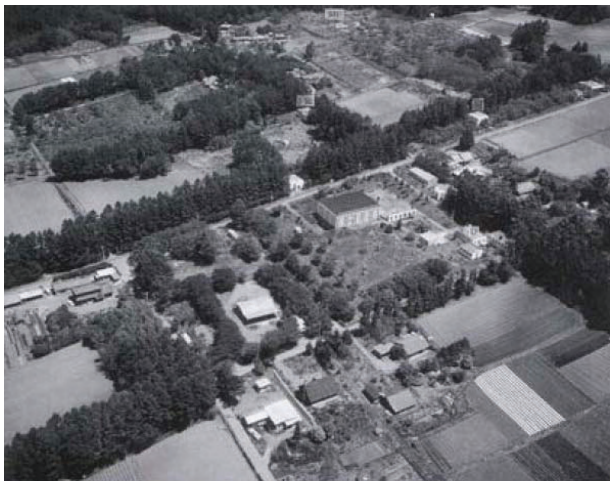


Fig. 1. Aerial View of Akeno Observatory and 1 km^2 Array Area

to detect Ultra-High Energy Cosmic Rays (UHECRs) in the energy range of 10^{20} eV.

One of the distinctive features of Akeno experiments is that the measurements were made over five decades of energies well covering 10^{15} eV - 10^{20} eV by using both the surface detector for electromagnetic component, and the shielded detector for muon component (Fig.2). The wide energy coverage was accomplished by the arrays of scintillation detectors of various inter-detector spacings from 3 m to 1 km and with different triggering conditions. This feature of Akeno air shower measurement is well demonstrated in Fig.3, in which the spectra from Akeno 1 km^2 array for $10^{14.5}$ eV - $10^{18.8}$ eV [1] and AGASA for $10^{18.5}$ eV - $10^{20.3}$ eV [2] are plotted.

*1 M. Nagano et al., J. Phys. **G10**, 1295 (1984); M. Nagano et al., J. Phys. **G18**, 423 (1992).

*2 M. Takeda et al., Astropart. Phys. **19**, 447 (2003).



Fig. 2. One of the muon detector housings with concrete shielding.

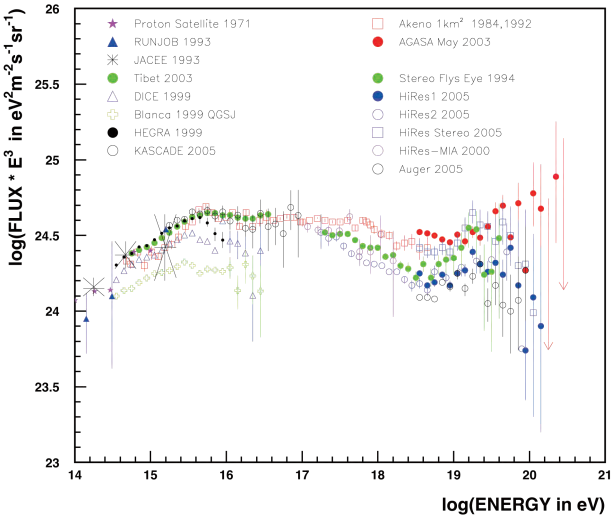


Fig. 3. Akeno energy spectrum measurements for 10^{15} eV - 10^{20} eV.

AGASA

The AGASA was composed of 111 surface detectors, each with plastic scintillator of 2.2 m^2 area and 5 cm thickness. The counters were deployed with ∼1 km spacing covering the ground area of approximately 100 km^2 in the suburban area of Akeno, outside of the observatory campus. The AGASA served as the largest air shower array in the world since its commissioning in 1990 until it stopped data taking in January 2004, when the construction of the succeeding experiment, Telescope Array (TA), started in Utah. The AGASA was dismantled in 2007 together with other Akeno air shower arrays.

An exposure of 5.8 × 10^{16} m^2 s sr above 10^{19} eV was accumulated by AGASA in 13 years of operation. Extensive air showers with zenith angles smaller than 45° and with core

locations inside the array area were used for the analysis. The AGASA reported an extension of the energy spectrum beyond the predicted Greisen-Zatsepin-Kuzmin (GZK) cutoff in 1998 [3] and a total of eleven UHECR events were observed above 10^{20} eV by 2003.

Measurement of UHECRs

Since the AGASA measurement in 1998, the High Resolution Fly's Eye (HiRes) [4], the Pierre Auger Observatory (PAO) [5], and the Telescope Array (TA) [6] measured the energy spectra of UHECRs with higher statistics.

The HiRes observed the UHECR using the fluorescence telescope. The PAO and the TA measure the energy spectra using the surface array consisting of either water tanks (PAO) or plastic scintillators (TA), but the energy scale of the array is determined by the fluorescence telescope using a subset of events observed by the fluorescence telescope and surface array at the same time. The adoption of the energy scale by the fluorescence telescopes is based on its small dependence on the air shower simulation.

The energy spectra above 10^{18} eV by AGASA and other experiments are compiled and compared by the working group represented by UHECR experiments in the UHECR2012 symposium held in 2012 [7]. The result is plotted in Fig.4 with the energy scale of each experiment adjusted to a reference energy, which is set halfway between PAO and TA/HiRes.

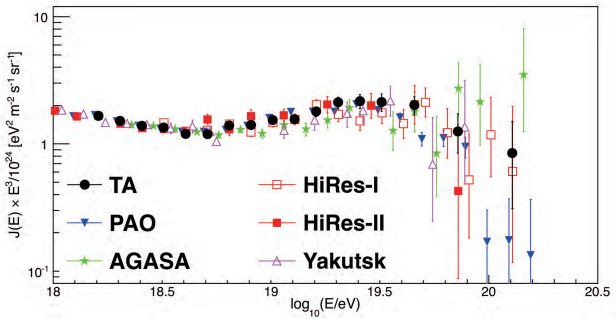


Fig. 4. Compilation of UHECR energy spectra (UHECR2012). The energy scales were adjusted as ×1.10 for PAO, ×0.91 for TA and HiRes, ×0.65 for AGASA and ×0.56 for Yakutsk.

The HiRes, PAO and TA confirmed a flux suppression above approximately $10^{19.7}$ eV. Although the AGASA spectrum does not demonstrate the cutoff structure, the number of events above 10^{20} eV became only two after the energy rescaling, making the claim of the extended spectrum statistically insignificant. The estimate of systematic uncertainty of the energy measurement is approximately 20% for all the experiments, and rescalings for the TA/HiRes and PAO are within this limit. Rescaling of the surface array energy for AGASA and Yaktsuk indicates that there exist larger systematic uncertainties than originally estimated by running the air shower simulation. This difference of energy scale obtained by the surface array and by the fluorescence telescope remains as a basic question in the understanding of the air shower phenomena.

Recent Research Activities

The study of UHECRs by AGASA in Akeno was succeeded by the TA experiment in Utah, USA since 2008. After the cessation of AGASA, the Akeno Observatory has been used for small scale cosmic ray experiments, astrophysical observations and as a test and maintenance facility by the ICRR and university researchers. Fig.5 shows a recent photograph of the main site of the Akeno Observatory.

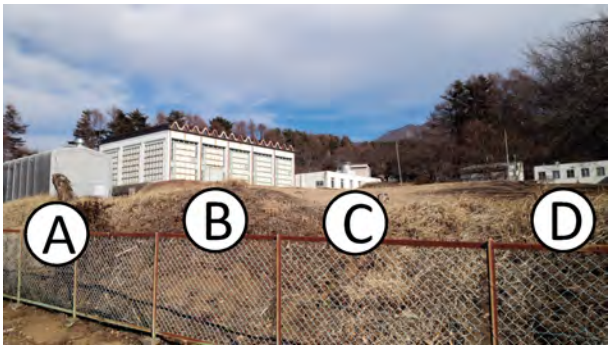


Fig. 5. The main site of the Akeno Observatory. There are the movable tent for a small atmospheric Cherenkov telescope (A), the large experimental hall (B), the research building (C) and the lodging facility (D) from the left.

In 2020, as countermeasures against COVID-19 infection, an air conditioner and a heat-exchange ventilator were installed in the large room of the research building, and a heat-exchange ventilator was installed in the dining room of the lodging facility along with some other measures.

Observation by the multi-color imager for transients, survey and monstrous explosions (MITSuME) by N. Kawai (Tokyo Institute of Technology) et al.

One of the three MITSuME robotic telescopes was installed in the Akeno Observatory in 2003 (Fig. 6). The telescope has an aperture of 50 cm, an FOV of 28' × 28' and is equipped with a tricolor CCD camera capable of $g'R_CI_C$-bands photometry (g':400∼550 nm, Rc:570∼730 nm, Ic:730∼ 850 nm). It is operated remotely from the Tokyo Tech at the Ookayama Campus via a dedicated line. The operation of the telescope has continued in FY2021 as described below [8].

Upon receiving a GRB alert, it directs the telescope toward the GRB direction within two minutes, and makes a prompt observation of the GRB and its afterglow. The follow-up observation of GRBs was continued by the MITSuME telescope. Information about GRB events was reported to Gamma-Ray Burst (GRB) Coordinates Network Circular (GCNC).

In order to perform follow-up visible-light observations of gravitational wave objects, the MITSuME participated in

*3 M. Takeda et al., Phys. Rev. Lett. **81**, 1163 (1998).
*4 R.U. Abbasi et al., Phys. Rev. Lett. **100**, 101101 (2008).
*5 J. Abraham et al., Phys. Lett. **B685**, 239 (2010).
*6 T. Abu-Zayyad et al., Astrophys. J. **768**, L1 (2013).
*7 http://indico.cern.ch/conferenceDisplay.py?confId=152124

*8 N. Kawai et al., Research Result Presentations Meeting of the ICRR Inter-University Research Program 2021.

J-GEM (Japanese collaboration for Gravitational-wave ElectroMagnetic follow-up) and GROWTH(Global Relay of Observatories Watching Transients Happen) to establish worldwide observation network focusing on the electromagnetic identification of gravitational wave sources as one of scientific themes. In FY2021, the observation of gravitational wave by LIGO/Virgo was stopped. Therefore, the MITSuME participated in the follow-up observation of IceCube neutrino events that was derived from J-GEM.

The MITSuME team also conducted long-term monitoring observations of X-ray binary starts and blazars. The MITSuMe has also participated OISTER (Optical and Infrared Synergetic Telescopes for Education and Research).



Fig. 6. The dome in which the MITSuME telescope was installed in Akeno.

Observation of galactic cosmic rays by large area muon telescope by A. Oshima (Chubu University) et al.

Telescopes consisting of four layers of proportional counter tubes, each covering an area of 25 square meters, have been operating in three muon houses at the Akeno Observatory, continuously measuring cosmic ray muons since 2003. Figure 2 shows one of the three muon houses, M8. The modal energy of the primary cosmic rays is approximately 2.5 GeV, corresponding to a 2-meter-thick concrete ceiling of the muon house at the latitude of the Akeno Observatory. The Akeno muon observation complements the muon observations conducted by the GRAPES-3 experiment in Ooty, India. Our muon observation aims to measure the modulation effects and anisotropy of galactic cosmic rays in the region of around 100 GeV and to detect transient phenomena of cosmic rays. This is expected to help us understand the flow of cosmic rays in the interplanetary magnetic field and provide clues to solve the mysteries of cosmic ray propagation. Additionally, we are challenging the establishment of a new space weather observation method through simultaneous multi-directional observations with high statistical precision. We have been updating the aging data acquisition system, and in 2018, the repair of the data acquisition system at M5 was completed. Since then, continuous observations have been conducted at M5, except during power outages and other interruptions. Currently, there are plans to upgrade the data acquisition system for the Akeno muon observation to an FPGA-based circuit. This upgrade will be implemented sequentially for M1, M8, and M5.

Research and development for a small atmospheric Cherenkov telescope at the Akeno Observatory by T. Yoshikoshi (ICRR) et al.

An alt-azimuth telescope with an aperture of three meters (Fig. 7) was setup in the Akeno Observatory for various prototype tests with atmospheric Cherenkov observations of gamma rays on the ground [9]. This telescope is the only telescope to observe atmospherice Cherenkov light emitted from air showers induced by TeV gamma rays in Japan.

In January 2021, the telescope was used to observe the Crab Pulsar in the visible light region for about ten hours. The collected data were analyzed in FY2021. The result was used to improve the signal-to-noise ratio of the Crab Pulsar observation and to study the removal of external noise.

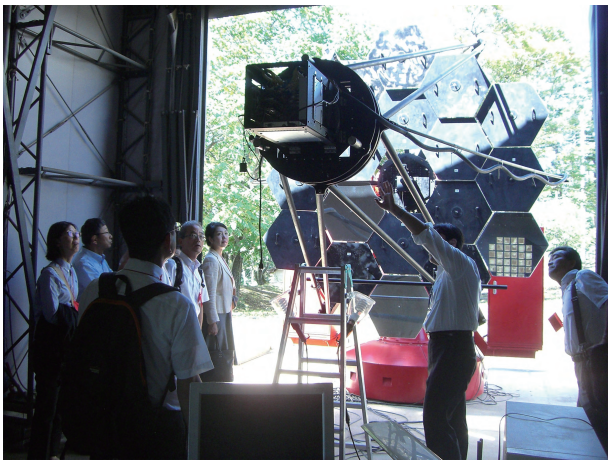


Fig. 7. The Cherenkov telescope at the tour of the 40th anniversary of the Akeno Observatory in 2017.

Dark matter and Interstellar Meteoroid Study (DIMS) at the Akeno Observatory by F. Kajino (Konan University) et al.

The Dark Matter and Interstellar Meteoroid Study (DIMS) is a new experiment that aims at searching for macroscopic dark matter and interstellar meteoroids [10][11][12]. Nuclearites are nuggets of stable Strange Quark Matter (SQM), which are neutral in charge and hypothetical super-heavy macroscopic particles (macros), and may be important components of the dark matter in our universe. Nuclearites of galactic origins is expected to have a typical velocity of about 250 km/s in galactic frame. The DIMS team studies the possibility of searching for such fast moving particles using very high-sensitivity CMOS camera with a wide field of view. In the first stage, the DIMS system consists of 4 high-sensitivity CMOS camera stations. and is going to be constructed at the Telescope Array cosmic-ray experimental site in Utah, USA. Due to COVID-19 pandemic, the DIMS team did not transport the DIMS systems to Utah, and one of the systems was installed on the roof of the research building at the Akeno Observatory as shown in Fig. 8. The observed Geminids Meteor Shower taken by

[*9] M. Ohishi et al., 33rd ICRC, (Rio deJaneiro), 587 (2013).
[*10] D. Barghini et al., PoS(ICRC2021)500.
[*11] D. Shinto et al., PoS(ICRC2021)502.
[*12] F. Kajino et al., PoS(ICRC2021)554

the DIMS camera at the Akeno Observatory was shown in Fig. 9. The preliminary results on limiting magnitudes of stars and the number of meteors as a function of magnitude were reported [13]. Three camera systems are installed at the Kiso Observatory, Shinshu University and Akeno Observatory for stereoscopic observations.



Fig. 8. The DIMS camera installed on the roof of the research building at the Akeno Observatory in August 2021.



Fig. 9. Geminids Meteor Shower that was taken by DIMS camera at the Akeno Observatory on December 13th, 2021. Approximately 500 meteoroids are superimposed on the photograph.

Research and development for the Telescope Array observation in Utah by the TA collaboration and others

All the TA fluorescence imaging cameras and a part of the TA surface detectors were assembled in the Akeno Observatory by the TA collaboration team. All the unit mirrors of the TA fluorescence telescope were tested and the atmospheric monitoring lidar of TA using YAG laser was developed. In JFY 2015, the R&D of the surface detectors were performed for the TAx4 project that aims at quadrupling the TA surface detector array in Utah. In August in 2016, 2017 and 2018 the TAx4 and TALE (TA Low Energy extension) scintillator counters were assembled.

The assembly of the surface detectors for the TALE-infill array [14] that is described in the TA section was scheduled at the Akeno Observatory in 2020, but due to the COVID-19 epidemic, the assembly had to be postponed. The 50 surface detectors for the TALE-infill array were assembled at the Akeno Observatory from the middle of October to early November in 2021. Figure 10 shows one of the surface detectors that was being assembled.



Fig. 10. A surface detector for the TALE-infill array that was being assembled at the Akeno Observatory. The student was aligning the ends of bundled fibers.

*[13] F. Kajino et al., Research Result Presentation Meeting of the ICRR Inter-University Research Program 2021.

*[14] S. Ogio et al., "The status of the TALE surface detector array and a TALE infill project", PoS(ICRC2021)255.

KAMIOKA OBSERVATORY

Located in Kamioka town, Hida city, Gifu Prefecture, about 200 km west of Tokyo, Kamioka Observatory was established in 1995 to operate the Super-Kamiokande experiment (SK). The laboratories are located 1000 m underground (2700 m water equivalent) in the Kamioka mine, accessible through a 1.7 km horizontal tunnel. Surface research buildings and dormitories are a 15-minute drive from the underground laboratories. In addition, the next-generation neutrino experiment project, Hyper-Kamiokande, began its construction in 2020 with the University of Tokyo and KEK as host organizations. The construction is currently underway underground in the Kamioka mine, with the aim of beginning observations in 2027.

The Super-Kamiokande experiment made groundbreaking discoveries regarding neutrino oscillations by observing atmospheric and solar neutrinos. The discovery of atmospheric neutrino oscillation was further confirmed by a long baseline neutrino oscillation experiment, K2K, which ran from 1999 to 2004 using an accelerator neutrino beam produced by KEK proton synchrotron accelerator. The successor T2K experiment, which began in 2009, used a higher-intensity neutrino beam from the J-PARC proton accelerator. In 2011, T2K provided the first indication of the conversion of muon neutrinos into electron neutrinos. Since 2014, T2K has been using a muon anti-neutrino beam to investigate the differences between neutrino and anti-neutrino oscillations, aiming to understand why matter exists in the universe.

The underground site's low cosmic ray flux and low seismic noise environment make it ideal for various particle physics and astrophysics studies. A dark matter experiment conducted in Lab-C, called XMASS, started in 2010 using an 800-kg liquid xenon detector. The data collection ended in 2019, and the experiment yielded valuable low-background data for dark matter interactions and rare phenomena. A 100-m-long laser interferometer, a prototype for the 3-km gravitational wave antenna (KAGRA), was also located at the observatory. The NEWAGE experiment, conducted in Lab-B, focused on a tracking-type detector for dark matter detection, led by the Kobe University group. CANDLES, a double beta decay experiment using ^{48}Ca led by the Osaka University group, is ongoing in Lab-D.

The SK-Gd project aims to improve neutrino detection sensitivity by adding gadolinium to Super-Kamiokande, and the research has been conducted in Lab-E. A low-background Germanium detector and an inductively coupled plasma mass spectrometry system were installed in Lab-1 and Lab-A to measure extremely low-radioactivity backgrounds. The Lab-G area was excavated in 2015, and by 2016, SK-Gd equipment, including a Gd dissolving system, pre-treatment system, and Gd-water circulation system, was installed. Additional preparations for Gd loading were performed. In 2018, work was conducted to repair a water leak from the SK tank, and tests on the SK-Gd equipment were carried out in 2019. In 2020, soluble Gd salt was added to pure water to achieve a Gd concentration of 0.03% by 2022. This upgrade allows the identification of low-energy anti-neutrinos, enabling the world's first observation of relic supernova neutrinos via inverse beta decay. This upgrade also enhances the ability to study the ordering of the neutrino mass, matter–antimatter asymmetry, and proton decay.

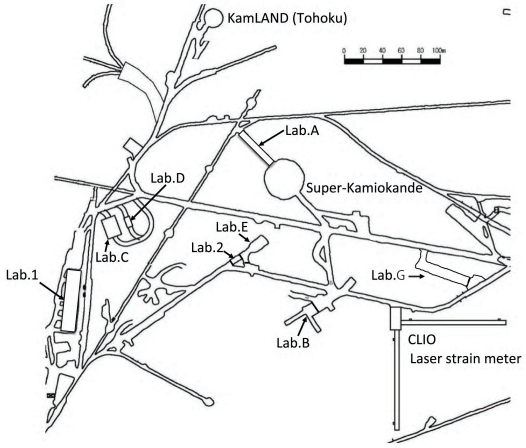


Fig. 1. Kamioka Underground Observatory.



Fig. 2. The surface buildings in Mozumi.

KAGRA OBSERVATORY

KAGRA observatory is located in the Ikenoyama-mountain on the border between Gifu and Toyama prefecture, about 35 km south of Toyama city in Japan. The observatory was established in 2016 in order to operate Large-scale Cryogenic Gravitational Wave Telescope "KAGRA". KAGRA itself has a L-shape tunnel facility, and it is located more than 200m under Mt.Ikeno-yama. The corner station of the L-shape tunnel is accessible through a 500-m horizontal access tunnel from Atotsu area. The observatory has its own surface research buildings and rental space in the community center of Hida city located about 5km away from the Atotsu entrance of KAGRA.

KAGRA aims to observe gravitational waves (GWs) as one of observatories of the world GW detection network including Advanced-LIGO, Advanced-Virgo and planned LIGO-India. KAGRA project (formerly named LCGT) was partially approved in 2010 as one of Leading-edge Research Infrastructure Program, and also supported by Program for Promoting Large-scale Science Projects, Subsidy for Facilities Expense and Grants-in-Aid for Scientific Research from Ministry of Education, Culture, Sports, Science and Technology (MEXT).

In the KAGRA project, Institute for Cosmic Ray Research plays a role of a host promoting institute, and National Astronomical Observatory of Japan (NAOJ) and High Energy Accelerator Research Organization (KEK) are the co-host institutions, then more than 447 researchers in 99 institutes and universities in the world are collaborating for construction and data analysis of KAGRA.

The tunnel excavation started in May 2012, and finished in March 2014. After that, the basic laboratory environment was prepared until September 2015. A Michelson interferometer with 3km arm (iKAGRA) was demonstrated in March 2016, and the first engineering run was performed until May 2016. In 2019, all the interferometer components had been installed to complete the KAGRA Observatory that adopts a power re-cycled Fabry-Perot Michelson type interferometer with the resonant sideband extraction. On February 25th, 2020, KAGRA started its first observation run. After a two-week observation run "O3GK" with GEO600 in April 2020, we conducted a four-week observation with LIGO at the start of "O4a" in June 2023. We will continue to improve sensitivity and conduct international observations to contribute to the progress of gravitational wave astronomy.



Fig. 1. Surface Research Building.



Fig. 2. Atotsu Entrance of KAGRA.

RESEARCH CENTER FOR COSMIC NEUTRINOS

The Research Center for Cosmic Neutrinos (RCCN) was established in 1999 with the aim of conducting research on neutrino and related topics. Members of this center are participating in the Super-Kamiokande experiment, exploring the properties of neutrinos using data of atmospheric neutrinos and accelerator neutrinos, and search for neutrino emissions from high-energy celestial objects in the universe. we have provided the occasion to discuss theoretical ideas and experimental results on neutrino physics. Additionally, we are involved in the project of next-generation neutrino experiment, Hyper-Kamiokande, conducting research and development on the 50-cm diameter photomultiplier tube, and advancing preparations for the construction of the detector scheduled for 2026, with the ongoing goal of advancing neutrino research into the future.

The center also plays a role in the joint research program of ICRR. In addition to accepting research on neutrinos, as the facility utilization, in collaboration with the Computer Committee, the center manages a large-scale computer system used for joint research at this research institute by cosmic ray researchers nationwide(Fig 1). This computer system has a total of approximately 3,300 CPU cores, 9 petabytes of large capacity disk, and data transfer performance of 18 gigabytes per second. It is capable of analyzing large amounts of data obtained from cosmic ray observation experiments and generating simulation data that require high CPU capability. Since its update in the fiscal year 2020, it has been operated stably. Additionally, the center serves as the acceptance for joint research program by primary cosmic ray group, and operates the low-background experimental laboratory underground(see Fig 2). Furthermore, it accepts joint research solely for computer usage and research meetings related to future plans, among other activities.

The center also supports outreach activities for the general public regarding cosmic ray research. Since 2009, ICRR has jointly held public lecture events twice a year in spring and summer with the Kavli Institute for the Physics and Mathematics of the Universe (Kavli IPMU). Specifically, for the spring event, the center collaborates with the public relations office to plan and implement it. In the fiscal year 2023, on April 22nd (Sat), a public lecture event titled ”Astronomy and Medicine through Gamma-ray Observations” was held at the Kashiwa-no-ha Conference Center. The event featured Professor Masato Takita from our research institute and Associate Professor Shinichiro Takeda from Kavli IPMU as speakers. They discussed the exploration of PeVatron, a cosmic ray source believed to originate within our galaxy, and the application of gamma-ray observations in the field of medicine. Additionally, a cross-talk session between the two speakers was conducted to address questions from the audience. Approximately 150 people attended the event in person, and the lecture was also streamed on YouTube, attracting about 500 viewers with around 1000 views.



Fig. 1. Photo of the central computer facility in ICRR upgraded in 2014.



Fig. 2. Photo of the low-background underground facility in ICRR.

HIGH ENERGY ASTROPHYSICS FACILITY IN CANARIAS

High Energy Astrophysics Facility in Canarias, established on April 1, 2019 in La Palma, Canary Islands, Spain is the actual base of international collaborations on CTA (Cherenkov Telescope Array) project co-hosted by CTA group of ICRR.

The Cherenkov Telescope Array (CTA) is the next generation ground-based observatory for gamma-ray astronomy at very-high energies, participated by more than 1400 researchers from 25 countries. With more than 70 telescopes located in the northern and southern hemispheres, CTA will be the world's largest and most sensitive high-energy gamma-ray observatory. The CTA-Japan consortium is making a significant contribution to the construction of Large-sized Telescopes (LSTs), four telescopes of which are planned to construct at northern hemisphere site in La Palma. The first LST was completed and made the first light at the end of December of 2018.

Establishment of the local corporation assets were needed for daily activities such as local procurement and employment to manage and operate the site. High Energy Astrophysics Facility in Canarias was established as a room inside the building of CALP (The Centro de Astrofísica en La Palma), a branch of IAC (Instituto de Astrofisca de Canarias).



Fig. 1. High Energy Astrophysics Facility in Canarias.

APPENDICES

A. ICRR Workshops and Ceremonies

B. ICRR Seminars

C. List of Publications

(a) Papers Published in Journals

(b) Conference Papers (Proceedings)

D. Doctoral Theses

E. Public Relations

(a) ICRR News

(b) Public Lectures

(c) Visitors

F. Inter-University Research Activities

G. List of Committee Members

(a) Board of Councillors

(b) Advisory Committee

(c) Inter-University Research Advisory Committee

H. List of Personnel

A. ICRR Workshops and Ceremonies

38th International Cosmic Ray Conference (ICRC2023)

Date: July 26 -August 3, 2023
Place : Nagoya University, Nagoya, Japan

Outline: The 38th International Cosmic Rays Conference was held at Nagoya University for nine days from July 26 to August 3, 2023. ICRC has been organized every two years and it has been 4 years since it was last held in person, because the former 37th ICRC was forced to be held online due to the COVID-19 pandemic. Participants of ICRC2023 were 1,429 researchers from 55 countries: 1,099 in person (257 from Japan and 842 from other countries) and 330 online. More than 1,500 presentations and active discussions on cosmic-ray-related fields were made. Much interesting progress was found in the following topics: the rapid development of gravitational wave observation as the additional new topic in ICRC2023, the development of neutrino observation, the gamma-ray observation with wide energy range and study of cosmic-ray origins, the progress of extremely high energy cosmic-ray observation, Dark Matter search with high precision, the development of multi-messenger astronomy combined traditional multi-wavelength astronomy with the above-mentioned new messengers. On July 30th, the public lecture was held at the same venue, with a talk by Nobel Prize winner in physics, Takaaki Kajita.

Participants: 1429 participants including 330 attending online from 55 countries



Fig. 1. 38th International Cosmic Ray Conference (ICRC2023)

LIGO-Virgo-KAGRA Collaboration Meeting

Date: September 11 - 15, 2023

Place : Toyama International Conference Center in Toyama City, Toyama Prefecture, Japan

Outline: The LIGO-Virgo-KAGRA (LVK) Collaboration, an international joint observation network for gravitational waves, held an international conference (LVK Meeting) at the Toyama International Conference Center in Toyama City for five days from September 11 to 15.

The LVK Meeting has been held twice a year in North America and Europe, and this is the first time it has been held in Japan. About 370 local researchers (collaborators) from 20 countries and about 560 remote participants have participated. They shared information and engaged in lively discussions on the current status and future of the instruments and research. Many young collaborators also participated, introducing their latest research by poster presentations and deepening exchanges with researchers from other countries.

Also, the KAGRA site tour was conducted daily during the meeting, and about 280 people participated in the tour. The KAGRA is constructed underground of Kamioka to avoid ground vibrations, unlike LIGO (two locations in the U.S.) and VIRGO (Italy) in Europe, which are above ground, and the mirror, the heart of the device, is cooled to cryogenic temperatures to reduce thermal noise.

Participants: 370 participants and 560 remote participants



Fig. 2. LVK Meeting at the Toyama International Conference Center

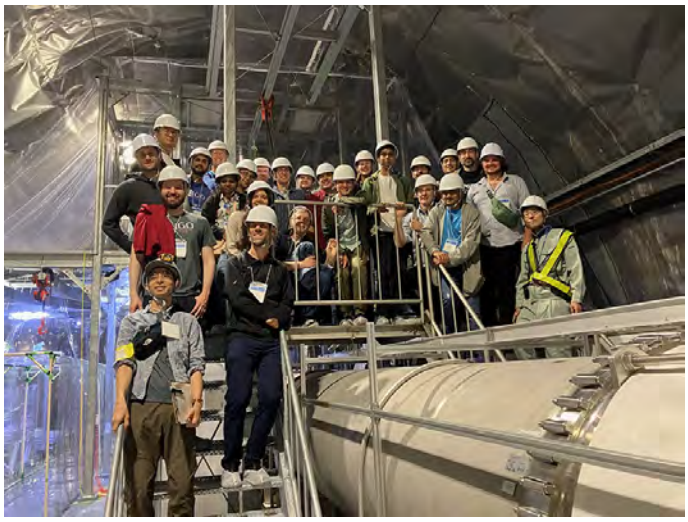


Fig. 3. KAGRA site tour

The Symposium “New Development of Multi-messenger Astronomy” held in Kashiwa Campus, Commemorating the NNSO Reorganization

Date: November 1 - 2, 2023
Place : Kashiwa Campus, The University of Tokyo, Japan

Outline: The first symposium commemorating the establishment of “Next-generation Neutrino Science and Multi-messenger Astronomy Organization” was held on 1-2, November, 2023 in UTokyo Kashiwa Campus.

The predecessor organization, “Next-generation Neutrino Science Organization (NNSO)”, was launched in October 2017 in cooperation with the Institute for Cosmic Ray Research (ICRR), the Kavli Institute for the Physics and Mathematics of the Universe (Kavli IPMU), and the School of Science in the University of Tokyo. The Earthquake Research Institute also joined this organization in 2019. The purpose of the NNSO was to pioneer the future of neutrino physics developing neutrino research techniques and detector technologies. In particular, the NNSO promoted its flagship facility, the Hyper-Kamiokande.

In October 2023, the NNSO was reorganized into the “Next-generation Neutrino Science and Multi-messenger Astronomy Organization” to expand our research activities into the field of multi-messenger astronomy. The new organization promotes multi-messenger astronomy, which is based on collaborative research with disparate “messengers”: electromagnetic waves (Radio, Optical/Infrared, X-ray, Gamma-ray), cosmic rays, neutrinos, and gravitational waves, coordinating the observation groups and experts in theory and data science.

The symposium was attended by 108 researchers not only the NNSO members but also people from Chiba University, Kyoto University, Tohoku University, Waseda University, Osaka University, National Astronomical Observatory of Japan, Gifu University, and Tokyo City University. After the opening address by the NNSO President Takaaki Kajita, 32 researchers made presentations and answered questions from participants.

Participants: 108 participants



Fig. 4. The Symposium “New Development of Multi-messenger Astronomy”

B. ICRR Seminars

1. April, 4, 2023: Dr. Yuhang Zhao (APC, France), “Experiment efforts to go beyond the standard quantum limit in gravitational wave detectors”
2. April, 6, 2023: Dr. Anatael Cabrera (IJPLab), “SuperChooz Exploration: Reactor & Solar Neutrino Physics”
3. April, 17, 2023: Dr. Kumiko Kotera (Institut d’Astrophysique de Paris), “Towards EeV Neutrino Astronomy with GRAND”
4. July, 5, 2023: Dr. Marta Ewelina Babicz (U. Zurich), ”Design and Optimization of the SiPM Array for Event Reconstruction in the DARWIN Experiment”
5. July, 6, 2023: Dr. Saul Alonso Monsalve (ETH Zurich), ”Machine learning for neutrino experiments”
6. July, 10, 2023: Dr. Jiro Shimoda (ICRR), ”Roles of Cosmic-Rays in Astrophysics: The History of Our Galaxy”
7. August, 8, 2023: Dr. Reina Maruyama (Yale University), “Resolving DAMA”
8. August, 9, 2023: Dr. Karsten M. Heeger (Yale University), “Probing the Nature of Neutrino Mass”
9. November, 20, 2023: Prof. Cecilia Lunardini (Arizona State University Department of Physics, visiting NAOJ), “Neutrinos and gravitational waves from core collapse supernovae: towards a multimessenger approach”
10. January, 25, 2024: Dr. Hang Bae Kim (Hanyang University, Korea; Visiting professor of ICRR), “Search for the source of ultra-high energy cosmic rays – Energy spectrum anisotropies”
11. February, 19, 2024: Dr. Qing Lin (University of Science and Technology of China), “PandaX-4T Experiment and its Recent Progress”
12. March, 13, 2024: Dr. Federico Urban (CEICO, Institute of Physics of the Czech Academy of Sciences), “What we can learn from cross-correlations between UHECRs and galaxies”
13. March, 27, 2024: Prof. Takaaki Kajita (ICRR), ”Looking Back on My Research Activities in ICRR”

C. List of Publications

(a) Papers Published in Journals

1. ”First Dark Matter Search with Nuclear Recoils from the XENONnT Experiment”, E. Aprile et al. (XENON Collaboration), Phys. Rev. Lett. **131**, 041003, Jul. 2023.
2. ”Detector signal characterization with a Bayesian network in XENONnT”, E. Aprile et al. (XENON Collaboration), Phys. Rev. D **108**, 012016, Jul. 2023.
3. ”The triggerless data acquisition system of the XENONnT experiment”, E. Aprile et al. (XENON Collaboration), JINST **18** P07054, Jul. 2023.
4. ”Direct dark matter searches with the full data set of XMASS-I”, XMASS Collaboration, Phys. Rev. D **108**, 083022 (2023), Oct. 2023.
5. ”Search for events in XENON1T associated with gravitational waves”, E. Aprile et al. (XENON Collaboration), Phys. Rev. D **108**, 072015, Oct. 2023.
6. ”Rapid analysis of ^{226}Ra in ultrapure gadolinium sulfate octahydrate”, Y Sakakieda, K Hosokawa, F Nakanishi, Y Hino, Y Inome, A Sakaguchi, Y Takaku, S Yamasaki, K Sueki, M Ikeda, H Sekiya, PTEP, Volume **2023**, Issue 10, October 2023, 103H01, Sep. 2023.
7. ”Development of a low-background HPGe detector at Kamioka Observatory”, K Ichimura, H Ikeda, Y Kishimoto, M Kurasawa, A A Suzuki, Y Gando, M Ikeda, K Hosokawa, H Sekiya, H Ito, A Minamino, S Suzuki, PTEP, Volume **2023**, Issue 12, December 2023, 123H0, Nov. 2023.

8. ”Searching for Heavy Dark Matter near the Planck Mass with XENON1T”, XENON collaboration, Phys. Rev. Lett. **130**, 261002, 2023,, Jun. 2023.

9. ”Design and performance of the field cage for the XENONnT experiment”, XENON collaboration, Eur. Phys. J. C **84**, 138, 2024, Feb. 2024.

10. ”Measurement of the cosmogenic neutron yield in Super-Kamiokande with gadolinium loaded water”, M. Shinoki et al. (The Super-Kamiokande Collaboration), Phys. Rev. D **107**, 092009, May. 2023.

11. ”Search for Astrophysical Electron Antineutrinos in Super-Kamiokande with 0.01% Gadolinium-loaded Water”, M. Harada et al. (The Super-Kamiokande Collaboration), 2023 ApJL **951** L27, Jul. 2023.

12. ”Measurement of the neutrino-oxygen neutral-current quasielastic cross section using atmospheric neutrinos in the SK-Gd experiment”, S. Sakai et al. (The Super-Kamiokande Collaboration), Phys. Rev. D **109**, L011101, Jan. 2024.

13. ”Updated T2K measurements of muon neutrino and antineutrino disappearance using 3.6×10^{21} protons on target”, T2K Collaboration, Phys. Rev. D **108**, 072011, Oct. 2023.

14. ”Measurements of the ν_μ and $\bar{\nu}_\mu$-induced coherent charged pion production cross sections on ^{12}C by the T2K experiment”, T2K Collaboration, Phys. Rev. D **108**, 092009, Nov. 2023.

15. ”Measurements of neutrino oscillation parameters from the T2K experiment using 3.6×10^{21} protons on target”, T2K Collaboration, The European Physical Journal C Volume **83**, article number 782 (2023), Sep. 2023.

16. ”Direction-sensitive dark matter search with 3D-vector-type tracking in NEWAGE”, Satoshi Higashino et al., PTEP **2023** 103F01, Oct. 2023.

17. ”High-pressure xenon gas time projection chamber with scalable design and its performance at around the Q value of ^{136}Xe double-beta decay”, Yoshida, M., et al., PTEP **2023** 013H01, Dec. 2023.

18. ”Nuclear deexcitation simulator for neutrino interactions and nucleon decays of ^{12}C and ^{16}O based on TALYS”, Seisho Abe, PhysRevD.**109**.036009, Feb. 2024.

19. ”A method to measure the quenching factor for recoil energy of oxygen in bismuth germanium oxide scintillators”, Ommura, Y., Ito, H., Yano, T., Minamino, A., Ishitsuka, M, 2023 JINST **18** T04006, Apr. 2023.

20. ”First measurement of muon neutrino charged-current interactions on hydrocarbon without pions in the final state using multiple detectors with correlated energy spectra at T2K”, K. Abe et al. (T2K Collaboration), Phys. Rev. D **108**, 112009 , Dec. 2023.

21. ”Hyper-Kamiokande construction status and prospects”, K. Abe and H. Tanaka, Front. Phys. **12**:1378254., Mar. 2024.

22. ”Multiwavelength study of the galactic PeVatron candidate LHAASO J2108+5157”, CTA LST collaboration, Astronomy & Astrophysics, Volume **673**, id.A75, May. 2023.

23. ”Multimessenger Characterization of Markarian 501 during Historically Low X-Ray and γ-Ray Activity”, MAGIC Collaboration, et al., 2023 ApJS **266** 37, Jun. 2023.

24. ”Sensitivity of the Cherenkov Telescope Array to TeV photon emission from the Large Magellanic Cloud”, CTA Consortium, Monthly Notices of the Royal Astronomical Society, Volume **523**, pp.5353-5387, Aug. 2023.

25. ”Observations of the Crab Nebula and Pulsar with the Large-sized Telescope Prototype of the Cherenkov Telescope Array”, CTA LST Collaboration, The Astrophysical Journal, Volume **956**, Issue 2, id.80, Oct. 2023.

26. ”Star tracking for pointing determination of Imaging Atmospheric Cherenkov Telescopes. Application to the Large-Sized Telescope of the Cherenkov Telescope Array”, CTA LST Collaboration, Astronomy & Astrophysics, Volume **679**, id.A90, Nov. 2023.

27. ”Performance of the joint LST-1 and MAGIC observations evaluated with Crab Nebula data”, CTA LST Collaboration, MAGIC Collaboration, Astronomy & Astrophysics, Volume **680**, id.A66, Dec. 2023.

28. ”MAGIC detection of GRB 201216C at z = 1.1”, MAGIC Collaboration, MNRAS **527**, 3, pp.5856-5867, Oct. 2023.

29. ”Multi-year characterisation of the broad-band emission from the intermittent extreme BL Lac 1ES 2344+514”, MAGIC Collaboration, Astronomy & Astrophysics, Volume **682**, id.A114, 26 pp.:, Feb. 2024.

30. ”The variability patterns of the TeV blazar PG 1553 + 113 from a decade of MAGIC and multiband observations”, MAGIC Collaboration, MWL collaborators, MNRAS **529**, 4, pp.3894-3911, Mar. 2024.

31. ”Constraints on the intergalactic magnetic field from Fermi/LAT observations of the ‘pair echo’ of GRB 221009A”, Vovk, Ievgen; Korochkin, A. ; Neronov, A. ; Semikoz, D., Astronomy & Astrophysics, Volume **683**, id.A25, Mar. 2024.

32. ”Measurement of the size of the gamma-ray source in blazar B0218+357 based on microlensing at the 100 GeV energy band”, Vovk, Ievgen; Neronov, A. , Astronomy & Astrophysics, Volume **684**, id.A39, Apr. 2024.

33. ”Effects of the Galactic Magnetic Field on the UHECR Correlation Studies with Starburst Galaxies”, Ryo Higuchi et al., 2023 ApJ **949** 107, Jun. 2023.

34. ”Measurement of the forward η meson production rate in p-p collisions at $\sqrt{s}$ = 13 TeV with the LHCf-Arm2 detector”, Adriani, O., Berti, E., Betti, P. et al., J. High Energ. Phys. **2023**, 169 (2023), Oct. 2023.

35. ”An extremely energetic cosmic ray observed by a surface detector array”, Telescope Array Collaboration, Science **382**, 903-907 (2023), Nov. 2023.

36. ”The energy spectrum of cosmic rays measured by the Telescope Array using 10 years of fluorescence detector data”, Telescope Array Collaboration, Astropart. Phys., **151** (2023) 102864, Sep. 2023.

37. ”Ultra high energy cosmic rays. The intersection of the Cosmic and Energy Frontiers”, A. Coleman, et al., Astropart. Phys., **149** (2023) 102819, Jul. 2023.

38. ”Measurement of the transverse single-spin asymmetry for forward neutron production in a wide pT range in polarized $p+p$ collisions at $\sqrt{s} = 510$ GeV”, RHICf Collaboration, Phys. Rev. D **109**, 012003, Jan. 2024.

39. ”RAIKOU: A General Relativistic, Multi-Wavelength Radiative Transfer Code”, Tomohisa Kawashima, Ken Ohsuga, and Hiroyuki R. Takahashi, 2023 ApJ **949** 101, Jun. 2023.

40. ”Search for a Black Hole Binary in Gaia DR3 Astrometric Binary Stars with Spectroscopic Data”, Ataru Tanikawa et al, 2023 ApJ **946** 79, Apr. 2023.

41. ”Spectral analysis of a parsec-scale jet in M87: Observational constraint on the magnetic field strengths in the jet”, H. Ro, M. Kino, B.-W. Sohn, K. Hada, J. Park, M. Nakamura, Y. Cui, K. Yi, A. Chung, J. Hodgson, T. Kawashima, et al.,, A&A **673**, A159 (2023), May. 2023.

42. ”Monitoring the Size and Flux Density of Sgr A* during the Active State in 2019 with East Asian VLBI Network”, Xiaopeng Cheng, Ilje Cho, Tomohisa Kawashima, Motoki Kino, Guang-Yao Zhao, Juan-Carlos Algaba, Yutaro Kofuji, Sang-Sung Lee, Jee-Won Lee, Whee Yeon Cheong, Wu Jiang, Junghwan Oh, Galax 11, 46(15pp), Mar. **2023**.

43. ”Comparison of Polarized Radiative Transfer Codes used by the EHT Collaboration”, B. S. Prather, J. Dexter, M. Moscibrodzka, et al., 2023 ApJ **950** 35, Jun. 2023.

44. ”A Ring-like Accretion Structure in M87 Connecting its Black Hole and Jet”, R.-S. Lu, K. Asada, T. P. Krichbaum, et al., Nature volume **616**, pages 686–690 (2023), Apr. 2023.

45. ”Direct Measurement of the Cosmic-Ray Helium Spectrum from 40 GeV to 250 TeV with the Calorimetric Electron Telescope on the International Space Station”, O. Adriani, Y. Akaike, K. Asano, et al., PRL **130**, 171002(8pp), Apr. 2023.

46. ”Non-Thermal Emissions from a Head-Tail Radio Galaxy in 3D Magnetohydrodynamic Simulations”, Takumi Ohmura, Katsuaki Asano, Kosuke Nishiwaki, Mami Machida, and Haruka Sakemi, ApJ **951** 76, Jul. 2023.

47. ”Charge-Sign Dependent Cosmic-Ray Modulation Observed with the Calorimetric Electron Telescope on the International Space Station”, O. Adriani, Y. Akaike, K. Asano, et al., PRL **130**, 211001(6pp), May. 2023.

48. ”The History of the Milky Way: The Evolution of Star Formation, Cosmic Rays, Metallicity, and Stellar Dynamics over Cosmic Time”, Jiro Shimoda, Shu-ichiro Inutsuka, and Masahiro Nagashima, PASJ 2024, **76**(1), 81–97, Jan. 2024.

49. ”Dynamical Energy Dissipation of Relativistic Magnetic Bullets”, Yo Kusafuka, Katsuaki Asano, Takumi Ohmura, and Tomohisa Kawashima,, MNRAS **526**, 512–522 (2023) , Sep. 2023.

50. ”High-Energy Neutrino Constraints on Cosmic-Ray Re-Acceleration in Radio Halos of Massive Galaxy Clusters”, Kosuke Nishiwaki, Katsuaki Asano, and Kohta Murase, 2023 ApJ **954** 188, Sep. 2023.

51. ”A Search for Pulsars around Sgr A* in the First Event Horizon Telescope Dataset”, P. Torne, K. Liu, R. P. Eatough, et al., 2023 ApJ **959** 14, Nov. 2023.

52. ”Decomposing the Spectrum of Ultra-Luminous X-ray Pulsar NGC 300 ULX-1”, Shogo B. Kobayashi, Hirofumi Noda, Teruaki Enoto, Tomohisa Kawashima, Akihiro Inoue, and Ken Ohsuga, 2023 ApJ **955** 124, Sep. 2023.

53. ”Precessing Jet Nozzle Connecting to a Spinning Black Hole in M87”, Y. Cui, K. Hada, T. Kawashima, et al., Nature **621**, 711-715, Sep. 2023.

54. ”Simulations of Two-Temperature Jets in Galaxy Clusters: I. Effect of Jet Magnetization on Dynamics and Electron Heating”, Takumi Ohmura, and Mami Machida, A&A **679**, A160 (2023), Nov. 2023.

55. ”Simulations of two-temperature jets in galaxy clusters: II. X-Ray Property of Forward Shock”, Takumi Ohmura, Mami Machida, and Hiroki Akamatsu, A&A **679**, A161 (2023), Nov. 2023.

56. ”Gamma Rays from a Reverse Shock with Turbulent Magnetic Fields in GRB 180720B”, M. Arimoto, K. Asano, K. S. Kawabata, et al., Nat Astron (2023), Nov. 2023.

57. ”Direct Measurement of the Spectral Structure of Cosmic-Ray Electrons + Positrons in the TeV Region with CALET on the International Space Station”, O. Adriani, Y. Akaike, K. Asano, et al., PRL **131**, 191001(7pp),, Nov. 2023.

58. ”First M87 Event Horizon Telescope Results. IX. Detection of Near-horizon Circular Polarization”, K. Akiyama, A. Alberdi, W. Alef, et al.,, ApJL **957** L20(42pp) (2023), Nov. 2023.

59. ”Efficiency of Turbulent Reacceleration by Solenoidal Turbulence and its Application to the Origin of Radio Megahalos in Cluster Outskirts”, Kosuke Nishiwaki, Gianfranco Brunetti, Franco Vazza, and Claudio Gheller,, ApJ, **961**, 15(12pp), , Jan. 2024.

60. ”Ordered Magnetic Fields around the 3C 84 Central Black Hole”, G. F. Paraschos, J.-Y. Kim, M. Wielgus, et al., A&A **682**, L3(15pp), Feb. 2024.

61. ”The Persistent Shadow of the Supermassive Black Hole of M 87 . Observations, Calibration, Imaging, and Analysis”, K. Akiyama, A. Alberdi, W. Alef, et al., A&A **681**, A79(63pp), Jan. 2024.

62. ”Radiation Process in Relativistic MHD Waves: The Case of Circularly Polarized Alfvén Waves”, Ryota Goto, and Katsuaki Asano, ApJ, **965**, 178(9pp), , Apr. 2024.

63. ”Evidence for a gamma-ray molecular target in the enigmatic PeVatron candidate LHAASO J2108+5157”, Eduardo DE LA F UENTE, et al., Astron.and Astrophys.**675**, L5 (2023), Jul. 2023.

64. ”Detection of a new molecular cloud in the LHAASO J2108+5157 region supporting a hadronic PeVatron scenario”, Eduardo DE LA F UENTE, et al., Publ. Astron. Soc. Japan (2023) 00 (0), 1–21, Apr. 2023.

65. ”Observation of Gamma Rays up to 320 TeV from the Middle-aged TeV Pulsar Wind Nebula HESS J1849-000”, M. Amenomori et al (The Tibet AS gamma Collaboration), 2023 ApJ **954** 200, Sep. 2023.

66. ”On the Source Contribution to the Galactic Diffuse Gamma Rays above 398 TeV Detected by the Tibet ASγ Experiment”, S. Kato et al., ApJL, **961** L13 (4pp), 2024, Jan. 2024.

67. ”Search for subsolar-mass black hole binaries in the second part of Advanced LIGO’s and Advanced Virgo’s third observing run”, Abbott R,Others (LIGO-Virgo-KAGRA collaboration), MNRAS **524**, 5984–5992 (2023), Feb. 2023.

68. ”Population of Merging Compact Binaries Inferred Using Gravitational Waves through GWTC-3”, Abbott R,Others (LIGO-Virgo-KAGRA collaboration), Phys. Rev. X **13**, 011048, Mar. 2023.

69. ”Fixed-target charmonium production and pion parton distributions”, Wen-Chen Chang, Jen-Chieh Peng, Stephane Platchkov, and Takahiro Sawada, Phys. Rev. D **107**, 056008, Mar. 2023.

70. ”Rapid hierarchical inference of neutron star equation of state from multiple gravitational wave observations of binary neutron star coalescences”, Anarya Ray, Michael Camilo, Jolien Creighton, Shaon Ghosh, Soichiro Morisaki, Phys. Rev. D **107**, 043035, Feb. 2023.

71. ”Constraints on the Cosmic Expansion History from GWTC–3”, Abbott R,Others (LIGO-Virgo-KAGRA collaboration), Astrophys. J. **949** 76, Jun. 2023.

72. ”Open Data from the Third Observing Run of LIGO, Virgo, KAGRA, and GEO”, Abbott R,Others (LIGO-Virgo-KAGRA collaboration), Astrophys. J. Suppl. **267** 29, Jul. 2023.

73. ”Pion PDFs confronted by fixed-target charmonium production”, Wen-Chen Chang, Chia-Yu Hsieh, Yu-Shiang Lian, Jen-Chieh Peng, Stephane Platchkov & Takahiro Sawada , AAPPS Bull.Volume **33**, article number 15, (2023), Jul. 2023.

74. ”Localization of binary neutron star mergers with a single cosmic explorer”, Pratyusava Baral, Soichiro Morisaki, Ignacio Magaña Hernandez, Jolien Creighton, Phys. Rev. D **108**, 043010, Aug. 2023.

75. ”Binary tree approach to template placement for searches for gravitational waves from compact binary mergers”, Chad Hanna, Soichiro Morisaki et al., Phys. Rev. D **108**, 042003, Aug. 2023.

76. ”Improved ranking statistics of the GstLAL inspiral search for compact binary coalescences”, Leo Tsukada , Soichiro Morisaki, et al., Phys. Rev. D **108**, 043004, Aug. 2023.

77. ”Overview of KAGRA : Data transfer and management”, Akutsu T,Others KAGRA Collaboration, Prog. Theor. Exp. Phys. **2023** 10A102, Sep. 2023.

78. ”Multipole tidal effects in the post-Newtonian gravitational-wave phase of compact binary coalescences”, Tatsuya Narikawa, Phys. Rev. D **108**, 063029, Sep. 2023.

79. ”Measurement of flavor asymmetry of the light-quark sea in the proton with Drell-Yan dimuon production in $p+p$ and $p+d$ collisions at 120 GeV”, J. Dove , T. Sawada et al., Phys. Rev. C **108**, 035202, Sep. 2023.

80. ”Search for Gravitational Waves Associated with Fast Radio Bursts Detected by CHIME/FRB during the LIGO-Virgo Observing Run O3a”, Abbott R,Others (LIGO-Virgo-KAGRA collaboration), Astrophys. J. ApJ **955** 155, Sep. 2023.

81. ”First results of axion dark matter search with DANCE”, Yuka Oshima, Hiroki Fujimoto, Jun’ya Kume, Soichiro Morisaki, Koji Nagano, Tomohiro Fujita, Ippei Obata, Atsushi Nishizawa, Yuta Michimura, Masaki Ando, Phys. Rev. D **108**, 072005, Oct. 2023.

82. ”Probing the Solar Interior with Lensed Gravitational Waves from Known Pulsars”, Ryuichi Takahashi, Soichiro Morisaki, Teruaki Suyama, The Astrophysical Journal ,ApJ **957** 52, Oct. 2023.

83. ”Searching for gravitational wave echoes from black hole binary events in the third observing run of LIGO, Virgo, and KAGRA collaborations”, Nami Uchikata, Tatsuya Narikawa, Hiroyuki Nakano, Norichika Sago, Hideyuki Tagoshi, and Takahiro Tanaka, Phys. Rev. D **108**, 104040, Nov. 2023.

84. ”Upper limit on scalar field dark matter from LIGO-Virgo third observation run”, Koki Fukusumi, Soichiro Morisaki, Teruaki Suyama, Phys. Rev. D **108**, 095054, Nov. 2023.

85. ”Rapid localization and inference on compact binary coalescences with the Advanced LIGO-Virgo-KAGRA gravitational-wave detector network”, Soichiro Morisaki, Rory Smith, Leo Tsukada, Surabhi Sachdev, Simon Stevenson, Colm Talbot, and Aaron Zimmerman, Phys. Rev. D **108**, 123040, Dec. 2023.

86. ”GWTC-3: Compact Binary Coalescences Observed by LIGO and Virgo during the Second Part of the Third Observing Run”, Abbott R,Others (LIGO-Virgo-KAGRA collaboration), Phys. Rev. X **13**, 041039, Dec. 2023.

87. ”Ground strains induced by the 2022 Hunga-Tonga volcanic eruption, observed by a 1500-m laser strainmeter at Kamioka, Japan”, Akiteru Takamori, Akito Araya, Kouseki Miyo, Tatsuki Washimi, Takaaki Yokozawa, Hideaki Hayakawa & Masatake Ohashi, Earth, Planets and Space volume **75**, Article number: 98 (2023), Jun. 2023.

88. ”Performance of the KAGRA detector during the first joint observation with GEO 600 (O3GK)”, H. Abe et al. KAGRA Collaboration, Prog. Theor. Exp. Phys. **2023** 10A101, Oct. 2023.

89. ”GWTC-2.1: Deep extended catalog of compact binary coalescences observed by LIGO and Virgo during the first half of the third observing run”, Abbott R,Others (LIGO-Virgo-KAGRA collaboration), Phys. Rev. D **109**, 022001 , Jan. 2024.

90. ”A Joint Fermi-GBM and Swift-BAT Analysis of Gravitational-wave Candidates from the Third Gravitational-wave Observing Run”, Fletcher C,Others (LIGO-Virgo-KAGRA collaboration), The Astrophysical Journal, **964**:149 (35pp), Mar. 2024.

91. ”The SSA22 H I Tomography Survey (SSA22-HIT). I. Data Set and Compiled Redshift Catalog”, Mawatari, Ken ; et al., 2023 AJ **165** 208, Apr. 2023.

92. ”The Stellar Mass – Black Hole Mass Relation at $z \sim 2$ Down to $\mathscr{M}_{\rm BH} \sim 10^7 M_\odot$ Determined by HETDEX”, Zhang, Yechi et al.,, 2023 ApJ **948** 103, May. 2023.

93. ”Photometric IGM tomography with Subaru/HSC: the large-scale structure of Lyα emitters and IGM transmission in the COSMOS field at $z \sim 5$”, Kakiichi, Koki et al., MNRAS **523**, 1772–1798 (2023) , Aug. 2023.

94. ”Quasar Luminosity Function at z = 7”, Matsuoka, Yoshiki et al., 023 ApJL **949** L42, Jun. 2023.

95. ”The Spitzer Coverage of HSC-Deep with IRAC for Z studies (SHIRAZ). I. IRAC Mosaics”, Annunziatella, Marianna et al., 2023 AJ **166** 25, Jun. 2023.

96. ”Cosmological-scale Lyα Forest Absorption around Galaxies and AGNs Probed with the HETDEX and SDSS Spectroscopic Data”, Sun, Dongsheng et al., 2023 ApJ **951** 25, Jun. 2023.

97. ”Morphologies of Galaxies at $z \gtrsim 9$ Uncovered by JWST/NIRCam Imaging: Cosmic Size Evolution and an Identification of an Extremely Compact Bright Galaxy at $z \sim 12$”, Ono, Yoshiaki et al., 2023 ApJ **951** 72, Jul. 2023.

98. ”EMPRESS. IX. Extremely Metal-poor Galaxies are Very Gas-rich Dispersion-dominated Systems: Will the James Webb Space Telescope Witness Gaseous Turbulent High-z Primordial Galaxies?”, Isobe, Yuki et al, 2023 ApJ **951** 102, Jul. 2023.

99. ”EMPRESS. XI. SDSS and JWST Search for Local and z$\sim$ 4-5 Extremely Metal-poor Galaxies (EMPGs): Clustering and Chemical Properties of Local EMPGs”, Nishigaki, Moka et al, 2023 ApJ **952** 11, Jul. 2023.

100. ”Big Three Dragons: Molecular Gas in a Bright Lyman-break Galaxy at z = 7.15”, Hashimoto, Takuya et al., 2023 ApJ **952** 48, Jul. 2023.

101. ”SILVERRUSH. XIII. A Catalog of 20,567 Lyα Emitters at z = 2-7 Identified in the Full-depth Data of the Subaru/HSC-SSP and CHORUS Surveys”, Kikuta, Satoshi. Et al., 2023 ApJS **268** 24, Sep. 2023.

102. ”FOREVER22: the first bright galaxies with Population III stars at redshifts $z \simeq 10-20$ and comparisons with JWST data”, Yajima, Hidenobu, et al., MNRAS **525**, 4832–4839 (2023), Aug. 2023.

103. ”Subaru High-z Exploration of Low-luminosity Quasars (SHELLQs). XVIII. The Dark Matter Halo Mass of Quasars at z$\sim$6”, Arita, Junya, et al., 2023 ApJ **954** 210, Sep. 2023.

104. ”No strong radio absorption detected in the low-frequency spectra of radio-loud quasars at $z > 5.6$”, Gloudemans, A. J., et al., A&A **678**, A128 (2023), Oct. 2023.

105. ”Plausible association of distant late M dwarfs with low-frequency radio emission”, Gloudemans, A. J. , et al., A&A **678**, A161 (2023), Oct. 2023.

106. ”ALMA FIR View of Ultra-high-redshift Galaxy Candidates at z$\sim$ 11-17: Blue Monsters or Low-z Red Interlopers?”, Fujimoto, Seiji, et al., ApJ **955** 130, Sep. 2023.

107. ”Redshift Evolution of Electron Density in the Interstellar Medium at z$\sim$ 0-9 Uncovered with JWST/NIRSpec Spectra and Line-spread Function Determinations”, Isobe, Yuki; et al., 2023 ApJ **956** 139, Oct. 2023.

108. ”An enhanced abundance of bright galaxies in protocluster candidates at z$\sim$ 3-5”, Toshikawa, Jun, et al., MNRAS **527**, 6276–6291 (2024), Oct. 2023.

109. ”Constraint on the event rate of general relativistic instability supernovae from the early JWST deep field data”, Moriya, Takashi et al., MNRAS **526**, 2400–2402 (2023), Sep. 2023.

110. ”JWST Census for the Mass-Metallicity Star Formation Relations at z = 4-10 with Self-consistent Flux Calibration and Proper Metallicity Calibrators”, Nakajima, Kimihiko, et al., 2023 ApJS **269** 33, Nov. 2023.

111. ”A JWST/NIRSpec First Census of Broad-line AGNs at z = 4-7: Detection of 10 Faint AGNs with M BH 106-108 Msun and Their Host Galaxy Properties”, Harikane, Yuichi et al., 2023 The Astrophysical Journal, Volume **959**, Issue 1, id.39, 18 pp., Dec. 2023.

112. ”JWST Identification of Extremely Low C/N Galaxies with [N/O] $\gtrsim$ 0.5 at z$\sim$ 6-10 Evidencing the Early CNO-cycle Enrichment and a Connection with Globular Cluster Formation”, Isobe, Yuki et al, 2023 The Astrophysical Journal, Volume **959**, Issue 2, id.100, 16 pp., Dec. 2023.

113. ”Pure Spectroscopic Constraints on UV Luminosity Functions and Cosmic Star Formation History from 25 Galaxies at $z_{spec} = 8.61-13.20$ Confirmed with JWST/NIRSpec”, Harikane, Yuichi et al., The Astrophysical Journal, Volume **960**, Issue 1, id.56, 22 pp, Dec. 2023.

114. ”EMPRESS. XII. Statistics on the Dynamics and Gas Mass Fraction of Extremely Metal-poor Galaxies”, Xu, Yi et al., The Astrophysical Journal, Volume **961**, Issue 1, id.49, 15 pp., Jan. 2024.

115. ”MAMMOTH-Subaru. III. Lyα Halo Identified by Stacking 3300 Lyα Emitters at z = 2.2-2.3”, Haibin Zhang et al , The Astrophysical Journal, Volume **961**, Issue 1, id.63, 9 pp, Jan. 2024.

116. ”MAMMOTH-Subaru. V. Effects of Cosmic Variance on Lyα Luminosity Functions at z = 2.2-2.3”, Ke Ma et al, The Astrophysical Journal, Volume **961**, Issue 1, id.102, 12 pp. , Jan. 2024.

117. ”Sub-parsec-scale jet-driven water maser with possible gravitational acceleration in the radio galaxy NGC 1052”, Kameno, Seiji et al., PASJ2024 psae015, Mar. 2024.

118. ”JWST and ALMA Multiple-line Study in and around a Galaxy at z = 8.496: Optical to Far-Infrared Line Ratios and the Onset of an Outflow Promoting Ionizing Photon Escape”, Fujimoto, Seiji et al., The Astrophysical Journal, Volume **964**, Issue 2, id.146, 21 pp., Mar. 2024.

119. ”EMPRESS. XIII. Chemical Enrichment of Young Galaxies Near and Far at z$\sim$ 0 and 4-10: Fe/O, Ar/O, S/O, and N/O Measurements with a Comparison of Chemical Evolution Models”, Watanabe, Kuria et al., The Astrophysical Journal, Volume **962**, Issue 1, id.50, 17 pp., Feb. 2024.

120. ”Census for the rest-frame optical and UV morphologies of galaxies at z = 4-10: First phase of inside-out galaxy formation”, Ono, Yoshiaki et al., PASJ **76** 2(2024), Feb. 2024.

121. ”Stochastic effects on observation of ultralight bosonic dark matter”, Hiromasa Nakatsuka, Soichiro Morisaki, Tomohiro Fujita, Jun’ya Kume, Yuta Michimura, Koji Nagano, and Ippei Obata, Phys. Rev. D **108**, 092010, Nov. 2023.

122. ”Enhancement of second-order gravitational waves at Q-ball decay”, Shinta Kasuya, Masahiro Kawasaki, Kai Murai, JCAP05(2023)053, May. 2023.

123. ”Sub-GeV dark matter search at ILC beam dumps”, Kento Asai, Sho Iwamoto, Maxim Perelstein, Yasuhito Sakaki, Daiki Ueda, J. High Energ. Phys. **2024**, 129 (2024), Feb. 2024.

124. ”Muon $g-2$ and non-thermal leptogenesis in $U(1)_{L_\mu - L_\tau}$ model”, Shintaro Eijima, Masahiro Ibe, Kai Murai,, J. High Energ. Phys. **2023**, 10 (2023), May. 2023.

125. ”Interactions of electrical and magnetic charges and dark topological defects”, Akifumi Chitose, Masahiro Ibe, Phys. Rev. D **108**, 035044, Aug. 2023.

126. ”Constraint on Early Dark Energy from Isotropic Cosmic Birefringence”, Johannes R. Eskilt, Laura Herold, Eiichiro Komatsu, Kai Murai, Toshiya Namikawa, Fumihiro Naokawa, Phys. Rev. Lett. **131**, 121001, Sep. 2023.

127. ”Dai-Freed anomaly in the standard model and topological inflation”, Masahiro Kawasaki, Tsutomu T. Yanagida, J. High Energ. Phys. 2023, **106** (2023), Nov. 2023.

128. ”Model Building by Coset Space Dimensional Reduction Scheme Using Twelve-Dimensional Coset Spaces”, Kento Asai, Joe Sato, Ryosuke Suda, Yasutaka Takanishi, Masaki J. S. Yang, J. High Energ. Phys. **2023**, 213 (2023), Nov. 2023.

129. ”Clustering of Primordial Black Holes from QCD Axion Bubbles”, Kentaro Kasai, Masahiro Kawasaki, Naoya Kitajima, Kai Murai, Shunsuke Neda, Fuminobu Takahashi,, JCAP10(2023)049, Oct. 2023.

130. ”Hill-top inflation from Dai-Freed anomaly in the standard model — a solution to the iso-curvature problem of the axion dark matter”, Masahiro Kawasaki, Tsutomu T. Yanagida, JCAP 01 (2024) 014, Jan. 2024.

131. ”New Constraint on Dark Photon at T2K Off-Axis Near Detector”, Takeshi Araki, Kento Asai, Tomoya Iizawa, Hidetoshi Otono, Takashi Shimomura, Yosuke Takubo, J. High Energ. Phys. 2023, 56 (2023), Nov. 2023.

132. ”Precise Estimate of Charged Higgsino/Wino Decay Rate”, Masahiro Ibe, Yuhei Nakayama, Satoshi Shirai, J. High Energ. Phys. **2024**, 12 (2024), Mar.2024.

133. ”Axion curvaton model for the gravitational waves observed by pulsar timing arrays”, K. Inomata, M. Kawasaki, K. Mukaida and T.T. Yanagida, Phys. Rev. D **109** 043508, 45323.

134. ”Enhancement of gravitational waves at Q-ball decay including non-linear density perturbations”, Masahiro Kawasaki, Kai Murai, JCAP01(2024)050, Jan. 2024.

(b) Conference Papers (Proceedings)

1. ”A Bayesian source association analysis of UHECRs: Impact of the Galactic magnetic field and composition”, Watanabe, K; Fedynitch, A; Capel, F; Sagawa, H, 6th international symposium on Ultra High Energy Cosmic Rays (UHECR), OCT 03-07, 2022

2. ”Estimation and reduction of the biases by the galactic magnetic field on the UHECR correlation studies”, Higuchi, R; Sako, T; Fujii, T; Kawata, K; Kido, E, 6th international symposium on Ultra High Energy Cosmic Rays (UHECR), OCT 03-07, 2022

3. ”Auger@TA: Deploying an independent Pierre Auger Observatory SD microarray at the Telescope Array Project Auger@TA Working Group Report”, Mayotte, S; Caraça-Valente, J; Covault, C; Fujii, T; Im, S; James, R; Johnsen, J; Kampert, KH; Kern, H; Matthews, J; Mayotte, E; Mocellin, AB; Quinn, S; Rautenberg, J; Roth, M; Sagawa, H; Sako, T; Sarazin, F; Sato, R; Schmidt, D; Thomas, S; Wörner, G; Auger, P, 6th international symposium on Ultra High Energy Cosmic Rays (UHECR), OCT 03-07, 2022

4. ”The JEM-EUSO Program for UHECR Studies from Space”, Parizot, E; Casolino, M; Picozza, P; Ebisuzaki, T; Bertaina, ME; Fuglesang, C; Haungs, A; Kajino, F; Klimov, P; Olinto, A; Ricci, M; Sagawa, H; Szabelski, J; Wiencke, L, 6th international symposium on Ultra High Energy Cosmic Rays (UHECR), OCT 03-07, 2022

5. ”Measurement of the cosmic ray energy spectrum with the TAx4 SD array”, Fujisue, K, 38th International Cosmic Ray Conference (ICRC2023), JUL 26-Aug 3, 2023

6. ”A study of the systematic effects on the energy scale for the measurement of UHECR spectrum by the TA SD array”, Ogio, S and Fujita. K, 38th International Cosmic Ray Conference (ICRC2023), JUL 26-Aug 3, 2023

7. ”Cosmic ray mass composition measurement with the TALE hybrid detector”, Fujita, K, 38th International Cosmic Ray Conference (ICRC2023), JUL 26-Aug 3, 2023

8. ”Measurement of UHECR energy spectrum with the Pierre Auger Observatory and the Telescope Array”, Bergman, DR; Deligny, O; Fenu, F; Fujii, T; Fujita, K; Kim, JH; Lhenry-Yvon, I; Maris, I; Luce, Q; Roth, M; Salamida, F; Tsunesada, Y; Verzi, V, 38th International Cosmic Ray Conference (ICRC2023), JUL 26-Aug 3, 2023

9. ”Development of a general purpose air shower simulation tool COSMOS X”, T. Sako, T. Fujii, K. Kasahara, H. Menjo, N. Sakaki, A. Taketa, Y. Tameda and the COSMOS X development team, International Cosmic Ray Conference (ICRC2023), July 26 - August 3, 2023

10. ”Measurement of cosmic-ray energy spectrum with the TALE detector in hybrid mode”, H. Oshima, et al., International Cosmic Ray Conference (ICRC2023), July 26 - August 3, 2023

11. ”TA SD analysis for inclined air showers”, K.Takahashi et al., International Cosmic Ray Conference (ICRC2023), July 26 - August 3, 2023

12. ”Status of the LHCf experiment”, Ohashi, K; Adriani, O; Berti, E; Betti, P; Bonechi, L; Bongi, M; D’Alessandro, R; Detti, S; Haguenauer, M; Itow, Y; Kasahara, K; Kitagami, Y; Kondo, M; Matsubara, Y; Menjo, H; Muraki, Y; Papini, P; Piparo, G; Ricciarini, S; Sako, T; Sakurai, N; Scaringella, M; Shimizu, Y; Tamura, T; Tiberio, A; Torii, S; Tricomi, A; Turner, WC; Yoshida, K, 6th international symposium on Ultra High Energy Cosmic Rays (UHECR), OCT 03-07, 2022

13. ”Performance evaluation of LHCf-ATLAS ZDC joint measurement using proton beam”, Kondo, M; Adriani, O; Berti, E; Betti, P; Bonechi, L; Bongi, M; D’Alessandro, R; Detti, S; Haguenauer, M; Itow, Y; Kasahara, K; Kitagami, Y; Matsubara, Y; Menjo, H; Muraki, Y; Ohashi, K; Papini, P; Piparo, G; Ricciarini, S; Sako, T; Sakurai, N; Scaringella, M; Shimizu, Y; Tamura, T; Tiberio, A; Torii, S; Tricomi, A; Turner, WC; Yoshida, K; Citron, Z; Cole, B; Grosse-Perdekamp, M; Lantz, C; Longo, R; MacLean, D; Moyal, Y; Shenkar, S; Steinberg, P; Sudit, L; Tate, A, 6th international symposium on Ultra High Energy Cosmic Rays (UHECR), OCT 03-07, 2022

14. ”TIBET ASgamma: Dawn of sub-PeV gamma-ray astronomy”, Sako, T.K.— Amenomori, M.— Asano, S.— Bao, Y.W.— Bi, X.J.— Chen, D.— Chen, T.L.— Chen, W.Y.— Chen, X.— Chen, Y.— Cirennima— Cui, S.W.— Danzengluobu— Ding, L.K.— Fang, J.H.— Fang, K.— Feng, C.F.— Feng, Z.— Feng, Z.Y.— Gao, Q.— Gomi, A.— Gou, Q.B.— Guo, Y.Q.— Guo, Y.Y.— Hayashi, Y.— He, H.H.— He, Z.T.— Hibino, K.— Hotta, N.— Hu, H.— Hu, H.B.— Hu, K.Y.— Huang, J.— Jia, H.Y.— Jiang, L.— Jiang, P.— Jin, H.B.— Kasahara, K.— Katayose, Y.— Kato, C.— Kato, S.— Kawahara, I.— Kawashima, T.— Kawata, K.— Kozai, M.— Kurashige, D.— Labaciren— Le, G.M.— Li, A.F.— Li, H.J.— Li, W.J.— Li, Y.— Lin, Y.H.— Liu, B.— Liu, C.— Liu, J.S.— Liu, L.Y.— Liu, M.Y.— Liu, W.— Liu, X.L.— Lou, Y.-Q.— Lu, H.— Meng, X.R.— Meng, Y.— Munakata, K.— Nagaya, K.— Nakamura, Y.— Nakazawa, Y.— Nanjo, H.— Ning, C.C.— Nishizawa, M.— Noguchi, R.— Ohnishi, M.— Okukawa, S.— Ozawa, S.— Qian, L.—

Qian, X.— Qian, X.L.— Qu, X.B.— Saito, T.— Sakakibara, Y.— Sakata, M.— Sako, T.— Sako, T.K.— Sasaki, T.— Shao, J.— Shibata, M.— Shiomi, A.— Sugimoto, H.— Takano, W.— Takita, M.— Tan, Y.H.— Tateyama, N.— Torii, S.— Tsuchiya, H.— Udo, S.— Wang, H.— Wang, Y.P.— Wangdui— Wu, H.R.— Wu, Q.— Xu, J.L.— Xue, L.— Yang, Z.— Yao, Y.Q.— Yin, J.— Yokoe, Y.— Yu, N.P.— Yuan, A.F.— Zhai, L.M.— Zhang, C.P.— Zhang, H.M.— Zhang, J.L.— Zhang, X.— Zhang, X.Y.— Zhang, Y.— Zhang, Y.— Zhang, Y.— Zhao, S.P.— Zhaxisangzhu— Zhou, X.X.— Zhou, Y.H.

15. ”Modeling of the galactic cosmic-ray anisotropy at TeV energies using an intensity-mapping method in an MHD model heliosphere”, T. K. Sako on behalf of the Tibet ASγ collaboration, and N. V. Pogorelov, International Cosmic Ray Conference (ICRC2023), July 26 - August 3, 2023

16. ”Highlights from the Tibet ASgamma Experiment”, M. Anzorena, et al., International Cosmic Ray Conference (ICRC2023), July 26 - August3, 2023

17. ”Mega ALPACA to explore multi-PeV gamma-ray sky in the southern hemisphere”, T. Sako, et al., International Cosmic Ray Conference (ICRC2023), July 26 - August 3, 2023

18. ”First observational results of the ALPAQUITA air shower array in Bolivia”, K. Kawata, et al., International Cosmic Ray Conference (ICRC2023), July 26 - August 3, 2023

19. ”New Front end and trigger electronics for the ALPACA experiment”, M. Anzorena, et al., International Cosmic Ray Conference (ICRC2023), July 26 - August3, 2023

20. ”Recent progress on a radon detector with electrostatic collection”, Nakano, Y., ,

21. ”Demonstration of Tl-208 background reduction using topological information of Cherenkov light and observation of Zr-96 two neutrino double beta decay”, Fukuda, Y.— Moriyama, S.— Hiraide, K.— Ogawa, I.— Gunji, T.— Kurosawa, S., ,

22. ”Comparison of cross section models for neutrino-induced single pion production”, Yamauchi, K.— Ishitsuka, M.— Hayato, Y., ,

23. ”Comprehension of AmBe+BGO source to calibrate neutron tagging in electron antineutrino physics”, T. Yano, H. Ito, M. Ishitsuka, Y. Hino, M. Harada, A. Minamino and R. Shibayama, 38th International Cosmic Ray Conference (ICRC2023), 26 July - 3 August, 2023

24. ”CAGMon: A Novel Tool for Identifying and Diagnosing Coherent Associations and Causalities between Multi-channels of the Gravitational Wave Detector”, Jung, P; Oh, SH; Kim, YM; Son, EJ; Yokozawa, T; Washimi, T; Oh, JJ, 20th International Workshop on Advanced Computing and Analysis Techniques in Physics Research (ACAT), NOV 29-DEC 03, 2021

25. ”Study of Newtonian noise from the KAGRA cooling system”, Bajpai, R.— Tomaru, T.— Suzuki, T.— Yamamoto, K.— Ushiba, T.— Honda, T., ,

26. ”Status of the underground gravitational wave detector KAGRA”, Ushiba, T., ,

D. Doctoral Theses

1. The Measurement of the Energy Spectrum and Depth of Maximum Shower Development of Ultra-High-Energy Cosmic Rays Collected by the Telescope Array with the Hybrid Trigger Mode,
SHIN, Heungsu,
Ph.D Thesis, Jun. 2023

2. Optimal Alignment Sensing and Control for interferometric Gravitational Wave Telescope with Sapphire Mirrors,
TANAKA, Kenta,
Ph.D Thesis, Sep. 2023

3. Relations between Quasar Activity and Galaxy Mergers through High-Resolution Imaging and Spectroscopy,
TANG, Shenli ,
Ph.D Thesis, Sep. 2023

4. Measurement of neutrons produced in atmospheric neutrino interactions at Super- Kamiokande,
   HAN, Seungho,
   Ph.D Thesis, Mar. 2024
5. Physical and Chemical Properties of the Interstellar Medium at the Early Stage of GalaxyFormation Probed by Deep Optical and Near-Infrared Spectroscopy,
   ISOBE, Yuki,
   Ph.D Thesis, Mar. 2024
6. The measurement of the highest-energy cosmic ray energy spectrum with the extended surface detector array of the Telescope Array experiment,
   FUJISUE, Kozo,
   Ph.D Thesis, Mar. 2024
7. Multi-messenger emission from galaxy clusters: Constraints on non-thermal phenomena in intra-cluster medium,
   NISHIWAKI, Kosuke,
   Ph.D Thesis, Mar. 2024
8. Precise Estimate of Chargino Decay Rates,
   NAKAYAMA, Yuhei,
   Ph.D Thesis, Mar. 2024

E. Public Relations

(a) ICRR News

ICRR News is a quarterly publication written in Japanese about scientific and educational activities at ICRR.

Below lists the main topics in the issues published in FY 2023:

No.116 (2023 Spring-Summer)

- Features : MEXT Ministerial S&T Award Ceremony and Memorial Lecture for Two Winners: Emeritus Prof. Masahiro Teshima, Assistant Prof. Yuichi Harikane Held at Kashiwa-No-Ha Conference Center
- Features: Press Release 2023.4.26, Astronomers image for the first time a black hole's accretion flow together with a powerful jet
- Features : Press Release 2023.3.23, First Dark Matter Search with Nuclear Recoils from the XENONnT Experiment
- Reports : The 28th ICRR x IPMU Public Lecture Held in Hybrid -style with About 660 People : Masato Takita, ICRR Prof., Shinichiro Takeda, IPMU Assistant Prof. Present Latest Results
- Reports : 2023 ICRR Spring School for Undergraduate Students Held in Person for the First Time in Four Years
- Awards : Dr. Seiji Fujimoto (Received Ph.D from The University of Tokyo) Wins ASJ Young Astronomer Award 2022
- Awards : Prof. Ouchi, Assistant Prof. Ono and Harikane (Observational Cosmology Group) win PASJ Excellent Paper Award 2022
- Awards : Prof. Hiroko Miyahara (Musashino Art University) Wins 43th Saruhashi Award
- Awards : Dr. Sei Kato (Project Researcher) Wins School of Science Encouragement Award
- Awards : Akinori Matsumoto(D1), Koya Umeda (D1) Win Excellence Award on Qualifying Examination in FoPM Program
- Topics : Emeritus Prof. Hiroyuki Sagawa(Incunbent ICRR Senior Fellow) Gives Lecture for Senior Members Group
- Topics : The 7th Meeting of the Hyper-Kamiokande Experiment Financial Forum (HKFF) –Representatives of 15 countries participate in discussing the current status and new funding needed to start the experiment
- Topics : Twenty-five Year Anniversary of the Announcement of Atmospheric Neutrino Oscillation which leads to Prof. Kajita's 2015 Novel Prize in Physics

- Topics : KAGRA Starts O4 Observing Run
- Topics : ICRR Catalogue 2023 Published
- Information : Staff Reassignment
- Information : ICRR Seminar

No.117 (2023 Autumn)

- Features : Commemoration Ceremony and Commemorative Lecture Celebrating Norikura Observatory's 70th Anniversary
- Features : Features : Special Contribution from Mr. Tetsu Kobayashi, Deputy Editor, Science and Technology News Section, the Asahi Shimbun
- Features : Press Release 2023.11.24, The Highest Energy Cosmic Ray Among Observed at Telescope Array Experiment Found
- Features : Press Release 2023.11.24, Exploration of Relativistic Jets in Gamma-ray Bursts with Gamma-ray and Optical Polarization Measurements
- Features : Press Release 2023. 11.9, The Oxygen Mystery in the Early Universe: Unveiling a Rapid Increase
- Features : Press Release 2023.9.28, Two-decade monitoring of M87 unveils a precessing jet connecting to a spinning black hole
- Reports : Kashiwa Campus Open Days 2023
  - Crosstalk of Director Nakahata, Prof. Kajita on "the 25 years Anniversary of Announcement of Neutrino Oscillation"
  - ICRR Fellow Talks in in Uchu Café: Dr. Hitoshi Oshima and Dr. Sei Kato
- Reports : Daniela Hadasch, ICRR Assistant Professor Talks about High Energy Gamma-Ray Astronomy at ICRR Science Café in Tamarokuto Science Center
- Reports : Assitant Prof. Shima Shimizu (KEK) Talks at Online Event for Female Students "Yappari Butsuriga Suki"
- Awards : Project Researcher Hitoshi Oshima Wins Young Excellent Oral Presentation Award in Annual Meeting of the Society of Photography and Imaging of Japan
- Awards : Project Assistant Professor Christophe Bronner Wins the 18th Young Scientist Award of the Physical Society of Japan
- Topics : Commemorating Workshop " Development of Multi Messenger Astronomy" Held by Reorganized NNSO
- Topics : The Italian National Institute for Nuclear Physics (INFN), KEK and UTokyo Sign MoU to Promote Hyper-Kamiokande Project
- Topics : Completion of the main cavern dome section of the Hyper-Kamiokande experiment
- Topics : ICRR Calendar 2024 for Sale
- Topics : Super-Kamiokande Reusable Shopping Bag for Limited Sale
- Topics : Annual Report 2022 Published
- Topics : Call for Participats of Spring School 2024
- Information : Staff Reassignment
- Information : ICRR Seminar

(b) Public Lectures

- "Public Lecture for the entrance ceremony of Saitama University," Apr. 3, 2023, Saitama Super Arena, Saitama-City, Saitama, Takaaki Kajita (ICRR, The University of Tokyo).

- ”Public Lecture at IFCS-EFTF-ATF 2023,” May. 16, 2023, Toyama International Conference Center, Toyama-City, Toyama, Takaaki Kajita (ICRR, The University of Tokyo).
- ”Public Lecture for Daejeon Dongsin Science High School in Korea,” May. 24, 2023, Online, Takaaki Kajita (ICRR, The University of Tokyo).
- ”Public Lecture for JSPS FoS Club,” Jun. 16, 2023, Waseda Campus, Waseda University, Shinjuku-Ku, Tokyo, Takaaki Kajita (ICRR, The University of Tokyo).
- ”Public Lecture for J-Parc,” Jul. 1, 2023, Tokai Cultural Center, Naka-Gun, Ibaraki, Takaaki Kajita (ICRR, The University of Tokyo).
- ”Public Lecture for Tokyo Metropolitan University,” Jul. 5, 2023, Online, Takaaki Kajita (ICRR, The University of Tokyo).
- ”Public Lecture for ICRC2023,” Jul. 30, 2023, Toyoda Auditorium of Nagoya University, Nagoya-City, Aichi, Takaaki Kajita (ICRR, The University of Tokyo).
- ”Public Lecture for ASPRIM2023,” Aug. 12, 2023, Space Park, Koriyama-City, Fukushima, Takaaki Kajita (ICRR, The University of Tokyo).
- ”Public Lecture for the Japan Society for Aeronautical and Space Sciences,” Oct. 17, 2023, Toyama International Conference Center, Toyama-City, Toyama, Takaaki Kajita (ICRR, The University of Tokyo).
- ”Public Lecture for the 82nd Annual Meeting of the Japan Neurosurgical Society,” Oct. 25, 2023, Pacifico Yokohama, Yokohama-City, Kanagawa, Takaaki Kajita (ICRR, The University of Tokyo).
- ”Public Lecture for the 50th Anniversary of University of Tsukuba,” Oct. 29, 2023, Tokyo Campus, Tsukuba University, Bunkyo-Ku, Tokyo, Takaaki Kajita (ICRR, The University of Tokyo).
- ”Public Lecture for the 50th anniversary of Shinshu Science Education Society,” Nov. 2, 2023, Chino Cultural Complex, Chino-City, Nagano, Takaaki Kajita (KAGRA Observatory, ICRR, The University of Tokyo).
- ”Public Lecture for the Annual Meeting of Micro Manufacturing Association,” Nov. 17, 2023, Salesforce Tokyo office, Chiyoda-Ku, Tokyo, Takaaki Kajita (KAGRA Observatory, ICRR, The University of Tokyo).
- ”Public Lecture for the Establishment commemorative ceremony of Railway Technical Research Institute,” Dec. 11, 2023, Railway Technical Research Institute, Kokubunji-City, Tokyo, Takaaki Kajita (KAGRA Observatory, ICRR, The University of Tokyo).
- ”Public Lecture for Sakura Science Program,” Dec. 13, 2023, Meikei High School, Tsukuba-Chity, Ibaraki, Takaaki Kajita (KAGRA Observatory, ICRR, The University of Tokyo).
- ”Public Lecture for Ig Nobel Face-to-Face 2023 in Japan,” Dec. 17, 2023, Miraikan, Koto-Ku, Tokyo, Takaaki Kajita (KAGRA Observatory, ICRR, The University of Tokyo).
- ”Public Lecture for Junior High School Students in Higashimatsuyama City,” Dec. 19, 2023, Higashimatsuyama Citizen’s Cultural Center, Higashimatsuyama-City, Saitama, Takaaki Kajita (KAGRA Observatory, ICRR, The University of Tokyo).
- ”Public Lecture for the 44th Annual Meeting of the Laser Society of Japan,” Jan. 16, 2024, Plaza Heisei, Koto-ku, Tokyo, Takaaki Kajita (KAGRA Observatory, ICRR, The University of Tokyo).
- ”Public Lecture for the 90th Anniversary of the Japan Society of Precision Engineering,” Mar. 13, 2024, The University of Tokyo, Bunkyo-ku, Tokyo, Takaaki Kajita (KAGRA Observatory, ICRR, The University of Tokyo).
- ”The 28th ICRR x Kavli IPMU Public Lecture,” Apr. 22, 2023, Kashiwa-no-ha Conference Center, Kashiwa-City, Chiba, Masato Takita (ICRR, The University of Tokyo).
- ”Public Lecture for Astronomy Pub,” May. 20, 2023, Mitaka NETWORK University, Mitaka-City, Tokyo and Online, Yuichi Harikane (ICRR, The University of Tokyo).
- ”Public Lecture for Space Science Café by Oita Maizuru High School,” Jul. 19, 2023, Online, Yoshiaki Ono (ICRR, The University of Tokyo).
- ”Public Lecture for Yomiuri Culture Center,” Jul. 22, 2023, The Yomiuri-Shimbun, Chiyoda-Ku, Tokyo, Masami Ouchi (ICRR, The University of Tokyo).

- ”Sendai Daini High School,” Aug. 4, 2023, ICRR, Kasashiwa-City, Chiba, Hiroyuki Sagasa, Masaki Iwaya (ICRR, The University of Tokyo).
- ”Science Café,” Sep. 3, 2023, Tamarokuto Science Center, Nishi Tokyo-City, Tokyo, Daniela Hadash (ICRR, The University of Tokyo).
- ”Hokkaido Asahikawa Nishi High School,” Sep. 13, 2023, ICRR, Kasashiwa-City, Chiba, Jiro Shimoda (ICRR, The University of Tokyo).
- ”Public Lecture for the 26th Annual Meeting of Japan Society for Medical Gases,” Oct. 21, 2023, Sola City Conference Center, Chiyoda-Ku, Tokyo, Masami Ouchi (ICRR, The University of Tokyo).
- ”Kashiwa Campus Open Days,” Oct. 28, 2023, ICRR, Kasashiwa-City, Chiba, Masayuki Nakahata (ICRR, The University of Tokyo).
- ”Kashiwa Campus Open Days,” Oct. 28, 2023, ICRR, Kasashiwa-City, Chiba, Takaaki Kajita (ICRR, The University of Tokyo).
- ”Kashiwa Campus Open Days,” Oct. 28, 2023, ICRR, Kasashiwa-City, Chiba, Sei Kato (ICRR, The University of Tokyo).
- ”Kashiwa Campus Open Days,” Oct. 28, 2023, ICRR, Kasashiwa-City, Chiba, Hitoshi Oshima (ICRR, The University of Tokyo).
- ”Public Lecture for Asahi Culture Center,” Jan. 13, 2024, Asahi Culture Center Shinjuku, Shinjuku-ku, Tokyo, Yuichi Harikane (ICRR, The University of Tokyo).
- ”Utokyo Kashiwa Campus Science Camp,” 2024/2/19-2024/2/22, ICRR, Kasashiwa-City, Chiba.
- ”Public Lecture for Kawasaki City Metrology Association,” Feb. 22, 2024, Kawasaki City Hall, Kawasaki-City, Kanagawa, Yuichi Harikane (ICRR, The University of Tokyo).
- ”Kamioka Junior High School,” May. 12, 2023, Kamioka Junior High School, Hida-City, Gifu, Yoichi Asaoka (Kamioka Observatory, ICRR, The University of Tokyo).
- ”Researcher’s Talk,” Jun. 18, 2023, Kamioka Lab, Hida-City, Gifu, Kazufumi Sato (Kamioka Observatory, ICRR, The University of Tokyo).
- ”Gifu Prefectural Yoshiki High School,” Jul. 7, 2023, Kamioka Observatory, Hida-City, Gifu, Yosuke Kataoka (Kamioka Observatory, ICRR, The University of Tokyo).
- ”Geo Space Adventure,” Jul. 15, 2023, Kamioka Observatory, Hida-City, Gifu, Katsuki Hiraide, Yasuhiro Takemoto (Kamioka Observatory, ICRR, The University of Tokyo).
- ”Keio Shonan Fujisawa Senior High School,” Jul. 20, 2023, Kamioka Observatory, Hida-City, Gifu, Takaomi Yano (Kamioka Observatory, ICRR, The University of Tokyo).
- ”Toyama Prefectural Toyama High School,” Jul. 28, 2023, Kamioka Observatory, Hida-City, Gifu, Yoshinari Hayato (Kamioka Observatory, ICRR, The University of Tokyo).
- ”Utokyo’s Open Campus for high School Students,” Aug. 2, 2023, Online, Shoei Nakayama (Kamioka Observatory, ICRR, The University of Tokyo).
- ”Kibogaoka Senior High School,” Aug. 3, 2023, Kamioka Observatory, Hida-City, Gifu, Makoto Miura (Kamioka Observatory, ICRR, The University of Tokyo).
- ”Hirameki Tokimeki Science,” Aug. 4, 2023, Kamioka Observatory, Hida-City, Gifu, Masayuki Nakahata, Kei Ieki (Kamioka Observatory, ICRR, The University of Tokyo).
- ”Senior High School Attached to Kyoto University of Education,” Aug. 17, 2023, Kamioka Observatory, Hida-City, Gifu, Hiroyuki Sekiya (Kamioka Observatory, ICRR, The University of Tokyo).
- ”Nanao High School,” Aug. 18, 2023, Kamioka Observatory, Hida-City, Gifu, Jun Kameda (Kamioka Observatory, ICRR, The University of Tokyo).
- ”Asahi Culture Center Shinjuku,” Oct. 14, 2023, Asahi Culture Center Shinjuku, Shinjuku-ku, Tokyo, Shigetaka Moriyama (Kamioka Observatory, ICRR, The University of Tokyo).

- ”Senior College,” Oct. 18, 2023, Kamioka Community Hall, Hida-City, Gifu, Yoichi Asaoka (Kamioka Observatory, ICRR, The University of Tokyo).
- ”Resesarcher’s Talk,” Oct. 22, 2023, Kamioka Lab, Hida-City, Gifu, Keishi Hosokawa (Kamioka Observatory, ICRR, The University of Tokyo).
- ”Public Lecture for the Annual Meeting of Japan Radioisotope Association,” Oct. 26, 2023, Toyama International Conference Center, Toyama-City, Toyama, Atsushi Takeda (Kamioka Observatory, ICRR, The University of Tokyo).
- ”Shizuoka Prefectural Fujieda Higashi High School,” Nov. 1, 2023, Shizuoka Prefectural Fujieda Higashi High School, Fujieda-City, Shizuoka, Masato Shiozawa (Kamioka Observatory, ICRR, The University of Tokyo).
- ”Super-Kamiokande Open House,” Nov. 3, 2023, Kamioka Observatory, Hida-City, Gifu, Motoyasu Ikeda, Kei Ieki, Takaomi Yano, Yuki Kanemura, Masayuki Nakahata, Ko Abe (Kamioka Observatory, ICRR, The University of Tokyo).
- ”Public Lecture for Super-Kamiokande Open House,” Nov. 3, 2023, Kamioka Community Hall, Hida-City, Gifu, Shigetaka Moriyama (Kamioka Observatory, ICRR, The University of Tokyo).
- ”Support program of Gifu University for female junior high and high school students to choose science-related career paths,” Nov. 11, 2023, Kamioka Community Hall, Hida-City, Gifu, Yumiko Takenaga (Kamioka Observatory, ICRR, The University of Tokyo).
- ”Public Lecture for the 43rd Annual Meeting of the Japan Society of Nuclear Medicine Technology,” Nov. 17, 2023, Grand Front Osaka North Tower, Kita-ku, Osaka, Masato Shiozawa (Kamioka Observatory, ICRR, The University of Tokyo).
- ”Fusion Energy Forum,” Feb. 28, 2024, National Institute for Fusion Science, Toki-City, Gifu, Yoshinari Hayato (Kamioka Observatory, ICRR, The University of Tokyo).
- ”Keio Shonan Fujisawa Senior High School,” Mar. 1, 2024, Kamioka Observatory, Hida-City, Gifu, Yoshinari Hayato (Kamioka Observatory, ICRR, The University of Tokyo).
- ”Utokyo’s Lab Tour for High School Students,” Mar. 26, 2024, Online, Katsuki Hiraide (Kamioka Observatory, ICRR, The University of Tokyo).
- ”Ishikawa Prefectural Kanazawa Izumigaoka High School,” Mar. 28, 2024, Kamioka Observatory, Hida-City, Gifu, Makoto Miura (Kamioka Observatory, ICRR, The University of Tokyo).
- ”Toyama Prefectural Toyama High School,” Jul. 6, 2023, Kamioka Observatory, Hida-City, Gifu, Takashi Uchiyama (KAGRA Observatory, ICRR, The University of Tokyo).
- ”Science Seminar for GSA,” Jul. 15, 2023, Kamioka Community Hall, Hida-City, Gifu, Osamu Miyakawa (KAGRA Observatory, ICRR, The University of Tokyo).
- ”Keio Shonan Fujisawa Senior High School,” Jul. 20, 2023, Kamioka Observatory, Hida-City, Gifu, Masatake Ohashi (KAGRA Observatory, ICRR, The University of Tokyo).
- ”Researcher’s Talk,” Jul. 23, 2023, Kamioka Lab, Hida-City, Gifu, Masatake Ohashi (KAGRA Observatory, ICRR, The University of Tokyo).
- ”Kibogaoka Senior High School,” Aug. 4, 2023, Kamioka Observatory, Hida-City, Gifu, Shoichi Oshino (KAGRA Observatory, ICRR, The University of Tokyo).
- ”Dialogue with Dr.Genda,” Aug. 19, 2023, Kamioka Community Hall, Hida-City, Gifu, Masatake Ohashi (KAGRA Observatory, ICRR, The University of Tokyo).
- ”Dialogue with Author Yoko Ogawa,” Oct. 14, 2023, Funatsu-za, Hida-City, Gifu, Masatake Ohashi (KAGRA Observatory, ICRR, The University of Tokyo).
- ”Public Lecture for esse-sense Academic Talk,” Oct. 18, 2023, Recorded at Tokyo Midtown Yaesu, Chuo-Ku, Tokyo, Takaaki Kajita (ICRR, The University of Tokyo).
- ”Open College in Hida,” Oct. 21, 2023, Hida Earth Wisdom Center, Hida-City, Gifu, Takayuki Tomaru (KAGRA Collaborator, NAOJ).
- ”Open College in Hida,” Oct. 21, 2023, Hida Earth Wisdom Center, Hida-City, Gifu, Dan Chen (KAGRA Collaborator, NAOJ).

- ”Public Lecture for Hidakami Academia,” Oct. 28, 2023, Hida-Kamioka High School, Hida-City, Gifu, Masatake Ohashi (KAGRA Observatory, ICRR, The University of Tokyo).
- ”Researcher’s Talk,” Nov. 12, 2023, Kamioka Lab, Hida-City, Gifu, Takaaki Yokozawa (KAGRA Observatory, ICRR, The University of Tokyo).
- ”Public Lecture for Tokyo City University,” Dec. 6, 2023, Setagaya Campus, Tokyo City University, Setagaya-Ku, Tokyo, Takaaki Kajita (KAGRA Observatory, ICRR, The University of Tokyo).
- ”Public Lecture for Tokyo City University,” Dec. 6, 2023, Setagaya Campus, Tokyo City University, Setagaya-Ku, Tokyo, Masatake Ohashi (KAGRA Observatory, ICRR, The University of Tokyo).
- ”The 29th ICRR x IPMU Public Lecture,” Dec. 10, 2023, Yasuda Auditorium, Hongo Campu, The University of Tokyo, Osamu Miyakawa (KAGRA Observatory, ICRR, The University of Tokyo).
- ”Graduate School of Science, Kyoto University,” Feb. 29, 2024, Kamioka Observatory, Hida-Chty, Gifu, Takahiro Sawada (KAGRA Observatory, ICRR, The University of Tokyo).
- ”Keio Shonan Fujisawa Senior High School,” Mar. 1, 2024, Kamioka Observatory, Hida-Chty, Gifu, Osamu Miyakawa (KAGRA Observatory, ICRR, The University of Tokyo).

(c) Visitors

Kashiwa Campus (Total: 22 groups, 2,328 people)

- Junior High and High schools: 6 groups
- Universities and Graduate schools: 2 groups
- Researchers: 11 groups
- Inspections: 0 group
- Press: 2 groups
- Others: 1 group

KAMIOKA Observatory (Total: 88 groups, 1,286 people)

- Junior High and High schools: 16 groups
- Universities and Graduate schools: 14 groups
- Researchers: 15 groups
- Inspections: 26 groups
- Press: 7 groups
- Others: 10 groups

KAGRA Observatory (Total: 54 groups, 807 people)

- Junior High and High schools: 3 groups
- Universities and Graduate schools: 7 groups
- Researchers: 13 groups
- Inspections: 16 groups
- Press: 5 groups
- Others: 10 groups

F. Inter-University Research Activities

Numbers of Researchers

		Number of Applications	Number of Adoptions	Number of Researchers
Facility Usage				
Kamioka Observatory	Domestic	41	41	1,918
	International	5	5	95
Akeno Observatory	Domestic	6	6	92
Norikura Observatory	Domestic	8	8	90
Primary Cosmic rays, Kashiwa underground facility	Domestic	6	6	32
	International	1	1	42
KAGRA Observatory	Domestic	25	25	694
	International	10	10	189
High Energy Astrophysics Facility in Canarias	Domestic	14	14	565
	International	1	1	43
Laboratorial Facilities in Kashiwa	Domestic	1	1	11
	International	2	2	59
Large-Scale Comping System in Kashiwa	Domestic	14	14	208
	International	1	1	18
Conference Facilities in Kashiwa	Domestic	5	5	104
Overseas Facilities (Utah, Tibet and Bolivia)	Domestic	17	17	305
	International	6	6	213
Annual Sums	Domestic	137	137	4,019
	International	26	26	659

Joint Research				
Neutrino and Astroparticle Research	Domestic	41	41	1,918
	International	5	5	95
High Energy Cosmic Ray Research	Domestic	60	60	1,280
	International	9	9	315
Astrophysics and Gravity Research	Domestic	27	27	743
	International	10	10	189
Research Center for Cosmic neutrinos	Domestic	9	9	78
	International	2	2	60
Annual Sums	Domestic	137	137	4,019
	International	26	26	659

Research Project Titles

1. Astroparticle physics using the Super-Kamiokande detector
2. Study of atmospheric neutrino flux and neutrino oscillations
3. Study of simulation for atmospheric neutrino
4. Study of flavor identification of atmospheric and beam neutrinos
5. Study of solar neutrino energy spectrum
6. Precise measurement of Day/Night effect for B8 solar neutrinos
7. Study for Supernova monitor
8. Study of Supernova Relic Neutrinos

9. Search for proton decay via $e^+\pi^0$ mode
10. Study of proton decay p $\rightarrow \nu K^+$
11. Study in upward-going muons and high energy neutrinos
12. Sidereal daily variation of $\sim$10TeV galactic cosmic ray intensity observed by the Super Kamiokande
13. Neutrino search associated with astronominal transient events
14. Measurement of charge ratio and polarization of cosmic ray muon using undergraund particle physics experiments
15. Tokai to Kamioka Long Baseline Experiment T2K
16. Neutrino interaction study using accelerator data
17. Study for improvement of neutrino oscillation measurement in T2K expriment
18. Energy calibration for Super-Kamiokande
19. Research and development of computer simulation of Super-Kamiokande detector
20. Development of low concentration radon detection system
21. Hyper-Kamiokande project
22. Development of the Large Aperture Photodetector for a next-generation neutrino detector
23. Development of software for the next generation neutrino detector
24. New Photogrammetry Calibration for Super-Kamiokande and Hyper-Kamiokande
25. Measurement of radon in underground laboratoried and evaluate of effects from radon to experiments
26. Study for lowering backgrounds of radioisotopes in large volume detectors
27. Development of a radioactivity assay system for underground experiments
28. Measurement of neutron flux at the Kamioka underground laboratory
29. Trace level measurements of radioactive impurities for undeground experiments, such as Super-Kamiokande with ICPMS
30. RI measurement for SK-Gd project with HPGe detector
31. Generation three direct dark matter search experiment
32. A Search for Dark Matter using Liquid Xenon Detector
33. Detector structure study for future direct dark matter search experiment
34. Improvement of ultra-low radioactivity molecular sieves and implementation in dark matter search experiment
35. Research and Development for XENONnT and future Dark Matter Searches
36. Direction-sensitive dark matter search
37. A study on the near-infrared emission of liquid xenon
38. Study of double beta decay of ^{48}Ca
39. Studies on the background evaluation using laser spectroscopy analysis
40. Searches for neutrinoless double beta decay with high-pressure Xenon gas detector
41. Strain, tilt, seismic measurement in Kamioka-mine
42. R & D for a Small Atmospheric Cherenkov Telescope in Akeno Observatory
43. Development of new surface detector for observation ultra high energy cosmic ray
44. Observation of the Galactic Cosmic Ray Intensities using the Large Area Muon Telescopes

45. Multi-Color Imager for Transients, Survey and Monstrous Explosions
46. Research on geoid measurement technology using astronomical plumb deviation measurement
47. Space weather observation using muon hodoscope at Mt. Norikura
48. Observation of cosmogenic nuclides concentrations at Mt. Norikura
49. Study of secondary cosmic rays from Thundercloud at Mt. Norikura
50. Investigation of alpine plants on Mt. Norikura
51. Atmospheric mercury speciation dynamics and mercury wet deposition monitoring at the high-altitude
52. Evaluation of atmospheric SO2 to cloud acidification at free troposhere through atmospheric observation at Mt. Norikura
53. A new study for high precision measurement of muons at Mt.Norikura
54. Citizen Science ”Thundercloud Project” to elucidate the particle acceleration and interaction between cosmic rays and thunderclouds
55. Very-High-Energy Gamma-ray Observatory CTA Project
56. Development of Focal Plane Instruments for the CTA Large Sized Telescopes
57. Development of the readout system for the CTA large sized telescopes
58. Engineering runs of the first Large Size Telescope of CTA and construction of LST2-4 in La Palma Canary Islands, Spain
59. Commissioning and upgrade of the onsite data center for CTA North in La Palma, Spain
60. Development of SiPM modules for CTA-LST (3)
61. Development of the CTA/LST telescope control system
62. maintenance and operation of the optical and power systems in CTA LST
63. CTA-Japan Physics Research
64. Development of analysis method and initial observation with CTA Large-Sized Telescope
65. Development of camera for CTA small-sized telescopes
66. CTA Monte Carlo Simulation
67. Search for neutrino sources with the Large-Aperture Atmospheric Cherenkov Telescope
68. The extreme Universe viewed in very-high-energy gamma rays 2023
69. Study of High Energy Gamma-ray Objects with the MAGIC telescope
70. Kashiwa Dark Matter Symposium 2023
71. Development of a background reconstruction toolbox for the LST1 prototype and the upcoming CTA
72. Study of Extremely-high Energy Cosmic Rays by Telescope Array
73. R&D of the measurement of atmospheric transparency at the Telescope Array site
74. Study of very high energy cosmic rays around 10^{17} eV with the TALE hybrid experiment
75. Evaluation of optical characteristics of atmospheric fluorescence telescope by standard light source mounted on drone
76. Development and analysis of night cloud observation by CCD camera for automatic observation of air fluorescence detector
77. Observing ultrahigh-energy cosmic rays with new fluorescence detectors at Telescope Array site
78. Research and development of a Fresnel lens air fluorescence telescope for the next generation UHECR observation
79. Experimental Study of High-energy Cosmic Rays in the Tibet ASγ experiment

80. Sidereal daily variation of $\sim$10TeV galactic cosmic ray intensity observed by the Tibet air shower array
81. Study of the composition of cosmic-rays at the Knee
82. A study on variation of interplanetary magnetic field with the cosmic-ray shadow by the sun.
83. Air shower observation for high-energy gamma ray and cosmic ray detections at the Chacaltaya Cosmic Ray Observatory
84. Study of High Energetic Radiation from Thundercloud in the Altiplano
85. Study of solar magnetic fields using the cosmic-ray Sun's shadow observed at the southern hemishpere
86. Study of high-energy cosmic-ray anisotropy at the Chacaltaya Cosmic Ray Observatory
87. Development of an advanced Compton camera using SOI pixel semiconductor
88. Design study of a Compton camera for study of cosmic rays
89. Study of Fast Moving Dark Matters and Meteoroids using High Sensitivity CMOS Camera System
90. Study on High Energy Cosmic-ray Sources by Observations in Space with CALET
91. Comparative study of high energy astrophysical phenomena
92. Development of a new code for cosmic-ray air shower simulation
93. Cosmic ray interactions in the knee and the highet energy regions
94. Development of improvements and test observations for the elucidation of very-high energy particle emitting objects by NTA
95. Clear identification of very high energy particle sources by NTA
96. Project for make "Cosmic Ray" to a common word (Application of Virtual Reality technology)
97. Development of the data acquisition system for the extension of the TA$\times$4 surface detectors
98. YMAP symposium 2023
99. Observation of airshower fluorescence light at the TA-FD site by using an Imaging UV telescope
100. Investigating the gamma-ray signatures of feedback microphysics in star-forming environments
101. Search for UHECR sources considering the galactic magnetic field and the mass composition
102. Research of Large-scale Gravitational wave Telescope(XIII)
103. Study of Gravitational-wave by cryogenic laser interferometer CLIO in KAMIOKA Mine(VII)
104. Development of Monitor and Interlock System for KAGRA
105. Research on cryogenic payload for KAGRA
106. Development of conduction cooling schemes for KAGRA
107. R&D for the intensity stabilization of the laser system in KAGRA
108. Development of scattered light measurement technique and noise reduction for improving sensitivity in KAGRA IV
109. Development of optical cavity for ultranarrow stable lasers
110. Study of Environmental Noise Reduction in KAGRA
111. Study of the environmental noise of KAGRA detector by environmental injection
112. Noise characteristics analysis using machine learning and deep learning and its application to interferometer diagnosis (III)
113. Development of glitch data analysis system for improving gravitational detection
114. Search for poorly modeled gravitational wave signal using KAGRA

115. Reduction of Non-Stationary Noise in KAGRA
116. Development of a noise source identification tool for improving the sensitivity of KAGRA telescope
117. Development of a new caliabration method and sensitivity improvement for gravitational wave telescope based on thermal nosie
118. Numerical Simulation of Electro-Magnetic Wave Propagation in Gravitational wave Detector XI
119. Development of a high performance sapphire mirror suspension
120. Control and automatic operation for KAGRA
121. Construction of KAGRA data transfer and storage system (9)
122. Promotion of collaborative research to incorporate KAGRA data into the low latency international gravitational wave search network (3)
123. Construction of a diagnostic system for the gravitational wave detector
124. Test measurement of underground gravity measurement at micro-meter scale
125. Precise geophysical observation at the Kamioka underground site and modeling of crustal activities
126. Gravitational Wave Data Analysis
127. Cosmic Reionization and Galaxy Formation Probed with Large Optical Near-Infrared Telescopes
128. Evolution of the universe and particle physics
129. Detection of time variations for cosmogenic nucleid Be-7
130. Time profile of radioactive Cs concentration and its aerosol size distribution in local area
131. Development of new analysis techniques for supernova neutrino observation by Super Kamiokande
132. Behavior of radionuclides in the marine environment
133. Frontier of the planetary material science
134. Measurement of the intrinsic radioisotopes in electron-tracking Compton telescopes for studying the radiation mechanism of extragalactic diffuse gamma-rays
135. Water Purification System R&D for Precision Neutrino Detectors
136. Precise calculation of the atmospheric neutrino flux
137. CRC workshop for future plans in cosmic ray research
138. Light scattering measurement in the water using the Super-Kamiokande detector
139. Study of supernova neutrinos in Super-Kamiokande
140. Data Taking, Calibrations, Measurements and Analysis with Super-Kamiokande I – VI
141. Towards a multiphysics liquid Xe TPC with scintillation and charge multiplication readouts
142. Hyper-Kamiokande OD PMTs QA
143. Research and Development of the high-performance segment mirrors and the camera entrance windows for the CTA Large Size Telescopes
144. Ultra-high-energy cosmic-ray origin studies with the Telescope Array and TAx4 surface detector
145. Study of Anisotropy of Ultra High Energy Cosmic Rays with Telescope Array and TAx4
146. Study of high-energy cosmic rays at a high altitude in Tibet, China
147. Study for Galactic CR origin using the ALPACA air shower array in Bolivia
148. Constraining the nature of the emission in PeVatrons observed by Alpaca.

149. Bayesian analysis on the origin of ultra-high energy cosmic ray events collected by the TA experiment
150. Study of the signals and reconstruction of cosmic ray events via surface detectors from the Telescope Array and the Pierre Auger cosmic ray detectors
151. Synergies at new frontiers at gamma-rays, neutrinos and gravitatinal waves.
152. Filter cavity experiments for the frequency dependent squeezed light for KAGRA
153. Measuring the birefringence of the sapphire mirrors installed in the KAGRA detector
154. Position control system for silicon monolithic suspension in cryogenic gravitational waves detectors.
155. Implementing Sophisticated Data Analysis Methods on KAGRA Data
156. Applications of machine learning technique on gravitational wave detection
157. Study the Gravitational Wave with the Most Modern Technology
158. Noise Subtraction of KAGRA Data using Machine Learning Method: DeepClean
159. Developing a template-free method of searching gravitational wave signals with autoregressive modeling
160. Low-Latency Localization and Parameter Estimation of Gravitational Waves Using Probabilistic Deep Learning
161. Self interacting dark matter and gravitational waves
162. A water monitoring system for Hyper-Kamiokande
163. Constraining systematics at T2K and SuperKamiokande oscillation analyses using neutrino-nucleus interaction models

G. List of Committee Members

(a) Board of Councillors

NAKAHATA, Masayuki	ICRR, The University of Tokyo
MORIYAMA, Shigetaka	ICRR, The University of Tokyo
OGIO, Shoichi	ICRR, The University of Tokyo
KAWASAKI, Masahiro	ICRR, The University of Tokyo
OKOSHI, Shinichi	Graduate School of Science, The University of Tokyo
SAITO, Nobuhito	The University of Tokyo
SAITO, Naohito	Institute of Particle and Nuclear Studies, KEK
AOKI, Shinya	Yukawa Institute for Theoretical Physics, Kyoto University
TSUNETA, Saku	National Astronomical Observatory of Japan
KAJINO, Fumiyoshi	Faculty of Science and Engineering, Konan University
MORI, Masaki	College of Science and Engineering, Ritsumeikan University
YOKOYAMA, Junichi	Research Center for the Early Universe, The University of Tokyo
YAMADA, Toru	Institute of Space and Astronautical Science
ASAI, Shoji	International Center for Elementary Particle Physics, The University of Tokyo
KUSANO, Kanya	Institute for Space-Earth Environmental Research, Nagoya University
TAKITA, Masato	ICRR, The University of Tokyo

(b) Advisory Committee

NAKAHATA, Masayuki	ICRR, The University of Tokyo
KITANO, Ryuichiro	KEK Theory Center
YAMAZAKI, Ryo	College of Science and Engineering, Aoyama Gakuin University
SEIYA, Yoshihiro	Graduate School of Science, Osaka Metropolitan University
WADA, Michiharu	Wako Nuclear Science Center, Institute of Particle and Nuclear Studies, KEK
NAKAJIMA, Yasuhiro	Graduate School of Science, The University of Tokyo
TSURU, Takeshi	Graduate School of Science, Kyoto University
TAJIMA, Hiroyasu	Institute for Space-Earth Environmental Research, Nagoya University
ITOW, Yoshitaka	Institute for Space-Earth Environmental Research, Nagoya University
KANDA, Nobuyuki	Graduate School of Science, Osaka Metropolitan University
NISHIJIMA, Kyoshi	School of Science, Tokai University
TAKITA, Masato	ICRR, The University of Tokyo
MORIYAMA, Shigetaka	ICRR, The University of Tokyo
OGIO, Shoichi	ICRR, The University of Tokyo
KAWASAKI, Masahiro	ICRR, The University of Tokyo
SHIOZAWA, Masato	ICRR, The University of Tokyo
OHASHI, Masatake	ICRR, The University of Tokyo
KUBO, Hidetoshi	ICRR, The University of Tokyo

(c) Inter-University Research Advisory Committee

TSUNESADA, Yoshiki	Graduate School of Science, Osaka Metropolitan University
KANDA, Nobuyuki	Graduate School of Science, Osaka Metropolitan University
NISHIJIMA, Kyoshi	School of Science, Tokai University
MORI, Masaki	College of Science and Engineering, Ritsumeikan University
NAKAMORI, Takeshi	Faculty of Science, Yamagata University
SHIOMI, Atsushi	College of Industrial Technology, Nihon University
ASO, Yoichi	National Astronomical Observatory of Japan
TAKEUCHI, Yasuo	Graduate School of Science, Kobe University
TAKITA, Masato	ICRR, The University of Tokyo
MIYOKI, Shinji	ICRR, The University of Tokyo
OKUMURA, Kimihiro	ICRR, The University of Tokyo
NODA, Koji	Institute for Advanced Academic Research, Chiba University
SEKIYA, Hiroyuki (Organizer)	ICRR, The University of Tokyo
NAKAHATA, Masayuki (Observer)	ICRR, The University of Tokyo

H. List of Personnel

Director NAKAHATA, Masayuki,

Vice-Director TAKITA, Masato

ICRR HQ in Kashiwa Campus

- High Energy Cosmic Ray Division

Scientific Staff	ASANO, Katsuaki,	ENOMOTO, Ryoji,	HADASCH, Daniela,
	KAWAGUCHI, Kyohei,	KAWATA, Kazumasa,	KIM, Hang Bae,
	KUBO, Hidetoshi,	MATTHEWS, John Norman,	MAZIN, Daniel,
	NODA, Koji,	NONAKA, Toshiyuki,	OGIO, Shoichi,
	OHISHI, Michiko,	OHNISHI, Munehiro,	SAITO, Takayuki,
	SAKO, Takashi,	SAKO, Takashi,	SASAKI, Makoto,
	SHIMODA, Jiro,	STRZYS, Marcel,	TAJIMA, Hiroyasu,
	TAKEDA, Masahiro,	TAKITA, Masato,	VOVK, Ievgen,
	YAMAMOTO, Tokonatsu,	YOSHIDA, Tatsuo,	YOSHIKOSHI, Takanori,
Technical Staff	AOKI, Toshifumi,	KHANGULYAN, Dmitry,	KOIZUMI, Chikako,
	OHOKA, Hideyuki,	SEKINO, Koichi,	TAMURA, Akiko,
Research Fellow	ANZORENA, Marcos,	FUJITA, Keitaro,	FUKAMI, Satoshi,
	INADA, Tomohiro,	KATO, Sei,	KAWASHIMA, Tomohisa,
	KOBAYASHI, Yukiho,	OHMURA, Takumi,	OSHIMA, Hitoshi,
	SAGAWA, Hiroyuki,	SHIN, Heungsu,	TAKEISHI, Ryuji,
	WADA, Tomoki,	YEUNG, Kin Hang,	
Secretary	IDOMURA, Takako,	KAMO, Miwako,	SHIRAGA, Ryoko,
	SUGAHARA, Midori,	TAKAGI, Akiko,	

- Astrophysics and Gravity Division

Scientific Staff	HARIKANE, Yuichi,	IBE, Masahiro,	KAWASAKI, Masahiro,
	ONO, Yoshiaki,	OUCHI, Masami,	
Research Fellow	ASAI, Kento,	LIANG, Yongming,	

Kamioka Observatory

Director	SHIOZAWA, Masato,		
Scientific Staff	ABE, Ko,	ASAOKA, Yoichi,	BRONNER, Christophe,
	GONIN, Michel,	HAYATO, Yoshinari,	HIRAIDE, Katsuki,
	HOSOKAWA, Keishi,	IEKI, Kei,	IKEDA, Motoyasu,
	ITOW, Yoshitaka,	KAMEDA, Jun,	KATAOKA, Yosuke,
	MIURA, Makoto,	MORIYAMA, Shigetaka,	NAKAHATA, Masayuki,
	NAKANO, Yuki,	NAKAYA, Tsuyoshi,	NAKAYAMA, Shoei,
	NISHIMURA, Yasuhiro,	SATO, Kazufumi,	SEKIYA, Hiroyuki,
	TAKEDA, Atsushi,	TAKEMOTO, Yasuhiro,	TANAKA, Hidekazu,
	YANO, Takatomi,	DI LODOVICO, Francesca Romana,	PLAYFER, Stephen Michael,
Administrative Staff	KITANO, Ayano,	YOSHIDA, Takuto,	
Public Relations Staff	TAKENAGA, Yumiko,		
Technical Staff	HAMA, Satoshi,	HIGASHI, Tetsuji,	ISHITA, Katsumi,
	MINE, Shunichi,	ONOUE, Tatsuya,	
Research Fellow	ABE, Seisho,	NOGUCHI, Yohei,	
Secretary	DOI, Kyoko,	MAEDA, Yukari,	NISHIDA, Hiromi,
	OGAWA, Chitose,		

KAGRA Observatory

Director	OHASHI, Masatake,		
Scientific Staff	AONO, Yuri,	MIO, Norikatsu,	MIYAKAWA, Osamu,
	MIYOKI, Shinji,	MORISAKI, Soichiro,	NARIKAWA,Tatsuya,
	OSHINO, Shoichi,	SAWADA,Takahiro,	TAGOSHI, Hideyuki,
	TAKAHASHI, Hirotaka,	TOMARU, Takayuki,	UCHIYAMA, Takashi,
	USHIBA, Takafumi,	YAMAMOTO, Kazuhiro,	YAMAMOTO, Takahiro,
	YOKOZAWA, Takaaki,	YUZURIHARA, Hirotaka,	
Administrative Staff	KATO, Daichi,	OKINAKA, Mihoko,	
Technical Staff	AOUMI, Masakazu,	KAMIIZUMI, Masahiro,	KIMURA, Nobuhiro,
	NAKAGAKI, Koji,	NODE, Ayako,	OMAE, Akio,
	PENA ARELLANO, Fabian,	SAKAI, Akiko,	SAKAMOTO, Eri,
	SHIMODE, Katsuhiko,	TAKAHASHI, Masahiro,	TAKASE, Takashi,
	TANAKA, Kenta,	YAMAGUCHI, Hirokazu,	YASUI, Hiromi,
	YOSHIMURA, Mitsuharu,		
Research Fellow	TUYENBAHEV, Darkhan,	UCHIKATA, Nami,	
Secretary	KIKUCHI, Rie,	KUDO, Naomi,	NOJIRI, Midori,

High Energy Astrophysics Facility in Canarias

Director	KUBO, Hidetoshi,		

Research Center for Cosmic Neutrinos

Director	OKUMURA, Kimihiro,		
Scientific Staff	KAJITA, Takaaki,	TASHIRO, Takuya,	TOKANAI, Fuyuki,
Technical Staff	AOYAMA, Shohei,	SHINOHARA, Masanobu,	
Secretary	KITSUGI, Atsuko,	MASHIMA, Chieko,	

Norikura Observatory

Director	SAKO, Takashi,		
Technical Staff	AWAI, Kyosuke,	HAYAKAWA, Hideaki,	IMANISHI, Hidenori,
	INOME, Yusuke,	OKAZAKI, Nao,	SHIMODAIRA, Hideaki,
	TOMURA, Tomonobu,	USHIMARU, Tsukasa,	

Akeno Observatory

Director	OGIO, Shoichi,		
Technical Staff	EBISAWA, Yutaka,		

Graduate Students

Doctor	ABE, Shotaro,	BAXTER, Joshua Ryo,	CHIBA, Renichi,
	FUJISUE, Kozo,	GOTO, Ryota,	HAN, Seungho,
	HASHIYAMA, Kazuaki,	ISOBE, Yuki,	IWAYA,Masaki,
	KANEMURA, Yuki,	KASAI, Kentaro,	KATO, Takashi,
	KAWASHIMA, Teruyoshi,	KUSAFUKA, Yo,	LEE, Eunsub,
	MATSUMOTO, Akinori,	MIKI, Shintaro,	NAKAYAMA, Yuhei,
	NISHIWAKI, Kosuke,	OHTANI, Yoshiki,	SHIMIZU, Kotaro,
	SUN, Dongsheng,	TAKAHASHI, Kaoru,	TAMAKI, Masahide
	TANG, Shenli,	TOMIYA, Takuya,	UMEDA, Hiroya
	WANG, Xubin,	WATANABE, Keiichi,	XU, Yi,
	YOKOE, Yoshichika,	ZHANG, Yechi,	

Master	ABOUNNASR-MARTINS, Théo,	AOKI, Takafumi,	CHITOSE, Akifumi,
	FUJII, Shingo,	GARG, Suyog,	ICHINOSE, Yuto,
	ITOKAWA, Takumi,	KAMINAGA, Yoshino,	KOBAYASHI, Kazuya,
	KOCHI, Hiroki,	KOYAMA, Chisato,	MIYAMOTO, Shinya,
	MIZUNO, Atsushi,	MURAKAMI, Yasuhiro,	NAKANE, Minami,
	NEDA, Shunsuke,	TSUCHIDA, Shunsuke,	USUI, Kazuki,
	YAMAMURA, Shunsei,	YANAGISAWA, Hiroto,	ZHU, Chenghao,

Administrative Division

Administrative Staff	AKAIDA, Yohei,	AKASHI, Yoko,	AKIYAMA, Makiko,
	FUKUHARA, Nana,	IKEDA, Hiroshi,	MARUMORI, Yasuko,
	MATSUMOTO, Yasuo,	NAKAYA, Yukiko,	NAMAI, Hiroki,
	OKANO, Yuka,	SAITO, Akiko,	SATO, Hiroki,
	WATANABE, Taishi,	YAMAGISHI, Yukinao,	YAMAGUCHI, Akiko,
	YAZAKI, Keiichi,		
Research Administrator	KURACHI, Masafumi,	MORITA, Mihoko,	OTA, Ritsuko,
	SATO, Ritsuko,		
Public Relations Staff	ITO, Yoriko,	NAKAMURA, Makio,	
Archive Room	NAKAMURA, Kenzo,		



INSTITUTE FOR COSMIC RAY RESEARCH
THE UNIVERSITY OF TOKYO

Address 5-1-5, Kashiwanoha, Kashiwa-shi, Chiba, 277-8582 Japan
TEL +81-4-7136-3102
FAX +81-4-7136-3115
URL www.icrr.u-tokyo.ac.jp

ICRR
Institute for Cosmic Ray Research
University of Tokyo